

MONASH UNIVERSITY
THESIS ACCEPTED IN SATISFACTION OF THE
REQUIREMENTS FOR THE DEGREE OF
DOCTOR OF PHILOSOPHY

ON..... 9 November 2004.....

.....
Sec. Research Graduate School Committee

Under the Copyright Act 1968, this thesis must be used only under the normal conditions of scholarly fair dealing for the purposes of research, criticism or review. In particular no results or conclusions should be extracted from it, nor should it be copied or closely paraphrased in whole or in part without the written consent of the author. Proper written acknowledgement should be made for any assistance obtained from this thesis.

ERRATA

Page vi, 1st paragraph, 5th sentence: "...and $[010]_b // [01\bar{2}]_a$." for "...and $[010]_b // [01\bar{2}]_a$."

Page 23, 2nd paragraph: "Bagaryatsky" for "Bagaryatskii"

Page 28, 2nd paragraph: "Bagaryatsky" for "Bagaryatskii"

Page 32, final paragraph: "[156-158]." for "[156-158]"

Page 59, 1st paragraph, line 5 and line 11: "§3.3" for "§4.3"

Page 60, 1st paragraph: "...using conventional TEM." for "...using conventional TEM.."

Page 119, Figure 5.31(a): No scale marker; the long axis of the dislocation loop upon which precipitation has proceeded is approximately 300 nm.

Page 176, near mid-page: " $(100)_b // (100)_a$, $(0\bar{2}1)_b // (014)_a$ " for " $(100)_b // (100)_a$, $[0\bar{2}1]_b // [014]_a$ "

Page 189, near top of page: " $(100)_b // (100)_a$, $(0\bar{2}1)_b // (014)_a$ " for " $(100)_b // (100)_a$, $[0\bar{2}1]_b // [014]_a$ "

Page 191, near top of page: " $(100)_b // (100)_a$, $(0\bar{2}1)_b // (014)_a$ " for " $(100)_b // (100)_a$, $[0\bar{2}1]_b // [014]_a$ "

Page 203, near bottom of page: " $(100)_b // (100)_a$, $(0\bar{2}1)_b // (014)_a$ " for " $(100)_b // (100)_a$, $[0\bar{2}1]_b // [014]_a$ "

Page 212, Reference 101: "Sankaran, R. and Laird, C." for "Sandaram, R. and Laird, C."

ADDENDUM

Page 88, 1st paragraph, 1st sentence: "Dislocation loops were observed not to grow significantly..." for "Dislocation loops were observed to cease significant growth..."

Precipitation at Dislocations in Al-Cu-Mg Alloys

**A Thesis Submitted for the Degree of
Doctor of Philosophy**

Graham B. Winkelman

B. Eng. (Hons), University of South Australia

M. Eng. Sc., University of Queensland

November 2003

School of Physics and Materials Engineering
Monash University
Melbourne, Victoria,
Australia

Contents

1.0	INTRODUCTION	1
1.1	Precipitation Processes	1
1.2	Research Design	2
1.3	Overview of the Thesis	3
2.0	BACKGROUND AND FORMULATION OF RESEARCH DIRECTION	5
2.1	Processing of Al-Cu-Mg Alloys for Mechanical Properties	6
2.1.1	Prerequisites for Age-Hardening in a Generic Alloy	6
2.1.2	Phase Equilibria in Al-Cu-Mg Alloys	8
2.1.3	The Hardening Response of Al-Cu-Mg Alloys	10
2.1.4	Microstructural Changes during Ageing in Al-Cu-Mg Alloys	11
2.2	Aspects of Precipitate Nucleation and Growth	15
2.2.1	Classical Homogeneous Nucleation	15
2.2.2	Heterogeneous Nucleation at Dislocations	16
2.3	Strengthening Precipitates in Al-Cu-Mg Alloys	19
2.3.1	The θ'' and θ' -Phases	19
2.3.2	The Ω -Phase	21
2.3.3	GPB Zones	22
2.3.4	The S-Phase	23
2.3.5	The T'-Phase	32
2.4	Implications for the Present Work	33
3.0	RESEARCH DESIGN AND METHODOLOGY	34
3.1	Alloy Selection and Preparation	35
3.2	Dislocation Distribution and Thermal Processing	37
3.2.1	Introduction of Dislocation Sub-Structure	38
3.2.2	Thermal Processing	40
3.3	Hardness Testing	42

3.4	Transmission Electron Microscopy	45
3.4.1	Foil Preparation	45
3.4.2	Conventional Imaging and Diffraction	46
3.4.3	High Resolution Electron Microscopy	50
3.4.3.1	Background to the Technique	51
3.4.3.2	Imaging of Particles in Aluminium Alloys	52
3.4.4	Summary of TEM Facilities and Techniques	54
4.0	AGEING RESPONSE OF TERNARY Al-Cu-Mg ALLOYS	55
4.1	Response to Ageing of Al-Cu-Mg Alloys	56
4.1.1	Series I - Al-1.1Cu-xMg Alloys	56
4.1.2	Series II - Al-xCu-1.7Mg Alloys	57
4.1.3	Strategic Selection of Alloys	59
4.2	Microstructural Evolution	60
4.2.1	Vacancy Condensation (Dislocation) Loops	60
4.2.2	Precipitation Processes in Al-1.1Cu-xMg Alloys	64
4.2.3	Precipitation Processes in Al-xCu-1.7Mg Alloys	67
4.2.4	Prolonged Over-Ageing	70
4.3	Pre-Aged Al-Cu-Mg - Microstructural Evolution and Hardness	72
4.3.1	Micro-Indentation Hardness	72
4.3.2	Precipitation Processes - Pre-Aged Al-1.1Cu-xMg Alloys	74
4.3.3	Precipitation Processes - Pre-Aged Al-xCu-1.7Mg Alloys	80
4.4	Interpretation of Results	84
4.4.1	Microstructure and Corresponding Hardness	84
4.4.2	Influence of Initial Dislocation Substructure	88
4.5	Chapter Summary and Directions of the Present Research	89
5.0	PRECIPITATES AT DEFECTS IN Al-Cu-Mg ALLOYS	91
5.1	Dislocation Loop Crystallography	92
5.1.1	Dislocation Loops in $\{110\}_\alpha$	93
5.1.2	Dislocation Loops in $\{111\}_\alpha$	97
5.1.3	Summary of Loop Characteristics	103
5.2	Precipitation of θ'-Phase at Dislocation Loops	104

5.3	Precipitation of Ω-phase at Dislocation Loops	106
5.4	Precipitation of S-phase at Dislocation Loops	107
5.4.1	Nucleation Upon Dislocation Loops Lying in $\{110\}_\alpha$	110
5.4.2	Nucleation Upon Dislocation Loops Lying in $\{111\}_\alpha$	114
5.4.3	Nucleation on Loops Intermediate between $\{111\}_\alpha$ and $\{011\}_\alpha$	120
5.5	Interpretation of Results	122
5.6	Chapter Summary and Directions for Present Research	128
6.0	CRYSTALLOGRAPHY AND MORPHOLOGY OF S-Phase	130
6.1	Alloy Selection and Heat Treatment	131
6.2	Orientation of S-Phase	132
6.2.1	Magnitude of Rotation	132
6.2.2	Particle-Matrix Orientation Relationship	143
6.3	The Macroscopic Habit Plane of the S-Phase	148
6.3.1	The Habit Plane of Interfaces with Ledges	148
6.3.2	Characteristics of Interfacial Steps	154
6.3.3	Exceptions to the Model of Macroscopic Interface Orientation	157
6.4	Lattice Parameter of S-phase Unit Cell	159
6.5	Aspect Ratio of S-phase Precipitates	164
6.6	Interfacial Coherency	165
6.6.1	Coherent Interfaces of Laths of Standard Orientation	166
6.6.2	Interfaces with Ledges	168
6.6.2.1	Ledges of $1c_s$ Riser Height	168
6.6.2.2	Ledges of $2c_s$ Step Height	171
6.7	Interpretation of Results	173
6.7.1	Redefinition of the Orientation of S-phase Precipitates	174
6.7.2	The Strained Lattice of the S-phase in ROR1 and ROR2	177
	Thickness of Particles in ROR1	184
6.7.4	Moiré Intersections and Precipitate Thickness in ROR2	185
6.8	Chapter Summary	189

7.0	NUCLEATION AND GROWTH OF THE S-Phase REVISITED	190
7.1	Location of Precipitates in ROR1 and ROR2 at Dislocation Loops	191
7.2	Selection of Precipitate Crystallography	193
8.0	SUMMARY AND CONCLUSIONS	201
9.0	REFERENCES	207

Abstract

The work presented here concentrates upon the characteristics of heterogeneous precipitation at dislocations in Al-Cu-Mg alloys, focussing upon, but not limited to, precipitates of the orthorhombic S-phase (Al_2CuMg). In recognition of the preference of this phase for nucleation at dislocations, it is perhaps surprising that there has not, to date, been a systematic evaluation of the influence of strain field characteristics on the (poorly understood) range of precipitate crystallography displayed. A series of 10 artificially aged Al-Cu-Mg alloys of systematically varying composition and based on the ternary alloy Al-1.1Cu-1.7Mg [at.%] have been studied by both conventional and high-resolution TEM. Artificial ageing for 60 s at 150°C led to the generation of a high density of dislocation loops lying in $\{110\}_\alpha$ and $\{111\}_\alpha$, the relative proportions of which was a function of alloy chemistry. In agreement with published literature, precipitates of the S-phase formed as elongated particles along $\langle 100 \rangle_\alpha$, sharing a crystallographic relationship with the aluminium matrix such that $(100)_s // (100)_\alpha$, $[001]_s // [021]_\alpha$ (parallel to the coherent habit plane of the particle) and $[010]_s // [01\bar{2}]_\alpha$. This orientation relationship was labelled Rational Orientation Relationship 1 (ROR1). A second rational orientation of the S-phase has been defined, described by $(100)_s // (100)_\alpha$ and $[0\bar{2}1]_s // [014]_\alpha$ (coherent habit plane), and has been labelled ROR2. Particles in ROR1 form at dislocation loops in $\{110\}_\alpha$ (pure edge dislocation), while dislocation loops that lie parallel to $\{111\}_\alpha$ gave rise to particles in both ROR1 and ROR2, where the latter forms at segments of the dislocation line that have an appreciable screw component. ROR1 and ROR2 are separated by a lattice rotation of $6.9^\circ \pm 0.25^\circ$, and an apparently continuous variation in lattice orientation is observed between the limits defined by these orientations. The orientation of the macroscopic particle-matrix interface varies systematically as the lattice orientation varies, and is composed of steps $1e_s$ in height. An anisotropic change in the lattice parameters defining the unit cell of the S-phase is both expected and observed when comparing particles in ROR1 and ROR2.

The observations are discussed in the context of an analysis of mechanisms of strain accommodation in the course of individual nucleation events, where it is concluded that accommodation of the lattice misfit vector of the precipitates (dilatation) is not a significant factor leading to heterogeneous nucleation of S-phase at dislocations. This is in contrast to the formation of θ'' at dislocations observed in the present work, where the accommodation of a volume contraction in the distorted matrix near the dislocation regarded to be important. In the absence of a dilatational volume change, a rationale is provided for the accommodation of a shear strain component during S-phase formation.

Statement of Sources

This thesis contains no material which has been accepted previously for the award of any other degree or diploma in any university or other institute and, to the best of my knowledge and belief, it contains no material previously published or written by any other person, except where due reference is made in the text of the thesis.

[REDACTED]

Graham B. Winkelman
Melbourne, November 2003

Acknowledgments

I have been fortunate to benefit greatly from the influence of my supervisors and I owe a great debt of thanks to Professor Barry C. Muddle and Dr. Krishnamurthy Raviprasad for their guidance, honesty and inspiration during the project. Associate Professor Simon P. Ringer (University of Sydney) and Professor Ian J. Polmear are also thanked for their advice during early candidature. Dr. Jian-Feng Nie, Dr. Joanne Etheridge, Professor John P. Hirth and Dr. Laure Bourgeois are thanked for technical discussions.

I also acknowledge the following individuals who have helped in various ways known to them: Dr. Stan P. Lynch (Defence Science and Technology Organisation), Shaun Bulcock (University of Sydney), Julie Fraser, Jim Mitchell, Silvio Mattevich, Renji Pan, Claude Urbani, Chamini Mendis, Layla Godfrey, John Whale (Deakin University), Ian McKay and Stavroula Moutsos. Members of the workshop in the School of Physics and Materials Engineering at Monash University are gratefully acknowledged for their willingness and ability to help at all times.

Finally, love and thanks to Leanne, Mum and Dad and family in Adelaide and Melbourne, and friends in Melbourne and Adelaide.

List of Acronyms

(hkl)	Set of planes indexed using Millers indices
1-DAP	One-dimensional atom probe field-ion microscope
3-DAP	Three-dimensional atom probe field-ion microscope
a_1, b_1, c_1	Lattice parameters of the unit cell
AA	Artificially aged
AP	Atom probe
\mathbf{b}	Burgers vector of a dislocation
\mathbf{B}	Vector parallel to electron beam direction
BF	Bright field
CBED	Convergent beam electron diffraction
CCW	Counter-clockwise
C_s	Spherical aberration in TEM
CW	Clockwise
$d(hkl)$	Lattice spacing of planes indexed as (hkl)
DF	Dark field
EDXS	Energy dispersive X-ray spectrometry
fcc	Face-centred cubic
$\mathbf{g}(hkl)$	Reciprocal lattice vector normal to diffracting plane (hkl) , with magnitude $1/d(hkl)$
hcp	Hexagonal close-packed
HREM	High resolution transmission electron microscopy
IADS	International Alloy Designation System
LFZ	Loop-free zone
NA	Naturally aged
PALS	Positron Annihilation Lifetime Spectroscopy
PFZ	Precipitate-free zone
Q	Quench
ROR	Rational Orientation Relationship
SAED	Selected-area electron diffraction
SFC	Stacking fault contrast
SSSS	Super-saturated solid solution of alloying elements in aluminium
ST	Solution treatment
TEM	Transmission electron microscopy
UMIS	Ultra-microhardness Indentation System
VHE	Vickers hardness equivalent
VHN	Vickers hardness number
α	Solid solution of alloying elements in aluminium
β	Angle between Moire intersection plane and matrix planes
ξ	Section
ξ	Dislocation line direction

1.0 Introduction

1.1 Precipitation Processes

It has been suggested that the discovery of age-hardening in Al-rich Al-Cu-Mg alloys [1] was the first new method of hardening in alloys since the quenching of steel in the second millennium before Christ [2]. Subsequent investigations into the age-hardening effect [3-5] in these alloys began a process of understanding that continues to the present day. Forming the basis of the important 2000 series of wrought aluminium alloys, Al-Cu-Mg alloys are widely used in the aircraft manufacturing industry, where the high hardness and strength of appropriately processed components contribute to the high degree of damage tolerance displayed in service. The achievement of high hardness and strength in these alloys is dependent upon the presence of a dispersion of solute-rich second-phase particles (precipitates), which serve to strengthen the alloy by impeding the movement of mobile crystal defects (dislocations). The *scale* and *distribution* of second-phase particles are critical to the resultant strength of the alloy [2] and the factors controlling precipitate distributions in these alloys have been studied extensively.

The formation of solute-rich second-phase particles in the Al-Cu-Mg system follows directly from alloy thermodynamics, where the alloy seeks to lower its free energy by reducing the supersaturation of alloying elements quenched into the material following higher-temperature solution treatment in a single-phase region. At room temperature, the decomposition is slow while artificial ageing at temperatures between 100°C and 190°C [6,7] accelerates the decomposition. Precipitation in this system is characterised by *solid-state nucleation* and *growth*. Selected precipitate species forming in these alloys favour nucleation within the strain field surrounding the core of pre-existing dislocations, and the precipitate species of principal interest include θ'

and the S-phase. Both of these species are observed to be present in a wide compositional range of technologically significant alloys.

The distribution of pre-existing crystal defects obviously influences the subsequent distribution of heterogeneously-nucleated precipitates in these alloys following artificial ageing, and this has implications for the mechanical properties achieved. For example, the introduction of dislocations by thermomechanical processing prior to precipitation (e.g. [8]) may be used to refine the distribution of precipitates of the S-phase, leading to an improved hardening response. Although these processes have received wide coverage in the literature, there is only cursory attention given to the manner in which the characteristics of the dislocation influence precipitate variant selection and morphology. For example, the observed range of crystallography of precipitates of the S-phase, including a rigid-body rotation of the precipitate lattice away from the well-described rational orientation relationship, has not been investigated with respect to the specific nature of the dislocations upon which they nucleate.

Therefore, it is the aim of this thesis to report an examination of the influence of dislocation character upon the crystallography of strengthening precipitates in the Al-Cu-Mg system, with particular reference (though not limited) to precipitates of the S-phase. In order to achieve this, it will be demonstrated that a new appreciation of the morphology and crystallography of the S-phase is necessary, and this forms a significant component of the work presented here.

1.2 Research Design

Ten Al-Cu-Mg alloys have been prepared, spanning a Cu:Mg atomic ratio of 0.1 – 8.5 in the ternary alloys. Analysis of a subset of four alloys aged isothermally at 150°C comprised the bulk of the research performed. Precipitates of the S-phase were expected to be present across the compositional spectrum of this core alloy group at maximum hardness. Depending upon alloy chemistry, other types of precipitate were anticipated, including GP zones, θ'' , θ' and Ω -phase in Cu-rich alloys, and GPB zones and T-phase in Mg-rich alloys.

Those linear defects upon which heterogeneous precipitation can proceed in crystalline materials may be introduced by a number of processes, including vacancy condensation and plastic deformation. The former process occurs in association with a decline in vacancy supersaturation, and results in the collapse of vacancy discs to form dislocation loops. Compared with a random inherent or introduced (i.e. by deformation) dislocation arrangement, the distinct advantage of

using dislocation loops as candidate dislocation line segments in the study of heterogeneous precipitate nucleation is the excellent reproducibility of Burgers vector and line direction. This allows numerous nucleation events to occur in effectively identical strain fields. Considering this advantage, the present work will be limited to the observations of precipitate nucleation and growth at vacancy condensation (dislocation) loops. A rationalisation of the crystallography of the precipitates at the loops will be demonstrated. It is expected that the observations made and principles derived should be directly applicable to precipitate nucleation upon intrinsic or introduced dislocations in those cases where the strain fields are analogous.

1.3 Overview of the Thesis

To achieve the stated aim, this thesis will begin in Chapter 2 with a review of the literature, covering such topics as the barriers to second-phase nucleation and the current state of knowledge regarding the nucleation, growth and crystallography of the expected precipitate phases in the present system. This will be followed in Chapter 3 by a presentation of the experimental design and techniques applied. Chapter 4 provides a description of an experimental investigation into the hardening characteristics of decomposing super-saturated solid solutions of 10 Al-rich Al-Cu-Mg alloys. During this general exploration, a subset of four alloys is identified for further analysis. The microstructural evolution leading to a distribution of second-phase material is recorded in these four alloys exposed to several applied heat treatment regimes using conventional transmission electron microscopy. The purpose of this chapter is to establish those precipitates present at peak hardness, and to assess the extent to which these precipitates favour nucleation at dislocations. Other issues raised by the results of this chapter are not dealt with in great depth.

Chapter 5 is concerned initially with the nature of the dislocation loops in the group of four alloys, with particular reference to the strain environment produced in the matrix by the various forms. Following this, the characteristics of precipitate morphology in these alloys are investigated, on the condition that the nucleation event occurred at or near a dislocation loop. Several unresolved issues are isolated with respect to the heterogeneous nucleation of S-phase at dislocations. The development of these issues requires a better understanding of the crystallography of precipitates of the S-phase than that which is currently available. Hence, chapter 6 is concerned solely with individual precipitates of the S-phase and attention is concentrated upon the structure and morphology of the embedded particles, with particular

reference to the orientation relationship and the nature of stable particle-matrix interfaces. Only passing reference is made to the nature of the strain field in which the S-phase has nucleated. The analysis undertaken in this chapter leads to new definitions of the crystallography of embedded S-phase precipitates. Chapter 7 combines this new knowledge gained in chapter 6 with the observations recorded in chapter 5 regarding nucleation and growth of the S-phase in the strain field of the dislocation. Conclusions from the present work are recorded in chapter 8.

2.0 Background and Formulation of Research Direction

The research presented here is based upon the development in understanding of wrought heat-treatable Al-Cu-Mg alloys of the 2000 series in the International Alloy Designation System (IADS). The use of Al-Cu-Mg alloys as suitable materials for load-bearing applications is predicated upon the increase in hardness that may be achieved through either ambient or elevated temperature ageing following solution treatment and quenching. The incidence of heterogeneous nucleation at dislocations during ageing is of particular interest due to its influence on properties, and this is reflected in the topics covered in this background to the research.

The chapter begins with a general appreciation of the field in which this research is being performed. This extends to a definition of the requirements of a generic alloy for age-hardening and the quantified impact of a distribution of precipitates upon alloy hardness. The hardening response and microstructural changes of Al-Cu-Mg alloys during ageing will also be discussed here with a view to identifying the nature of the technologically-significant *strengthening* precipitates. The physical processes of second-phase nucleation and growth of particles are of critical importance to the implementation of a suitable distribution of precipitates, and the second section of this chapter deals with these issues, thus forming a theoretical framework. Following this, detailed references will be made to the current understanding of the characteristics of individual strengthening precipitates in the Al-Cu-Mg system, with particular reference to precipitate crystallography, morphology and nucleation/growth characteristics where appropriate. Finally, the unresolved issues surrounding heterogeneous nucleation at dislocations of strengthening precipitates in Al-Cu-Mg alloys are summarised, defining the direction of the present work.

2.1 Processing of Al-Cu-Mg Alloys for Mechanical Properties

The essential attributes that qualify a generic aluminium alloy as amenable to age-hardening will be identified in the following section. The Al-Cu-Mg system will then be treated specifically, with reference to the phase equilibria and the identity of second-phase particles in aged microstructures. Following this, the current state of knowledge of the time-temperature-hardness matrix for Al-Cu-Mg alloys will be summarised, followed immediately by a summary of the changes in microstructure during artificial ageing as a function of the phase field in which individual alloys are found.

2.1.1 Prerequisites for Age-Hardening in a Generic Alloy

The essential feature of an alloy predisposed to strengthening via a dispersion of second-phase particles in the parent matrix is the decreasing solubility of alloying elements with decreasing temperatures. A schematic phase diagram of a generic binary alloy of components A and B is provided in figure 2.1. An alloy of composition A-xB forms a homogeneous solid solution of the equilibrium α phase when heated to a temperature within the range ΔT_1 . Slow (equilibrium) cooling of the solid solution from this temperature to T_3 proceeds via the following reaction: $\alpha(SSSS) \rightarrow \alpha + \beta$ where $\alpha(SSSS)$ is a *supersaturated solid solution* of B (and vacancies) in A, and β is a stable precipitate comparatively rich in solute B. The microstructure following slow cooling can be relatively coarse, since there is ample time at elevated temperature for extensive

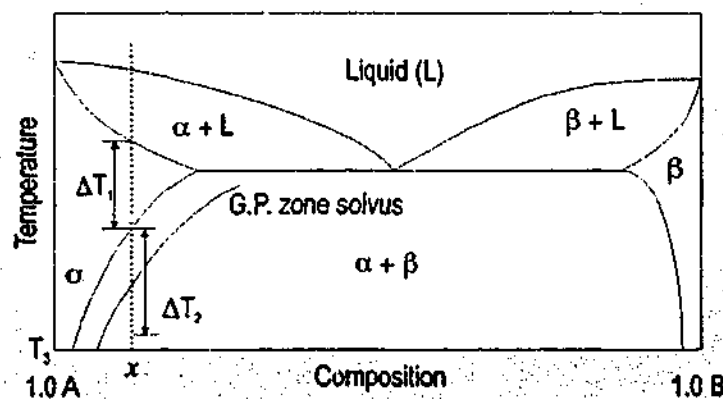
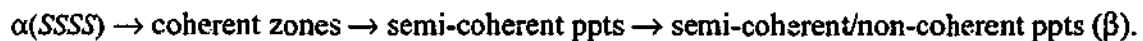


Figure 2.1 Model phase diagram of alloy A-B displaying a decreasing solubility of B in A with decreasing temperature at composition A-xB.

diffusion of solute atoms. However, if the alloy is cooled rapidly from within the range ΔT_1 to T_3 at a faster rate, decomposition during cooling will be suppressed and only α (SSSS) will form. This phase, which is metastable at T_3 , will seek to lower its free energy by reducing the supersaturation of B (and vacancies) in A. If T_3 corresponds to normal ambient temperatures, the kinetics of decomposition may be comparatively slow. Reheating (*artificial ageing*) of the alloy A-xB in the temperature range ΔT_2 accelerates the decomposition, and can result in a fine dispersion of B-rich second-phase particles throughout the parent α matrix in the form of precipitates. Decomposition usually occurs via a series of intermediate coherent *zones* or semi-coherent phases, which form because they present a systematically lower energy barrier to nucleation, and the decomposition sequence typically takes the form of:



Artificial ageing within ΔT_2 , at a temperature above the solvus for coherent GP zones (indicated in fig. 2.1) prevents their formation, and the decomposition proceeds through the direct formation of precipitates. The generation of second-phase precipitates (that act as barriers for dislocations) during artificial ageing of a supersaturated solid solution in alloys that exhibit limited solid solubility is the basis for age-hardening.

The hardness of a metal or alloy derives from its resistance to dislocation movement, or *plastic deformation*. In *pure* metals, the Peierls-Nabarro stress [9,10] determines the resistance to dislocation [11-14] movement. In *alloys*, solid solution hardening [15-30], chemical locking [31] and clustering or short-range order [32,33] can all contribute to the hardening of solid solutions. However, the most *significant* increases in hardness and strength are realised through the presence of second-phase particles [34-46]. If the particles are penetrable by the dislocations (coherent, intermediate phases), precipitate *shearing* will occur. Otherwise, dislocation *looping* occurs and these two cases are presented schematically in figures 2.2(a) and 2.2(b) respectively. Figure 2.2(c) plots strength against particle size for a microstructure containing a prescribed volume percentage of second-phase material. The portion of the curve at A relates to shearable particles, and demonstrates that the resistance to shearing increases with particle dimensions. As the size of shearable particles increases, the strength of the alloy increases until the particles are of a size that enables them to resist shearing, and dislocations are then forced to by-pass the particles. The stress required to render the dislocations mobile in such a particle array decreases as the particle size and the separation of particles both increase.

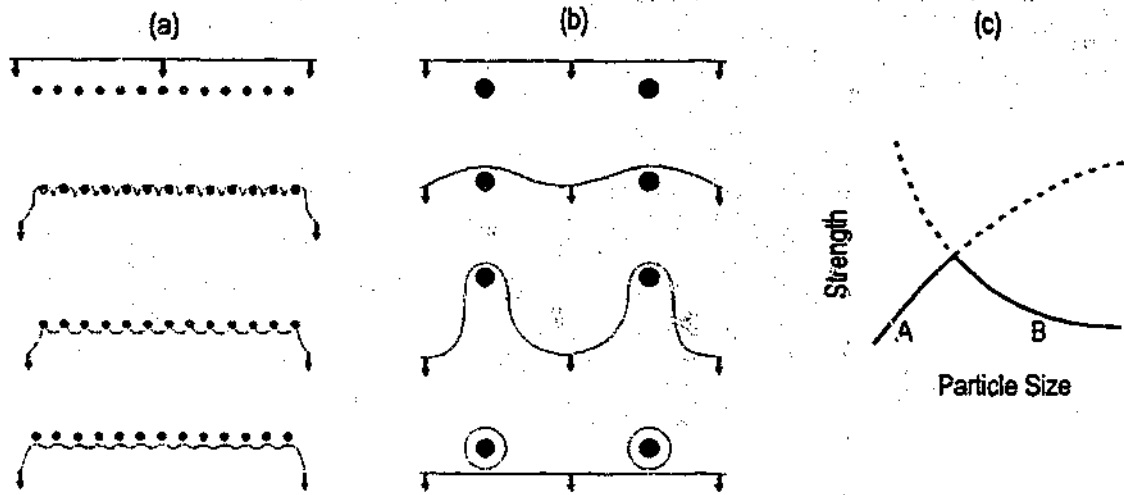


Figure 2.2 (a) Shearing and (b) looping of precipitates by a moving dislocation. (c) An optimum precipitate size exists with respect to alloy strength.

The Orowan equation [34,36,38,46-48] defines the stress increment in a matrix containing shear-resistant particles, and for spherical precipitates:

$$\Delta\tau = 2 \left\{ \frac{Gb}{4\pi\sqrt{1-\nu}} \right\} \left\{ \frac{1}{\lambda} \right\} \left\{ \ln \frac{D_p}{r_0} \right\} \quad \text{Equation 2.1}$$

where $\Delta\tau$ is the increase in critical resolved shear stress expected, ν is Poissons ratio, r_0 is the core radius of the dislocations, λ is the precipitate spacing and D_p is the precipitate diameter. The particle spacing varies for systems containing precipitates of different shape, orientation and distribution. Modified Orowan equations have been developed for microstructures containing plate-shaped and rod-shaped particles [47,49], indicating the variable resistance to dislocation movement of arrays of precipitates of varying morphology.

2.1.2 Phase Equilibria in Al-Cu-Mg Alloys

Alloys with compositions in appropriate phase fields in the aluminium rich corner of the isothermal (190°C) Al-Cu-Mg ternary phase diagram (fig. 1.3) [7,50,51] exhibit the equilibrium precipitate phases θ (tetragonal Al_2Cu), S (orthorhombic Al_2CuMg) and T (Al_6CuMg_4). During appropriate artificial ageing regimes, such alloys may contain various precursors and these have been tabulated together with the equilibrium phases in table 2.1 [7]. Also included is the orthorhombic Ω -phase (Al_2Cu) (metastable) which forms in alloys with high Cu:Mg ratios [52].

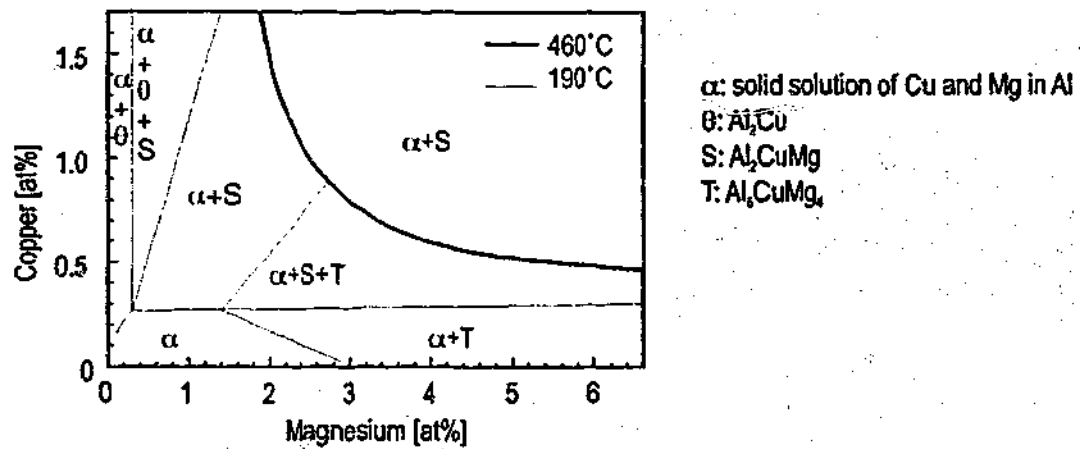


Figure 2.3 Section of Al-Cu-Mg phase diagram at 460°C and 190°C (after [7,50,51]).

Table 2.1 Summary of zones and precipitates found in Al-Cu-Mg ternary alloys (after [7]).

Precipitate	Structure and Composition	Comments
GP Zones	Platelets (Cu)	Parallel to $\{001\}_\alpha$. Probably single layer of Cu atoms.
θ''	Tetragonal Al_2Cu $a = 0.404 \text{ nm}$ $c = 0.768 \text{ nm}$	Cu and Al atoms are ordered on $\{001\}_\alpha$ planes. Every third plane composed of Cu atoms. Form as discs.
θ' Phase	Tetragonal Al_2Cu $a = 0.404 \text{ nm}$ $c = 0.580 \text{ nm}$	Semi-coherent plates nucleated at dislocations. Form on $\{100\}_\alpha$.
θ Phase	Body-centred Tetragonal Al_2Cu $a = 0.607 \text{ nm}$ $c = 0.487 \text{ nm}$	Incoherent equilibrium phase.
Ω Phase	Orthorhombic Al_2Cu $a = 0.496 \text{ nm}$ $b = 0.859 \text{ nm}$ $c = 0.848 \text{ nm}$	Forms as thin plates on $\{111\}_\alpha$. Only observed occasionally in ternary Al-Cu-Mg alloys.
GPB Zones	Rods (Cu, Mg)	Guinier-Preston-Bagaryatsky zones. Form parallel to $\langle 100 \rangle_\alpha$. Complex structure not yet fully understood.
S''	Orthorhombic Al_2CuMg $a = 0.404 \text{ nm}$ $b = 0.925 \text{ nm}$ $c = 0.718 \text{ nm}$	Coherent, elongated parallel to $\langle 100 \rangle_\alpha$.
S' Phase	Orthorhombic Al_2CuMg $a = 0.404 \text{ nm}$ $b = 0.925 \text{ nm}$ $c = 0.718 \text{ nm}$	Semi-coherent and nucleated at dislocations. Form as laths in $\{210\}_\alpha$ along $\langle 100 \rangle_\alpha$.
S Phase	Orthorhombic Al_2CuMg $a = 0.400 \text{ nm}$ $b = 0.923 \text{ nm}$ $c = 0.718 \text{ nm}$	Incoherent (or partially coherent) equilibrium phase. Elongated parallel to $\langle 100 \rangle_\alpha$.
T Phase	Body-centred Cubic Al_6CuMg_4 $a = 1.425 \text{ nm}$ (161 atoms in cell).	Isomorphous with the T-phase ($\text{Mg}_{32}(\text{Al}, \text{Zn})_{49}$) in the Al-Zn-Mg system.

2.1.3 The Hardening Response of Al-Cu-Mg Alloys

Both Al-Cu and Al-Mg binary alloys of sufficient solute content undergo an apparently single-stage increase to maximum hardness following solution treatment and many hours at elevated temperature [53,54]. The progressive addition of the third component to the binary alloys, creating alloys in the industrially-important phase fields $(\alpha+\theta)$, $(\alpha+\theta+S)$, $(\alpha+S)$ and $(\alpha+S+T)$ [7] (fig. 2.3) leads to changes in the hardening response during artificial ageing. As for alloys of binary Al-Cu, ternary alloys in the $(\alpha+\theta)$ phase field (high Cu:Mg ratio) usually undergo a single-stage increase in hardness after many hours of artificial ageing following solution treatment and quenching [55]. An example is provided in figure 2.4 of the hardening reaction at three different ageing temperatures for an alloy of composition Al-1.7Cu-0.3Mg [56,57].

However, alloys in the $(\alpha+\theta+S)$ and $(\alpha+S)$ phase fields harden in two (or three) distinguishable stages during artificial isothermal ageing [53,55,58-63] within the temperature range of 110°C - 200°C. The first stage accounts for up to 70% of the total hardness increment, yet occurs typically within 60 s of the commencement of ageing. The second increase in hardness occurs following longer ageing periods, allowing a *hardness plateau* to be described between the hardening stages. Figure 2.5 [64] reveals the two-stage hardness profile for Al-1.1Cu-1.7Mg $(\alpha+S)$ at 150°C and 200°C. Alloys in the $(\alpha+S+T)$ phase field display a less pronounced two-stage hardening response during ageing at temperatures between 150°C and 225°C [58,61], while $(\alpha+T)$ alloys harden following extended ageing via a single rise to maximum hardness [54].

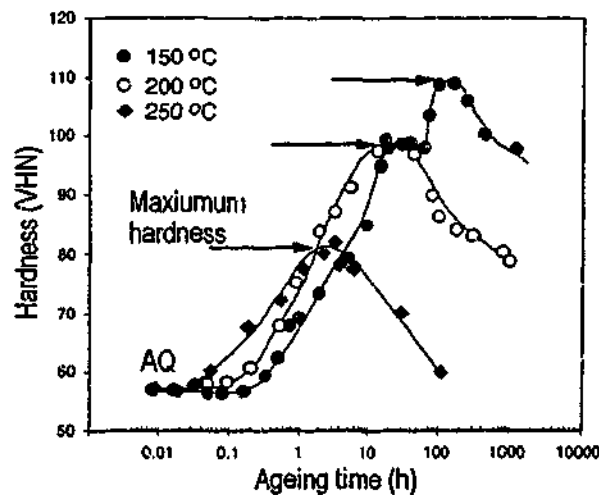


Figure 2.4 Ageing curves for Al-1.7Cu-0.3Mg $(\alpha+\theta+S)$ phase field) at 150°C, 200°C and 250°C, exhibiting a single rise in hardness (after [56,57]).

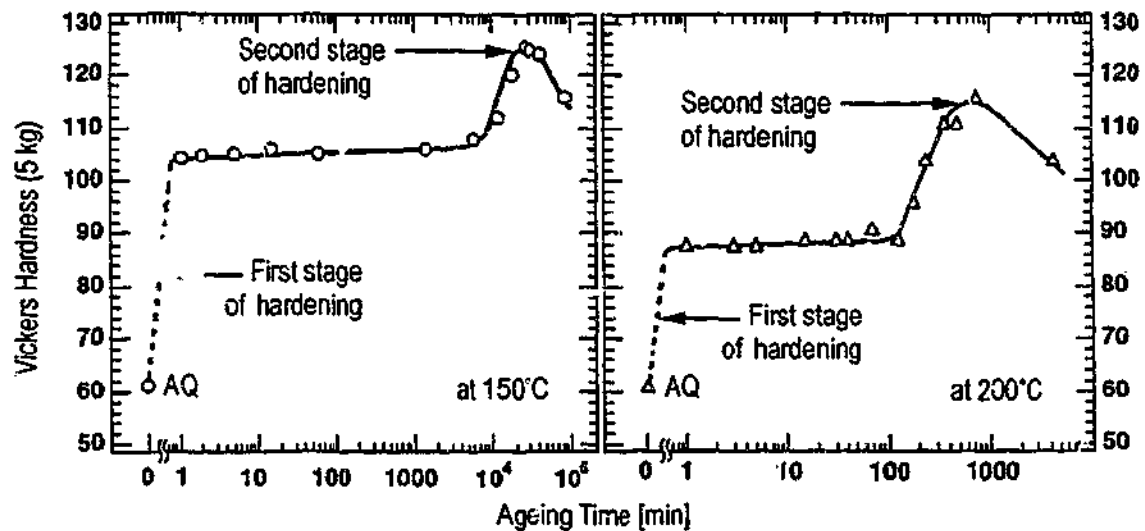


Figure 2.5 Ageing curves for Al-1.1Cu-1.7Mg (α +S phase field) at 150°C and 200°C, exhibiting a two-stage hardness trace (after [64]).

2.1.4 Microstructural Changes during Ageing in Al-Cu-Mg Alloys

The identity and distribution of solute species in Al-Cu-Mg alloys that are associated with specific points of the hardening cycle (e.g. minimum hardness, maximum hardness etc.) is of significant technological interest and have been studied extensively, although some conjecture still remains. Clearly, the presence of specific precipitate species is predicated first upon the compositional phase field in which the alloy lies and, accordingly, (α + θ), (α +S) and (α +S+T) alloys are treated separately. Firstly, a note regarding alloy microstructures. Depending upon the magnitude of, and the time spent at, the applied artificial ageing temperature, the distribution of solute atoms may be uniformly distributed, locally concentrated in clusters or take the form of discrete second-phase particles (i.e. zones or precipitates). Single solute atoms or atom clusters cannot be imaged using electron microscopy, since the technique relies on diffraction contrast due to variations in scattered intensity with location in the sample. Previous investigations of pre-precipitation microstructures in aluminium alloys have resorted to specialist techniques including positron annihilation lifetime spectroscopy (PALS) [65-69] and the relatively new technique of one or three-dimensional atom probe field-ion microscopy (1-DAP or 3-DAP) [56,59,60,70-77]. In alloy microstructures with zones or precipitates, conventional and high-resolution transmission electron microscopy techniques (TEM, HREM) are widely used.

($\alpha+\theta$) Phase Field

Transmission electron microscopy studies of solution treated (515°C) and quenched alloy Al-1.7Cu-0.3Mg, a well-studied and representative example from the ($\alpha+\theta$) phase field, revealed that the as-quenched microstructure contained dislocation loops [76] and was free of precipitates. During ageing at 180°C for 15 s, these loops grew significantly, after which their size remained stable. According to I-DAP data, there were no zones or precipitates following ageing for 30s, but co-clusters of Cu and Mg were observed. The early stages of decomposition in Al-1.7Cu-0.3Mg alloys have also been studied by PALS [67]. Positron lifetime immediately following solution treatment and quenching was recorded as corresponding to the expected lifetime if the microstructure comprised single vacancies bound to individual solute atoms [67]. Positron lifetimes (recorded at 20°C) immediately after ageing for between 15 s and 300 s at 180°C were dramatically decreased from the quenched value [67], and were similar to those expected if the positrons were associated with Cu-rich sites, suggesting the formation of local aggregates rich in Cu and vacancies. From these results, it is clear that considerable change takes place in the arrangement of the solute atoms in the microstructure during short ageing times, despite the observation (§2.1.3) that there is no change in the hardness of these alloys in the first few minutes of ageing at elevated temperature.

Following 2.5 h at 180°C (below maximum hardness), the alloy Al-1.7Cu-0.3Mg contained a mixture of θ'' , θ' and S-phase [76], and the dislocation loops formed upon quenching from solution treatment were obscured by the precipitation. Ageing for 100 h at 150°C and 30 h at 200°C elicited maximum hardening in this alloy [56], and the microstructure contained θ'' , θ' and S-phase in the former case, and θ' and S-phase in the latter, together with several minor phases including the Ω -phase [52,78-80] and σ -phase [81-83].

($\alpha+S$) Phase Field

The alloy Al-1.1Cu-1.7Mg is a well-studied and representative example from the ($\alpha+S$) phase-field. Rich in both Cu and Mg, and forming as rods parallel to $\langle 100 \rangle_{\alpha}$, shearable GPB zones [84,85] have generally been considered responsible for the first rise in hardness occurring within the first 60 s of ageing at elevated temperature. Recent conventional TEM, HREM and atom probe studies [64] have failed to detect the presence of GPB zones in this alloy following the first stage hardness increase, leading to the conclusion that the initial rapid-hardening observed in Al-Cu-Mg alloys is the product of a pre-precipitation phenomenon.

The detection of independent Cu clusters and Mg clusters in Al-1.1Cu-1.7Mg in the as-quenched condition [59,60], and Cu-Mg co-clusters following ageing for 300 s at 150°C has been reported using 1-DAP. In contrast to these reports, 3-DAP analysis has suggested little or no evidence of a uniform distribution of Cu-Mg co-clusters [64], representing a case where an analysis of larger volumes of material in 3-DAP has perhaps led to a more representative analysis of the microstructure. Uniformly distributed, same-species clusters (i.e. Cu-Cu and Mg-Mg) have been proposed qualitatively using 3-DAP data following initial rapid hardening [73], and it has been suggested that these may have as much or more influence than Cu-Mg co-clusters on the hardening behaviour.

It has been further proposed that, during the initial stages of artificial ageing, Cu and Mg atoms cluster or coalesce at the site of crystal defects, forming Cottrell atmospheres [18,19]. In so doing, these clusters form in a distinctly non-random dispersion [64,69,73]. The proposal suggests that mobile dislocations are locked or pinned in place by the solute, and thus form a sessile dislocation network. For plastic deformation to occur, the sessile dislocations must be torn from their solute atmospheres and accompanying low-energy state, or new dislocations generated. To date, the proposed pre-precipitation segregation of solute atoms to lattice defects has not been confirmed using 3-DAP. Recent work using PALS and Coincidence Doppler broadening of Al-1.3Cu-1.7Mg has shown that vacancy-Mg complexes form during quenching [69]. After 60 s of ageing at 150°C, the data suggests that the quenched-in vacancies bound to the Mg atoms easily migrate to vacancy sinks, and it has been proposed that the presence of Mg-Cu-vacancy complexes after 60 s of ageing is due to migrating Mg-vacancy complexes that capture Cu atoms and migrate jointly to vacancy sinks (dislocations). Solute atoms thus lock the dislocations. Taking into account the availability of Mg in this alloy, in comparison to the alloy studied by Somoza *et al.* [67,68] (where vacancy-copper complexes were formed after short time ageing in a Cu-rich alloy), the presence of Mg-Cu-vacancy complexes is considered plausible. Critically, the alloy studied by Somoza *et al.* [67,68] does not rapidly harden, while Al-1.3Cu-1.7Mg does. This suggests that the level of Mg must be greater than a certain value to allow the formation of Mg-vacancy complexes during quenching.

A distribution of precipitates of the S-phase and GPB zones has generally been held responsible for the maximum hardness [6,58,59,64,85-88]. Newer proposals for the hardening of these alloys suggest that GPB zones are the dominant strengthening phase [59,64]. Furthermore, it is suggested that the S-phase is relatively unimportant, since considerable growth of the S-phase occurs following the first hardness increase inside 60 s of ageing, during which the alloy is

observed to sustain a lengthy hardness plateau [59,64]. However, the observation that plastic deformation of commercial 2024 alloy [6] and of experimental alloys of the (α +S) phase field [8,89] leads to higher maximum hardness (via a distribution of heterogeneously-nucleated S-phase) suggests that this phase is not insignificant with respect to its potential to contribute to a hardening response. It has also been demonstrated that during over-ageing, the GPB zones are gradually replaced by matrix precipitation of the S-phase, which grows progressively coarser [59].

(α +S+T) Phase Field

The alloy Al-0.3Cu-4.6Mg reportedly undergoes initial rapid hardening, and the presence of S'' is associated with the change in mechanical properties [58], in addition to GPB zones [90]. The latter work [90] detected GPB zones with L1₀ crystal structure after 1 h and S'' after 4 h, and therefore the conclusion that they cause the rapid early hardening following 60 s ageing is largely conjecture. These findings have not been verified by 3-DAP, although this advanced technique failed to detect S'' in alloys of the (α +S) phase field [64]. Maximum hardness is associated with a distribution of GPB zones and S-phase precipitates, as for alloys in the (α +S) phase field.

2.2 Aspects of Precipitate Nucleation and Growth

The free energy balance that is commonly used to describe nucleation in solid state systems is related here, followed by a discussion of the implications in the case of heterogeneous nucleation at line defects.

2.2.1 Classical Homogeneous Nucleation

When a small volume of a product phase forms within a supersaturated matrix phase, there is a change in the free energy ΔG of the system consisting of the following components [91]:

1. At temperatures where the product phase is stable, the creation of a volume V of the product will cause a *reduction* in the free energy by $V\Delta G_v$, where ΔG_v is the difference in volume free energy of the parent and product phases.
2. The creation of an area, A , of interface will require a *free-energy increase* by $A\gamma$, where γ is the interfacial energy of the particle-matrix interface.
3. Generally, a product phase will not fit perfectly in the parent phase owing to a change in volume and shape, and a misfit strain energy equal to ΔG_s per unit volume of product will result. This *increases* the free-energy barrier to nucleation.

These components of the free-energy change are additive and are expressed as:

$$\Delta G = -V\Delta G_v + A\gamma + V\Delta G_s \quad \text{Equation 2.2}$$

The smallest energy barrier with respect to size and shape of the precipitate is called the *activation energy* for nucleation. In fluids, the shape corresponding to this condition is a sphere (thereby minimising the surface-to-volume ratio). In contrast, solids can maintain shear stress in equilibrium, and therefore the shape corresponding to the smallest energy barrier is not necessarily a sphere.

2.2.2 Heterogeneous Nucleation at Dislocations

Cahn [92] was the first to quantify the effectiveness of a dislocation in promoting nucleation, choosing as a model system a *strain-free* non-coherent precipitate lying in a cylinder parallel to the core of a straight dislocation. In Cahn's model, the strain energy of the dislocation favours nucleation, since the dislocation is removed along with its energy. The volume-energy (free-energy change between parent and product) favours nucleation, while a surface energy term opposes it. Figure 2.6(a) plots the change in free-energy against nucleus size for *homogeneous* nucleation. Nucleation proceeds when the radius, r , of a nucleus corresponds to a critical radius, r_{crit} , where the slope of the curve defining ΔG as a function of r is zero and is in transition from positive to negative slope. The curve labeled A in figure 2.6(b) corresponds to nucleation at a dislocation [92], and a critical radius can again be identified. When the supersaturation of solute elements is high, the volume energy term is high and the transformation accumulates a higher driving force. Curve B in figure 2.6(b) corresponds to this situation, and Cahn [92] has shown that the nucleation barrier is reduced to zero if the supersaturation is large enough. If the nucleation process requires long-range diffusion of solute atoms to feed the compositional change, the rate of precipitate growth will be governed solely by diffusion in these cases. The rate of heterogeneous precipitation is greater than the rate of homogeneous precipitation by a factor of 10^{78} for typical parameters [92], indicating the powerful influence of the pre-existing dislocation. As Cahn assumes, a transformation in a solid may be characterised by a homogeneous stress-free strain. However, typical transformations in an otherwise untransformed matrix produces stresses in the matrix and the precipitate, the magnitudes of which depend on the shape of the volume transformed and on the interface between the phases. Cahn's original model did not consider this.

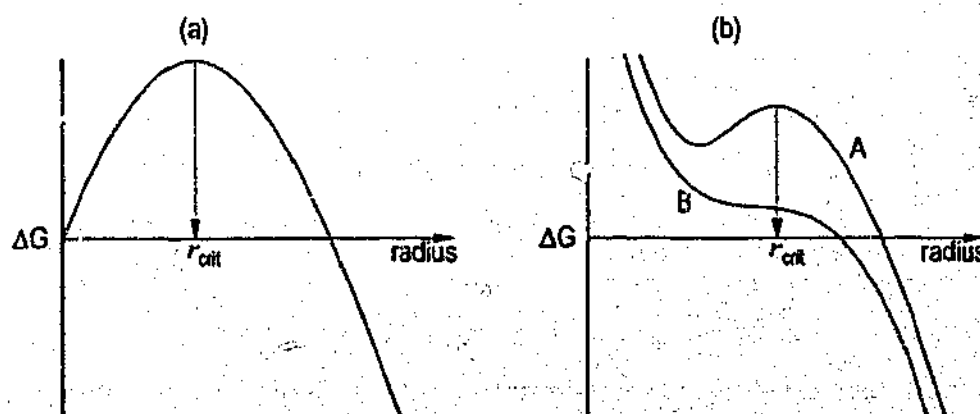


Figure 2.6 Homogeneous nucleation. (b) Heterogeneous nucleation at a dislocation (after [92]).

The free energy change ΔF accompanying nucleation at dislocations has been defined more recently in the literature [93,94] as:

$$\Delta F = -\Delta F_v + \Delta F_s + \Delta F_e + \Delta F_d + \Delta F_i \quad \text{Equation 2.3}$$

where ΔF_v = difference in free energy between parent and product

ΔF_s = the interfacial free energy

ΔF_e = the elastic strain energy in the matrix and nucleus

ΔF_d = the difference in line energy of the dislocation and that part remaining in the nucleus volume

ΔF_i = the interaction of the stress fields of the dislocation and nucleus.

The first three terms are analogous to the three terms in equation 2.2 describing homogeneous nucleation. The term ΔF_e arises from stresses due to differences in the specific volume of the parent and product phases, or lattice mismatch between the phases, and ΔF_d depends on the character of the dislocation. If the product phase completely replaces the dislocation line, the reduction in free energy is set equal to the line energy of the dislocation [94]. Pure edge dislocations have a greater line energy than screw dislocations. Finally, ΔF_i is applied in situations where the dislocation is only partially covered by the precipitate. According to Beaven and Butler [94], nucleation occurs on dislocations when the terms ΔF_d and ΔF_i are negative and large enough to counterbalance ΔF_e and ΔF_s . This implies that nucleation on screw dislocations is less favoured than on edge dislocations, since ΔF_d (screw) < ΔF_d (edge) and ΔF_i (screw) = 0 (radially symmetrical stress field, [94]). Several other authors have extended the initial theoretical work of Cahn [92] on incoherent nuclei at dislocations [93,95] to include a strain energy term and to consider the core energy of the dislocation. Other authors [96,97] have considered coherent nucleation, and all require assumptions. Beaven and Butler [94] suggest that the assumption of incoherence is unrealistic, while considerations of elasticity [98,99] in the case of coherent nucleation are dubious near the dislocation core. All of the theoretical approaches to precipitate nucleation at dislocations are complex.

The dilatational component of the ΔF_e is most commonly referred to during discussion of heterogeneous nucleation. However, the lesser known component of the term is the shear component, since it may be assumed that the elastic strain energy is perfectly general in nature.

Consider now the experimental observations of precipitate nucleation at dislocations. The principal misfit vector is defined by the direction and magnitude of the largest deformation (positive or negative dilatation) that must be applied to the matrix material to form the product material. An edge dislocation can best accommodate the volumetric lattice misfit, ΔF_v , of precipitate formation between a precipitate and the matrix if the Burgers vector of the dislocation is parallel to the misfit vector of the precipitate [36,94,95,100-102]. It is argued that this arrangement allows a large proportion of the transformation strain to be taken up by the established strain field of the dislocation. Accordingly, a product phase with a higher atomic density than the parent phase will favour formation in compressive regions near the dislocation core, while a product phase with lower atomic density will form preferentially in tensile regions. It is generally considered that classical diffusion-controlled precipitation reactions are not displacive, and therefore do not require the accommodation of a shear strain energy component to allow nucleation to proceed. However, some authors have invoked a shear component in the formation [103-108] of precipitates plates in aluminium alloys. These cases will be referred to later.

Another factor evidently influencing precipitation on dislocations is the plane in which the dislocation line lies [36,94,109-111]. Explicitly stated, it is observed that dislocation lies in the habit plane of the precipitate. Kelly and Nicholson [36] provide the example of the θ' phase forming on successive turns of a helical dislocation at those locations where the dislocation line is parallel to $\{100\}_\alpha$ (matrix phase) planes. Another example is η laths in Al-Zn-Mg alloys [109,110]. For pure edge dislocations, the Burgers vector is always perpendicular to the line direction and therefore precipitates tend to form along the dislocation line with a habit plane parallel to the line direction and perpendicular to the Burgers vector. There is no hydrostatic stress field around screw dislocations, and hence they are not anticipated to assist nucleation requiring a volumetric misfit. Hence, the selection rules can be summarised as:

1. The lattice misfit vector between a precipitate and the matrix is not perpendicular to the Burgers vector of the dislocation
2. The line direction of the dislocation lies parallel to the habit plane of the precipitate.

2.3 Strengthening Precipitates in Al-Cu-Mg Alloys

Aluminium-rich Al-Cu-Mg alloys aged artificially to maximum hardness in the temperature range 100-200°C are characterised by the presence of a high density of second-phase precipitates. The following section examines in more detail the specific characteristics of the strengthening precipitate phases in these alloys: θ'' and θ' , Ω , GPB zones, S-phase and T-phase. Consideration is given to the crystal structure, orientation relationship, interface structure and nucleation and growth mechanisms where appropriate. Particular reference will also be made to the recorded and/or predicted susceptibility of these precipitates to heterogeneous nucleation in the strain field of a dislocation.

2.3.1 The θ'' and θ' -Phases

In binary Al-1.7%Cu alloys, the equilibrium θ (Al_2Cu) phase forms only at ageing temperatures above 550K (277°C) [112]. The pre-cursor precipitate phases θ'' and θ' are, however, expected to form at lower artificial ageing temperatures in the range applied in typical age-hardening regimes (100-190°C [7]). The former phase has a tetragonal unit cell, consistent with that of a distorted fcc structure, in which the Cu and Al atoms are ordered on $(001)_\alpha$ planes (fig. 2.7(a)).

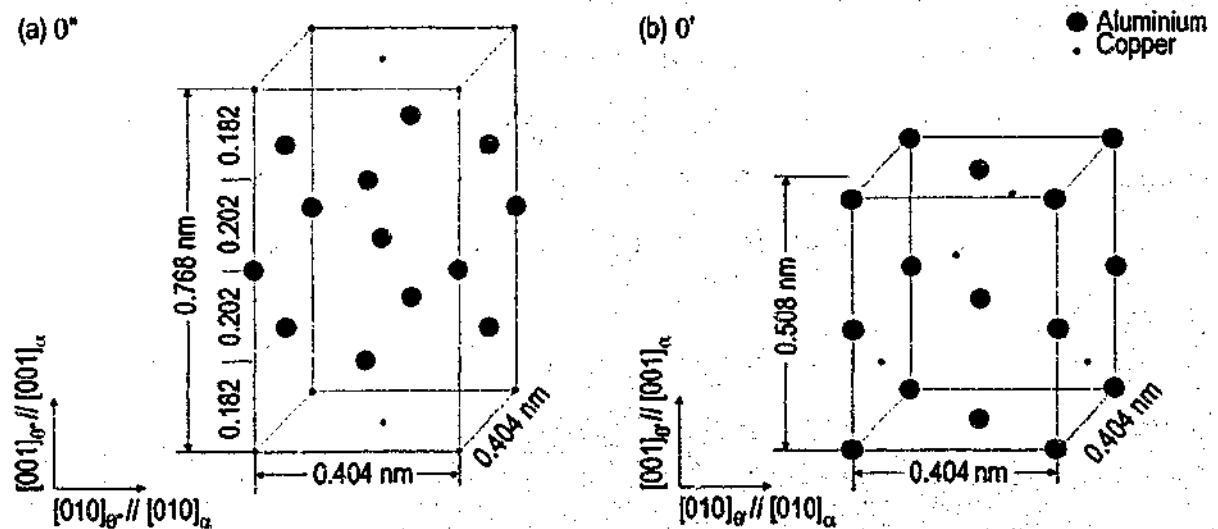


Figure 2.7 Atomic structure of (a) θ'' and (b) θ' .

Two unit cells of the aluminium matrix phase undergo a contraction from 0.808 nm (i.e. 2 unit cells of the aluminium matrix phase) to 0.768 nm (-4.95%). Therefore, the volume change is anisotropic, requiring contraction parallel to $[001]_{\alpha}$ only. The phase forms as platelets coherent with the matrix within a $\{001\}_{\alpha}$ habit plane, and the platelets are observable under electron beam illumination primarily due to the strain induced perpendicular to the plates. The following orientation relationship is observed:

$$(001)_{\theta''} // (001)_{\alpha}, [100]_{\theta''} // [100]_{\alpha}, [010]_{\theta''} // [010]_{\alpha}$$

The θ'' platelets are generally observed to form well away from dislocations [113,114], and are presumed to follow directly from uniformly distributed GP zones. The contraction parallel to $[001]_{\theta''}$ would presumably benefit from formation in the compressed region adjacent to the core of an edge dislocation, benefiting from a reduction in the component ΔF_e .

The unit cell of the θ' phase is also tetragonal (fig. 2.7(b)) and, like the θ'' phase, the atomic positions within $(001)_{\theta'}$ are near exactly matched with those of the matrix $\{001\}_{\alpha}$. The orientation relationship with the matrix is similar to that of θ'' . The dimension of the unit cell parallel to $[001]_{\alpha}$ is 0.58 nm, and it can be appreciated upon inspection that the number of atoms required by the unit cell is matched only by a volume of matrix material that is 1.5 unit cells in height, or 0.606 nm. Formation of the unit cell thus proceeds via a 4.29% contraction parallel to $[001]_{\theta'} // [001]_{\alpha}$, representing again an anisotropic volume change. The observed preferential formation of the θ' phase at matrix dislocations [115] suggests that the contraction is accommodated at the compressed region of the dislocation core. Precipitates exhibiting only two of the three available $\{001\}_{\alpha}$ habit planes are observed to nucleate at a single dislocation with a $\frac{1}{2}\langle 110 \rangle_{\alpha}$ Burgers vector [36,116], and it is rationalised that the dislocation is able to reduce the misfit in only two of the three $\langle 100 \rangle_{\alpha}$ directions. The misfit vector for the remaining precipitate is perpendicular to the Burgers vector of the dislocation, and the dislocation does not offer any accommodation of this misfit.

2.3.2 The Ω -Phase

The Ω -phase is particularly important in Al-Cu-Mg alloys microalloyed with Ag, where it forms in high number densities following elevated temperature ageing. The improved creep resistance at elevated temperatures of these alloys is attributed to the presence of the Ω -phase, and extensive investigations of its characteristics have been performed [7,63,79,80,117-120]. Defined to have a face-centred orthorhombic structure ($a = 0.496$ nm, $b = 0.859$ nm, $c = 0.848$ nm) [79,80] (fig. 2.8), it exhibits an orientation relationship of the form $(001)_{\Omega} // (111)_{\alpha}$ and $[010]_{\Omega} // [10\bar{1}]_{\alpha}$. More recently [121], a tetragonal structure has been proposed for Ω , where $a = b = 0.6066$ nm and $c = 0.496$ nm.

Various proposals for the nucleation of precipitates of the Ω phase in the Ag-containing quaternary alloy have been published, consistent with the observation of a uniformly distributed dispersion. It has been suggested [118] that Ω forms from a precursor, hexagonal Mg_3Ag , although this is unlikely due to thermodynamic reasons [79]. Kerry and Scott [121] proposed that the addition of Ag and Mg to Al-Cu alloys reduces the stacking fault energy and thereby increases the number of $\{111\}_{\alpha}$ stacking faults upon which Ω nucleates. However, nucleation of Ω is thought to be associated with the aggregation of Mg and Ag atoms on $\{111\}_{\alpha}$, a process aided by the size-effect of Mg atoms [122]. The addition of Ag to ternary Al-Cu-Mg alloy is thought to promote the formation of Ω by facilitating the nucleation kinetics of Mg-rich clusters

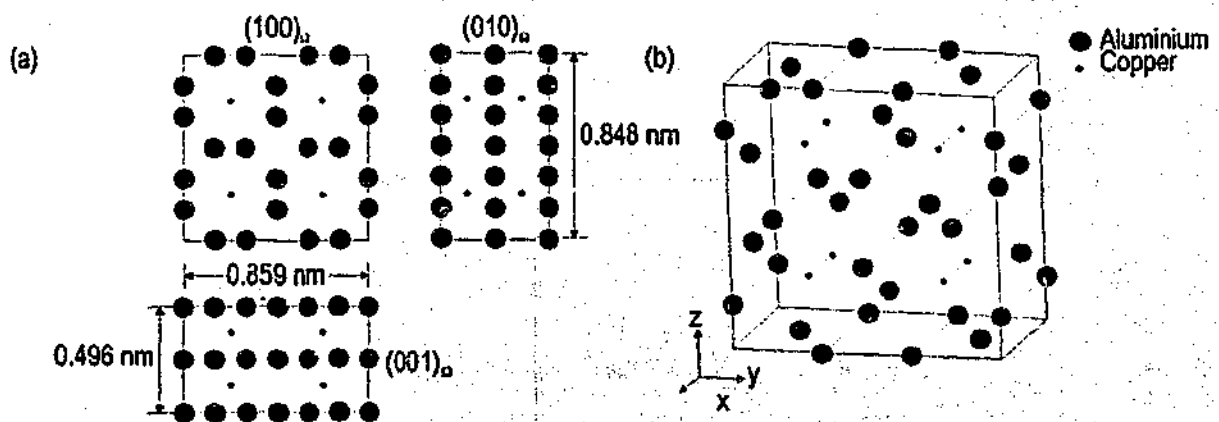


Figure 2.8 (a) The atomic position projections of the Ω -phase unit cell (b) Three-dimensional projection of the Ω -phase unit cell (after [79,80]).

on $\{111\}_\alpha$ planes [122] through a reduction in the elastic strain energy. It has recently been shown that Ag and Mg atoms form co-clusters after 5 s ageing at 180°C following quenching, and that these evolve continuously into Ω plates as ageing continues [123]. Strong segregation of Ag and Mg atoms at the broad α/Ω interface in well-defined Ω plates is believed to relieve coherency strain [118]. However, little is known about the origin of the Ω -phase in the ternary Al-Cu-Mg alloy.

The Ω precipitates have a low lattice misfit (0.02%) in the $\{111\}_\alpha$ habit plane but a large misfit (9.3%) normal to it [80]. Good atomic matching between $(001)_\alpha$ and $\{111\}_\alpha$ planes results in the high aspect ratio and the chosen habit plane as a means of minimizing the strain energy. Garg and Howe [78] showed that, in the quaternary Al-4.0Cu-0.5Mg-0.5Ag alloy, the Ω -phase nucleates with no preference to dislocation loops that may have formed in the matrix during the quench-age cycle. These authors also concluded that the sparse distribution of Ω in Ag-free Al-4.0Cu-0.5Mg ternary alloy also occurred with no preference to quenched-in defects. Similarly, plastic deformation (i.e. the introduction of dislocations) does not influence the precipitation of Ω in the ternary alloy [124]. This suggests that the nucleation of Ω is apparently insensitive to stress fields created by dislocations. Given the large lattice misfit exhibited by this phase, it is perhaps perplexing that it does not utilise the strain field provided by the dislocation in order to accommodate the volumetric misfit strain of formation.

2.3.3 GPB Zones

The zones labelled Guinier-Preston-Bagaryatsky (GPB) zones [125] form as rods parallel to $\langle 100 \rangle_\alpha$ matrix directions, approximately 1-2 nm in diameter and 4-8 nm in length [85]. There is no definitive model of the structure of these zones, although HREM studies [59,126,127] have provided atomic resolution images of the zones in an end-on orientation. GPB zones are not observed in association with dislocations, but rather they are observed uniformly throughout the microstructure. Since the structure of these zones is ill-defined, it is difficult to discuss the potential preference for nucleation at dislocations.

2.3.4 The S-Phase

Despite extensive study [58,59,61,62,87-89,107,126-151], the crystal structure, orientation relationship, morphology, interface structure and the nucleation and growth mechanisms of precipitates of the S-phase continue to be debated. Similarly, there is much conjecture over the existence of pre-cursors to the S-phase, commonly designated S'' and S'.

Evolution of precipitates and intermediate phases

Bagaryatskii [84] commented on the evolution of precipitates of the S-phase in Al-Cu-Mg alloys, and concluded the following sequence of precipitation from x-ray diffraction studies:



where S'' and S' are pre-cursors to the final equilibrium structure. The existence of S'' (or GPB2 zones) could not be confirmed in the work that followed soon thereafter [88,135]. However, more recent work apparently identified the presence of S'' [90,127], where its evolution from GPB zones is suggested, consistent with previous conclusions [8,84,125]. The distinction between S and S' is a slight difference in the lattice parameters [125], and S' is generally regarded as the coherent precipitate while S is the partially coherent equilibrium phase [7,130]. Gupta *et al.* [130] observed that the identification of S and S' are complicated by complex electron diffraction patterns. Nevertheless, these authors found evidence for a slight change in lattice parameter with ageing time, seemingly confirming that S is the equilibrium version of S'. Several authors have attempted to differentiate between the two precipitates on the basis of morphology [87], where S'-phase forms as lath-shaped precipitates (and is therefore coherent in the *habit plane*) while precipitates of S particles are larger and equiaxed normal to the long axis, and form at higher temperatures. It is generally regarded that the distinctions between S' and S are of insufficient consequence to justify two labels, and S-phase is the preferred term [59,85,88,107,126,129,130,136]. However, the terminology still persists [8,127], although it is accepted that the difference between the two is not a major structural one. In the present work and unless explicitly stated, the phase will be referred to only as S, notwithstanding the observations of others with respect to evident strain.

Table 2.2 Atomic coordinates of S-phase [107].

Element	Position	Symmetry	x	y	z
Al	8f	$m..$	0	0.356	0.056
Cu	4c	$m2m$	0	0.072	0.25
Mg	4c	$m2m$	0	0.778	0.25

Crystal Structure

Based on x-ray diffraction, Perlitz and Westgren [152] (PW) determined the unit cell dimensions of the S-phase to be $a_s = 0.400$ nm, $b_s = 0.923$ nm and $c_s = 0.714$ nm, space group $Cmcm$. A modified version of the PW model for S suggested a slightly modified unit cell with dimensions $a_s = 0.400$ nm, $b_s = 0.925$ nm and $c_s = 0.718$ nm [112]. Radmilovic *et al.* [107,153] (RaVel) proposed a further refinement of the unit cell dimensions ($a_s = 0.403$ nm, $b_s = 0.930$ nm and $c_s = 0.708$ nm), and exchanged the positions of the Cu and Mg atoms in the PW model following HREM image simulations. The coordinates according to the RaVel model (space group $Cmcm$ No. 63; Pearson symbol $oC16$) are given in table 2.2, and the structure is presented schematically in figure 2.9. It is to be noted that these findings have recently been challenged on the basis of first-principles total energy calculations [154], which suggest that the PW model is a better prediction of the structure than the RaVel model. The wide range of lattice parameters detected by researchers complicate the definitions of the structure of S. For example, Gupta *et al.* [130] suggested that at short ageing times, $b_s = 0.905$ nm and $c_s = 0.724$ nm, implying coherent S'. Following longer ageing times, $b_s = 0.918$ nm and $c_s = 0.713$ nm, and the phase is labelled the (incoherent) equilibrium S-phase [130].

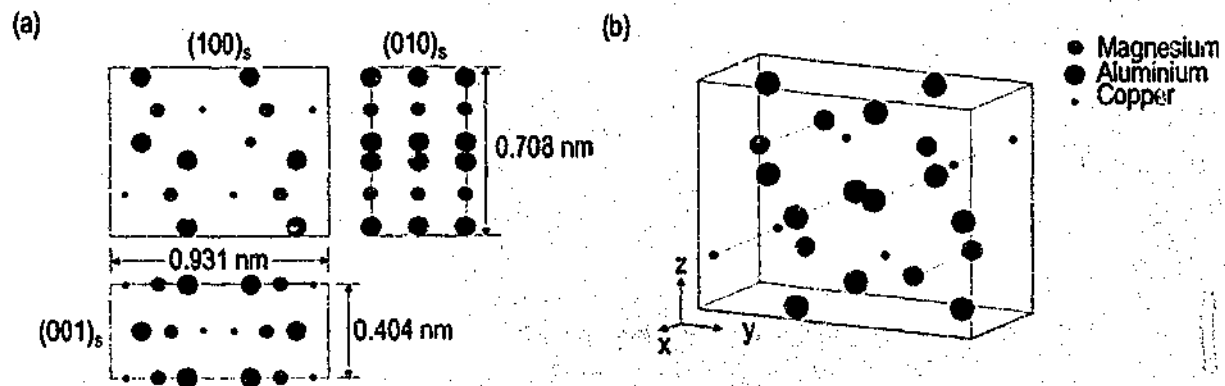


Figure 2.9 The atomic position projections of the unit cell of the S-phase (b) Three-dimensional projection of the S-phase unit cell (after [107,153]).

Orientation relationship, morphology and interface structure

The accepted crystallographic orientation relationship of the S-phase with the aluminium matrix is such that [84,85,125]:

$$(100)_s // (100)_\alpha, [001]_s // [021]_\alpha \text{ and } [010]_s // [0\bar{1}2]_\alpha.$$

This orientation relationship implies 12 crystallographically equivalent variants in the matrix phase. The difference in unit cell dimensions of parent and product phases parallel to $[100]_s // [100]_\alpha$ (0.405 nm and 0.403 nm for α -Al and S-phase respectively) is only 0.49%. Precipitate dimensions tend to be inversely proportional to the magnitude of the transformations strains [107,155], and the excellent match between the d -spacing of the planes in $[100]_s // [100]_\alpha$ is thought to be responsible for its selection as the preferred growth direction [88]. Dependent upon the alloy composition and the time/temperature of artificial ageing treatments, the elongated dimension of S-phase particles can typically be up to 1000 nm (~2500 unit cells) [89,130].

Owing to the elongated nature of precipitates of the S-phase parallel to $[100]_s // [100]_\alpha$, the shape of the particle cross-section *perpendicular* to the elongation axis is generally regarded as the most useful description of individual particle morphology. The crystal structure of the S-phase is not simple, and the symmetry of the phase can not be assumed in the way that it might for simple cubic structures. Prior to demonstrating the shape of the precipitates perpendicular to $[100]_s // [100]_\alpha$, it is useful to note the symmetry of the complex crystal structure parallel to this axis by reference to figure 2.10. Rotation (180°) about $[001]_s$ of the volume in figure 2.10(a) leads to the projected structure shown in figure 2.10(b), which can be described by the same unit cell orientation as that for figure 2.10(a), although translation of the selected volume is required parallel to $[001]_s$. Similarly for rotation (180°) about $[010]_s$ (fig. 2.10(c)). Figure 2.10(d) represents rotations (180°) of the precipitate volume in figure 2.10(a) about the two orthogonal axes and is obviously identical to figure 2.10(a). Therefore, any two precipitates with a common growth direction and where the respective $(001)_s$ are parallel may be described by the same orientation relationship, and this observation will be important. Furthermore, this analysis confirms the existence of 12 crystallographically equivalent variants of the S-phase in Al-matrix.

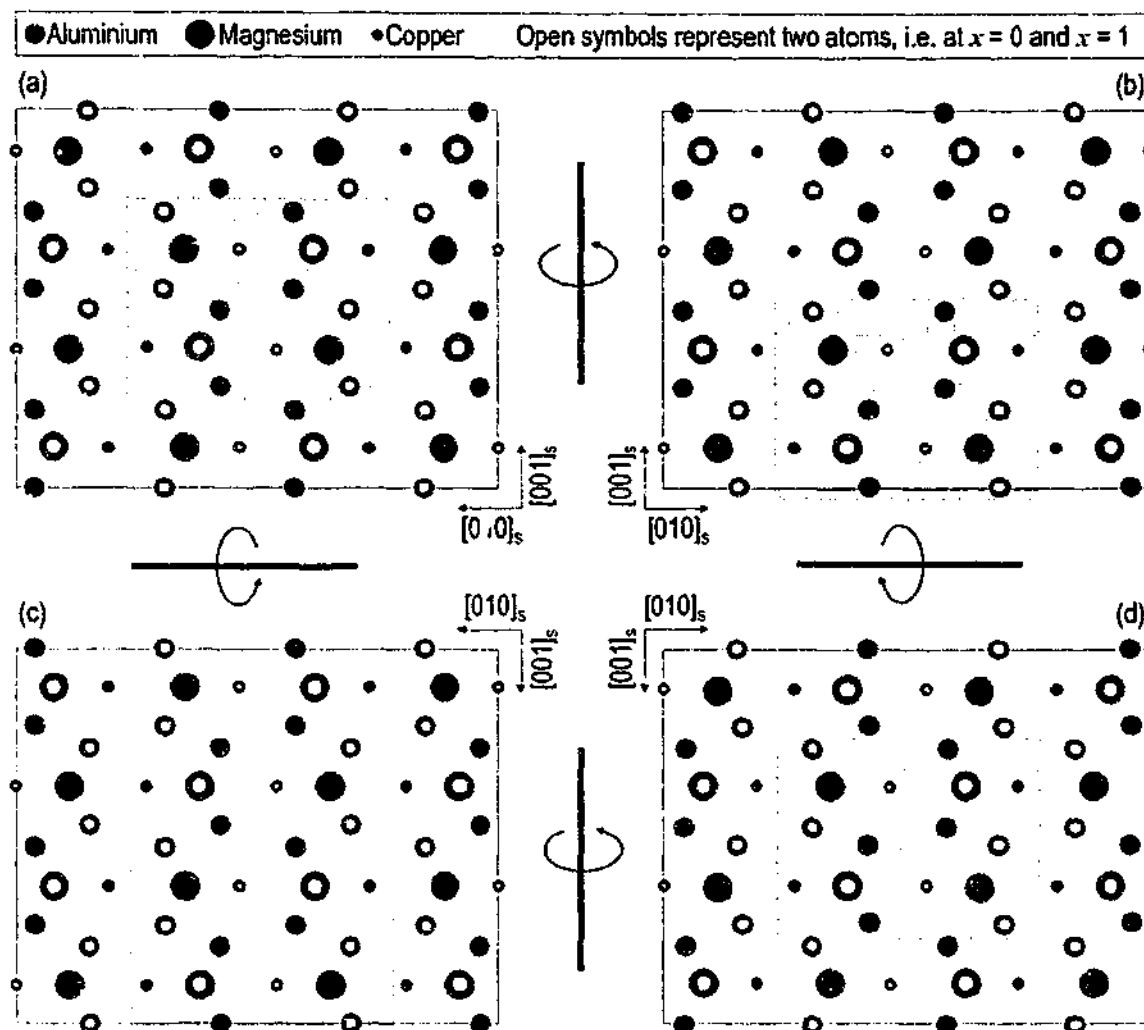


Figure 2.10 (a) Atomic positions projected parallel to $[100]_s$. A single unit cell is shaded. (b) Projected volume of (a) rotated 180° about $[001]_s$. (c) Projected volume of (a) rotated 180° about $[010]_s$. (d) Projected volume of (b) rotated 180° about $[010]_s$. In all cases (b) – (d), similar projected positions as those shaded in (a) are also shaded.

Table 2.3 contains the lattice misfit of the three principal planes of the S-phase calculated by Radmilovic *et al.* [107], based upon the lattice parameters of the RaVel model [107,153] and the

Table 2.3 Misfit along principal axes calculated from a plane matching criterion (after [107]).

Corresponding Planes	Al plane spacing (nm)	S-phase plane spacing (nm)	Strain (%)
$(100)_s // (100)_\alpha$	$1 \times d_{(100)} = 0.405$	$a = 0.403 \pm 0.001$	-0.49
$(010)_s // (01\bar{2})_\alpha$	$5 \times d_{(021)} = 0.906$	$b = 0.930 \pm 0.013$	+2.69
$(001)_s // (002)_\alpha$	$4 \times d_{(01\bar{2})} = 0.724$	$c = 0.708 \pm 0.010$	-2.28

accepted lattice parameter of pure aluminium at 20°C, 0.405 nm. Beyond the minimal misfit parallel to the growth direction of the particles, it might be expected that precipitates of the S-phase will have similar dimensions in both the $[010]_S$ and $[001]_S$ directions owing to similar misfit in these directions. However, the cross-section of typical precipitates of the S-phase perpendicular to $[100]_S // [100]_\alpha$ is elongated parallel to $[010]_S$ [75,133], and a typical example is shown in figure 2.11. Perfect lattice matching in the $(001)_S // \{021\}_\alpha$ plane is indicated in the inset of figure 2.11, suggesting that the habit plane is coherent along $[010]_S$, and hence the calculated strain in this direction (table 2.3) is apparently elastically accommodated. Precipitate growth in the c_S -direction normal to the habit plane is apparently inhibited by non-matching of the repeat distances [107] (fig. 2.12). This manifests itself in a non-equiaxed precipitate cross-section and the characteristic *lath* shape.

Radmilovic *et al.* [107] propose that the elongation parallel to $[010]_S$ occurs despite the estimated 2.69% strain because of the excellent two dimensional atomic matching between the $(001)_S$ and $\{021\}_\alpha$ planes, i.e. not only good matching parallel to the vector $[010]_S$ but also perpendicular to it. However, if the lattice parameters determined by Gupta *et al.* [130] are used rather than those of Radmilovic *et al.* [107,153], it is observed that the strain is effectively zero parallel to $[010]_S$ and $[001]_S$, indicating the selectivity of the calculation.

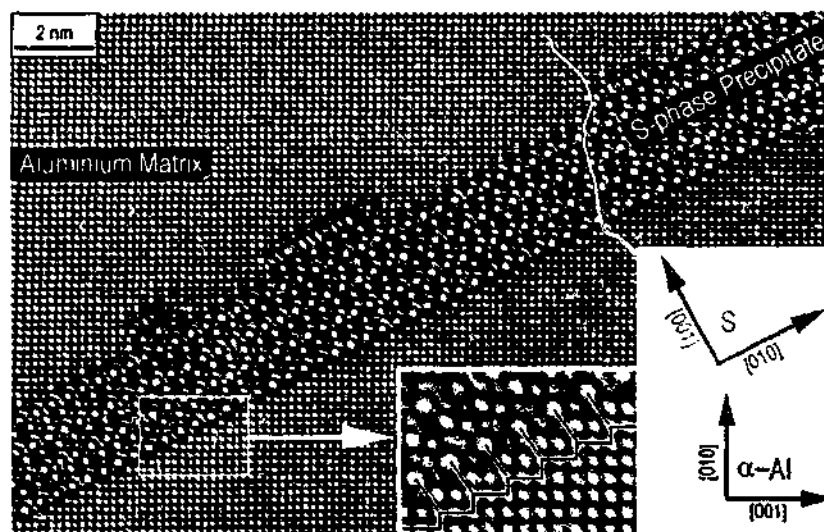


Figure 2.11 Typical precipitate of the S-phase, characterised by elongation parallel to $[010]_S$, leading to the lath morphology. The *principal* growth direction is parallel to $[100]_S // [100]_\alpha$ (into page face). Excellent atomic matching (coherency) at the interface is indicated in the inset.

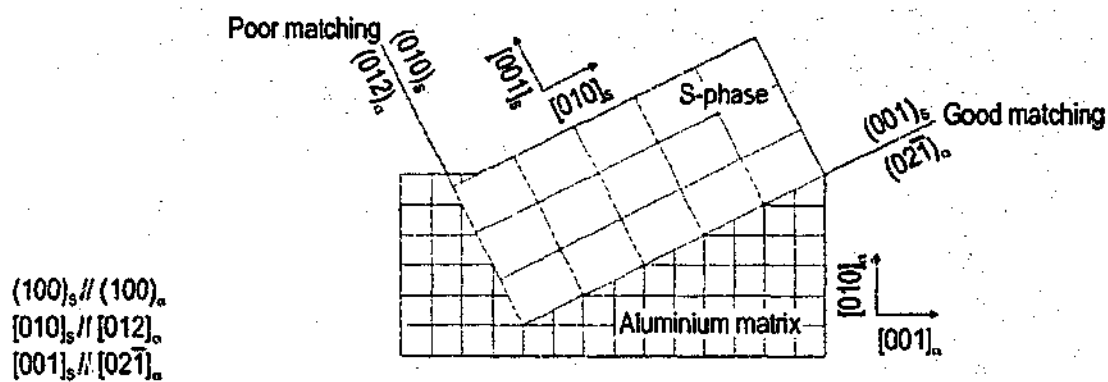


Figure 2.12 Excellent matching of lattice planes across $(001)_S // (0\bar{2}1)_A$, leading to secondary elongation in this plane. (Note: the primary elongation direction is parallel to $[100]_S // [100]_A$.)

The distinction is often made between 'lath-type' and 'rod-type' precipitates (e.g. [134]). In contrast to precipitate laths, a precipitate rod maintains an aspect ratio closer to unity in $(100)_S // (100)_A$, and the differences between two morphologies are illustrated schematically in figure 2.13. Recently, and due in large part to the improved resolution capabilities of modern electron microscopes, a greater appreciation of the differences in precipitate morphology have been achieved. For reasons that will later become clear, this discussion of precipitate morphology will begin with an appreciation of the changes in lattice *orientation* displayed by embedded S-phase precipitates.

Some scatter in the x-ray data of 4-5° away from the standard orientation relationship of S-phase was detected by Bageryatskii [125] at specific points in the ageing cycle, although the results were inconclusive. A clearer change in the orientation relationship has been observed more

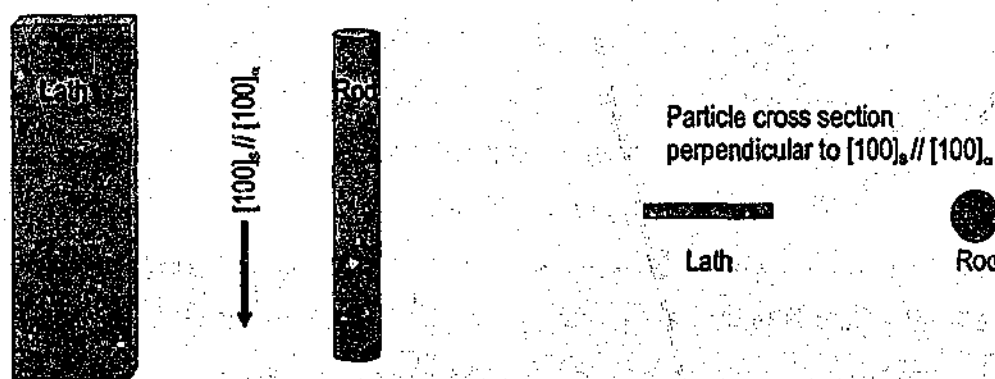


Figure 2.13 The two predominant particle morphologies of precipitates of the S-phase: laths and rods. Both are elongated in a direction parallel to $[100]_S // [100]_A$.

recently [75], described by a small but measurable ($\sim 3^\circ$) lattice rotation about the $[100]_s // [100]_a$ growth axis, although a connection between particle rotation and precipitate morphology was not initially made in great detail. Radmilovic *et al.* [107] subsequently expanded upon the morphological differences in S-phase and designated two distinct forms as Type I (standard orientation relationship) and Type II precipitates respectively [107], although maintaining that both precipitates were of lath morphology. The critical distinction in the crystallography of Type II precipitates was a lattice rotation of 5° away from the standard orientation about the $[100]_s // [100]_a$ long axis. These authors were not able to define a separate orientation relationship with the matrix. However, they did note that there were now 24 variants of the S-phase to consider: 12 of Type I and 12 of Type II. Recent studies suggest that the magnitude of rotation may be up to $\sim 6^\circ$ [131]. These changes in orientation relationship with the matrix were not being conclusively detected prior to 1996 [75] because HREM and diffraction from small volumes have only recently been applied routinely to engineering materials such as these.

Accompanying the apparent lattice rotation of the S-phase is an apparent change in the structure of the interface maintained between the parent matrix and the precipitate. The Type II (rotated) precipitates of Radmilovic *et al.* [107] are characterised by the presence of large steps at the interface, consistent in height with double the length of the $[001]_s$ lattice vector, or $2c_s$. The steps appear similar to those observed by Zhang *et al.* [134], although these latter authors did not detect a lattice rotation.

More recent data regarding the morphology of S-phase particles has been provided by Majimel *et al.* [131]. In plotting the length of the interface parallel to $(001)_s$ (i.e. the habit plane of the lath precipitate) as a function of the rotation from the standard orientation relationship, it was observed that lath-like precipitates at former dislocations have a decreasing misorientation from the standard orientation as particle length increases. For S-phase particles described as *homogeneously* nucleated (i.e. not obviously nucleated at a dislocation), the angle of rotation also reduced to zero as the length increased. This evidence confirms that precipitate rods are characterised by a lattice rotation away from the standard orientation relationship, while laths with large aspect ratio in the plane normal to the long axis maintain the well-known standard orientation. The average lattice rotation of rod-shaped particles was 4.5° [131], which is very close to that observed by Radmilovic *et al.* [107]. Despite this recent study, there remains no systematic definition of the morphological possibilities attainable. The conditions driving the differentiation in particle rotation about $[100]_s // [100]_a$ during the course of an applied heat treatment have not been addressed.

Recalling the distinction [130] between coherent particles and incoherent particles (S' and S respectively), it could be suggested that S' are oriented in the standard configuration (lath-shaped particles), while the S -phase describes those particles that are rotated about $[100]_s // [100]_a$. There is no reference in the literature to a proposal such as this.

Nucleation and growth of precipitates of the S-phase

It is likely that the factors leading to a *differentiation* in precipitate orientation and morphology noted in the literature have their origin in the local conditions in the solid during precipitate nucleation and growth. As such, the present section will address precipitate formation and growth processes.

Several authors [8,75,126,131,133,134,150] have concluded that laths of S -phase nucleate preferentially at edge dislocations [32]. Based upon the selection rules for precipitates at dislocations (§2.2.2), it could be suggested that the direction of the Burgers vector is parallel to, or a significant component is parallel to, the direction of maximum volumetric misfit vector. The strains parallel to the principal axes of the unit cell (table 2.3) have been calculated. However, as previously referred to, it is observed that the strain is near zero for fully coherent laths [130]. Radmilovic *et al.* [107,153], however, apply their self-determined lattice parameters, and find that an appreciable strain is to be accommodated parallel to $[001]_s$. Figure 2.14(a) is a depiction

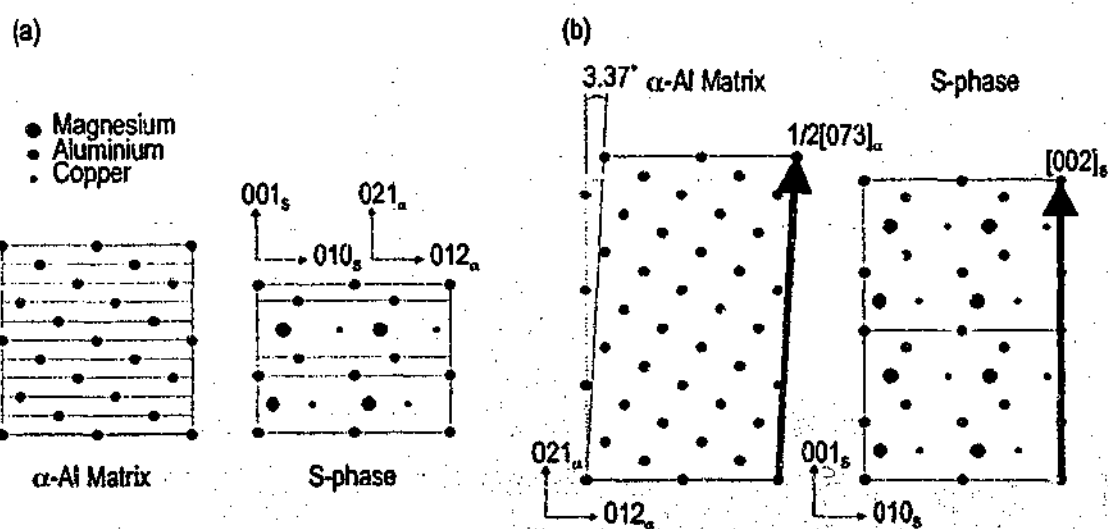


Figure 2.14 Transformation of a cell of atoms at atomic positions in the fcc crystal to the orthorhombic S -phase, leading to the formation of (a) Type I lath-shaped precipitates and (b) Type II precipitates with ledges $2c_s$ in height [107].

of the volume change, where five $\{021\}_\alpha$ planes transform directly to the S-phase via a compression parallel to $[001]_s$. Analysis of this type is clearly critically dependent upon the incorporation of accurate lattice constants. As an example, Wilson and Partridge [88] applied the lattice parameters of the S-phase proposed by the x-ray work of Silcock [85] and found that the maximum misfit occurred in a direction parallel to $[010]_s$ rather than $[001]_s$. With the general acceptance that the S-phase lattice can exist in strained versions (the origin of the proposed S' nomenclature), it would seem that assessment of the volume change during transformation in the manner described above may be misleading, since very different results can be obtained even within the quoted lattice parameters in the literature.

Radmilovic *et al.* [107] observed a small shear displacement of the matrix planes at nucleation of particles in the standard orientation relationship, but could not take the analysis any further [107,132]. The lattice correspondence between Type II precipitates and the matrix (fig. 2.14(b)) can be explained by a slightly skewed cell of the aluminium lattice transforming to two unit cells of the S-phase [107]. The difference in orientation of Type II precipitates thus results from an invariant line transformation strain. The correspondence can be written as:

$$[100]_\alpha \rightarrow [100]_s \quad [01\bar{2}]_\alpha \rightarrow [010]_s \quad \frac{1}{2}[073]_\alpha \rightarrow [002]_s$$

The transformation is achieved by a shear of 3.7° (the angle between $[073]_\alpha$ and $[021]_\alpha$) and a two-dimensional transformation strain resulting in a contraction of 8% along $[073]_\alpha$ and a 2.69% expansion along $[01\bar{2}]_\alpha$.

Summary

• The background information on the S-phase has raised several questions in the context of the present research that currently remain unanswered, and a number of these are summarised below:

- Does the differentiation in S-phase crystallography (lattice parameters, lattice orientation etc.) originate at the dislocation upon which nucleation takes place?
- Are there only two types of the S-phase, i.e. Type I (standard orientation relationship) and Type II, or is the current model incomplete?

- To what extent does the orientation and characteristics of the interface change for those particles that are rotated away from the standard orientation relationship?
- Can we modify the processing conditions of Al-Cu-Mg alloys so that the relative concentration of particles of the S-phase with prescribed orientation relationship and morphology is altered?
- Can differences in the lattice orientation of S-phase be correlated to a distinction between S' and S?

2.3.5 The T-Phase

The T-phase in Al-Cu-Mg alloys, Al_6CuMg_4 , is an isomorph of the phase labelled T-phase ($\text{Mg}_{32}(\text{Al}, \text{Zn})_{49}$) in Al-Zn-Mg alloys [156,157]. The phase has a body-centred cubic structure containing 161 [158] or 162 [156,157] atoms, and the lattice parameter is 1.416 nm – 1.425 nm [156-158]. Precipitates of the T-phase occur as irregularly-shaped precipitates. There is no evidence in the wider literature that the T-phase forms heterogeneously at dislocations.

2.4 Implications for the Present Work

Al-Cu-Mg alloys form the basis of an important class of aluminium alloys, and derive their appreciable hardness and strength from a dispersion of second-phase precipitates that form during appropriate elevated temperature ageing treatments. Several of the precipitates in this alloy system, including θ' and S-phase, display an affinity for nucleating at pre-existing dislocations. It is interesting to investigate the link, if any, between the crystallography of strengthening precipitates and the nature of the dislocations upon which these precipitates nucleate heterogeneously. It is important that dislocations upon which precipitation takes place are not introduced accidentally. As dislocation loops can not unintentionally be introduced into the system, they provide the ideal environment in which to study the potentially close link between dislocations and precipitates. Initially, all precipitates in the present system will be addressed. However, particular reference will be made to the not-so-well understood precipitates of the orthorhombic S-phase, the presence of which dominates industrially important Al-Cu-Mg alloys. The S-phase can adopt a range of crystallographic forms, the extent of which is poorly understood, particularly with regard to the role that dislocation character fulfils during heterogeneous precipitation. The technological significance of the present investigation is such that it leads to the possibility of designing the precipitate morphology and distribution in these and other alloys as a function of the initial dislocation distribution. Importantly, the microstructural design of alloys can potentially take advantage of the impact that precipitate size and shape have on the relevant parameters of the Orowan equation (§2.1.1), although a detailed study of this impact is beyond the scope of the present work.

3.0 Research Design and Methodology

It is a primary aim of this thesis to explore the link, if any, between the crystallography of individual precipitate phases and the nature of the dislocations upon which the precipitate nucleates heterogeneously, and the focus will be on the S-phase (Al_2CuMg). Fulfilment of these aims requires the critical selection of experimental variables including alloy chemistry and materials processing routes, and appropriate characterisation techniques. Moreover, the dislocations on which precipitation takes place are to be such that they are not introduced by material handling.

The aluminium-rich corner of the Al-Cu-Mg ternary phase diagram (§2.1.2, fig. 2.3) defines the broad compositional field from which the alloys were selected in the present work. All alloys studied were prepared from nominally pure ingredients, and the selection of alloy composition was based upon both the chemistry of industrial alloys and adequate coverage of the equilibrium phase fields. Justification for the precise selection of alloy composition is provided in this chapter. It was essential for processing of the selected alloys to be performed in such a way that the heterogeneous nucleation of precipitates was permitted, and this required the presence of dislocations in the microstructure prior to the nucleation of second-phase precipitates. The potential routes to achieving this outcome are discussed. Finally, the manner in which changes in mechanical properties and microstructure were monitored are described. This includes a justification and description of the techniques of hardness testing and transmission electron microscopy, which together have been the main tools of characterisation.

3.1 Alloy Selection and Preparation

The composition of the alloys chosen in this study are based on the IADS 2000 series of heat-treatable wrought aluminium alloys. The compositions of typical industrial alloys are provided in figure 3.1(a), while figure 3.1(b) indicates the location of these compositions in an isothermal section (190°C) of the Al-Cu-Mg phase diagram [7,50,51].

Alloys in the $(\alpha+S)$ and $(\alpha+S+T)$ phase fields harden during artificial ageing in two distinct stages (§2.1), where the first occurs within 60 s and the latter after extended ageing. Recently, new proposals have been made for the origins of hardening in these alloys, and the debate continues [59,60,64,69,73,159]. As a result of this recent research activity and as a minor component of the present work, further characterisation of this two-stage hardening behaviour was attempted. A composition of Al-1.1Cu-1.7Mg, which approximates to that of the industrial alloy 2618, defines an $(\alpha+S)$ phase field alloy that hardens in two-stages and was selected as the base alloy for the present work. Two alloy groups were prepared: Al-1.1Cu-xMg (Series I) and Al-xCu-1.7Mg (Series II), where x represents incremental additions of the third element up to the

IADS designation	Si	Fe	Cu	Mn	Mg	Zn	Cr	Ti	Other
2017	0.2-0.8	0.3	1.5-1.9	0.2-0.5	0.5-0.9	0.1	0.05	0.1	0.2Zr+Ti
2014	0.5-1.2	0.3	1.7-2.1	0.2-0.6	0.2-0.9	0.1	0.05	0.1	0.2Zr+Ti
2024	0.5	0.2	1.6-2.1	0.1-0.5	1.4-2.0	0.1	0.05	0.1	0.2Zr+Ti
2618	0.1-0.25	0.4-0.6	0.8-1.2		1.5-2.0	0.05		0.02-0.05	0.9-1.2N
2124	0.2	0.1	1.6-1.7	0.1-0.4	1.4-2.0	0.1	0.05	0.1	0.2Zr + Ti

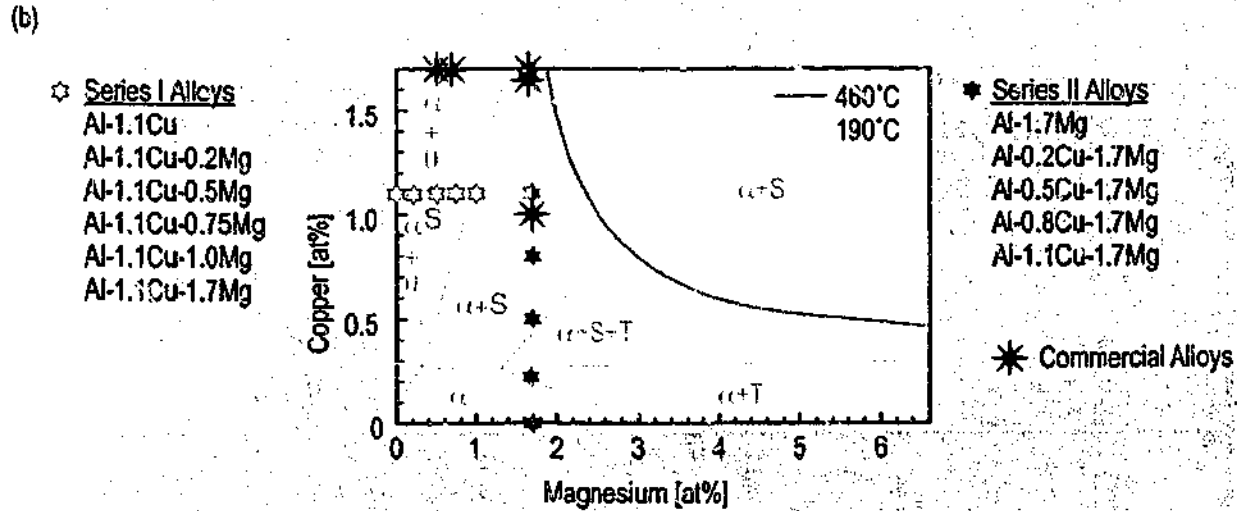


Figure 3.1 (a) Some common Al-Cu-Mg-based industrial alloys. (b) Isothermal section of the Al-Cu-Mg phase diagram, indicating the location of the selected compositions in the present work.

Table 3.1 Impurity elements in the high-purity primary alloy ingredients.

Impurities in Raw Material (ppm)													
Aluminium	Cr Cu Mn Ni Pb Sn Ti V Zn							B Fe Si			Ga	Mg	
	< 5							20			< 50	10	
Copper	Ag	As	Bi	Cd	Fe	Mn	Ni	Pb	Sb	Se	Sn	Te	Zn
	1	1	0.2	0.2	4	0.3	1	1	1	2	1	0.5	0.3
Magnesium	Fe Mn Si			Al Zn Zr			Ni Cu Sn Pb				Be Sr		
	< 100			< 50			< 20				< 10		

final composition of Al-1.1Cu-1.7Mg, as shown in figure 3.1(b). The incremental solute additions were selected to be representative of the important phase fields in the Al-rich corner of the phase diagram ($\alpha+\theta$, $\alpha+S$ and $\alpha+T$).

The purity of the raw ingredients was high - Al: 99.99%, Cu: 99.999% and Mg: 99.9%, and the impurity elements are shown in table 3.1. Aluminium granules (5-10 mm \varnothing) were placed in a 1 kg capacity graphite crucible and heated in a resistance furnace (in air) until molten. Upon attaining a temperature of 780°C, pure copper (200 μm foil) was added and 300 s hence, magnesium (as required) was added as cubes 10 mm on edge. Following stirring and within approximately 180 s of magnesium addition, the alloys were cast into pre-heated, graphite-lined steel book moulds (100 \times 150 \times 10 mm). The cast alloys were solution treated at 525°C (24 h), scalped and rolled to a thickness of 500 μm or 2.0 mm. All alloys were rolled without difficulty, apart from those alloys containing 1.7%Mg, where edge cracking of the sample was common. Three alloy samples from three different locations in the rolled sheet were assayed (table 3.2).

Table 3.2 Nominal and actual composition of the two series of ternary Al-Cu-Mg alloys examined.

	Nominal Composition	Actual Composition		
		Aluminium	Copper	Magnesium
Series I Al-1.1Cu-xMg	Al-1.1Cu	Bal.	1.11	0.02
	Al-1.1Cu-0.2Mg	Bal.	1.10	0.19
	Al-1.1Cu-0.5Mg	Bal.	1.13	0.56
	Al-1.1Cu-0.75Mg	Bal.	1.13	0.76
	Al-1.1Cu-1.0Mg	Bal.	1.12	0.99
	Al-1.1Cu-1.7Mg	Bal.	1.05	1.63
Series II Al-xCu-1.7Mg	Al-1.7Mg	Bal.	<0.01	1.74
	Al-0.2Cu-1.7Mg	Bal.	0.20	1.74
	Al-0.5Cu-1.7Mg	Bal.	0.47	1.68
	Al-0.8Cu-1.7Mg	Bal.	0.80	1.69
	Al-1.1Cu-1.7Mg	Bal.	1.05	1.63

3.2 Dislocation Distribution and Thermal Processing

The influence of pre-existing dislocations on precipitate nucleation and growth was the central issue in the present work, and therefore careful control was exercised over the treatment of the alloys prior to second-phase precipitation. Essentially, each alloy was processed to attain an appropriately dense dislocation microstructure prior to the nucleation of precipitates. A dislocation microstructure amenable to investigation in the present work was required to have the following characteristics:

4. *It was to be reproducible*, so that many examples of heterogeneous nucleation might occur in identical strain environments. This was essential for establishing a strong link, if it existed, between the precipitate crystallography and the heterogeneous nucleation site.
5. *It was to present to the supersaturated solid solution a range of different strain environments as heterogeneous nucleation sites rather than a single environment*, so that potentially systematic changes in precipitate crystallography could be investigated as a function of systematic changes in the strain environment created by the dislocation.
6. *It was to be easily produced by simple laboratory techniques* so that specimen preparation time and expense could be minimised.
7. *It was not to be introduced unintentionally by specimen handling*, so that all examples of dislocations form in the same manner.

The alternative methods of introducing dislocations into a supersaturated solid solution are discussed in the following section. The optimum alloy specimen dimension will also be discussed with respect to thermal processing and experimental control. Furthermore, the time and temperature to which the alloys were to be exposed during extended artificial ageing are considered in the context of a regime likely to generate a distribution of strengthening particles in fully-hardened alloy specimens.

3.2.1 Introduction of Dislocation Sub-Structure

Dislocations may be introduced into a super-saturated solid solution in several ways, including the *passive* method of vacancy coalescence leading to the formation of dislocation loops during and following quenching [160-179], and the *active* method of plastic deformation, first referred to in the initial proposals for the existence of dislocations themselves [11-14]. Consider first the *passive* method. Figure 3.2(a) is a depiction of the typical thermal processing route employed in the preparation of a foil for examination in a transmission electron microscope (TEM). A strip of alloy is solution treated, quenched, aged for 60 s at 150°C and then quenched at 20°C. A disc 3 mm in diameter is removed from the thermally-processed strip and prepared for TEM examination. Small dislocation loops are present immediately following quenching, as indicated. In addition, there are several other types of dislocations that are clearly not loops. During elevated temperature ageing for 60 s, the loops grow in a manner consistent with vacancy coalescence. The dislocation microstructure is, however, non-uniform and not reproducible with respect to dislocation loop density.

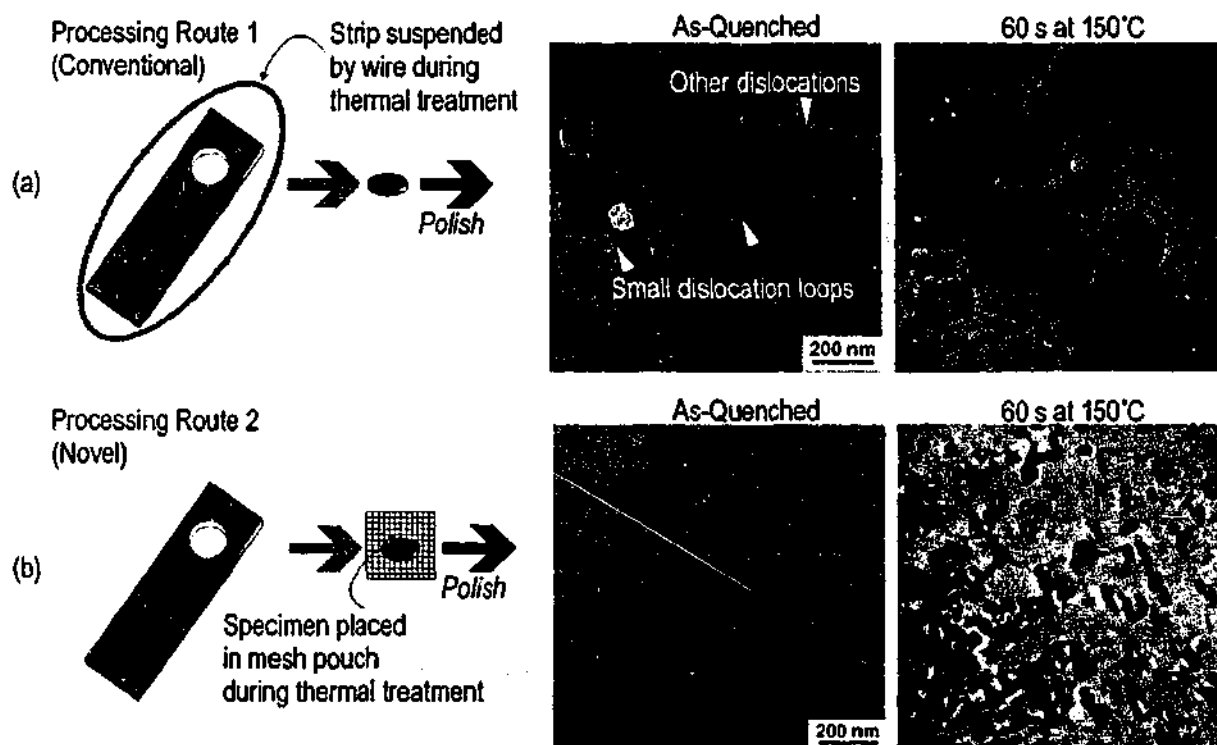


Figure 3.2 (a) Conventional processing route for TEM foil preparation. (b) Novel processing route employed in the present work, eliciting a dense and uniform distribution of dislocation loops

Consider now figure 3.2(b), which depicts an alternative route for sample processing. Discs 3 mm in diameter were removed from a strip of material *prior* to thermal processing, and placed in a steel mesh pocket (10×10 mm). The alloy disc is then solution treated, quenched, aged for 60 s at 150°C and then quenched at 20°C. The as-quenched microstructure is apparently free from visible dislocation loops, and contains a negligible concentration of non-loop defects. Elevated temperature ageing for 60 s elicits a comparatively high, uniform and reproducible density of similarly-sized dislocation loops when compared to the conventional processing route. There are very few dislocations other than dislocation loops. Dislocation loops are defined by a single dislocation where the line direction must change at least twice so that the dislocation can form a closed loop, and therefore it is expected that the strain environment around the dislocation core will change systematically. The method described is simple, and can be implemented using simple laboratory equipment. Therefore, the method meets the criteria stipulated for introducing an appropriately dense dislocation arrangement into a pre-precipitation microstructure.

Consider the introduction of dislocations via the *active* method of plastic deformation. Figure 3.3 is a TEM image of alloy Al-1.1Cu-0.5Mg that was quenched following solution treatment, plastically deformed ($\epsilon = 0.05$), aged at 150°C for 60 s and quenched at 20°C. Both dislocation loops and other dislocations were present, as indicated. However, the dislocation microstructure was random and not reproducible, and the aims of the present investigation were not to be significantly advanced by the introduction of dislocations via active plastic deformation.

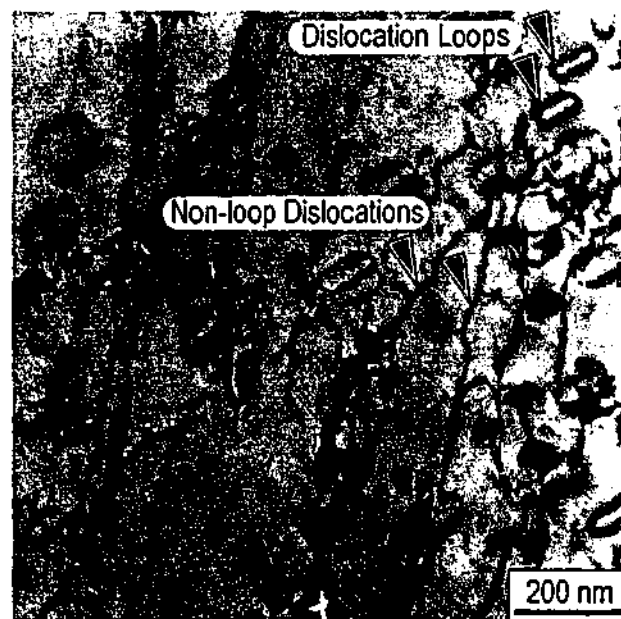


Figure 3.3 Al-1.1Cu-0.5Mg alloy deformed through a 5% strain by rolling, indicating the presence dislocations introduced by the plastic deformation, and by vacancy condensation (loops).

Consider the heat-transfer conditions when a 3 mm \varnothing disc of material at temperature T_1 is transferred to a medium at temperature T_2 , as, for instance, during immersion of the quenched disc (at room temperature) in an ageing bath at elevated temperature. The amount of heat Q required to change the temperature of the system is proportional to the mass m of the specimen and to the temperature difference, $\Delta T_{1,2}$. This is expressed in the following equation [180,181]:

$$Q = mc\Delta T_{1,2} \quad \text{Equation 3.1}$$

where c is the specific heat of the material (~ 900 J/kgK for aluminium) [181]. Since c and ΔT are common to alloy discs of any thickness, and since the thickness of the discs is directly proportional to m , the amount of heat required to change the temperature of the discs is directly proportional to the disc thickness. It is expected, therefore, that a thicker specimen will take longer to reach the temperature of the surrounding medium because it requires a greater amount of net heat input. The presumed migration of vacancies to form and grow vacancy condensation (dislocation) loops is a thermally activated process, as observed in figure 3.3. Therefore, reproducible loop microstructures require consistent vacancy migration rates, which can only be guaranteed by a *consistent sample thickness*.

Accordingly, all alloy specimens were prepared to have a consistent thickness during thermal processing so that direct microstructural comparisons could be made between alloys of different chemistry. Alloy samples processed for use as TEM foil material had a thickness greater than or equal to three times the grain size of the material to avoid the influence of surface effects [182] where the surface might, for example, act as a vacancy sink. Typical grain sizes in the current alloy specimens were 50 to 150 μm and it was decided that samples of 500 μm thickness be used.

3.2.2 Thermal Processing

According to the ternary phase diagram (fig. 3.1(b)), the solute in all alloy compositions is expected to be in solution at temperatures above 460°C, and solution treatment was performed at 525°C for 1 h in the present work. Specimens were quenched from 525°C into water at 20°C, and immediately placed in the ageing baths (within 5 s) at 150°C. Arresting the elevated temperature ageing at 60 s by quenching into water at 20°C showed, upon examination, a dense concentration of dislocation loops as discussed in the previous section. Extended ageing at

150°C has been applied in previous work [59,61,75] and has been shown to lead to second-phase precipitation and significant hardening, and similar treatments were thus applied in the present work. The thermal treatments are summarised in figure 3.4(a).

In addition to samples aged immediately following quenching from the solution treatment temperature, selected samples were exposed to a period of natural ageing at room temperature, following quenching and prior to artificial ageing (fig. 3.4(b)). Typically labelled a *pre-ageing* step, such treatments were modelled upon selected industrial heat-treatments (e.g. T7 heat treatment [7]). It was of interest to investigate the impact of such a pre-ageing step on the uniform dislocation loop microstructure and the subsequent precipitate nucleation, both at the dislocation and away from them.

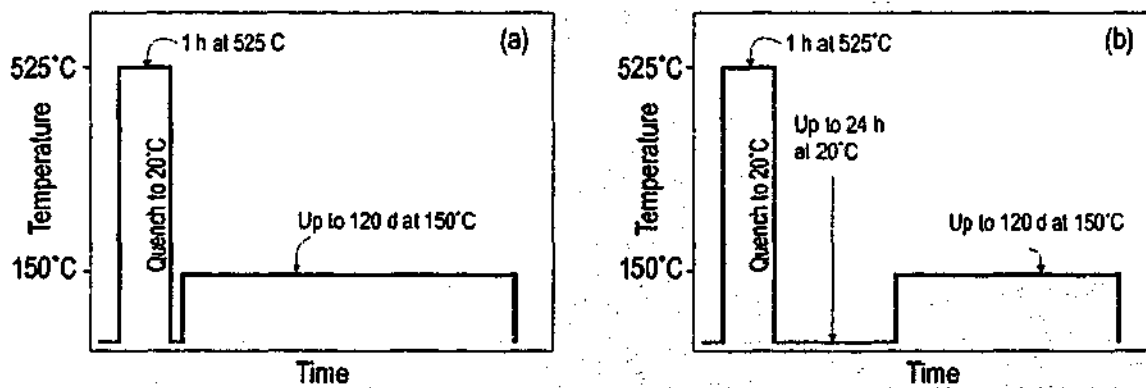


Figure 3.4 Thermal regimes applied in the current work: (a) Solution treatment (525°C) + quench (20°C) + artificial ageing (150°C). (b) Solution treatment (525°C) + quench (20°C) + pre-ageing (20°C) + artificial ageing (150°C).

3.3 Hardness Testing

Monitoring of specimen hardness (i.e. resistance to deformation in the units of load/area) is a reliable method of determining the response to age hardening of these alloys, and has been applied extensively in previous studies. Prior to the testing of *bulk* alloy samples (~1.5 mm thick) by a Vickers diamond under a 5 kg load, the specimen surface was prepared by abrasion using 1200 grit SiC paper prior to thermal processing. Reported hardness values (Vickers hardness number, VHN) represent the average of at least 10 individual measurements of the bulk samples and, where appropriate, the experimental errors of measurement (standard deviation) are presented together with average results. The maximum diagonal width of the indentations was ~500 μm , satisfying the stipulation of ASTM Standard E92-82 that the thickness of a specimen must be greater than 1.5 times the width of the diagonal.

As discussed, the specimen thickness selected for thermal processing of TEM foils was 500 μm . The microstructural evolution within such discs can not necessarily be directly correlated with the bulk hardness measurements (1.5 mm thickness), particularly during the very early stages of ageing. Direct correlation of the hardening behaviour of the alloys with the state of the microstructure would require monitoring of the hardening response of 500 μm thick samples. The loads supplied by a typical bulk Vickers hardness tester are too large for the comparatively thin specimen thickness of 500 μm , and therefore the hardening response must be monitored by microhardness measurements under smaller loads. A UMIS 2000 © ultra microhardness indentation system [183] was used for this purpose.

Specimens of 3 mm \varnothing and 500 μm thickness were thermally processed as appropriate and abraded to a thickness of 300 μm . The condition of the specimen surface is critical to the measurement of hardness using very small loads, and therefore one face of each disc was electropolished to eliminate surface deformation using a modified TEM foil preparation procedure (using a solution of 33 vol.% HNO_3 and 67 vol.% CH_3OH at -30°C at approximately 15 V (0.2 A)). Two discs were placed back-to-back in the specimen holder of a Tenopol 5 © twin-jet electropolisher, effectively protecting one broad surface of each disc from the incoming stream of solution, as described in figure 3.5. The polishing procedure was arrested at a set point in time corresponding to the removal of 100 μm of alloy from the exposed surfaces of the discs. The microindenter, when placed upon the polished surface, applied a load to a section of material

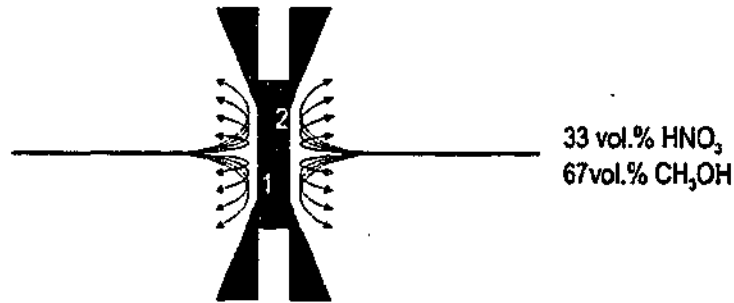


Figure 3.5 Twin-jet electropolishing technique for surface preparation of two microhardness specimens.

at least 200 μm thick, as indicated in the flow chart of figure 3.6. Up to five consecutive indentations were performed in a given session, and the specimen was translated automatically by 100 μm on the specimen stage between indentations. Figure 3.6(a) displays the surface typical of the specimens prepared and a series of four typical nano-indentations, while figure 3.6(b) shows a magnified image of the indentation created by the Berkovich indenter.

Microindentation testing using the UMIS 2000 © is different to conventional hardness testing in several ways. Most importantly, the UMIS 2000 © is force-driven, i.e. the indenter is driven into the surface of the material until a resistance is reached equal in magnitude to a predetermined force. The penetration depth of the indenter corresponding to the force equilibrium is measured and recorded. The apparatus can be programmed to achieve a series of incremental increases in load and, together with the corresponding series of penetration depths, the data can be plotted as

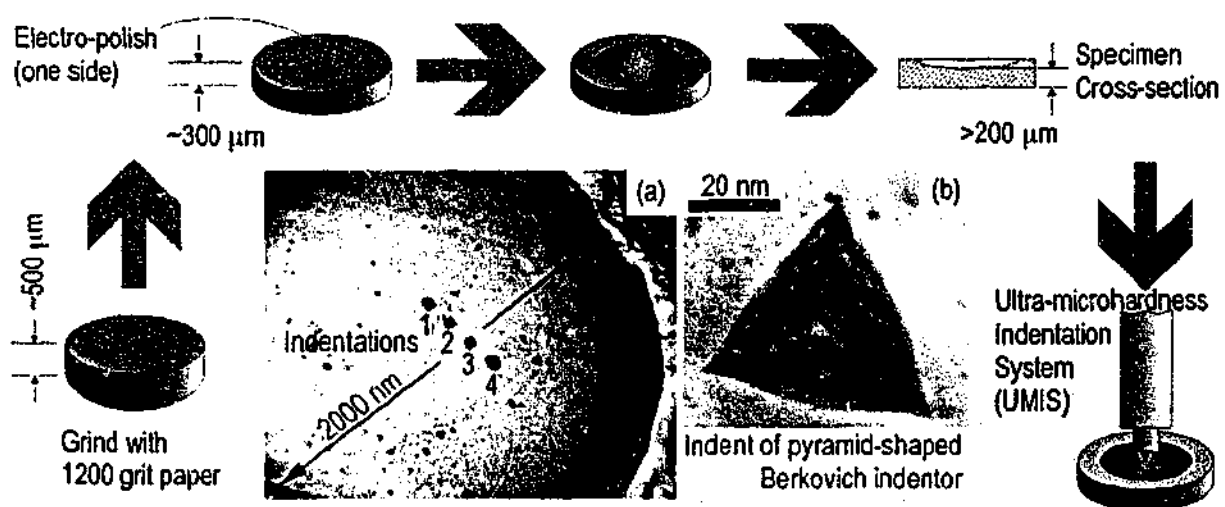


Figure 3.6 Flow chart of sample preparation for microindentation hardness testing. (a) The prepared surface of the specimen with four consecutive indentations. (b) An indentation into the specimen surface created by the specimen indenter.

a force-penetration curve for the loading cycle. Unloading curves may also be recorded, and the force-driven operation of the apparatus thus records the elastic recovery of the material.

In the present work, the apparatus was programmed to ramp up from a load of 0 to 1000 mN in 100 steps, and unload at the same rate. The force was not linearly increased, but applied in a stepped sequence defined by the relationship $Load = [N_s \sqrt{1000}/100]^2$, where N_s is the step number and the load increment, ΔL , is calculated as $\Delta L = [N_s \sqrt{1000}/100]^2 - [(N_s - 1) \sqrt{1000}/100]^2$. The procedure produces steps of approximately equal penetration (i.e. at low loads the load steps are small, while at high loads, the load steps are larger). Figure 3.7 includes five consecutive force-penetration curves for both the loading and unloading portions of one of the alloys in the present work. A large amount of information can be sourced from the curves (including the modulus of elasticity), but of singular interest here is the hardness at maximum depth, which is calculated as the ratio of load to area (N/m^2). The area, A , is calculated according to the equation provided in figure 3.7 as a function of the penetration depth, h_p , for the unique geometry of the Berkovich indenter. As an example, a load of 1000 mN and a penetration depth of 5500 nm equates to a hardness of 1.35 GPa. Experimental reproducibility was excellent, and in many cases the consecutive load-penetration plots overlapped perfectly for a given specimen, which indicated that the resistance of the microstructure to deformation was uniform. The hardness results were converted to a Vickers hardness equivalent by the UMIS 2000 © software.

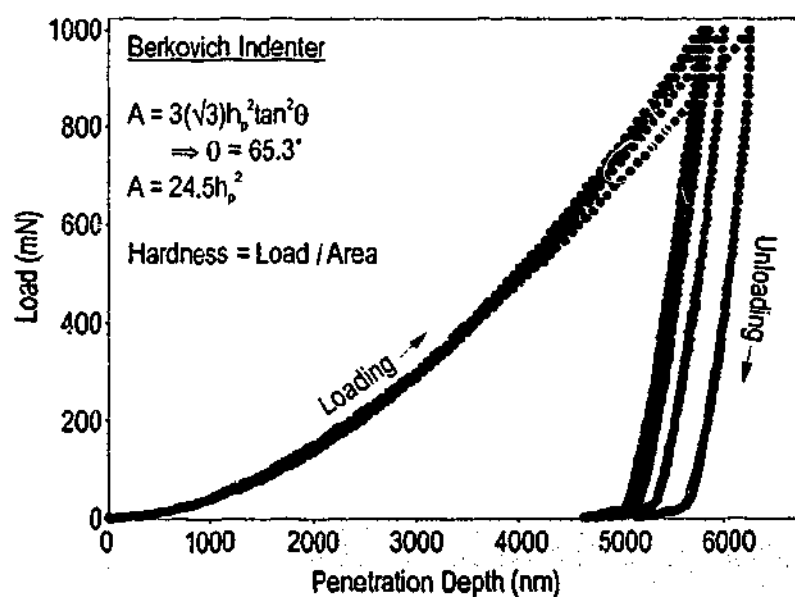


Figure 3.7 Five consecutive load-penetration curves for both the loading and unloading portions of five consecutive indentations in the present work.

3.4 Transmission Electron Microscopy

The advantage of analytical transmission electron microscopy over a range of alternative characterisation tools (e.g. conventional light microscopy, X-ray diffraction, neutron scattering) is its ability to provide a combination of imaging, diffraction and chemical analysis at high spatial resolution. In the current study, various transmission electron microscopes have been used in both imaging and diffraction modes, and the relevant details of the investigation are included below, preceded by an overview of the foil preparation technique employed.

3.4.1 Foil Preparation

Specimens were examined following (ST = solution treatment, Q = quench):

- ST (525°C) + Q (20°C)
- ST (525°C) + Q (20°C) + artificial ageing (150°C) + Q (20°C)
- ST (525°C) + Q (20°C) + pre-ageing (20°C)
- ST (525°C) + Q (20°C) + pre-ageing (20°C) + artificial ageing (150°C) + Q (20°C).

The thermally-processed alloy discs (3 mm \varnothing \times 500 μ m thick) were ground to approximately 100 μ m thickness using abrasive 1200 grit SiC paper and polished in a twin-jet electropolisher (using a solution of 33 vol.% HNO₃ and 67 vol.% CH₃OH at -30°C) at approximately 15 V (0.2 A) (fig. 3.8). Upon perforation of the disk, as detected by photo-sensors, the foil was carefully washed in high-purity ethanol, dried in air, and stored in a desiccating environment until examined in the TEM. Figure 3.8(a) is an image obtained using conventional light microscopy of the electropolished surface and the perforation near the centre of the foil, while figure 3.8(b) displays the sometimes buckled nature of the thin foil adjacent to the perforation.

In all cases, the minimum intervening period between the final quench at 20°C and examination in the microscope was 1.5 h (~0.5 h foil preparation, ~1 h microscope start-up and alignment). In cases where the specimen *was not* exposed to artificial ageing at 150°C (i.e. the as-quenched microstructure), the preparation time at 20°C for 1.5 h may significantly influence the microstructure, because the solute and vacancy concentrations in solution are very high

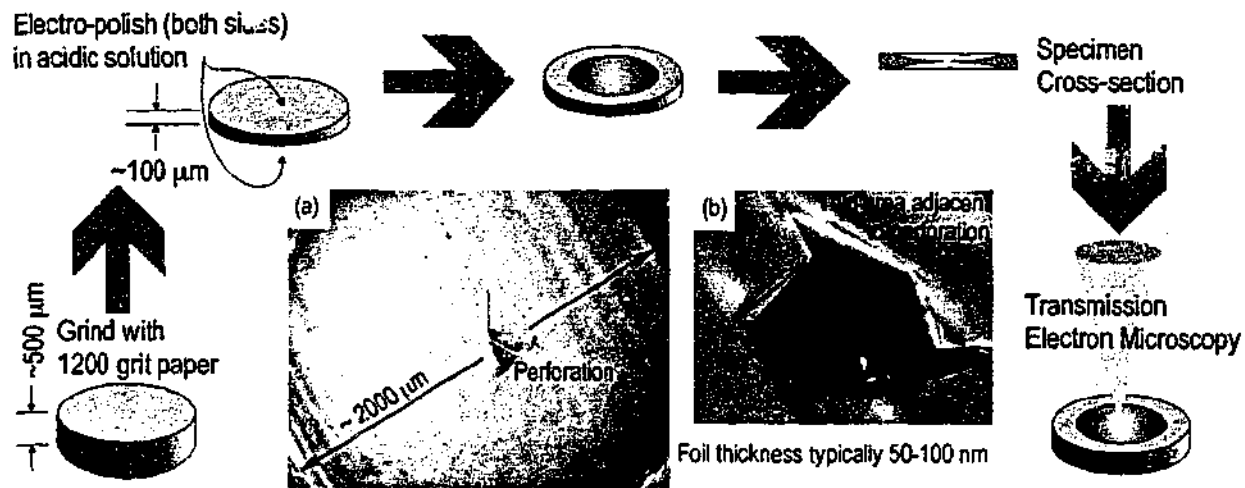


Figure 3.8 Flow chart of sample preparation for transmission electron microscopy. (a) The electropolished surface of the specimen with a perforation near the centre. (b) The thin area immediately around the perforation can be buckled.

immediately following quenching, and this should be appreciated when examining the relevant microstructures. In cases where the specimen was exposed to the artificial ageing temperature of 150°C during processing (60 s to 120 d in the present work), the preparation time of 1.5 h at room temperature is assumed to have minimal influence upon the microstructure, since the thermally-driven processes of vacancy and solute diffusion occur at a significantly slower rate at room temperature than at 150°C. Foils of specimens aged at 150°C for periods between 60 s and 3 d were examined within 1.5 – 2 h of final quenching. Foils of specimens aged at 150°C for between 3 and 10 d were typically examined within seven days of final quenching, while microstructures at maximum hardness and over-aged microstructures were examined up to three months following quenching.

3.4.2 Conventional Imaging and Diffraction

If a TEM specimen is sufficiently thin, an incident electron beam of sufficient energy (100 – 200 keV) passes either directly through the specimen volume, or is scattered by it. Both the electrons directly transmitted through the foil and those elastically scattered through characteristic Bragg angles by the atomic planes of the specimen may be collected as they emerge from the bottom surface of the foil and brought to focus in the back focal plane of the objective lens, defining a *diffraction pattern*. Bright-field (BF) electron microscopy is performed by inserting an objective aperture into the back focal plane of the objective lens and selecting only the transmitted beam to form the image. Alternatively, selection of a specific scattered beam of electrons in the objective

aperture leads to dark-field (DF) imaging. To maximise the *diffraction contrast* in both BF and DF microscopy, two-beam conditions were always used in the present work. Weak-beam DF (WBDF) microscopy is performed by exciting the relevant diffraction vector g under two-beam conditions, and translating the reflection g (using the DF coils on the microscope) to the optic axis [184]. The objective aperture is then inserted about the optic axis. The intensity of reflection g becomes very weak under these conditions, and hence the exposure times are very long (typically ~ 40 s). Both BF and WBDF imaging techniques on a Philips CM20 operating at 200 kV have been used in the present work. Figure 3.9(a) is a typical two-beam BF image of alloy Al-1.1Cu-0.5Mg solution treated at 525°C, quenched at 20°C and aged for 60s at 150°C, and figure 3.9(b) is the associated diffraction pattern. The resultant high density of dislocation loops is difficult to interpret because of the distortion induced in the crystal by the strain field of the dislocation. Figure 3.9(c) is a WBDF image of precisely the same area as that shown in figure 3.9(a). As demonstrated, the advantages of the WBDF technique include strong image contrast, which is extremely useful for estimating, for instance, the density of loops in a given volume of material. Therefore, the DF technique was favoured over BF conditions when characterising microstructures dominated by dislocations in those cases where extra resolution was necessary. For microstructures containing precipitates, BF imaging was predominantly used.

Apart from the directly transmitted beam parallel to the optic axis of the microscope, individual beams in the diffraction pattern pertain to sets of parallel atomic planes from which the electrons have been characteristically diffracted. The position of the spots is therefore a function of crystal plane orientation and spacing. Due to buckling of the thin foil, it is often useful to select only a fraction of the area of a single grain in the specimen to form the diffraction pattern by inserting a

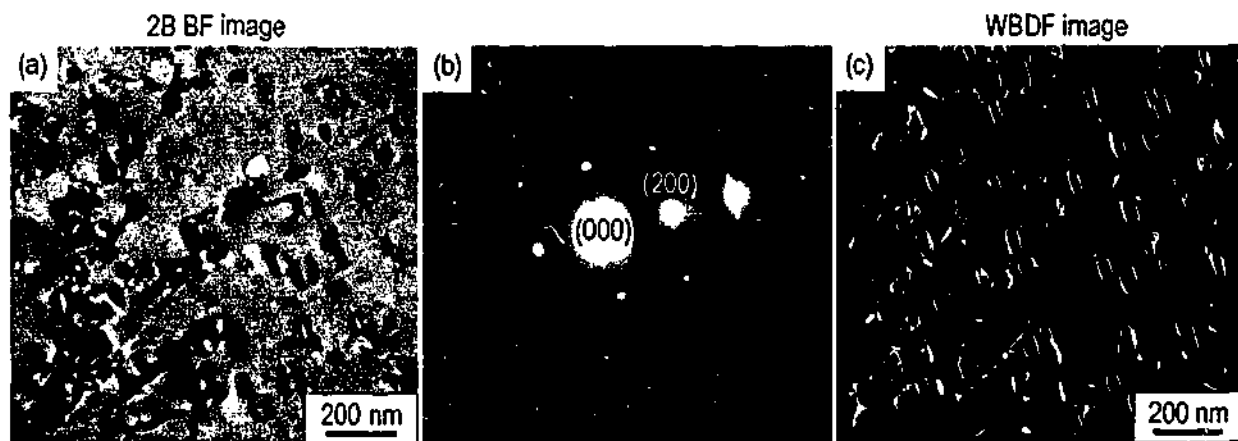


Figure 3.9 (a) Two-beam image of dislocation loops in alloy Al-1.1Cu-0.5Mg aged for 60 s at 150°C following quenching. (b) Associated diffraction pattern for (a). (c) WBDF image of the same area represented in (a).

selected-area aperture into the image plane, to create a virtual aperture in the specimen plane. The technique is termed selected area electron diffraction (SAED), and is generally performed under parallel-beam conditions and such that the electron beam is exactly aligned to a low-index zone axis of the specimen. There is a lower limit to the size of the selected-area aperture, beyond which the results of the technique are not representative of the specimen field selected. Components of the present work intentionally use a comparatively small field-limiting aperture, and particular reference will be made, where appropriate, to the potential errors introduced. However, unless explicitly stated, all SAED procedures employed here use a field-limiting aperture of sufficient size to avoid potentially spurious results.

An appreciation of the form of characteristic SAED patterns expected in the present work is attempted here, based upon the available crystallographic data of the *expected* precipitate phases. The isothermal section of the phase-diagram presented in §2.1 indicates that the phases θ , S and T should form under equilibrium conditions in at least one of the 10 alloys prepared in the present work. In binary Al-1.7%Cu alloys, ageing temperatures above 550°K (277°C) are required for the equilibrium θ phase to form [112]. The alloys in the present work contained up to 1.1%Cu and were aged at 150°C only. It is therefore expected that the equilibrium θ -phase would not form, and that the θ' -phase would instead be expected at this lower ageing temperature during prolonged ageing [112]. Several examples of characteristic experimental SAED patterns from the present work, observed parallel to $\langle 100 \rangle_{\alpha}$, are shown in figures 3.10(a)–(c) for three alloys in three separate phase fields corresponding to $(\alpha+\theta)$, $(\alpha+S)$ and $(\alpha+T)$ respectively (§2.1). The three experimental SAED patterns have distinguishing features, reflecting changes in the identity of secondary phases in the alloys. The alloys have been aged to various times as indicated.

Figures 3.10(d) and 3.10(e) are simulated SAED patterns parallel to $\langle 100 \rangle_{\alpha}$ generated using Digital Micrograph © and the currently accepted crystallographic data presented in §2.1 for the θ' and S-phase embedded precipitate phases and the matrix phase. The patterns includes the four first-order $\{002\}_{\alpha}$ spots and the four first-order $\{022\}_{\alpha}$ spots that symmetrically surround the direct beam, in direct correlation to the experimental diffraction patterns presented in figure 3.10(a)–(c). For each SAED pattern (apart from that representing the alloy in the $(\alpha+T)$ phase field, the $(02\bar{2})_{\alpha}$ quadrant is selected and magnified directly below the full SAED pattern as a representation of the full four-fold symmetry of the $[100]_{\alpha}$ pattern.

Consider first the simulated SAED pattern of a microstructure containing all variants of precipitates of θ' , figure 3.10(d). The calculated double-diffraction maxima are shown, in addition to directly diffracted beams, and the pattern compares well with the experimental SAED pattern of figure 3.10(a). Particular reference is made to the presence of intensity at the forbidden matrix position of $\{011\}_\alpha$, as indicated by the asterisks in figures 3.10(a) and 3.10(d). The four variants of the S-phase whose elongated growth direction (i.e. $[100]_S // [100]_\alpha$) is parallel

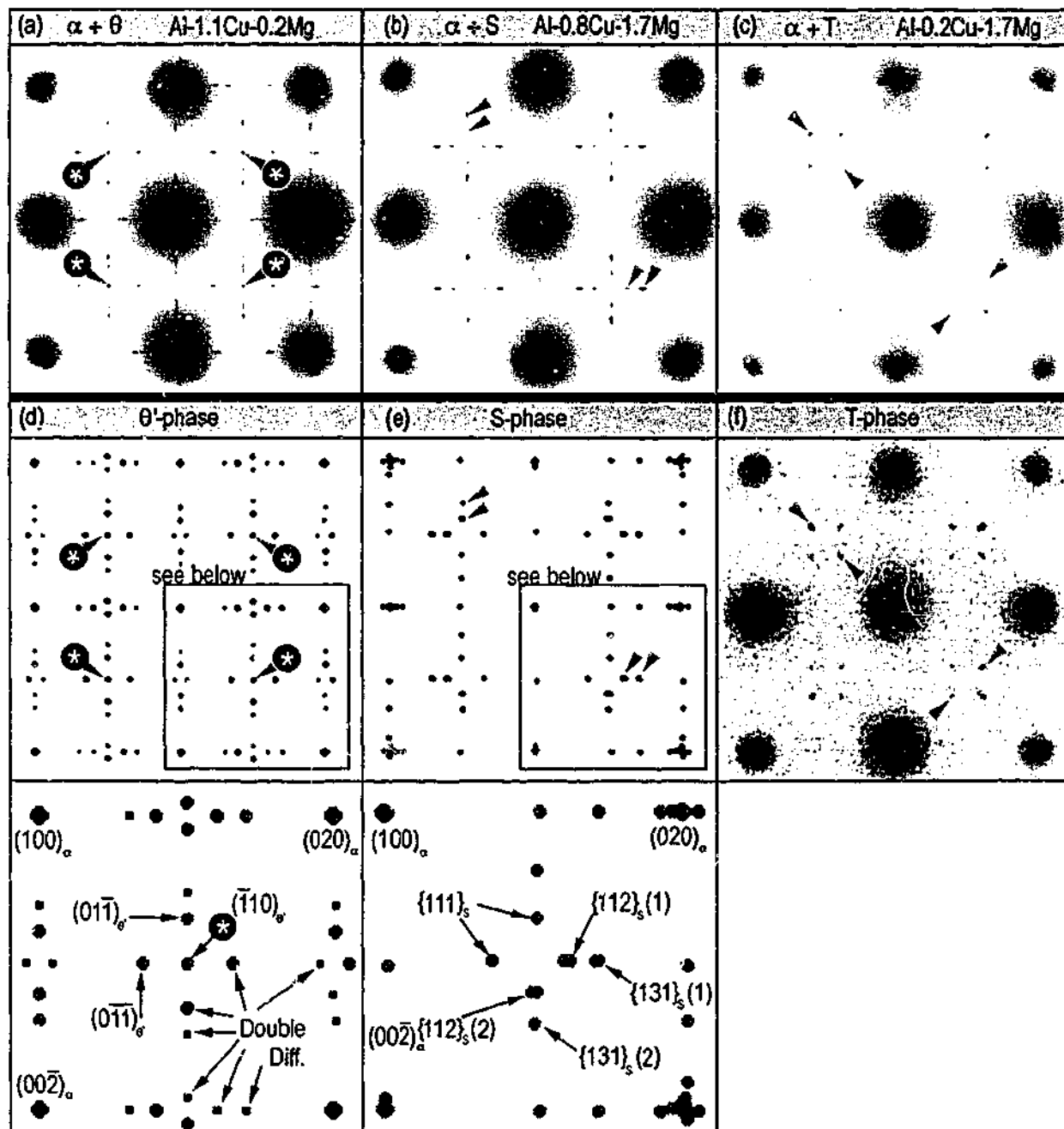


Figure 3.10 Experimental SAED patterns from the present work. Samples were solution treated (525°C), quenched and aged at 150°C for the specified time: (a) Al-1.1Cu-0.2Mg, 10 d (b) Al-0.8Cu-1.7Mg, 10 d (c) Al-0.2Cu-1.7Mg, 80 d. Simulated diffraction patterns: (d) θ' (e) S-phase (f) Experimental SAED pattern of a volume containing an isomorph of the T-phase [185].

to the electron beam ($[100]_{\alpha}$) present only a very small volume to the incident beam. Consequently, the intensity of diffracted beams originating from these four variants is small compared to the diffracted beams originating from the eight alternative variants which lie perpendicular to the beam. The simulated SAED pattern of figure 3.10(e) does not include these four variants oriented such that $[100]_{\beta} // [100]_{\alpha}$, and is in good agreement with the experimental SAED pattern of figure 3.10(b) for the alloy representing the $(\alpha+S)$ phase field and those in the wider literature [130,134]. The arrangement of precipitate reflections immediately surrounding the forbidden $\{011\}_{\alpha}$ positions is very similar to that surrounding the identical position in the alloy containing θ' . However, the simulated (and experimental) SAED patterns of microstructures containing S-phase are characterised by the absence of a precipitate reflection at $\{011\}_{\alpha}$ (confirmed by [134]), while microstructures containing θ' do have a reflection at this position. Hence, the presence of a reflection at the forbidden $\{011\}_{\alpha}$ position is a potential indication of the presence of θ' . If θ' is absent, then the reflections immediately surrounding the forbidden $\{011\}_{\alpha}$ can be used as an indication of the presence of S-phase. The crystal structure of the T-phase is complex and knowledge is incomplete (§2.3.5). Rather than exhaustive simulation of the diffraction patterns of the variants, an example of an experimental SAED pattern is provided from other work [185]. The pattern is obtained from a volume containing precipitates identified as the T-phase in an Al-10Mg-0.5Ag alloy, where the T-phase in these alloys is expected to be an isomorph of that found in the present system.

For those microstructures observed parallel to $(100)_{\alpha}$ by conventional TEM (§4.2, §4.3), the presence of secondary phases was established by direct microstructural imaging *in conjunction* with the SAED patterns presented in figure 3.10.

3.4.3 High Resolution Electron Microscopy

The present work seeks to identify changes in precipitate crystallography as a function of the strain environment in which nucleation and growth of precipitates proceeds. These changes in precipitate morphology might potentially include changes in the particle size, particle aspect ratio and the nature of the particle-matrix interface (i.e. interface orientation and the possible presence of steps and ledges). These changes occur at a scale comparable to the size of the unit cells of both the precipitates and the matrix. The dimensions of the fcc unit cell of the matrix phase is less than that of the S-phase, and has a $\{002\}_{\alpha}$ interplanar spacing of 0.2024 nm. The

conventional techniques of BF and DF electron microscopy are not capable of resolution to this limit. The technique of *high-resolution electron microscopy* (HREM) has thus been applied extensively in the present work to achieve the necessary level of morphological detail of the particles. High resolution electron microscopy is different to conventional TEM techniques, primarily in the manner through which contrast is generated during imaging. The study of atomic arrangements at interfaces is arguably the role in which HREM is most useful, yet several criteria must be met by the material interfaces, and these are discussed below.

3.4.3.1 Background to the Technique

The techniques of TEM discussed thus far have relied upon diffraction contrast to form an image. In HREM, both the direct beam *and* one or more of the diffracted beams are selected in the objective aperture, and the interference pattern thus created forms a *phase contrast* image.

Many excellent texts are available that consider both the theory and practice of HREM (e.g. [184,186-188]), and an exhaustive explanation of the now standard technique is not warranted here. However, some important aspects of phase contrast imaging will be briefly explained. Consider the case where we select the direct beam and one diffracted beam in the objective aperture, as in figure 3.11(a). It can be shown [184] that the intensity, I , of the interference pattern is a sinusoidal oscillation normal to g' that is of the form:

$$I = A^2 + B^2 - 2AB \sin(2\pi g' - \pi st) \quad \text{Equation 3.2}$$

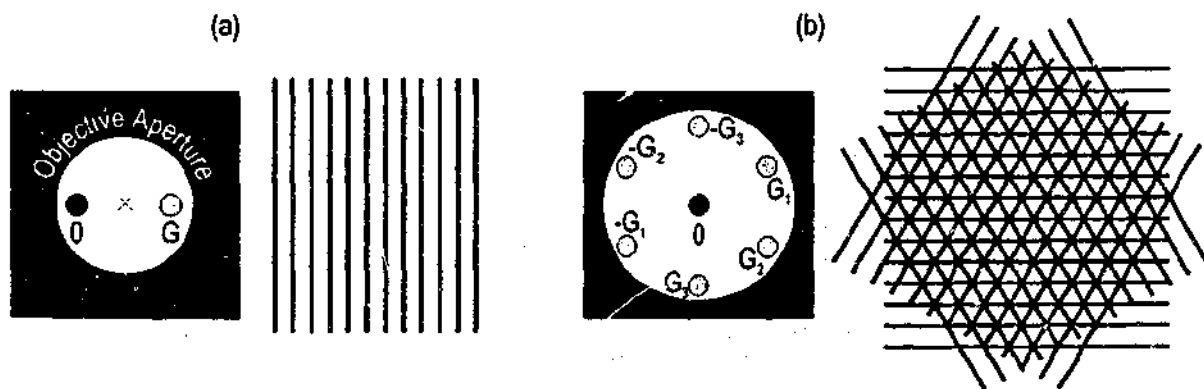


Figure 3.11 (a) Two beams (direct and one diffracted beam, G) are selected in the objective aperture, and the resultant interference pattern is periodic in one direction. (b) The direct and six diffracted beams are selected in the objective aperture, and the corresponding intensity pattern is periodic in three directions.

where g' is the diffraction vector (from 0 to G in fig. 3.11(a)), A and B are terms related to the amplitude of the direct and diffracted beams respectively, s is the magnitude of the excitation error and t is the thickness of the specimen. The excitation error is a measure of how far the beam deviates from the Bragg condition, and under usual conditions, this does not significantly impact upon the periodicity [184]. Importantly, the intensity varies sinusoidally with different periodicities for different values of g' . Figure 3.11(b) depicts the many-beam case, where six diffracted beams and the direct beam are selected in the objective aperture, and the resultant interference pattern is periodic in three directions. In general, the many-beam case is applied during practical HREM, utilising selected first order diffracted beams around the direct beam.

3.4.3.2

Imaging of Particles in Aluminium Alloys

The characterisation of atomic-scale changes in precipitate-matrix crystallography by high resolution imaging relies upon imaging of the interphase interface, and requires satisfaction of the following conditions [187], illustrated where appropriate in figure 3.12:

- The interface should be parallel to the incident-beam direction (figs. 3.12(a) and 3.12(b)).
- If interfacial steps are present in the interface, they should preferably be arranged such that they run parallel to the incident-beam direction (figs. 3.12(c) and 3.12(d)).
- The crystals on either side of the interface should both be aligned to an orientation suitable for structure imaging.

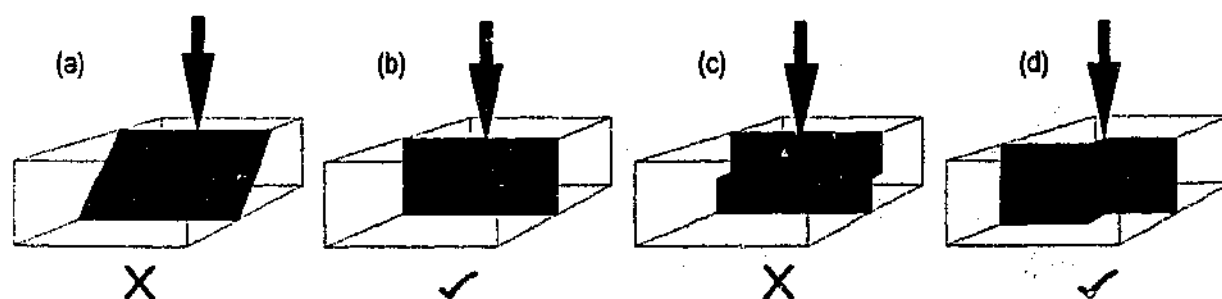


Figure 3.12 (a) The interface is not parallel to the incident electron beam, and therefore the interface is not suitable for examination in this orientation. (b) Suitable orientation for examination. (c) Interfacial steps running perpendicular to the incident electron beam, and therefore unsuitable for examination in this orientation. (d) Stepped interface in a suitable orientation for examination.

The major constituent phases expected in the alloys of the present work are θ' and S-phase, both of which are elongated parallel to $\langle 100 \rangle_{\alpha}$ directions. Particles of the former phase are plate-shaped with a broad interface parallel to $\{001\}_{\alpha}$. Particles of the S-phase, when observed in the standard orientation, are lath-shaped, with a broad interface parallel to $\{021\}_{\alpha}$. Implicitly, the broad particle-matrix interfaces of the plate or lath-shaped particles of θ' and S-phase respectively will always be parallel to $\langle 100 \rangle_{\alpha}$ directions, and accordingly, examination is always performed along this direction. Particles of the S-phase that are rotated about $[100]_s // [100]_{\alpha}$ exhibit steps on those (formerly planar) interfaces that are parallel to the $[100]_s$ growth axis $[131]$, making an electron beam direction of $[100]_s // [100]_{\alpha}$ the only plausible orientation for examination of the stepped interface.

Vectors g defined by the first-order diffraction spots in the $[100]_{\alpha}$ pattern are greater in magnitude than the vectors $g(002)_s$ and $g(020)_s$. Therefore, meaningful phase-contrast imaging of the matrix and precipitate phases may only proceed using an objective aperture with a size that includes the four first-order vectors $g\{002\}_{\alpha}$. Figure 3.13(a) shows the selection of the direct beam ($[100]_{\alpha}$) and four $\{002\}_{\alpha}$ diffracted beams in the objective aperture. The resultant interference pattern has a periodicity inversely proportional to the magnitude of the appropriate vectors g . This corresponds to interplanar spacing of the $\{002\}_{\alpha}$ planes in two dimensions, and allows interpretation of the interplanar spacing between these planes. Figure 3.13(b) is a HREM image from the present work of the $\{002\}_{\alpha}$ planes in aluminium, where $d_{(002)\alpha}$ is indicated.

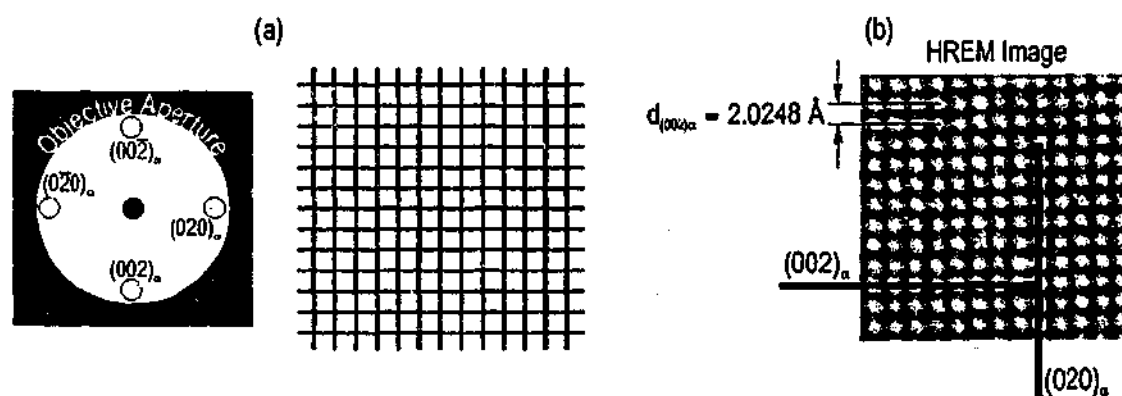


Figure 3.13 (a) Selection of the direct beam and the four $\{002\}_{\alpha}$ beams of the $(100)_{\alpha}$ zone axis in the objective aperture. (b) HREM image of the $\{002\}_{\alpha}$ planes in aluminium.

As will become clear in the later stages of the thesis, characterisation of the orthorhombic S-phase was heavily reliant upon the use of atomic resolution imaging to determine planar coherency across the interface between the matrix and the embedded particle. Implicit in this approach is the assumption that the lattice fringes observed under the electron beam exhibit a 1:1 correlation with the lattice planes in the real material. It is important to recognise the limitations of HREM in determining the true atomic positions in a crystalline specimen. Lattice fringes are not direct images of the structure, but they do give reliable information regarding the *spacing* of crystal planes [184]. In this manner, the phase-contrast imaging mode of HREM microscopes can be used to generate atomic resolution images that can be interpreted intuitively, without the need for extensive image simulation.

3.4.4 Summary of TEM Facilities and Techniques

Table 3.3 provides a summary of the electron-beam associated techniques applied in the present research.

Table 3.3 Summary of TEM facilities and the techniques applied in the current investigation.

Technique	Philips CM20 200 kV	JEOL 2011 200 kV
SAED	★	★
BF Imaging	★	★
DF Imaging	★	
HREM		★

4.0

Ageing Response of Ternary Al-Cu-Mg Alloys

As reviewed in §2.1.4, Al-Cu-Mg alloys within defined compositional limits undergo multi-stage hardening reactions during appropriate artificial ageing regimes. The relevant literature shows that at the artificial ageing temperature of 150°C, the first hardening stage accounts for up to 70% of the total hardening capacity of selected alloys and can occur within the first 60 s of ageing. It has recently been suggested that the first stage of hardening arises from a pre-precipitation phenomenon that relies upon a dispersion of solute clusters, while alternative views suggest that GPB zones, or S'' precipitates at dislocations are the hardening agents. Proposals for the origin of maximum hardness, attained following many days at 150°C, include the presence of θ'' and θ' precipitates in ($\alpha+\theta$) phase field alloys and GPB zones and S-phase in ($\alpha+S$) phase field alloys. Of these strengthening precipitates, θ' and S-phase display a strong preference for nucleation at crystal defects during artificial ageing. The aim of this chapter is to survey the distribution of all second-phase precipitates as a function of hardness in the aluminium-rich Al-Cu-Mg system, and correlate the precipitate distribution to the original distribution of crystal defects under a range of applied thermal regimes. Other issues raised by the results of this chapter are not dealt with in great depth.

The changes in microstructure and hardness that occur with time at elevated temperature following quenching have been investigated thoroughly using the experimental techniques of bulk hardness, microhardness and conventional TEM. The chapter includes a discussion of the relevant heterogeneous precipitation processes observed, and establishes priorities for those that warrant further investigation.

4.1 Response to Ageing of Al-Cu-Mg Alloys

4.1.1 Series I - Al-1.1Cu-xMg Alloys

Bulk hardness as a function of ageing time is shown in figure 4.1 for Al-1.1Cu-xMg alloys (where $x = 0, 0.2, 0.5, 0.75, 1.0$ and 1.7) aged at 150°C immediately following quenching. The as-quenched hardness increased with Mg content. The binary Al-Cu alloy showed no appreciable increase in hardness following a period of 10^4 s (2.8 h) at 150°C . Following an incubation time of 10^5 s (28 h), the hardness had increased by approximately 10%. Maximum hardness was attained following 20 d at 150°C . Similarly, the hardness-time curve for the Al-1.1Cu-0.2Mg alloys displayed a single rise to maximum hardness, although at a consistently higher hardness and in less time (10 d). In contrast, the Al-1.1Cu-0.5Mg alloy displayed a rapid increase in the hardness within the first 60 s of ageing. Similar hardening behaviour was evident in those alloys containing higher Mg/Cu ratios, as can be observed in figure 4.1. All Series I alloys containing greater than 0.5Mg experienced a secondary increase to maximum hardness after an extended period during which the hardness remained approximately constant following the initial rapid hardening (the *plateau* hardness). The time to achieve maximum hardness was reduced as the Mg content increased (e.g. Al-1.1Cu-0.5Mg: 14 d, Al-1.1Cu-1.7Mg: 7 d). The standard deviation about the average hardness measurement ranged between 4% (at maximum

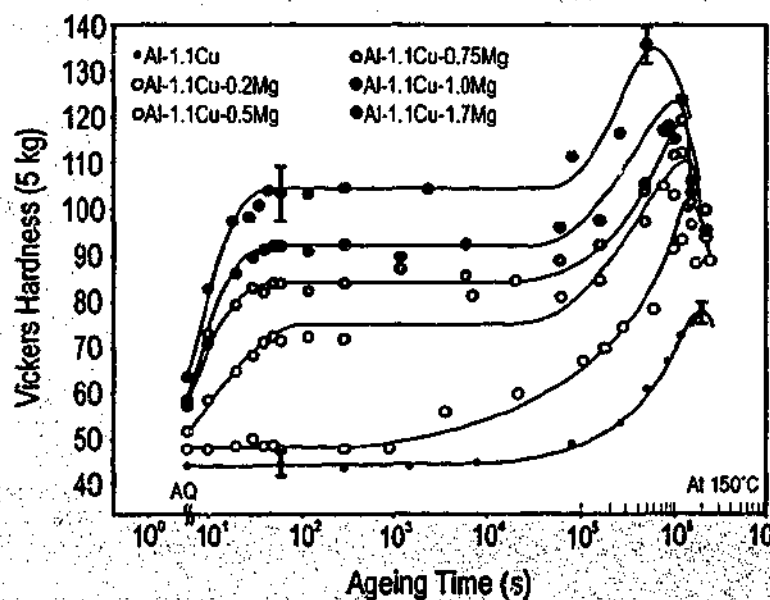


Figure 4.1 Hardness (5 kg Vickers) vs. ageing time at 150°C for Series I alloys.

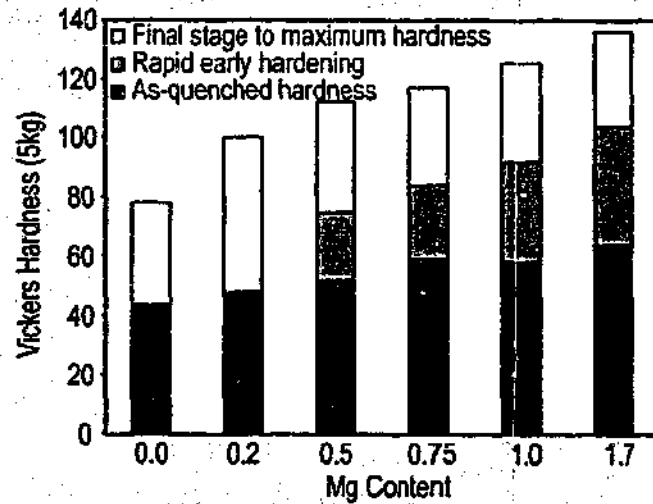


Figure 4.2 Contribution to maximum hardness of the stages of age-hardening at 150°C – Series I alloys.

hardness) and 6% (shorter ageing time), and the largest errors were recorded for those alloys aged for 60 s or less at 150°C. These errors were not large in comparison to the relative differences in the hardening response of these alloys. Hence, indicative error bars have been included in figure 2.1 for only the selected heat treatment of 60 s artificial ageing and also at maximum hardness for the Al-1.1Cu and Al-1.1Cu-1.7Mg alloys. Figure 2.2 presents the stages of hardening as increments of the maximum hardness of the alloy. As the Mg content increases, the hardness increment attained during the final rise in hardness decreases as a proportion of the total hardness difference between as-quenched and maximum hardness, implying an increase in the component attributable to initial rapid hardening.

4.1.2 Series II - Al-xCu-1.7Mg Alloys

Bulk hardness is plotted as a function of ageing time in figure 4.3 for Al-xCu-1.7Mg alloys (where $x = 0, 0.2, 0.5, 0.8$ and 1.1) aged at 150°C immediately following quenching. The as-quenched hardness increased with Cu content for Al-xCu-1.7Mg alloys. It has been shown that binary Al-Mg alloys containing up to 6% Mg do not age harden [54], and hence monitoring of the response of the present binary alloy to age-hardening was not recorded beyond 15 mins of ageing. Artificial ageing of the Al-0.2Cu-1.7Mg alloy resulted in a maximum hardness almost twice that of the as-quenched state. Alloys containing 0.8Cu or more displayed a distinct initial rapid hardening response within 60 s, while the Al-0.5Cu-1.7Mg alloy could not be classified unambiguously as rapidly hardening. Both Al-0.8Cu-1.7Mg and Al-1.1Cu-1.7Mg alloys displayed a hardness plateau between the initial increase in hardness and the second stage

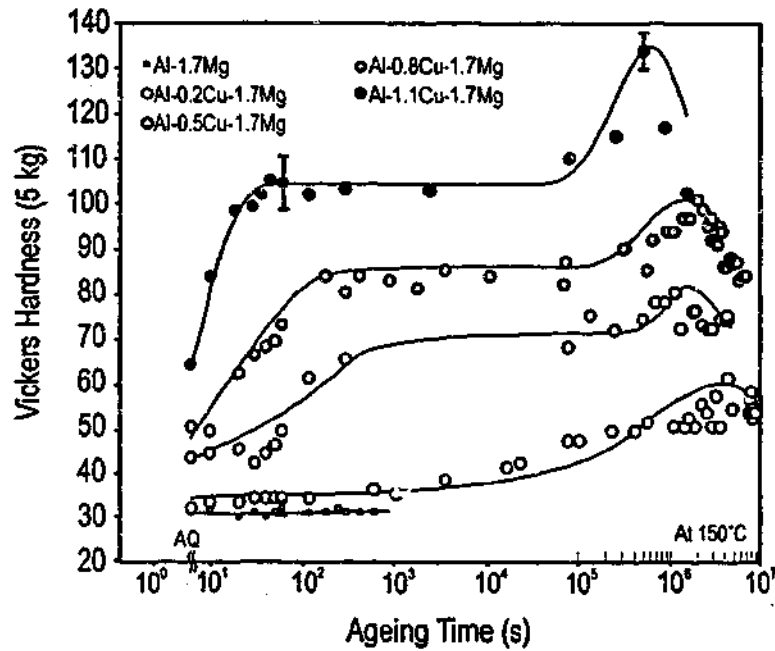


Figure 4.3 Hardness (5 kg Vickers) vs. ageing time at 150°C for Series II alloys.

increase to maximum hardness. The maximum hardness increased as the Cu content increased and the time to maximum hardness decreased (e.g. Al-0.8Cu-1.7Mg: 17 d, Al-1.1Cu-1.7Mg: 7 d). Indicative error limits are provided in figure 4.3 for selected treatments, as for Series I alloys. Relative contributions to the maximum hardness are summarised in figure 4.4. Similar to Series I alloys, an increasing total solute content is associated with an increased rapid hardening response. In contrast to Series I alloys, the component of the total hardness achieved above the as-quenched hardness during the second rise in hardness increases as the solute content increases and the initial rapid hardening component decreases.

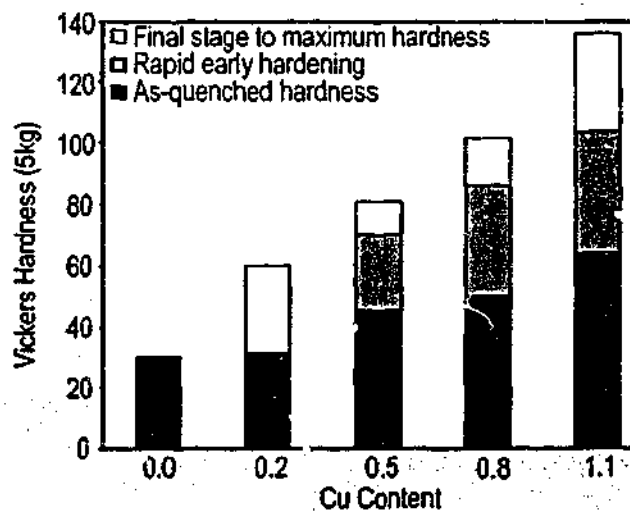
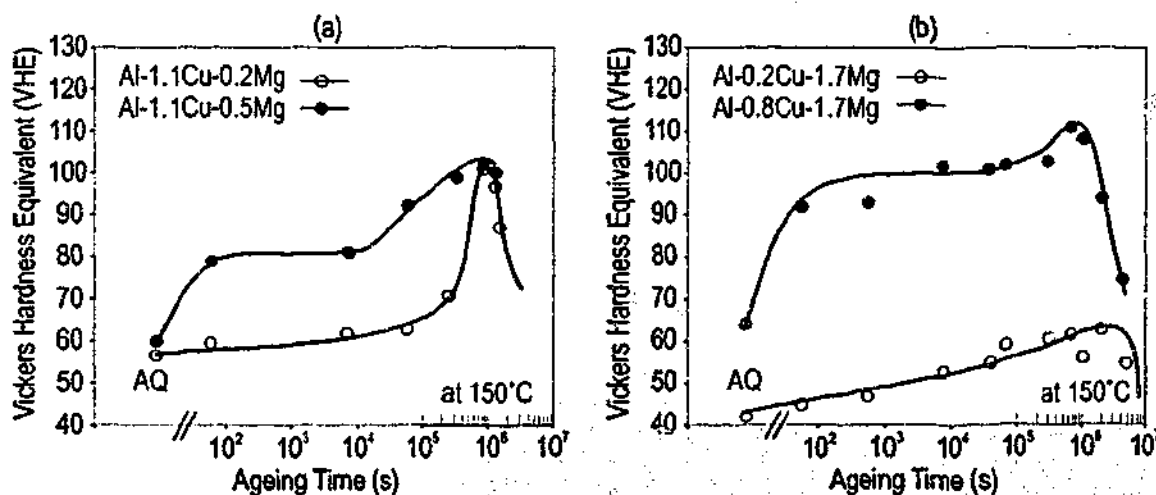


Figure 4.4 Contribution to maximum hardness of the stages of age-hardening at 150°C – Series II alloys.

4.1.3 Strategic Selection of Alloys

Two alloys from each alloy series were strategically chosen for further study, the compositions of which placed them either side of an apparently critical alloy composition dividing rapidly hardening and non-rapidly hardening compositions. Accordingly, Series I alloys Al-1.1Cu-0.2Mg and Al-1.1Cu-0.5Mg were selected, together with Series II alloys Al-0.2Cu-1.7Mg and Al-0.8Cu-1.7Mg. As discussed in §4.3, the hardening and microstructural responses to ageing of these alloys must be monitored for specimens of like size and shape if a correlation is to be sought between hardness and microstructure. The hardness results of figures 4.1 and 4.3 were recorded from bulk (1.5 mm thick) specimens, while the microstructural evolution will be recorded in specimens thermally processed as 3 mm \varnothing \times 500 μ m thick discs. Hence, disc specimens were prepared for microindentation hardness measurements in the manner described in §4.3. The four alloys revealed similar qualitative hardening traits (fig. 4.5) to those displayed in the bulk specimens, preserving the distinction between compositions that rapidly harden and those that do not. However, the time necessary to attain maximum hardness was reduced in all cases by up to 37% for those specimens thermally processed as discs. These hardness curves are referred to when examining the microstructure of the alloys.



Time to maximum hardness (days)	Thickness	Al-1.1Cu-0.2Mg	Al-1.1Cu-0.5Mg	Al-0.2Cu-1.7Mg	Al-0.8Cu-1.7Mg
	1.5 mm	15	14	46	16
	500 μ m	10	10	40	10

Figure 4.5 Microhardness indentation hardness testing of the four core alloys, showing similar traits to the 5kg Vickers hardness measurements (figs. 4.1 and 4.3), and the comparative times to maximum hardness in 1.5 mm and 500 μ m thick samples.

4.2 Microstructural Evolution

Following solution treatment at 525°C and quenching into water at 20°C, both vacancies and solute [189] are at concentrations in excess of equilibrium. During subsequent artificial ageing, both the vacancy and solute supersaturation decay as the alloy seeks to lower its free energy by attaining a thermodynamically stable vacancy and solute concentration in solution. This section records the microstructural evolution that accompanies decomposition using conventional TEM.

4.2.1 Vacancy Condensation (Dislocation) Loops

As-quenched microstructures of all four selected alloys, examined within 1.5 h of quenching, revealed a negligible density of defects, as exemplified in the BF image of as-quenched Al-1.1Cu-0.5Mg in figure 4.6(a) observed approximately parallel to $\langle 001 \rangle_{\alpha}$. If present, the loops were extremely small (<5nm in diameter), and occurred in very isolated pockets of several loops. The featureless appearance of the microstructure suggests that little has changed from that which was present immediately following quenching. Subsequent post-quench artificial ageing for 60 s at 150°C led to a distribution of loops with an appearance consistent with having been formed by the aggregation and collapse of vacancies into prismatic dislocation loops, as shown in the DF image of figure 4.6(b) of a specimen crystal oriented approximately parallel to $\langle 001 \rangle_{\alpha}$. Evidently, the rate of dislocation loop growth is at or near zero following 60 s of ageing after quenching, since further ageing for 10 min did not result in significant loop growth (fig. 4.6(c)).

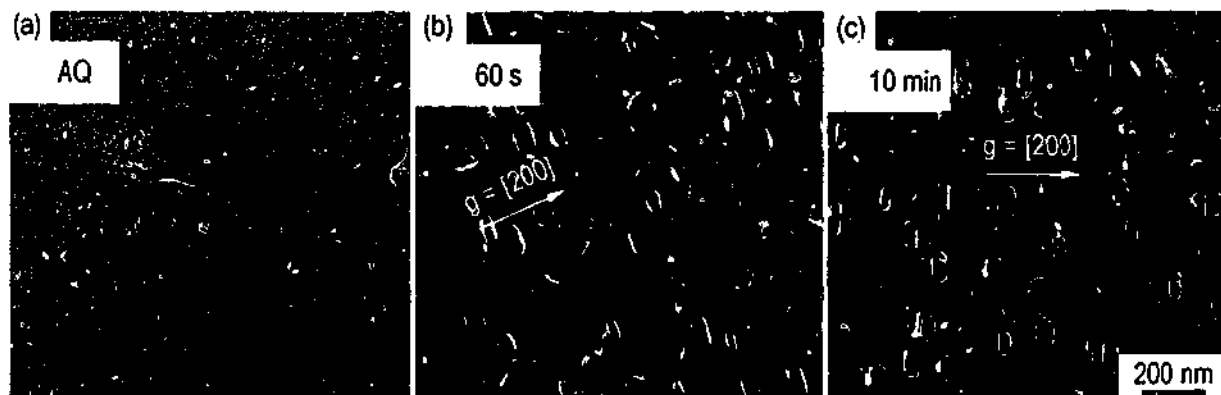


Figure 4.6 Al-1.1Cu-0.5Mg observed approximately parallel to $\langle 001 \rangle_{\alpha}$: (a) as-quenched, (b) aged at 150°C for 60 s (c) aged at 150°C for 10 min. Loop growth rate is effectively zero following 60 s ageing.

Figure 4.7 contains several BF images of the alloy Al-1.1Cu-0.5Mg quenched and immediately aged at 150°C for 60s. In all cases, a dense and uniform distribution of dislocation loops is present in the specimen volume, apart from those volumes adjacent to defects such as extended dislocations (fig. 4.7(a)), low-angle grain boundaries (fig. 4.7(b)) and high-angle grain boundaries (fig. 4.7(c)). These defects act as competitive sinks for the vacancies in excess of equilibrium. The loop-free zone is particularly clear near a grain boundary triple-junction, as arrowed in figure 4.7(d). In most cases, the loops near the fringes of the loop-free zones were coarser and appear in a less dense population than in regions well removed from loop-free zones.

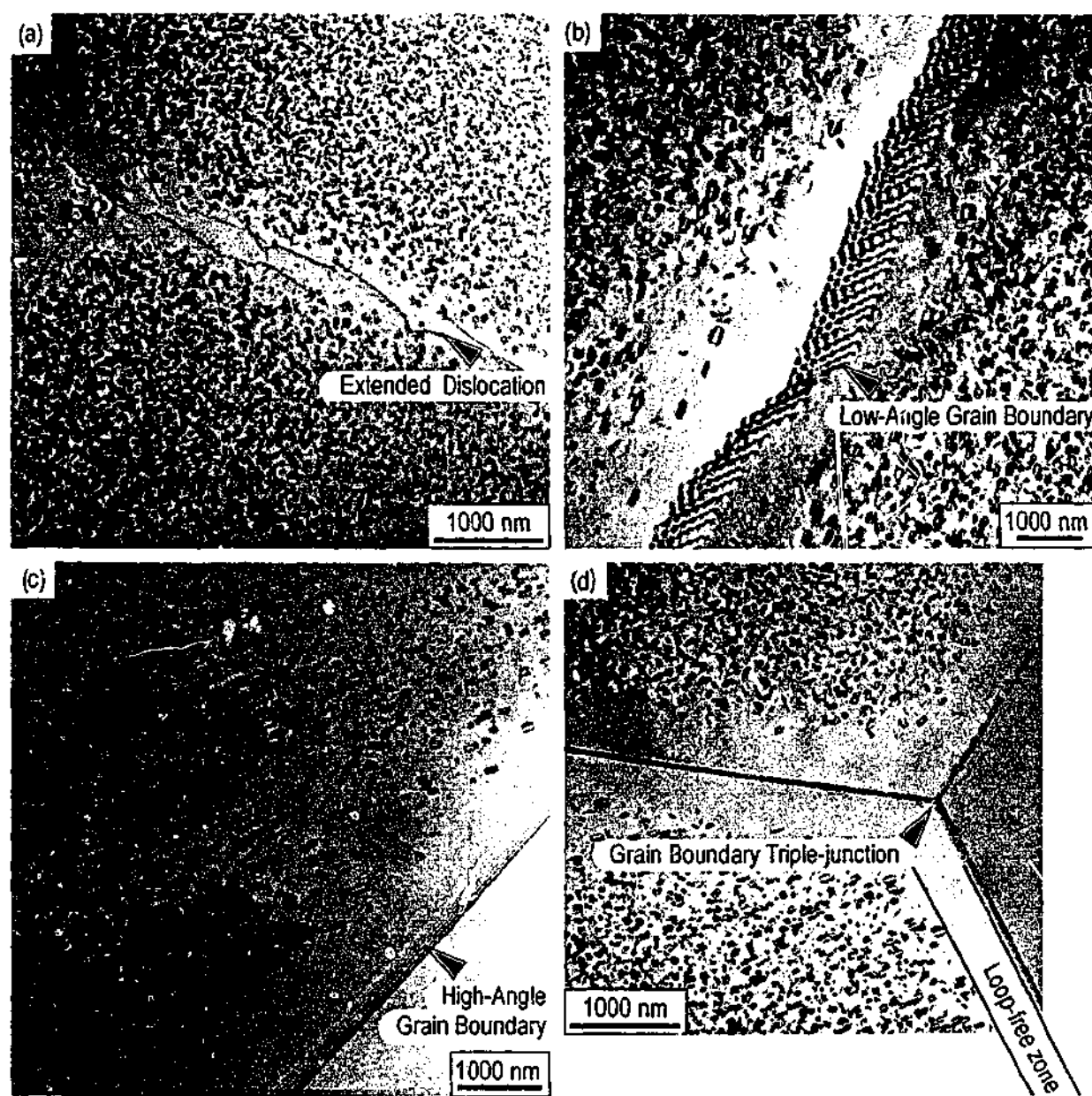


Figure 4.7 Loop-free zones in alloy Al-1.1Cu-0.5Mg aged for 10 min at 150°C following quenching, adjacent to an (a) extended dislocation (b) low-angle grain boundary (c) high angle grain boundary and (d) grain boundary triple-junction.

Figure 4.8 displays DF images recorded with the electron beam approximately parallel to a $\langle 001 \rangle_\alpha$ zone axis of eight alloys investigated in the present work. Figure 4.8(a) – 4.8(d) are Series I alloys containing 1.1Cu and a progressively increasing Mg content. Figure 4.8(e) – 4.8(h) are Series II alloys containing 1.7Mg and a progressively increasing Cu content. Specimens of each alloy were solution treated, quenched and subject to 60 s ageing at 150°C to ensure that dislocation loop growth was complete.

The two binary alloys displayed a non-uniform distribution of relatively coarse dislocation loops. Ternary additions to both binary alloys were observed to encourage a more uniform distribution of dislocation loops in all cases. In Series I alloys, the number density of loops was highest for the Al-1.1Cu-0.5Mg alloy, while the loops were generally larger in diameter for a higher total solute content. At no point in the examination of Series I alloys was stacking fault contrast (SFC) observed. Series II alloys contained loops both with and without SFC, and several are indicated in figures 4.8(e) and 4.8(f). Again, the loop diameter increased for Series II alloys that contained higher total solute content. The stability of an area of stacking fault is compromised when the size of the area increases [173,190]. Owing to the large size of the loops in the alloy Al-0.8Cu-1.7Mg and the increased stacking fault energy [191], stacking faults were not observed in the same number density as for Al-0.2Cu-1.7Mg, where the loops were generally smaller. The absence of SFC in a projected loop is not a reliable characteristics by which to judge the nature of the loops in these alloys, and other descriptions of the loop may be more reliable, e.g. habit plane and Burgers vector of the dislocation loops (§5.1). It is sufficient to recognise that all observations in specimens aged for 60 s are consistent with that of dislocation loops formed by the coalescence of vacancies.

A record of the microstructural evolution in these alloys at 150°C is presented in the following sections for specimens observed following quenching, and artificially aged for 60s, 17 hr, 3 d, at and ageing time corresponding to maximum hardness and at an ageing time twice that required for maximum hardness.

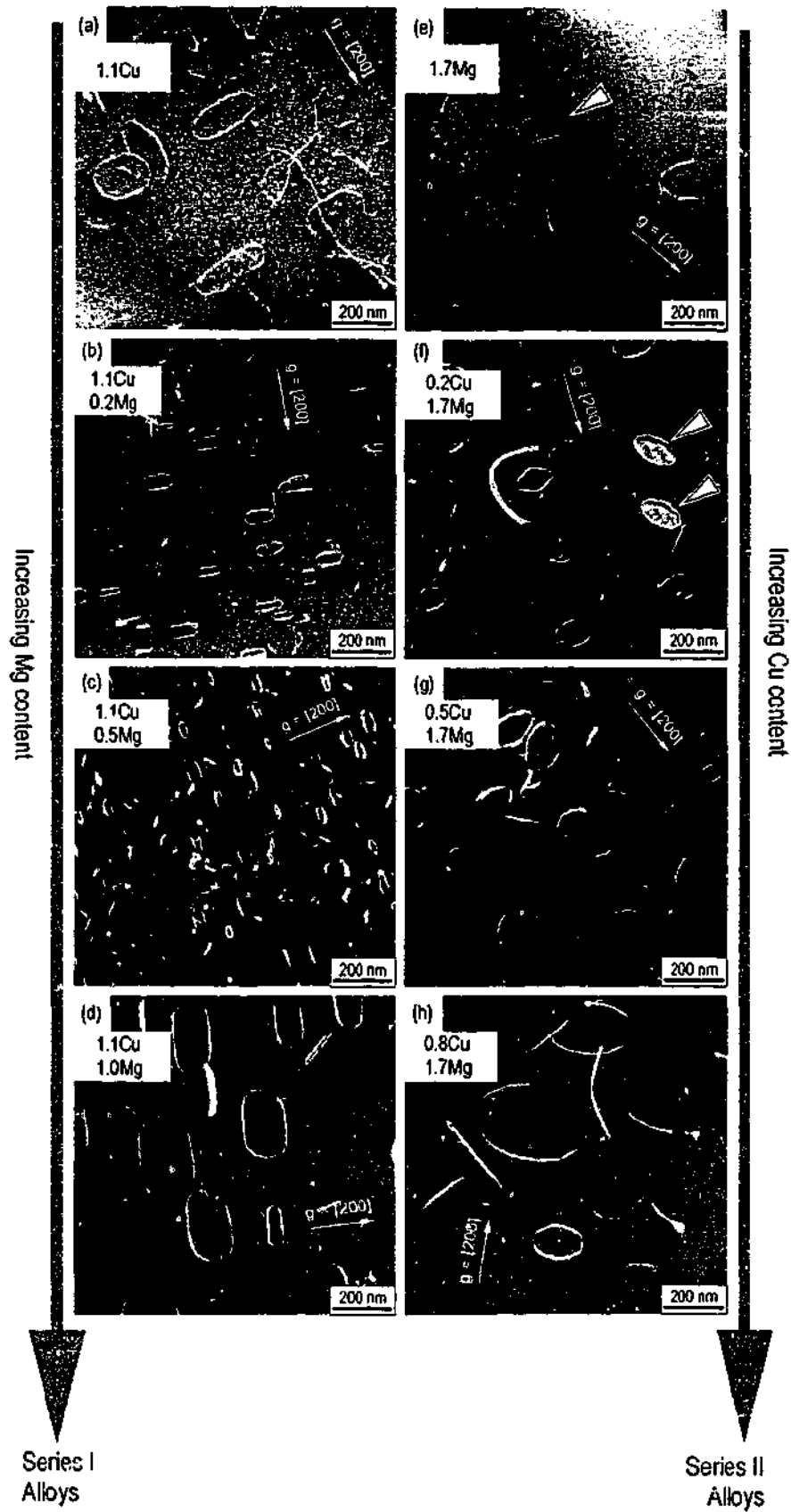


Figure 4.8 60 s at 150°C: (a)-(d) Al-1.1Cu-xMg (e)-(h) Al-xCu-1.7Mg.

4.2.2 Precipitation Processes in Al-1.1Cu-xMg Alloys

Figures 4.9 and 4.10 are representative TEM image panels of the microstructure of artificially-aged Al-1.1Cu-0.2Mg and Al-1.1Cu-0.5Mg alloys respectively. The techniques of BF and DF imaging have been applied where appropriate, and in all cases the crystals were oriented such that the electron beam was approximately parallel to $\langle 001 \rangle_{\alpha}$. In the as-quenched condition, there were no observable features apart from isolated dislocation loops (figs. 4.9(a) and 4.10(a)).

Ageing for 60 s at 150°C (figs. 4.9(b) and 4.10(b)) led to a uniform dispersion of vacancy condensation loops in both alloys. Second-phase precipitation was not observed in either alloy following this short ageing time, and the accompanying SAED patterns were consistent with this conclusion. The inserted SAED patterns contain only those electron beams diffracted by the matrix phase, as indexed. The microstructures following 17 h at 150°C are shown in figures 4.9(c) and 4.10(c). There was some contrast in the images in the vicinity of the (former) dislocation loops, particularly in the Al-1.1Cu-0.5Mg alloy, suggesting the presence of second-phase particles, and this contrast has been labelled in figure 4.10(c). The microstructure between the dislocation loops was featureless in both alloys at this ageing time, as is demonstrated in the magnified inset of figure 4.10(c). The microstructures following 3 d at 150°C, together with accompanying SAED patterns, are shown in figures 4.9(d) and 4.10(d). Although there is contrast in the BF image of the Al-1.1Cu-0.2Mg alloy (fig. 4.9(d)) consistent with the presence of precipitates at the dislocation loops, observation of the accompanying SAED pattern was not able to confirm this. This is attributed to an insufficient volume of precipitate to sufficiently diffract intensity. However, the SAED pattern of the Al-1.1Cu-0.5Mg alloy aged for 3 d (fig. 4.10(d)) does contain weak secondary diffraction spots, and the observations of the microstructure concur.

The microstructure following 10 d at 150°C (maximum hardness) for the two alloys are included in figures 4.9(e) and 4.10(e). The SAED patterns indicate the presence of a reflection at $\{011\}_{\alpha}$, a signature corresponding to $(\bar{1}10)_{\theta'}$ (see §4.3). This confirms that θ' is present in both alloys, and selected θ' precipitates (plates parallel to $\{001\}_{\alpha}$) have been labelled in the images. Particles consistent with the morphology of precipitates of the S-phase have also been labelled, and their presence is particularly obvious in the alloy Al-1.1Cu-0.5Mg (fig. 4.10(e)). At maximum hardness, fine contrast between the dislocation loops is recorded, as observed in the inset of figure 4.10(e). These features were absent in the alloy Al-1.1Cu-0.2Mg aged to maximum hardness (fig. 4.10(e)). Overaged microstructures (20 d) (figs. 4.9(f) and 4.10(f)) are included.

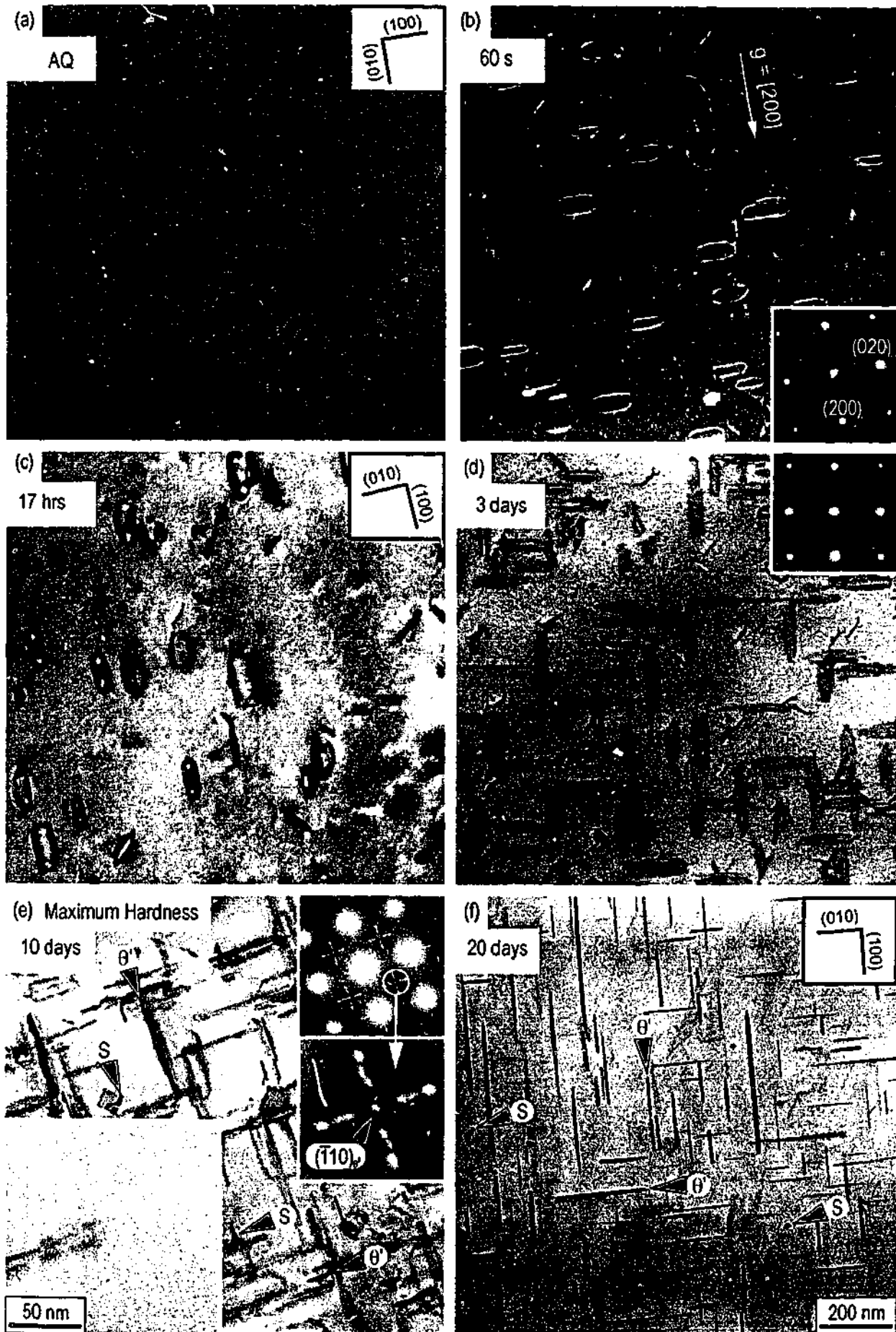


Figure 4.9 Microstructural evolution: Al-1.1Cu-0.2Mg, ST(525°C) + Q(20°C) + AA(150°C).

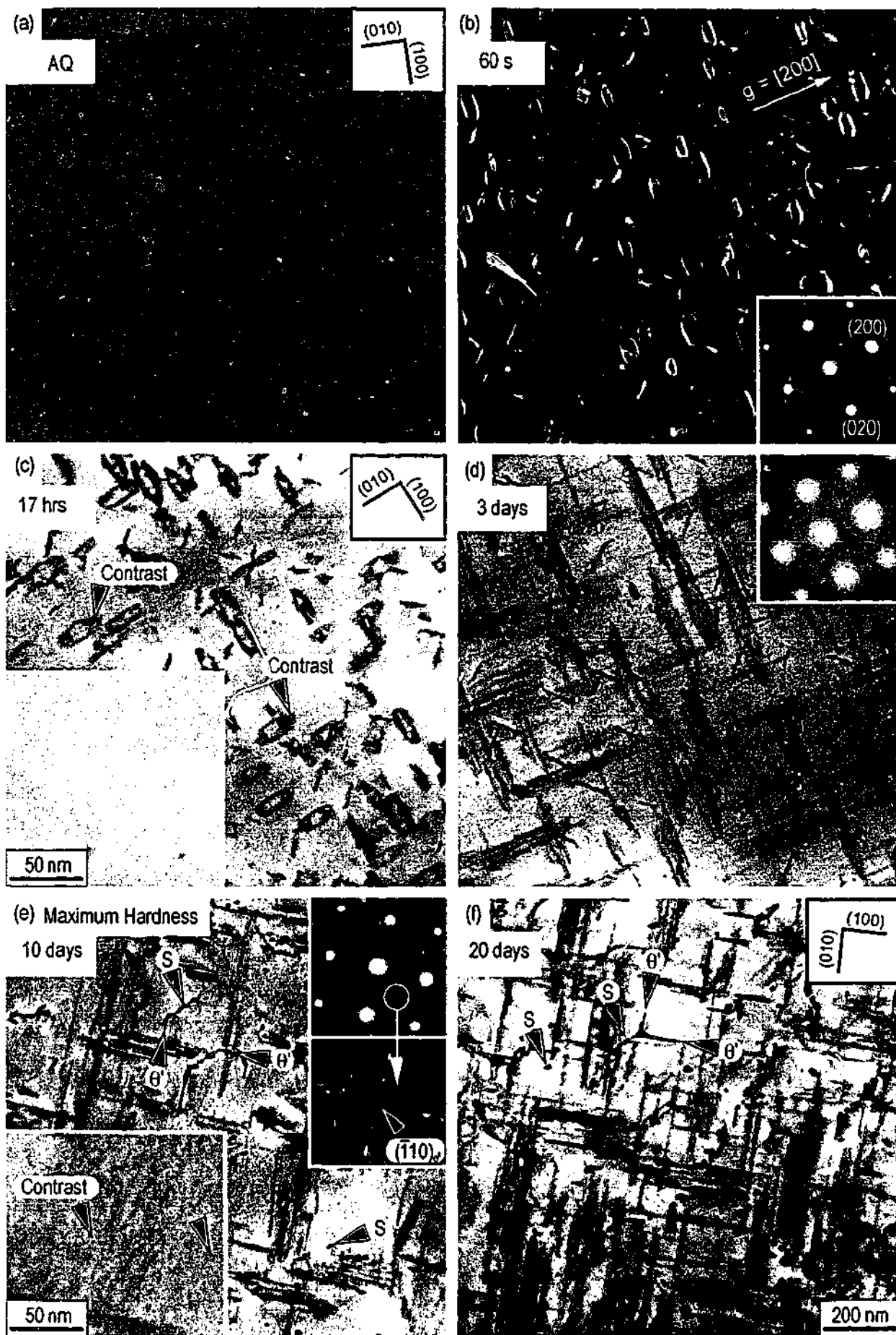


Figure 4.10 Microstructural evolution: Al-1.1Cu-0.5Mg, ST(525°C) + Q(20°C) + AA(150°C).

4.2.3 Precipitation Processes in Al-xCu-1.7Mg Alloys

The microstructural evolution at 150°C of alloys Al-0.2Cu-1.7Mg and Al-0.8Cu-1.7Mg is recorded in figures 4.11 and 4.12, respectively, in the form of BF and DF images obtained approximately parallel to $\langle 001 \rangle_{\alpha}$. Featureless as-quenched microstructures and a uniform dispersion of two or more varieties of dislocation loops after 60 s ageing at elevated temperature typified the response of these alloys to artificial ageing (figs. 4.11(a)(b) and 4.12(a)(b)). Following artificial ageing for 17 h (fig. 4.11(c) and 4.12(c)), some contrast in the BF images was evident adjacent to the loops, suggesting the possible nucleation and growth of precipitates of the S-phase. The material between the dislocation loops was free of second-phase material, as exemplified in the inset of alloy Al-0.8Cu-1.7Mg in figure 4.12(c). Further ageing for 3 d at 150°C (figs. 4.11(d) and 4.12(d)) resulted in the clear presence of second-phase material at the dislocation loops. However, the SAED patterns did not contain secondary diffracted beams to support the observations of the images, and it was presumed that the volume of second-phase material was too low to diffract sufficient intensity to form secondary diffraction spots.

Ageing of the alloys to maximum hardness (40 d and 10 d for Al-0.2Cu-1.7Mg and Al-0.8Cu-1.7Mg respectively) resulted in clear evidence in both the BF images and the SAED patterns of the presence of second-phase material (figs. 4.11(e) and 4.12(e)). There was no evidence in the images showing precipitates of the θ' phase (plates parallel to $\{001\}_{\alpha}$), and this observation was supported by the absence of precipitate reflections in the SAED pattern at $\{011\}_{\alpha}$ positions, as arrowed. The location of secondary spots in the SAED pattern is therefore consistent with those presented in §3.4 for the presence of S-phase, and this phase equilibria is expected from the phase field (§2.1.3) in which the alloy is placed, $(\alpha+S)$. At maximum hardness, S-phase precipitates persisted at the former dislocation loops. In addition, the matrix between the precipitate networks at former dislocation loops contained a distribution of finely-dispersed precipitates that appeared consistent with GPB zones [59,143]. The inset SAED patterns display streaking between the forbidden $\{011\}_{\alpha}$ positions, consistent with the presence of precipitates elongated parallel to $\langle 001 \rangle_{\alpha}$ [143], further supporting the presence of GPB zones. Images of the microstructure of over-aged specimens of alloys Al-0.2Cu-1.7Mg and Al-0.8Cu-1.7Mg (80 d and 20 d respectively) are provided (figs. 4.11(f) and 4.12(f)). The number density and size of the proposed GPB zones in the material between the precipitate networks was significantly reduced in both over-aged specimens, as indicated in the insets.

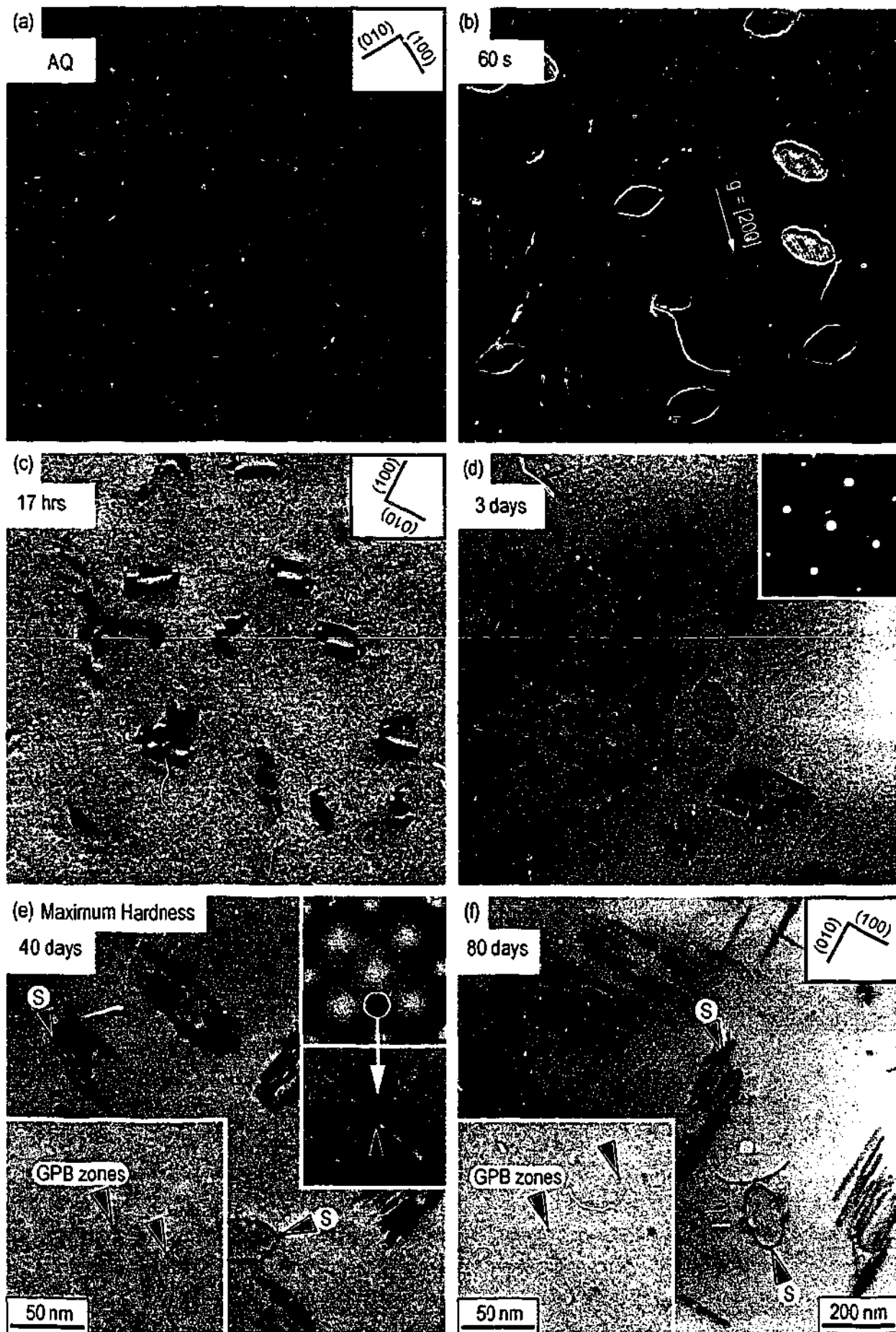


Figure 4.11 Microstructural evolution: Al-0.2Cu-1.7Mg, ST(525°C) + Q(20°C) + AA(150°C).

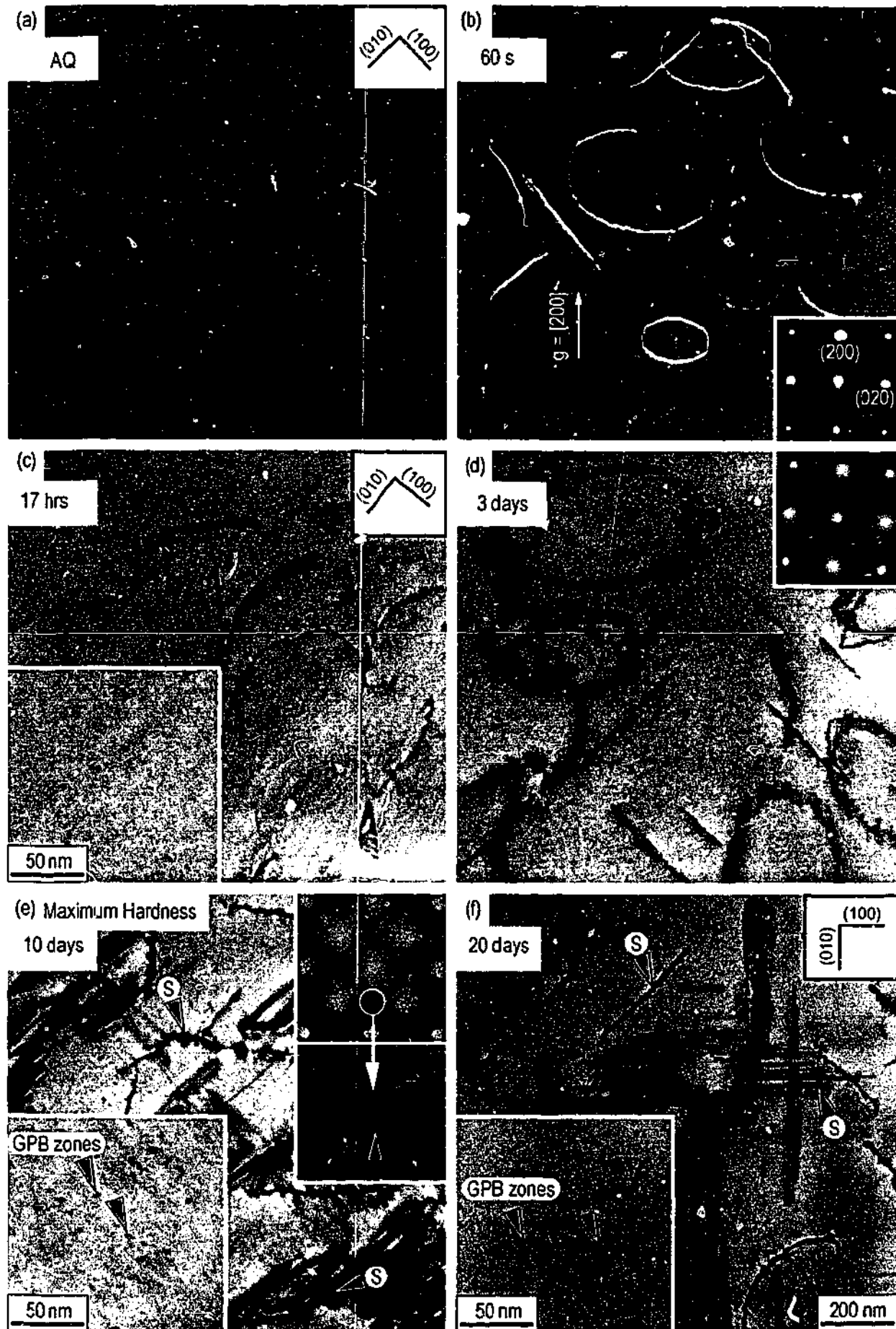


Figure 4.12 Microstructural evolution: Al-0.8Cu-1.7Mg, ST (525°C) + Q (20°C) + AA (150°C).

4.2.4 Prolonged Over-Ageing

Bright-field images observed approximately parallel to $\langle 001 \rangle_{\alpha}$ of severely over-aged (~ 120 d at 150°C) specimens of the four selected alloys are shown in figure 4.13. Precipitates plates of the θ' phase oriented such that their habit plane was perpendicular to the electron beam showed contrast unlike that observed previously in this work (examples are labelled as θ'_1 and θ'_2). This may be a result of thickening, loss of interfacial coherency [135] or precipitate impingement. Although, θ' is dominant, the S-phase is also present. In contrast, precipitates of the S-phase are

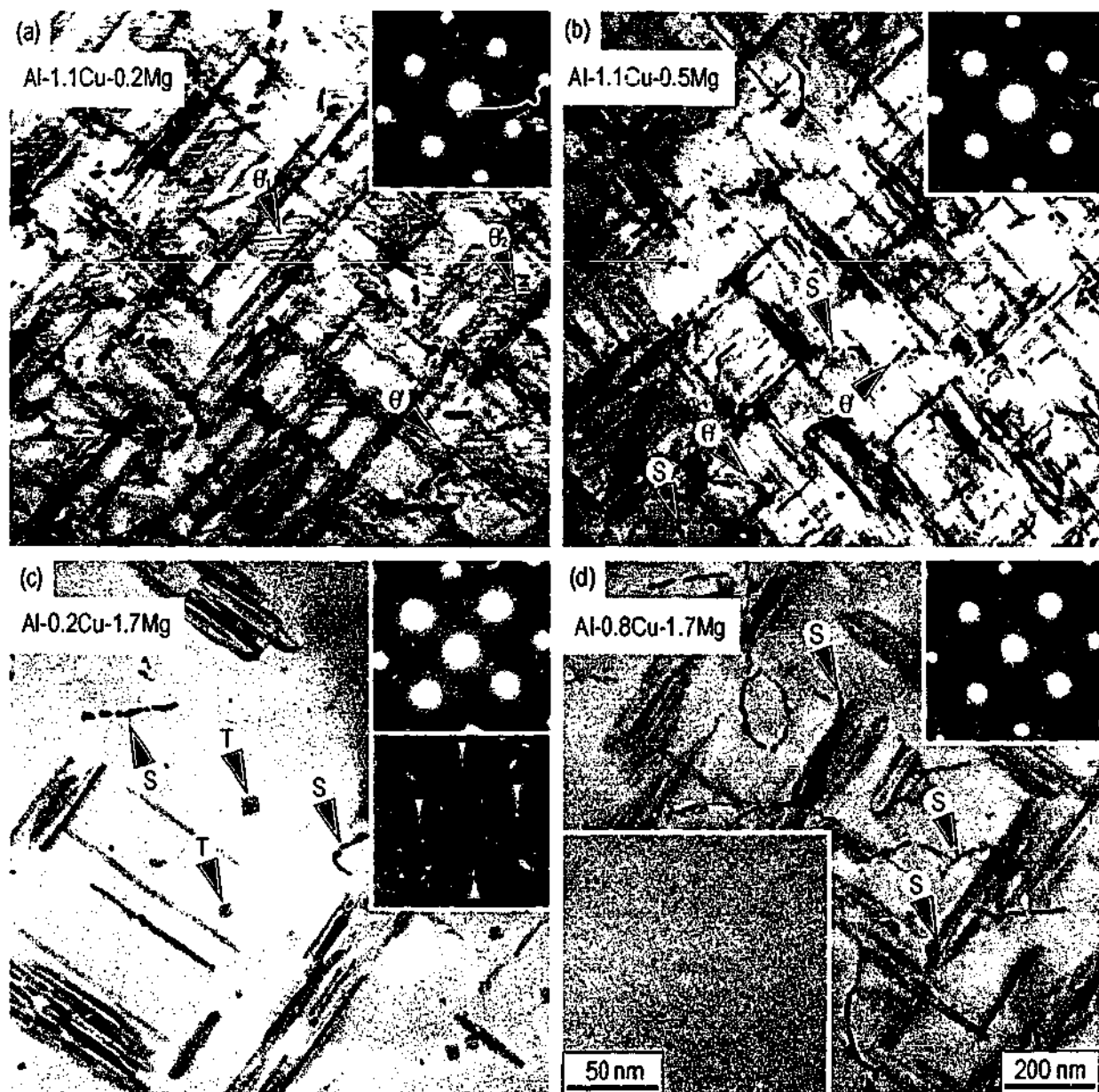


Figure 4.13 Over-aged microstructures (~ 120 d at 150°C) of (a) Al-1.1Cu-0.2Mg, (b) Al-1.1Cu-0.5Mg, (c) Al-0.2Cu-1.7Mg and (d) Al-0.8Cu-1.7Mg.

dominant in the severely over-aged microstructures of alloy Al-1.2Cu-0.5Mg and there is evidence that they have formed at positions well removed from the former dislocation loops. Prolonged over-ageing did not alter the distribution of the S-phase precipitates in the case of alloys of low Cu:Mg ratio, as shown in figures 4.13(c) and 4.13(d), where it is observed that the vast majority of precipitates are located at the former dislocation loops. The alloy Al-0.2Cu-1.7Mg displayed an additional form of second-phase particle, and accordingly, the accompanying SAED pattern indicates the presence of precipitates other than the S-phase. Reference to the SAED patterns of those phases expected from a consideration of the alloy phase field in §4.3 reveals that the extra spots can tentatively be identified as arising from the T-phase (Mg_4CuAl_6). This phase was present at positions removed from other precipitates and unrelated to the position of the pre-existing dislocation loops. The presence of T-phase was not observed previously in these alloys following ageing times up to 80 d in the present work (although it may have been present in small quantities), nor was it noted in the other three strategically-selected alloys under investigation in the present work, despite this being expected from a consideration of the phase field. Finally, the absence of contrast between the precipitate networks in alloys Al-0.2Cu-1.7Mg and Al-0.8Cu-1.7Mg indicates dissolution during over-ageing of the small precipitates labelled as GPB zones, which were present at the maximum hardness.

4.3 Pre-Aged Al-Cu-Mg - Microstructural Evolution and Hardness

Artificial ageing of Al-Cu-Mg alloys at 150°C immediately following solution treatment and quenching led to the formation of vacancy aggregates, and their subsequent collapse to form dislocation loops (§4.2.1). These loops then acted as heterogeneous nucleation sites for second-phase precipitation. A pre-ageing step is defined as a period of ageing at a lower temperature (often room temperature or slightly above), intentionally implemented following quenching and prior to the application of elevated temperature ageing. Pre-ageing regimes in the processing of Al-Cu-Mg alloy are practised industrially for improved hardenability [6]. Considering that the bulk properties of the alloys are a direct consequence of the microstructure, an investigation of the changes that this treatment imparts to the heterogeneous distribution of precipitates is of potential interest in the present context. Under the pre-ageing regimes implemented here, the alloys were aged at ambient temperature (*natural ageing*) (20°C) for periods up to 24 h prior to artificial ageing at 150°C for various periods up to maximum hardness and beyond. This report will first record the hardening response of pre-aged alloys, followed by microstructural characterisation at selected stages during artificial ageing.

4.3.1 Micro-Indentation Hardness

Plots of hardness (UMIS 2000 [183] at a maximum load of 1000 mN) as a function of ageing time at 150°C for the four pre-aged (2 and 24 h at 20°C) alloys are shown in figure 4.14. For comparison, the hardening response in the absence of a pre-ageing step is included for all alloys. The hardening response was, with the exception of the Al-0.2Cu-1.7Mg alloy, dramatically different to the hardening response in the absence of pre-ageing. Consider first the alloys of high Cu:Mg ratio (figs. 4.14(a) and 4.14(b)). Natural ageing of both alloys for 2 h led to hardness increases greater than that achieved following artificial ageing at 150°C for the same length of time. However, immediate artificial ageing eventually led to hardness increases up to maximum values similar to those obtained without pre-ageing. A similar result was obtained for the alloy Al-1.1Cu-0.2Mg after first naturally ageing for the longer period of 24 h followed by artificial ageing at 150°C. However, for the alloy Al-1.1Cu-0.5Mg, the extent of softening by reversion at 150°C after 24 h natural ageing was much reduced, so that the hardness actually remained above the plateau value observed when the alloy was subject to only artificial ageing at 150°C.

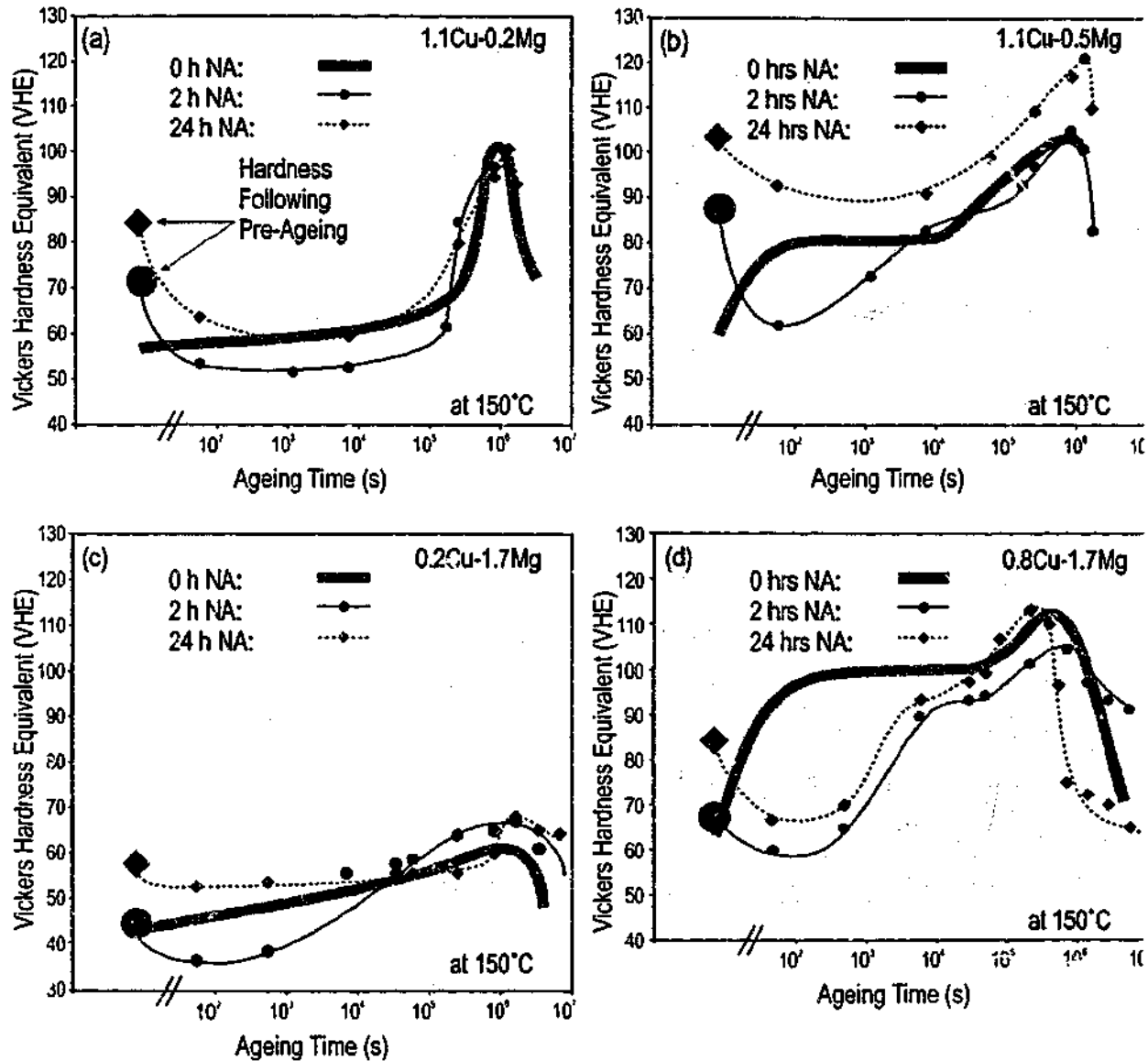


Figure 4.14 Microhardness results for samples pre-aged for 2 and 24 h at room temperature prior to elevated temperature ageing at 150°C: (a) Al-1.1Cu-0.2Mg, (b) Al-1.1Cu-0.5Mg, (c) Al-0.2Cu-1.7Mg, (d) Al-0.8Cu-1.7Mg.

Furthermore, the maximum hardness of the alloy was significantly increased if the alloy was first naturally aged for 24 h. The time to maximum hardness at 150°C was not significantly different to that required in the absence of pre-ageing (~10 d).

Natural ageing of both alloys Al-0.2Cu-1.7Mg and Al-0.8Cu-1.7Mg (figs. 4.14(c) and 4.14(d)) for 2 h led to small increases in hardness. However, softening occurred when the alloys were aged artificially at 150°C for 60 s. Extended ageing of the naturally-aged alloys at 150°C eventually led to hardness increases up to maximum values similar to those obtained through artificial ageing alone. A similar result was obtained for the alloys naturally aged for 24 h prior to artificial ageing. The maximum hardness of the Al-0.2Cu-1.7Mg and the Al-0.8Cu-1.7Mg

alloys were not significantly altered or improved by the application of pre-ageing prior to artificial ageing, and the time to maximum hardness was not dissimilar to that required in the absence of pre-ageing (40 d and 10 d for alloys Al-0.2Cu-1.7Mg and Al-0.8Cu-1.7Mg respectively).

4.3.2 Precipitation Processes – Pre-Aged Al-1.1Cu-xMg Alloys

There were no features observable either via imaging or diffraction techniques following 2 and 24 h natural ageing following quenching. Figure 4.15 displays a series of DF and BF images of specimens observed parallel to $\langle 001 \rangle_{\alpha}$, displaying the evolution of the microstructure in the alloy Al-1.1Cu-0.2Mg pre-aged for 2 h and 24 h followed by elevated temperature ageing. Artificial ageing for 60 s (figs. 4.15(a) and 4.15(b)) resulted in dislocation loops throughout the microstructure. Extremely fine features were observed between the loops, and their size increased in those specimens naturally aged for the longer period of 24 h prior to artificial ageing. These extremely fine features are arrowed in the inset of figure 4.15(b) for the alloy Al-1.1Cu-0.2Mg naturally aged for 24 h prior to elevated temperature ageing. Ageing for 3 d at 150°C following 2 and 24 h pre-ageing (figs. 4.15(c) and 4.15(d)) led to second-phase precipitation at the loops for both pre-ageing regimes. Furthermore, the fine dispersion of features between the precipitate loops was still present, as indicated. Ageing for 10 d (maximum hardness) at the elevated temperature (figs. 4.15(e) and 4.15(f)) resulted in growth of the precipitates (particularly θ'). A dispersion of precipitates was present between the larger precipitates with a form consistent with the morphology of S-phase. Diffraction evidence suggested the presence of θ' , possibly S-phase and a third phase, as indicated in the inset SAED pattern of figure 4.15(f). The additional diffraction spots were located at the $\frac{1}{3}\{022\}_{\alpha}$ and $\frac{2}{3}\{022\}_{\alpha}$ matrix positions. Following an assessment of the microstructural evolution in Al-1.1Cu-0.5Mg alloys, the origin of these extra diffraction spots in the SAED pattern will be discussed.

As for the Al-1.1Cu-0.2Mg alloy, the alloy Al-1.1Cu-0.5Mg was characterised by the formation of both dislocation loops and a dense dispersion of fine features between the dislocation loops, following a pre-ageing treatment (2 h and 24 h) plus 60 s ageing at 150°C (figs. 4.16(a) and 4.16(b)). The features are indicated in figure 4.16(a), and the size of these features increased with extended pre-ageing time. Although not investigated thoroughly in this work, the nature of these fine features between the loops can be appreciated from the inset in figure 4.16(b), a HREM image of the specimen observed parallel to $[100]_{\alpha}$. In most cases, the features lay parallel

to a projected $\{021\}_\alpha$ plane, in the manner of a standard lath precipitate of the S-phase (§2.3.4). Ageing for 3 d at 150°C (figs. 4.16(c) and 4.16(d)) resulted in heterogeneous nucleation of S and θ' at the dislocation loops. Also evident, as indicated in figure 4.16(d) is the persistence of features in the microstructure between the dislocation loops. Following 10 d at 150°C (maximum hardness), there were numerous precipitates of the θ' and S-phase at the former dislocation loops (figs. 4.16(e) and 4.16(f)). Also, precipitates consistent with the appearance of S-phase were present between the dislocation loops, as indicated in the inset of figure 4.16(f). Resembling the results of the pre-aged Al-1.1Cu-0.2Mg alloy, the pre-aged Al-1.1Cu-0.5Mg alloys displayed diffraction spots that could be indexed at $\frac{1}{3}\{022\}_\alpha$ and $\frac{2}{3}\{022\}_\alpha$ positions in the SAED pattern, representing diffracted electron beams not expected to originate from precipitates of either the S-phase or the θ' phase.

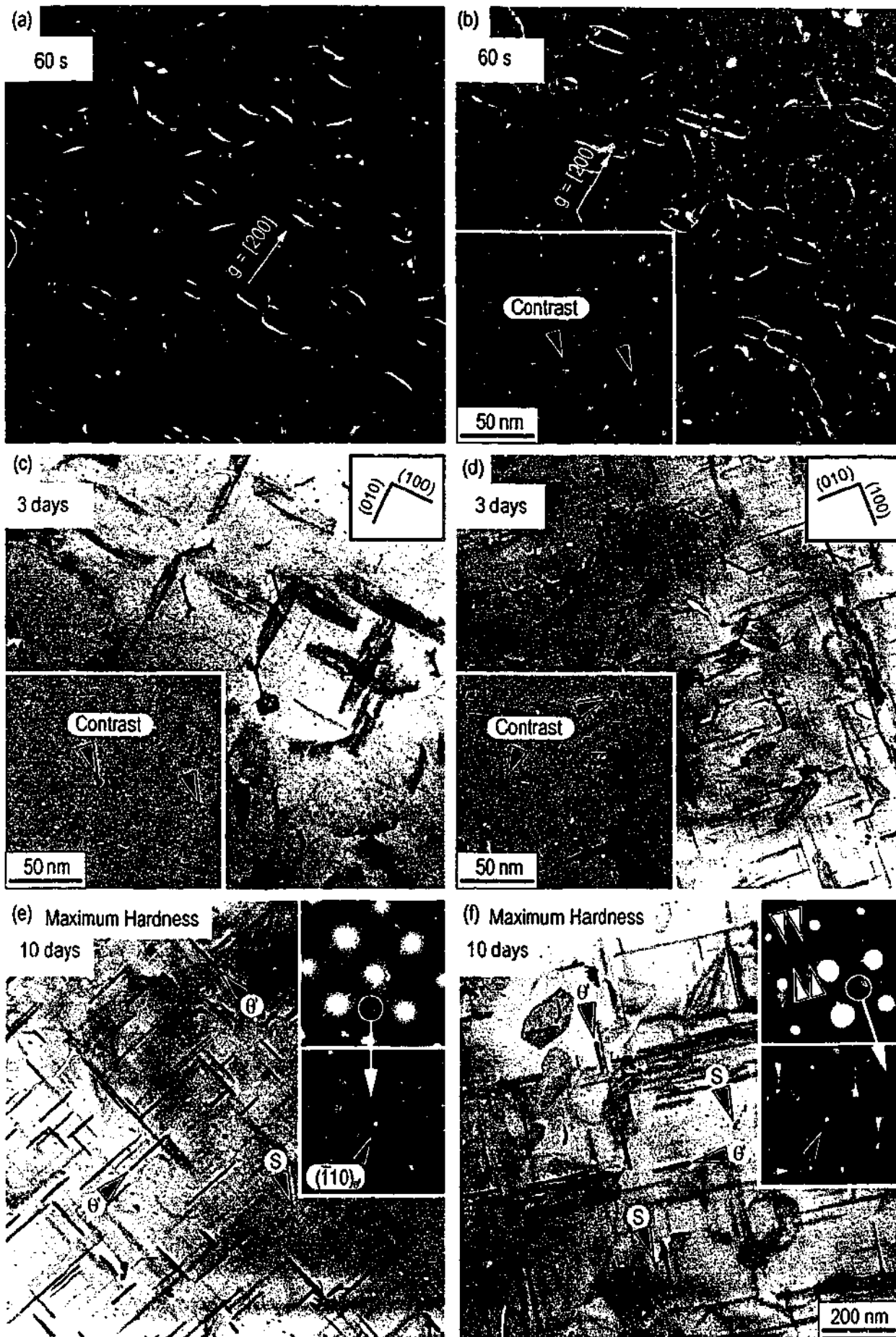


Figure 4.15 Al-1.1Cu-0.2Mg, AA(150°C) following (a)(c)(e) 2 h NA (b)(d)(f) 24 h NA.

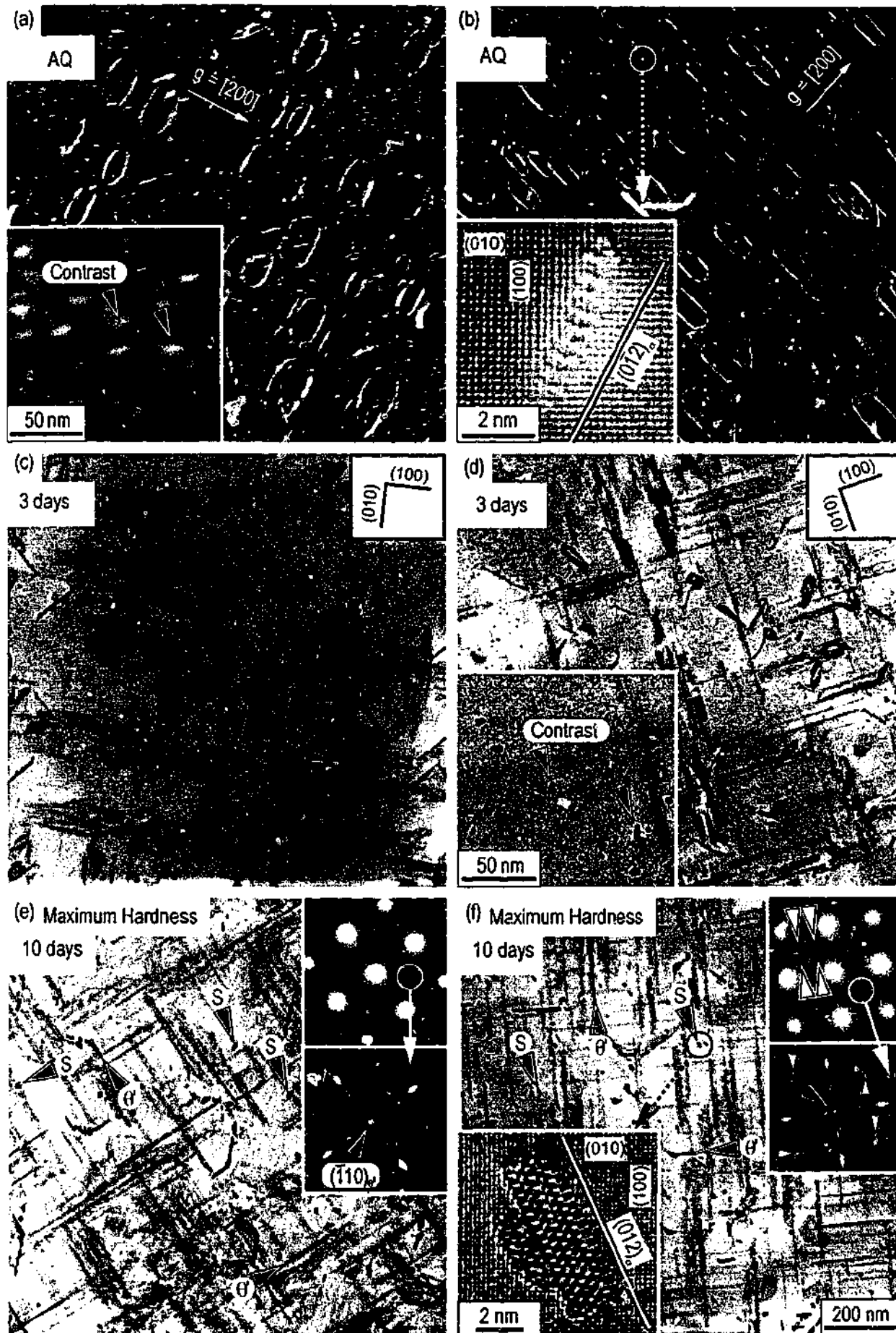


Figure 4.16 Al-1.1Cu-0.5Mg, AA(150°C) following (a)(c)(e) 2 h NA (b)(d)(f) 24 h NA.

Figure 4.17 is a series of BF micrographs of alloy Al-1.1Cu-0.5Mg alloy pre-aged for 2 h prior to ageing at 150°C. The specimen represented in figure 4.17(a) was observed parallel to $\langle 001 \rangle_{\alpha}$ and had been aged artificially for 3 d. The precipitates with a morphology that is not consistent with precipitates of either the θ' -phase or S-phase are arrowed. Tilting of the specimen to a $\langle 011 \rangle_{\alpha}$ electron beam orientation (fig. 4.17(b)) revealed that these unidentified precipitate plates were parallel to $\{111\}_{\alpha}$ matrix planes. These precipitates are likely be the orthorhombic Ω -phase ($\sim\text{Al}_2\text{Cu}$), which forms as hexagonal plates parallel to $\{111\}_{\alpha}$ [79,80], and they have been so

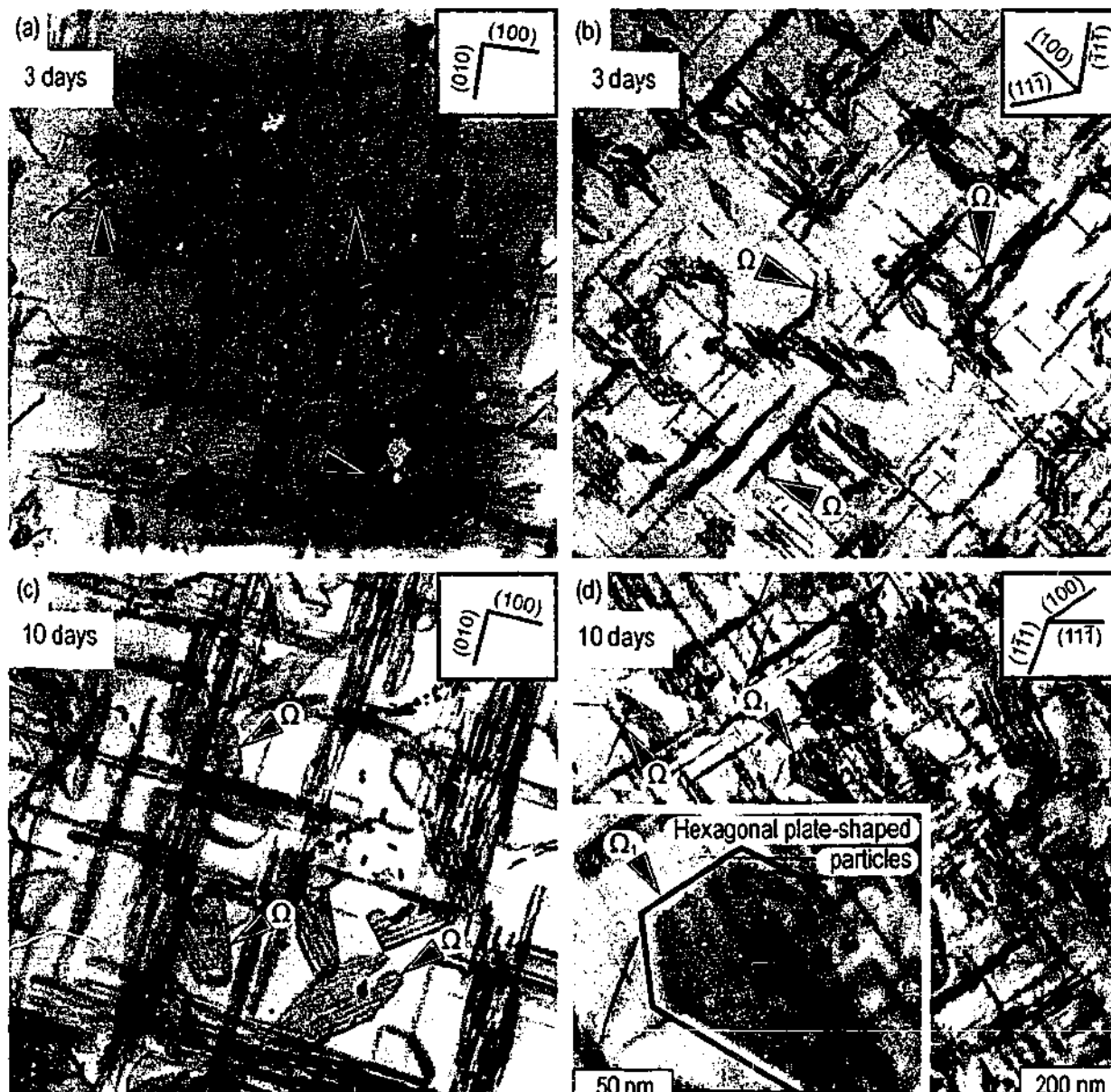


Figure 4.17 Plate-like precipitates parallel to $\{111\}_{\alpha}$ matrix planes in association with precipitate networks at former dislocation loops in Al-1.1Cu-0.5Mg alloy following 2 h pre-ageing prior to extended artificial ageing for ((a) and (b)) 3 d and ((c) and (d)) 10 d. Images were taken near the $\langle 001 \rangle_{\alpha}$ ((a) and (c)) and $\langle 011 \rangle_{\alpha}$ ((b) and (d)) zone axis. The precipitate plates parallel to $\{111\}_{\alpha}$ are arrowed.

labelled. The precipitates of the proposed Ω phase were found consistently in the vicinity of the precipitate networks at former dislocation loops following 3 d ageing. Bright-field images recorded parallel to $\langle 001 \rangle_{\alpha}$ and $\langle 011 \rangle_{\alpha}$ are shown in figures 4.17(c) and 4.17(d), respectively, for alloy Al-1.1Cu-0.5Mg pre-aged for 2 h and artificially aged for 10 d at 150°C. Growth of the proposed Ω plates is evident, as is the hexagonal shape of the precipitates (fig. 4.17(d)). The plate-shaped particles were $\geq \sim 200$ nm in breadth, and the typical foil thickness in these TEM specimens is ~ 100 nm. It is therefore expected that truncation of individual precipitate plates occurred during TEM specimen preparation, and this explains why association of the precipitate plates with a heterogeneous nucleation site is not evident for all plate-shaped particles in these thin specimens aged for 10 d at 150°C. Although precipitates such as these were very occasionally observed in alloys artificially aged immediately following quenching, their number density was significantly increased by the incorporation of a natural ageing treatment.

The extra diffraction spots at $\frac{1}{3}\{022\}_{\alpha}$ and $\frac{2}{3}\{022\}_{\alpha}$ in the SAED patterns are indicated in figure 4.18(b) for a typical microstructure that contains precipitates of the proposed Ω phase, as shown in figure 4.18(a). Selection of the precipitate reflection located at $\frac{2}{3}(220)_{\alpha}$ in a small objective aperture, and the subsequent DF image formed, excites several Ω plates, and it is therefore proposed that the extra diffraction spots are sourced from the proposed Ω plates. The precipitate spots proposed to originate by diffraction from the proposed Ω plates (fig. 4.19 (a)) is consistent with the indexing of simulated SAED patterns from Ω phase by Knowles and Stobbs [79], as shown in figure 4.19 (b).

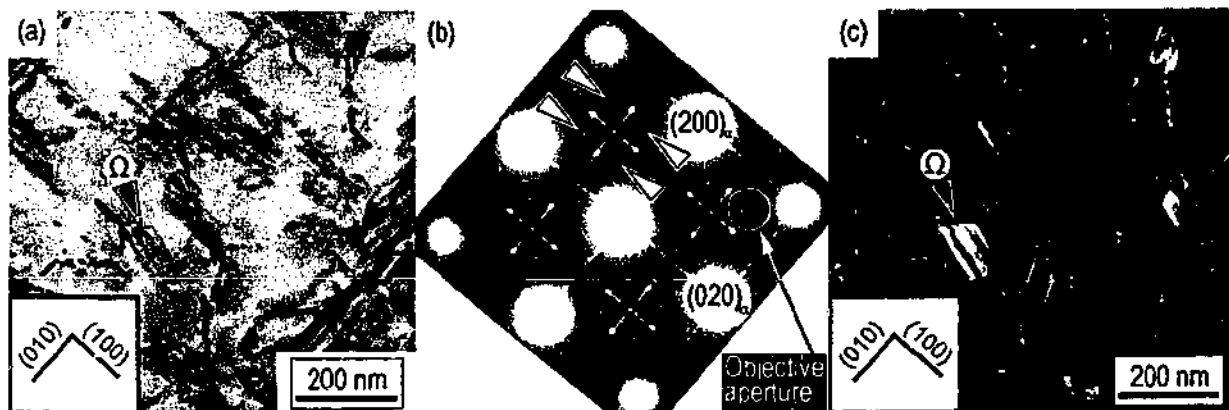


Figure 4.18 (a) BF image containing proposed Ω plates (arrowed). (b) SAED pattern of the microstructure in (a). (c) DF image formed with the precipitate reflection located at $\frac{2}{3}(220)_{\alpha}$, as indicated. The Ω plate is excited.

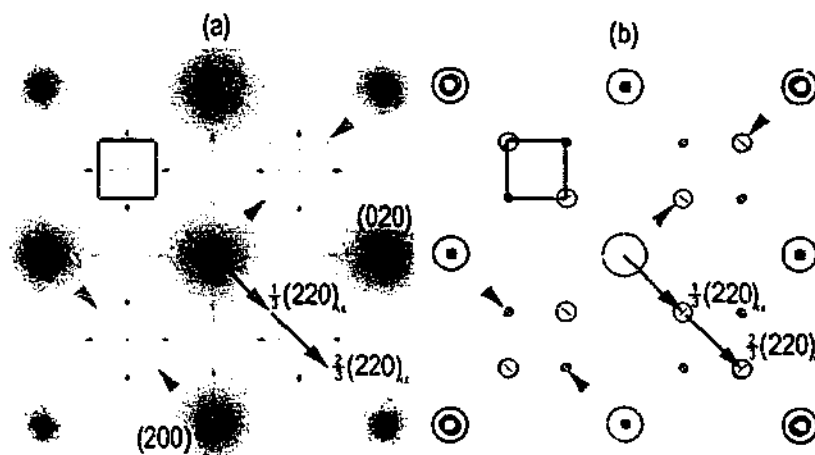


Figure 4.19 (a) Experimental $[001]_\alpha$ SAED pattern of a microstructure containing the proposed Ω -phase (Al-1.1Cu-0.5Mg pre-aged 2 h, 150°C for 10 d). (b) Calculated SAED pattern [78].

4.3.3 Precipitation Processes – Pre-Aged Al-xCu-1.7Mg Alloys

The evolution of microstructure at 150°C in the strategically-selected and pre-aged Series II alloys is displayed in figures 4.20 and 4.21 for alloys Al-0.2Cu-1.7Mg and Al-0.8Cu-1.7Mg, respectively, in the form of DF and BF images approximately parallel to $(001)_\alpha$. Pre-ageing for 2 h and 24 h of alloy Al-0.2Cu-1.7Mg (figs. 4.20(a) and 4.20(b)) followed by 60 s artificial ageing led to the presence of dislocations. However, particularly in the case of 24 h pre-ageing, the dislocation loop microstructure was complex, and far more random than that observed in the absence of pre-ageing, where regular loops were evident. Pre-ageing for 2 h followed by artificial ageing for 10 d and 40 d (maximum hardness) (figs. 4.20(c) and 4.20(e)) resulted in a very similar microstructure to that observed in the absence of pre-ageing, including the potential presence of GPB zones. However, precipitation upon the complex dislocation microstructure following 24 h pre-ageing, and 10 d and 40 d (maximum hardness) at 150°C, led to the formation of precipitate networks unlike that seen to this point in the investigation. Nevertheless, spots in the SAED pattern were consistent with the presence of S-phase precipitate particles, as indicated.

In the Al-0.8Cu-1.7Mg alloy, pre-ageing for 2 h and 24 h (figs. 4.21(a) and 4.21(b)) followed by 60 s artificial ageing resulted in the presence of dislocations. Artificial ageing for 3 d (figs. 4.21(c) and 4.21(d)) and 10 d (maximum hardness) (figs. 4.21(e) and 4.21(f)) resulted in precipitation upon the dislocations introduced during the initial 60 s. The microstructure between the dislocations at maximum hardness did not contain the small zones or precipitates labelled as GPB zones in the Al-0.8Cu-1.7Mg alloy that was not pre-aged (fig. 4.12(e)).

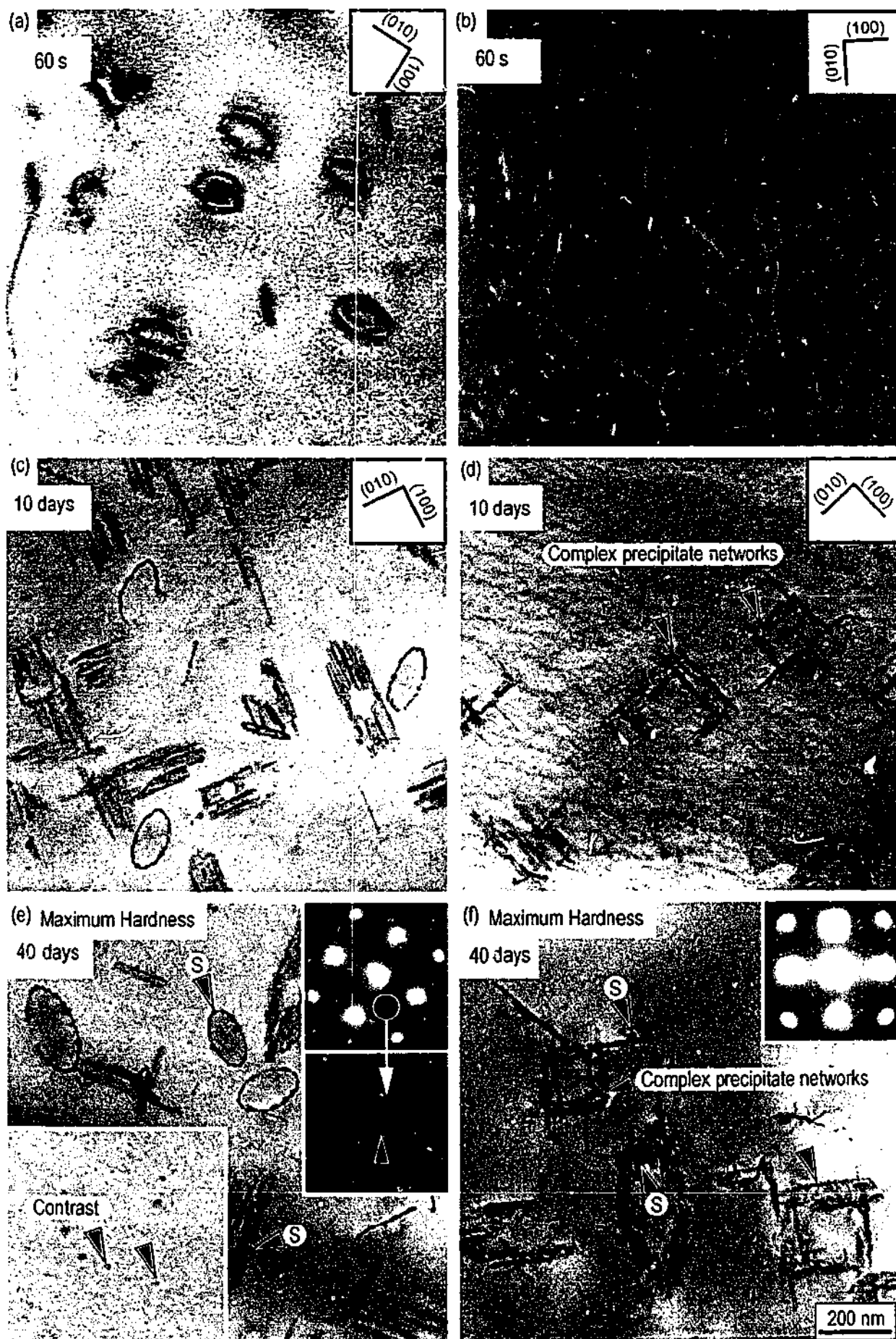


Figure 4.20 Al-0.2Cu-1.7Mg, AA(150°C) following (a)(c)(e) 2 h NA (b)(d)(f) 24 h NA.

The complex arrangement of precipitates of the S-phase at the complex dislocations loops in the pre-aged (24 h) Al-0.2Cu-1.7Mg alloy will now be further characterised. Figure 4.22(a) is a BF image approximately parallel to $\langle 001 \rangle_a$ of the microstructure of an over-aged (80 d at 150°C) specimen of the Al-0.2Cu-1.7Mg alloy. The S-phase was located at the complex former dislocation loops that formed in the early stages of elevated temperature ageing following quenching. In most cases, the elongated S-phase precipitates were approximately arranged at the corners of an orthorhombic volume. This is best illustrated in figure 4.22(b), which is a BF image of a precipitate network that has been tilted away from $\langle 001 \rangle_a$. Examples of precipitates of the S-phase parallel to each of the three potential axes of elongation ($\langle 001 \rangle_a$) are clear. These precipitate networks were very different to those that form at dislocation loops in the absence of pre-ageing, where a single growth direction was apparently able to describe all of the local precipitates at discrete dislocations loops. As with the case of specimens subject to immediate artificial ageing following quenching, the T-phase was distributed uniformly throughout the microstructure in the over-aged condition.

The modifications to the dislocation loops that were a product of pre-ageing in the Al-0.2Cu-1.7Mg alloys were extremely complex. Although a large number of possible loop complexes that could potentially yield the novel S-phase arrangements have been observed, it has not been possible to establish consistent characteristics.

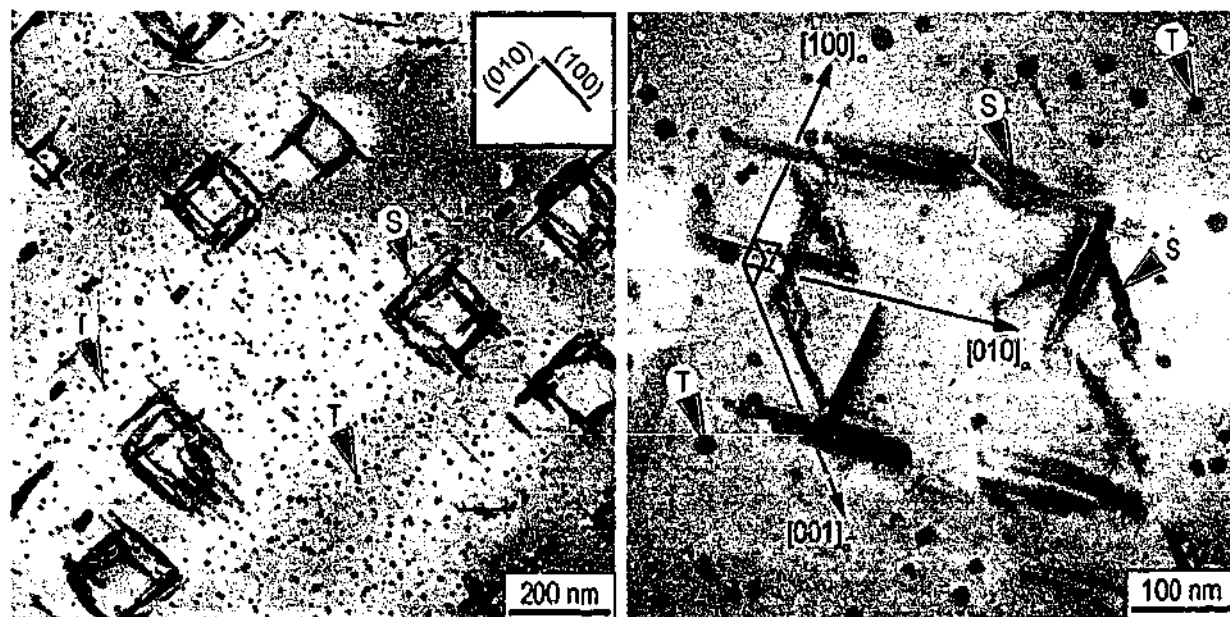


Figure 4.22 Overaged (80 d) specimen of the alloy Al-0.2Cu-1.7Mg following quenching and room temperature pre-ageing for 24 h, parallel to $\langle 001 \rangle_a$ (b) A precipitate network tilted away from $\langle 001 \rangle_a$.

4.4 Interpretation of Results

A total of at least five varieties of second-phase precipitate have been observed at or near maximum hardness in the four strategically-selected Al-Cu-Mg alloys in the present work: GPB zones, θ' , Ω , S-phase, and T-phase. This section evaluates firstly these observations with reference to the proposed microstructural models available in the literature for these alloys. Following this, the influence of the pre-precipitation defect distribution on the distribution of precipitates at maximum hardness is discussed. Of the precipitate phases present, those that nucleate heterogeneously are given special emphasis. Finally, optimum alloy chemistry and heat treatment conditions are proposed for the generation of a suitable distribution of selected precipitate species, the study of which will potentially lead to a greater understanding of heterogeneous nucleation in Al-Cu-Mg alloys.

4.4.1 Microstructure and Corresponding Hardness

Table 2.1 summarises the precipitate identity and distribution in the microstructures of the four selected alloys at maximum hardness following artificial ageing at 150°C.

Table 4.1 Summary of precipitate identity and distribution at maximum hardness in the selected alloys.

Alloy Specimens Artificially Aged Immediately Following Quenching					
	θ'	Ω	S	GPB	T(*)
Al-1.1Cu-0.2Mg	○■	○ (Very low density)	○	-	-
Al-1.1Cu-0.5Mg	○	○ (Very low density)	○	■ (Very low density)	-
Al-0.2Cu-1.7Mg	-	-	○	■	■
Al-0.8Cu-1.7Mg	-	-	○	■	-
Alloy Specimens Pre-Aged at Ambient Temperature Prior to Artificial Ageing					
Al-1.1Cu-0.2Mg	○■	○	○■	-	-
Al-1.1Cu-0.5Mg	○	○	○■	-	-
Al-0.2Cu-1.7Mg	-	-	○ (Complex loops)	■	■
Al-0.8Cu-1.7Mg	-	-	○	■	-

○ - Precipitation at or near loops. ■ - Precipitation away from loops. * - Only present in large quantities following maximum hardness.

The microstructural characteristics of specimens quenched and immediately aged will be discussed first, followed by the characteristics of pre-aged specimens.

Alloy Specimens Artificially Aged Immediately Following Quenching

As-quenched microstructures in all alloys were featureless. This suggests (1) that of those vacancies that did not annihilate during the quench, the bulk were retained in the solid solution, and (2) that the solute is distributed either uniformly in solution, or in aggregates so small that they were not resolvable in the electron microscope by the available imaging or diffraction techniques. The hardness of as-quenched specimens was always the minimum hardness of the alloys for those specimens aged immediately at 150°C following quenching. Nevertheless, owing to solid solution strengthening of the ternary alloys, the hardness of as-quenched specimens was significantly greater than that of pure aluminium which, according to Mondolfo [112], is ~14 VHN for 99.999% pure metal.

Two of the selected alloys (Al-1.1Cu-0.5Mg and Al-0.8Cu-1.7Mg) displayed a rapid increase in hardness within the first 60 s of artificial ageing. The origins of hardening during these early stages of ageing have been discussed previously (§2.1.5). The conclusion of Ringer *et al.* [59,60,73] that the initial rapid increase in hardness following quenching is a *pre-precipitate phenomena* is supported by the current observations. Furthermore, and within the limits of resolution of the currently applied techniques, the suggestion that the initial rapid increase in hardness results from the traditionally favoured distribution of GPB zones [84,85] or the presence of S'' at dislocations [58] could not be supported. The most significant change in the as-quenched microstructure following 60 s at 150°C, as observed by the techniques applied in the present work, is the formation of a high concentration of dislocation loops within the first 60 s of ageing. Vacancies in alloys with a vacancy concentration in excess of the thermal equilibrium coalesce to form vacancy discs, the collapse of which forms dislocation loops [175]. The alloy Al-1.1Cu-0.2Mg was also characterised by a distribution of dislocation loops of only a slightly lower number density than the alloy Al-1.1Cu-0.5Mg, and yet showed no trace of a rapid increase in hardness during artificial ageing. It is therefore concluded that the presence of dislocation loops alone is not responsible for the rapid initial increase in hardness.

In those alloys that do rapidly harden, alloys Al-1.1Cu-0.5Mg and Al-0.8Cu-1.7Mg, the hardness does not appreciably change for ~10 h and ~55 h, respectively, following the first 60 s of ageing. Beyond this hardness plateau, both alloys experience a rise to maximum hardness. The observation that the Al-0.8Cu-1.7Mg alloy begins to undergo the second rise in hardness

following a comparatively long hardness plateau when compared to the Al-1.1Cu-0.5Mg alloy is perhaps explained by the observation that second-phase precipitation had not commenced following 17 h at 150°C in alloy Al-0.8Cu-1.7Mg, while precipitation had commenced following similar ageing treatments in the Al-1.1Cu-0.5Mg alloy. This observation is perhaps attributable to the higher concentration of Mg in the former alloy, trapping vacancies and slowing down the precipitation kinetics. It is suggested that the beginning of the second increase in hardness in these alloys coincides with the early stages of growth of second-phase particles in both of these alloys. Those alloys that do not rapidly harden, Al-1.1Cu-0.2Mg and Al-0.2Cu-1.7Mg, also exhibited a hardness plateau, although shorter in duration. Second-phase precipitation in these alloys coincided with the rise to maximum hardness in the same manner as described for the two previous alloys.

In the Cu-rich Series I alloys, precipitates of θ' and S-phase at the former dislocation loops dominated the microstructure at maximum hardness. The volume of matrix between the precipitate networks at former dislocation loops was apparently free of second-phase particles in alloy Al-1.1Cu-0.2Mg. The matrix between the loops in Al-1.1Cu-0.5Mg alloys displayed faint, localised contrast the origin of which could not be firmly established. In the light of the assumed presence of GPB zones in the Mg-rich Series II alloys at similar positions between the loops, the faint, localised contrast in alloy Al-1.1Cu-0.5Mg may have arisen from a low number density of GPB zones in an alloy that has only a moderate Mg content. Over-ageing (softening) of Series I alloys was associated with precipitate coarsening, and a greater concentration of S-phase precipitates between the dislocation loops in alloy Al-1.1Cu-0.5Mg. In Series II alloys, the proposal [59] that GPB zones are a feature of microstructures at maximum hardness rather than of the microstructure following the initial rapid hardening response in alloys found in the (α +S) phase field (e.g. Al-0.8Cu-1.7Mg) is supported by the evidence presented here. The softening of alloys in the (α +S) phase field, following prolonged artificial ageing, was associated with the dissolution of GPB zones within the microstructure, and this leads to the conclusion that GPB zones are an important component of the microstructure with respect to the maximum hardness attainable. The Al-0.2Cu-1.7Mg alloy reached moderate hardness, concomitantly forming features consistent with GPB zones, and softening was again associated with zone dissolution and precipitate coarsening. Accordingly, it could be suggested that the hardening response is dictated solely by the presence/absence of the GPB zones. However, Series I alloys, as previously discussed, did not rely upon significant GPB zone number densities to deliver a hardening increment, while softening occurred through precipitate coarsening. Therefore, the

softening of alloys from the (α +S) phase field can be considered to be a combination of both GPB zone dissolution, and precipitate coarsening in the manner described for Series I alloys.

Alloy Specimens Pre-Aged at Ambient Temperature Prior to Artificial Ageing

As Sen and West [89] indicate, there are two issues pertaining to the effect of pre-ageing upon subsequent artificial ageing: namely, (1) changes in matrix solute supersaturation that may have taken place through the formation of zones or precipitates during pre-ageing, and (2) the potential role of these zones or precipitates in further precipitation at the elevated temperature.

Alloys pre-aged at room temperature actually increased in hardness while at room temperature, and the magnitude of the hardening response increased with the Cu content. The cause of this increase in hardness was not determined, but may lie in the presence of a fine dispersion of GP zones, as suggested by others [57,192], or other solute aggregations. However, this issue has not been addressed as GP zones do not form heterogeneously, and it is considered beyond the scope of the present work. In Series I alloys, softening during subsequent elevated temperature ageing was associated in all cases with the formation of (1) dislocation loops, and (2) small contrast centres in the matrix between the dislocation loops. The HREM imaging of the contrast centres revealed that they were consistent with the morphology of precipitates of the S-phase in the standard orientation, and the high number density of S-phase precipitates between the loops following further artificial ageing to peak hardness suggests that the initial phases have developed continuously into S-phase. The softening of alloy Al-1.1Cu-0.5Mg following 24 h natural ageing was not significant when compared to alloys naturally aged for 2 h, suggesting that the solute aggregations responsible for the hardness increase during natural ageing were more stable following the longer period of natural ageing. It is expected that the superior hardness displayed by pre-aged alloy specimens of Al-1.1Cu-0.5Mg, compared to that of specimens immediately aged following quenching, is due to this re-distribution of S-phase precipitates, where the parameter λ in the Orowan equation (the spacing between precipitate particles) (§2.1.1) is decreased.

Pre-ageing in Series II alloys contributed little to the maximum hardness achieved following artificial ageing. Slight increases in hardness were observed following natural ageing alone (particularly in the alloy Al-0.8Cu-1.7Mg), and subsequent elevated temperature ageing resulted in a drop in hardness similar to that observed in Series I alloys. However, there were no small centres of contrast, as observed in Series I. A complex dislocation loop microstructure was introduced into the alloy following natural ageing and a short (60 s) artificial ageing step.

4.4.2 Influence of Initial Dislocation Substructure

Dislocation loops were observed to cease significant growth following the first 60 s of ageing at 150°C in *all* alloys, in contrast to the observations of Shih *et al.* [8], who suggested that loops in Al-1.3Cu-1.5Mg alloys can continue to grow for up to 3 h at temperatures up to 240°C following quenching. Arrest of the growth of these loops is important in the context of the present work because the position of the line defect remains fixed, enabling subsequent precipitation at the loops to be correlated to the microstructure following 60 s ageing. There were no dislocation helices present in the alloys following the ageing treatments.

The initial loop microstructure clearly has implications for the precipitate distribution at maximum alloy hardness. The GPB zones in Series II alloys, seemingly critical to the attainment of maximum hardness, show no preference for heterogeneous nucleation at dislocations. Also, the T-phase (which is apparently present in large quantities only *after* maximum hardness in *one* of the Series II alloys examined) shows no preference for nucleation at or near a dislocation. Therefore, with respect to the remaining precipitate phases at the maximum hardness of alloys artificially aged immediately following quenching, θ' and S, it can be concluded that, with the possible exception of the alloy Al-1.1Cu-0.2Mg, the precipitate distribution is completely determined by the location of dislocation loops prior to precipitate nucleation. These precipitates formed at loops in all alloys with or without pre-ageing. As such, pre-aged material will not be investigated further with respect to the formation of these precipitates. However, pre-aged Series I alloys will be investigated further, since it has been shown here that the location of Ω -phase precipitates in the pre-aged Cu-rich alloys is associated with dislocation loops.

4.5 Chapter Summary and Directions of the Present Research

The novel materials processing parameters employed in the present research elicit a high concentration of dislocations loops in the four aluminium-rich Al-Cu-Mg alloys investigated. The impact that an initial dislocation microstructure has on the precipitate microstructure of an alloy of appropriate chemistry at maximum hardness has been shown to be significant. Thus, design of high-strength Al-Cu-Mg alloys will be immensely facilitated by understanding of the relationship between the nucleation site and the nucleating precipitate.

The nucleation of precipitates of θ' , Ω and S at line defects in these materials requires careful examination, and the processing conditions applied in the present work have been optimised in order to achieve this. A correlation is to be sought between the crystallography of the precipitates and the form of the dislocation upon which they nucleate. In order to achieve this, both the dislocation loops and the precipitates must be characterised individually, and these issues will be addressed in the following chapter. With respect to the individual precipitate species:

The θ' -phase

The phase only forms in the Series I alloys, and its absence in Series II alloys is a result of the phase field in which the alloys lie. The phase forms at dislocation loops in alloys that have been immediately aged following quenching or those subjected to a pre-ageing step prior to artificial ageing. In Al-1.1Cu-0.2Mg alloys, in which the precipitates dominate, the distribution of particles at maximum hardness is not always clearly linked to the original distribution of dislocation loops in the microstructure. Furthermore, pre-ageing of the alloys encourages the formation of θ' precipitates away from the dislocations loops ("homogeneous" nucleation). Therefore, the optimum alloy and processing conditions in which to observe the heterogeneous nucleation and growth of precipitates of the θ' -phase are:

Al-1.1Cu-0.5Mg, S1 + quench + immediate artificial ageing at 150°C

The Ω -Phase

Plate-like precipitates of the Ω -phase have been observed in Series I alloys in those alloys pre-aged at room temperature prior to elevated temperature ageing. The reported observation of the Ω -phase in ternary Al-Cu-Mg alloys in the literature [52] did not identify any preferred association (or nucleation site) for the $\{111\}_\alpha$ precipitate. However, it is clear from the current work that there is a preferred association of the Ω -phase with the network of precipitates located at the former dislocation loops. The original distribution of dislocation loops is more obvious in the Al-1.1Cu-0.5Mg alloy, and therefore the optimum alloy and processing conditions in which to observe the nucleation and growth of precipitates of the Ω -phase are:

Al-1.1Cu-0.5Mg, ST + quench + 2 h natural ageing + immediate artificial ageing at 150°C

The S-phase

The presence of the S-phase was recorded at maximum hardness in all of the strategically selected alloys in the present work. In Series I alloys, both θ' and S form at the loops. In Series II alloys, the S-phase was the only precipitate that nucleated at dislocations, and therefore an investigation of the relationship between the S-phase and dislocations is preferably carried out on this latter series. Therefore, the optimum alloy and processing conditions in which to observe the nucleation and growth of precipitates of the S-phase are:

Al-0.2Cu-1.7Mg, ST + quench + immediate artificial ageing at 150°C

Al-0.8Cu-1.7Mg, ST + quench + immediate artificial ageing at 150°C

5.0

Precipitates at Defects in Al-Cu-Mg Alloys

In the previous chapter it was confirmed that aluminium-rich Al-Cu-Mg alloys aged to maximum hardness have a microstructure characterised by a distribution of various combinations of θ' , Ω -phase, S-phase and T-phase precipitate particles and GPB zones. Apart from the latter two, these precipitates nucleate and grow almost exclusively in the vicinity of dislocation loops that form in high density during the very early stages of artificial ageing at elevated temperatures following quenching. Design of alloys suitable for structural applications requires a thorough understanding of the precipitation processes, and therefore heterogeneous precipitate nucleation is of obvious technological importance in Al-Cu-Mg alloys. Although the phenomenological observation of heterogeneous nucleation at dislocations is well established [95,106,109,110,170,193,194], there remains much conjecture regarding the role of the dislocation in the actual nucleation event [36,92] and its impact upon the final form and crystallography of the particle. It is the aim of the present chapter to assess the crystallography of all varieties of strengthening precipitates that nucleate at or near dislocation loops in the selected Al-Cu-Mg alloys. Ultimately, a link will be sought between the characteristics of the precipitate and the nature of the local strain field upon which it nucleated.

The chapter begins with a detailed characterisation of the crystallography of dislocation loops. Succeeding sections describe θ' -phase, Ω -phase and S-phase at or near dislocation loops in the selected alloy compositions and applied heat treatment conditions established in the summary of the previous chapter. The chapter will conclude with a general discussion of the results for these forms of precipitate, concentrating upon and drawing attention to those that warrant further investigation.

5.1 Dislocation Loop Crystallography

Closed loops are one of only three ways in which dislocations can terminate in a crystal [195], alternatively extending from one crystal surface to another, or ending in a node. A dislocation loop in a simple cubic crystal system is conceptualised in figure 5.1 [196]. A cut has been made between two horizontal planes of the crystal lattice, and, for a selected area of the plane (the black rectangle in figure 5.1(a)), a shift of one lattice spacing applied parallel to the plane of the cut. This has the effect of creating a rectangular dislocation loop, with segments characterised as either edge, screw or mixed (fig. 5.1(b)). Consider the case where a shift is applied *perpendicular* to the plane of the cut such that the action creates a monolayer void of atoms in the shaded rectangular area (fig. 5.1(c)). Following rejoining of the crystal, the loop created takes the form of a continuous pure edge dislocation (fig. 5.1(d)).

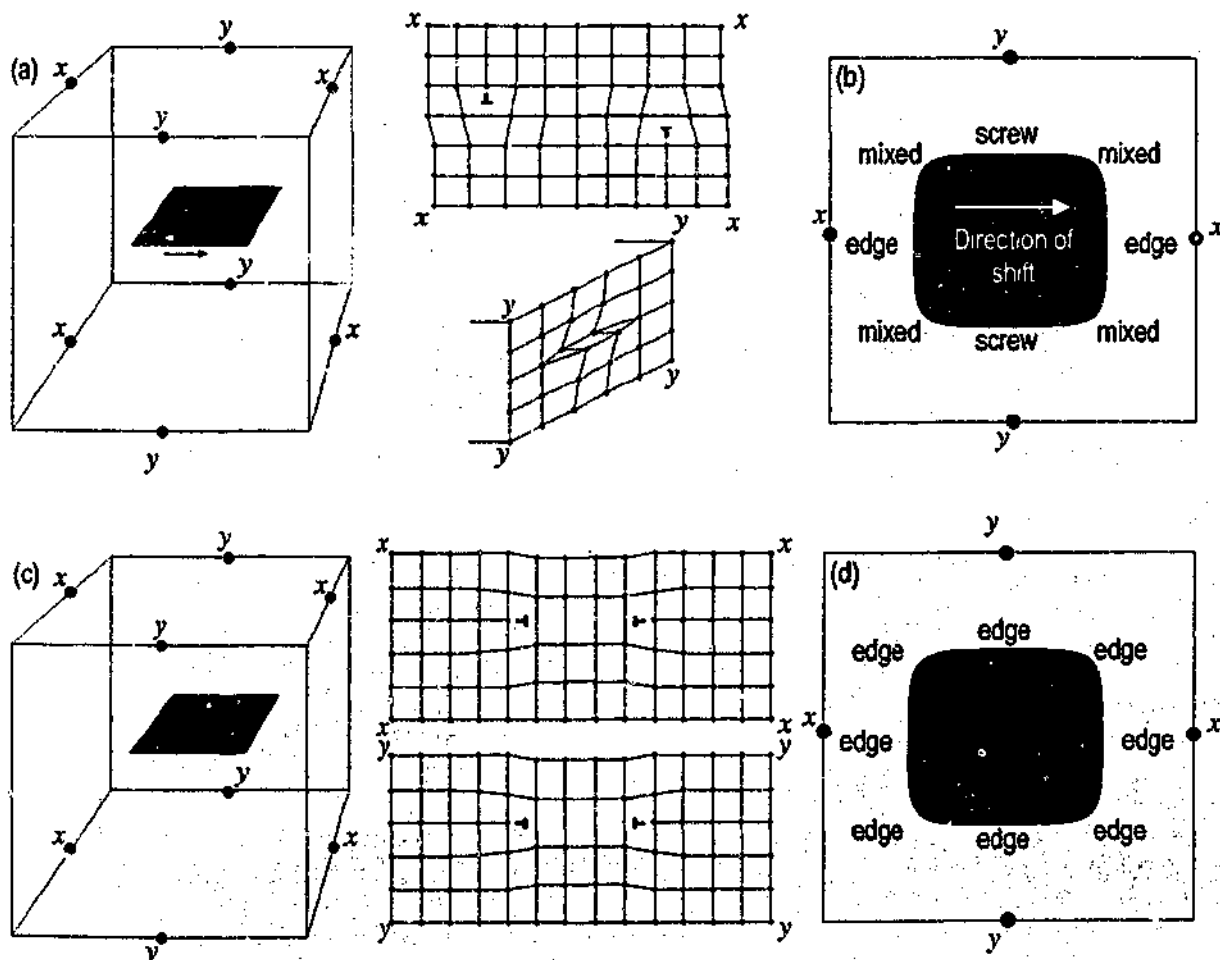


Figure 5.1 Conceptual creation of a dislocation loop of ((a) and (b)) mixed-character and ((c) and (d)) pure edge-character in a simple cubic system (after [195]).

Vacancy aggregation and condensation can result in vacancy discs (a planar void), the collapse of which into intrinsic dislocation loops is supported by numerous observations, both here and in the wider literature [174,175,197,198]. In the present work, it is exactly these types of loops that are present in high concentrations immediately following very short ageing times at elevated temperatures (§ 4.2.1), and two varieties of vacancy condensation loop were noted in chapter 4.

5.1.1 Dislocation Loops in $\{110\}_\alpha$

Figure 5.2(a) is a BF TEM image of an alloy volume containing a distribution of dislocation loops in Al-1.1Cu-0.5Mg alloys following solution treatment, quenching and 60 s of artificial ageing. The foil is oriented such that the electron beam is parallel to a direction of the type $\langle 100 \rangle_\alpha$, and short segments of line defect are parallel to planes of the type $\{110\}_\alpha$, as indicated. Tilting of specimens such as those shown in figure 5.2(a) shows that these line defects are in fact dislocation loops projected *end-on*, which therefore lie in $\{110\}_\alpha$. A specimen oriented parallel to $\langle 111 \rangle_\alpha$ is shown in figure 5.2(b). Segments of line defect are again observed parallel to planes of the type $\{110\}_\alpha$ and are shown to be end-on loops. The alloys Al-1.1Cu-0.2Mg and Al-1.1Cu-0.5Mg were observed to contain only loops lying in these planes, while a significant proportion of loops in the alloys Al-0.2Cu-1.7Mg and Al-0.8Cu-1.7Mg were also formed parallel to $\{110\}_\alpha$.

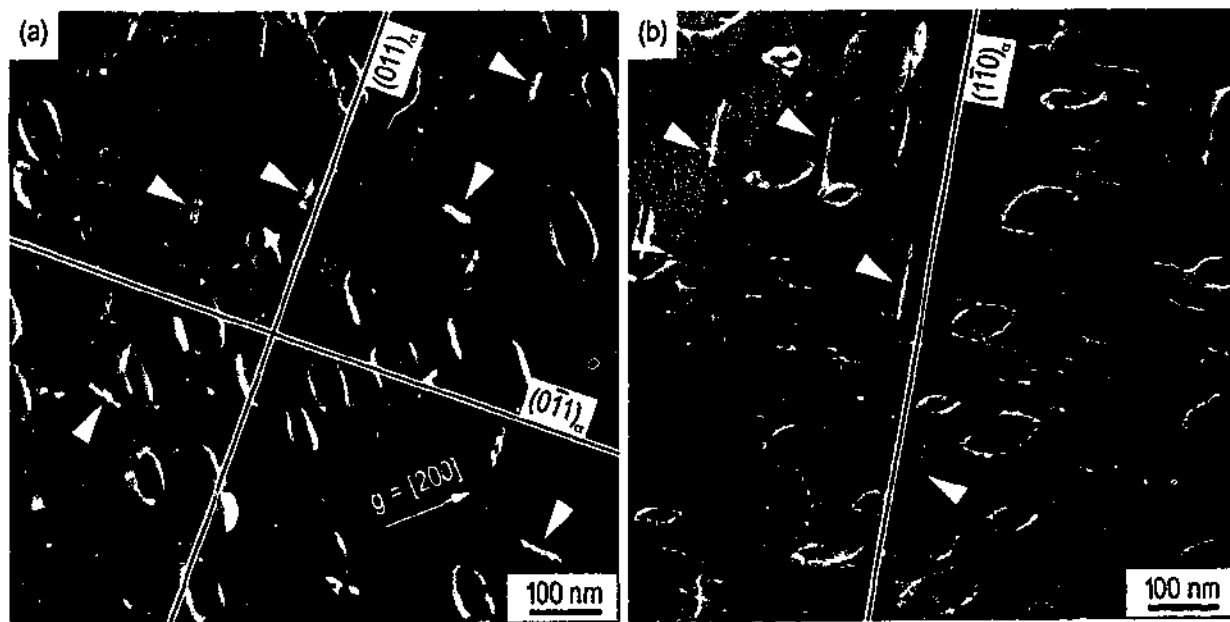


Figure 5.2 Loops parallel to $\{110\}_\alpha$ planes (arrowed) in Al-1.1Cu-0.5Mg alloy; viewed parallel to (a) $[100]_\alpha$ and (b) $[110]_\alpha$ directions.

At no stage of the thermal treatment cycle were stacking faults present in these loops, regardless of alloy chemistry. Hence, perfect stacking of atomic planes is preserved in a direction perpendicular to the plane of the loop. Therefore, the Burgers vector must be a lattice vector, or a multiple of a lattice vector, and this may be determined using the $g \cdot b$ invisibility criterion [199]. Several two-beam illumination conditions for two dislocation loops, A and B, are provided in figure 5.3. Consider Loop B in alloy Al-1.1Cu-0.5Mg in figure 5.3, which has been examined prior to the onset of precipitation with $b_B = b_1 b_2 b_3$. It is noted from:

Figure 5.3(b): $g \cdot b_B = [002] \cdot [b_1 b_2 b_3] = 0$, so that $b_3 = 0$;

Figure 5.3(e): $g \cdot b_B = [1-1-1] \cdot [b_1 b_2 0] = 0$, so that $b_1 = b_2$;

Figure 5.3(a): $g \cdot b_B = [020] \cdot [b_1 b_1 0] = \pm 1$, so that $b_1 = \pm 0.5$

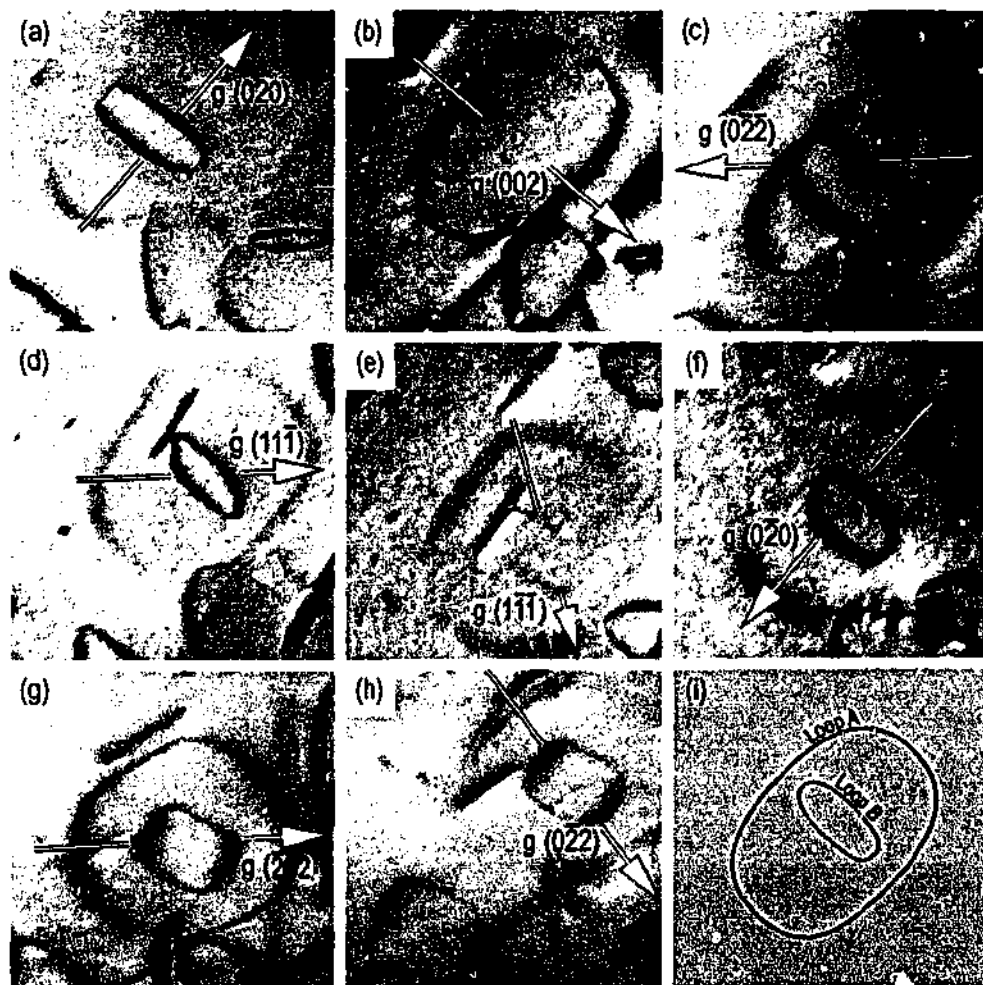


Figure 5.3 Dislocation loops A and B in Al-1.1Cu-0.5Mg alloy under systematic two-beam diffraction conditions: (a) – (c) beam \sim parallel to $[100]_a$, (d) – (f) $\sim [101]_a$, (g) – (h) $\sim [111]_a$.

Table 5.1 Calculation of $g \cdot b_B$ for the two-beam diffraction conditions presented in figure 5.3.

Fig.	$g \cdot b_B$	Product
5.4(c)	$[0-2-2] \cdot \pm \frac{1}{2} [110]$	± 1
5.4(d)	$[11-1] \cdot \pm \frac{1}{2} [110]$	± 1
5.4(f)	$[0-20] \cdot \pm \frac{1}{2} [110]$	± 1
5.4(g)	$[-202] \cdot \pm \frac{1}{2} [110]$	± 1
5.4(h)	$[0-22] \cdot \pm \frac{1}{2} [110]$	± 1

It is thus concluded that $b_B = \pm \frac{1}{2} [110]_a$. Note that the Burgers vector satisfies all of the remaining observations contained in figure 5.3, as shown in table 5.1. The elastic strain energy of a given dislocation is a function of its Burgers vector and the nature of the dislocation, i.e. edge, screw or mixed. The orientation of the Burgers vector with respect to the plane of the loop determines the nature of the dislocation. Therefore, a unique relationship is expected between the Burgers vector and the plane of the loop such that the lowest energy configuration is consistently developed for all loops observed in $\{011\}_a$. Since the mechanism of formation of a vacancy condensation loop is via planar void formation, the dislocation is expected to be pure edge upon collapse (fig. 5.1(c)).

The Burgers vector of loop B in figure 5.4 can be explicitly related experimentally to the unique plane in which the loop resides. Consider the model in figure 5.4 where the six planes of the type $\{110\}_a$ are shown, one of which must accommodate Loop B, which is projected as a continuous dislocation loop in all three electron beam directions in figure 5.3 and therefore *can not lie parallel to*:

$(011)_a$ or $(0\bar{1}1)_a$, since these planes are *parallel* to $B [100]_a$ - figure 5.4(a), or

$(\bar{1}01)_a$, since this plane is *parallel* to $B [101]_a$ - figure 5.4(b), or

$(\bar{1}10)_a$, since this plane is *parallel* to $B [111]_a$ - figure 5.4(c).

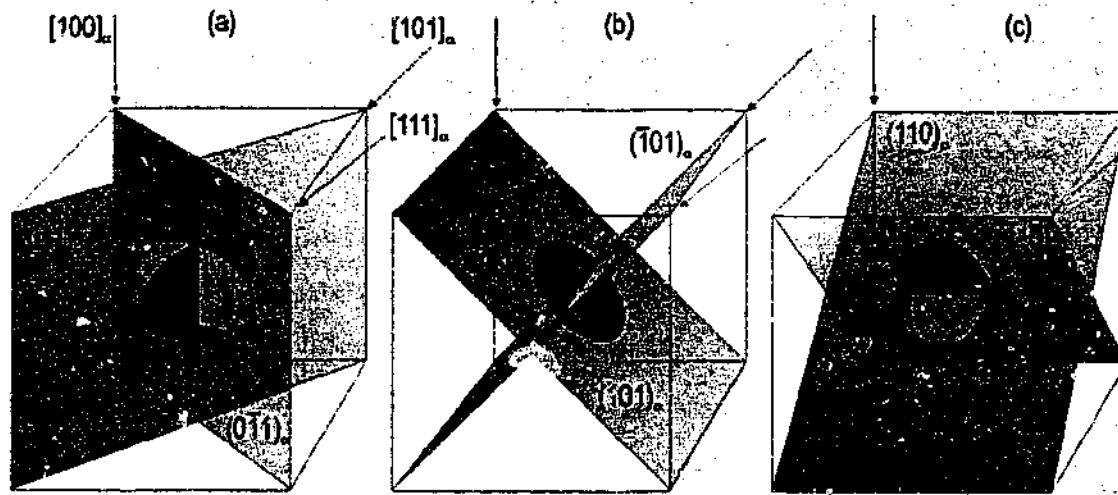


Figure 5.4 Planar dislocation loops parallel to the six variants of the $\{110\}_\alpha$ planes. Beam directions indicated by arrows and are labelled only in (a).

Therefore, loop B must lie in either $(101)_\alpha$ or $(110)_\alpha$. If loop B lies in $(101)_\alpha$, then a change in loop projection from $[101]_\alpha$ to $[111]_\alpha$ should decrease the observed area bound by the projected loop, since the projection is changing from one that is perfectly perpendicular to the loop to a projection that is $\sim 35^\circ$ from perpendicular. Figures 5.3 (g) and 5.3(h) show that the area bound by the loop actually *increases* under these conditions, and hence Loop B is not parallel to (101) . Intuitively, the area bound by a loop lying in $(110)_\alpha$ would increase under these conditions, and therefore it is concluded that loop B lies in $(110)_\alpha$. This self-consistent analysis implies that loops lying in $(110)_\alpha$ have a Burgers vector equal to $\pm \frac{1}{2}[110]_\alpha$, or, more generally, that the Burgers vector is always perpendicular to the plane of the loop and the dislocation line direction. This result is expected, and confirms the results of extensive past observations [173,174].

5.1.2 Dislocation Loops in $\{111\}_\alpha$

In high Mg alloys, Al-0.2Cu-1.7Mg and Al-0.8Cu-1.7Mg, a proportion of the dislocation loops contained planar stacking faults readily evident in samples oriented such that the electron beam was parallel to a $\langle 001 \rangle_\alpha$ direction. Figure 5.5(a) is a BF image of alloy Al-0.2Cu-1.7Mg quenched and aged at 150°C for 60 s. These loops are parallel to $\{111\}_\alpha$ planes (fig. 5.5(b)) in a manner consistent with the established theory of planar defects in fcc crystals.

Planar defects form in fcc lattices when vacancies condense on *close-packed* planes (i.e. $\{111\}_\alpha$) into monolayer discs which subsequent lattice relaxations convert to prismatic dislocation loops [197]. Two relaxation configurations are possible, which lead to imperfect and perfect dislocation loops, respectively [197]. In the former case, a direct collapse of the lattice planes introduces an intrinsic stacking fault (Frank sessile loop) surrounded by a dislocation of Burgers vector $\frac{1}{3}\langle 111 \rangle_\alpha$ (often known as a Frank partial dislocation) [174]. In the latter, the collapse of the vacancy disc is accompanied (or followed at some later stage) by a shear which restores the loop interior to perfect stacking and converts the loop Burgers vector to $\frac{1}{2}[110]_\alpha$ by the passage of a Shockley partial dislocation ($\frac{1}{6}\langle 112 \rangle_\alpha$) across the fault. To better understand this process, consider figure 5.6, which presents the well-known Thompson's Tetrahedron (e.g. [32]).

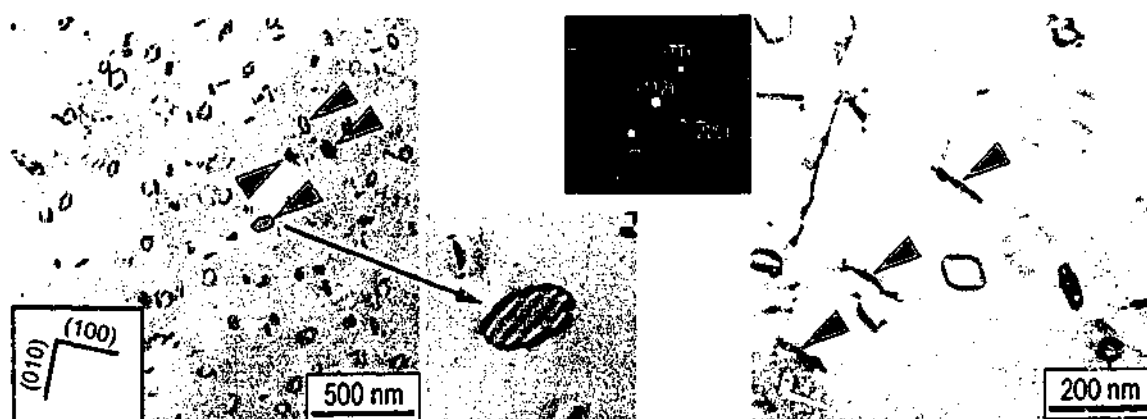


Figure 5.5 (a) Stacking fault contrast inside planar loops (arrowed) in $[001]_\alpha$ projection. (b) Crystal oriented such that the electron beam is parallel to $[112]_\alpha$, showing loops (arrowed) parallel to $\{111\}_\alpha$.

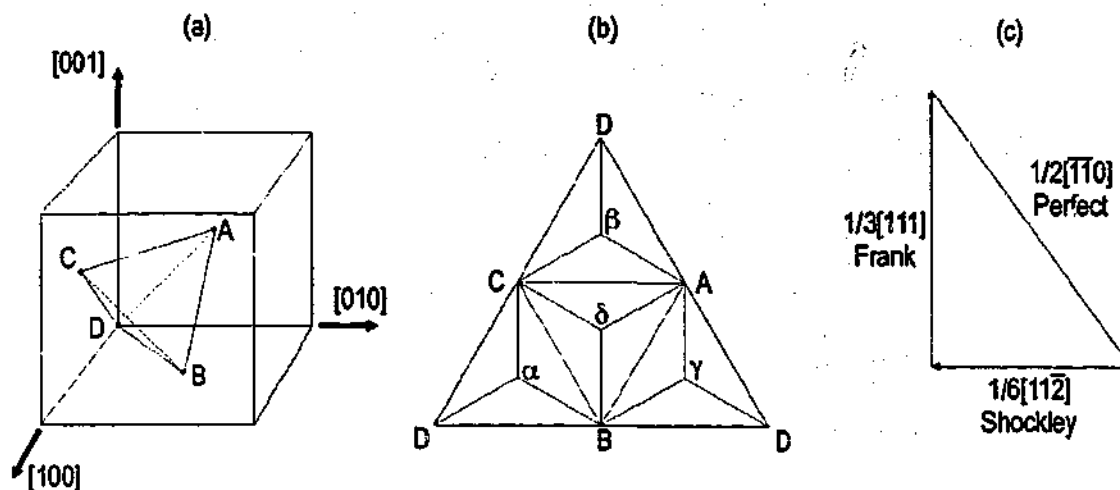


Figure 5.6 Thompson's Tetrahedron (after e.g. [32]) for fcc materials.

An edge of the tetrahedron, such as CB , represents the Burgers vector of a perfect dislocation, $\frac{1}{2}\langle 110 \rangle$. Vectors given by Greek-Roman letter combinations such as δC represent Shockley partials, except where the Greek and Roman letters are matched, such as γC , which indicates a Frank partial. An example of the reaction between Frank, Shockley and perfect dislocations becomes, in the above notation:

$$\delta D = \delta B + BD, \text{ i.e. } \frac{1}{3}[\bar{1}\bar{1}\bar{1}] = \frac{1}{6}[11\bar{2}] + \frac{1}{2}[\bar{1}\bar{1}0] \quad \text{Equation 5.1.}$$

Consider a Frank partial loop that lies parallel to $(111)_\alpha$ with Burgers vector $\frac{1}{3}[111]_\alpha$. In the manner of equation 1.1, the following energetically equivalent reactions may take place when the loop is unstable:

$$\frac{1}{3}[111]_\alpha = \frac{1}{6}[\bar{1}2\bar{1}] + \frac{1}{2}[110]$$

$$\frac{1}{3}[111]_\alpha = \frac{1}{6}[2\bar{1}\bar{1}] + \frac{1}{2}[101]$$

$$\frac{1}{3}[111]_\alpha = \frac{1}{6}[\bar{1}\bar{1}2] + \frac{1}{2}[011]$$

The Frank partial dislocation loop may undergo a transition to a dislocation loop with a Burgers vector parallel to one of the three $\frac{1}{2}\langle 110 \rangle_\alpha$ vectors that are 35.26° from the original Burgers vector, figure 5.7(a). The conversion of the loop is represented schematically in figures 5.7(b) and 5.7(c).

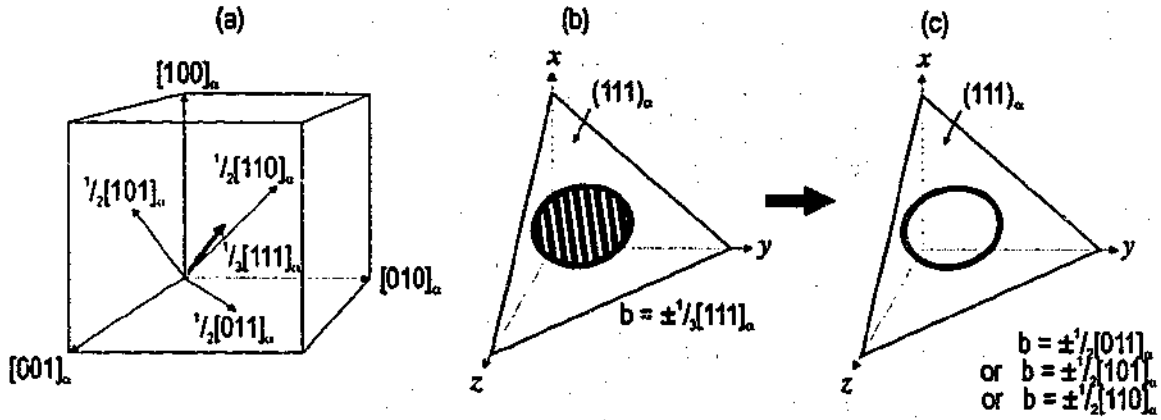


Figure 5.7 (a) A $\frac{1}{3}[111]_{\alpha}$ vector and the three vectors to which the Frank partial Burgers vector may decompose. (b) Stacking fault at a Frank partial loop. (c) Removal of stacking fault requires a Burgers vector conversion from $\frac{1}{3}[111]_{\alpha}$ to one of the three $\frac{1}{2}[011]_{\alpha}$ vectors shown in (a).

The selection of Shockley partial is most-likely dependent upon the local stresses in the microstructure at a given point in time, and therefore can not be predicted easily prior to the event [168]. Once this selection is made, conversion is achieved rapidly by the passage of the Shockley partial across the surface area of the fault, restoring perfect stacking [172-174,200].

In high Mg alloys following 60 s ageing at 150°C, it appeared that the majority of $\{111\}_{\alpha}$ loops were faulted, and thus had a Burgers vector of the form $\frac{1}{3}\langle 111 \rangle_{\alpha}$ perpendicular to the loop plane. However, after ageing for 10 min at 150°C, many of the loops observed were free of faults, implying a conversion to a Burgers vector of the form $\frac{1}{2}\langle 110 \rangle_{\alpha}$ [172-174,200,201]. Ageing for 17 hrs resulted in the complete absence of stacking faults within loop in the alloys. The equilibrium shape of loops lying in $\{111\}_{\alpha}$ corresponded to an *approximate* hexagon with linear segments parallel to $\langle 110 \rangle_{\alpha}$ directions, as shown in figure 5.8, where a series of BF images of loops in Al-0.2Cu-1.7Mg quenched and aged for 17 h at 150°C are shown. The electron beam direction is

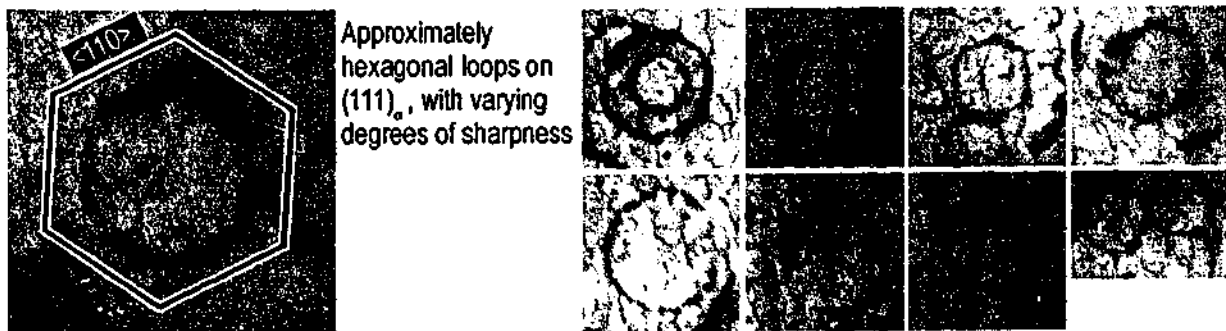


Figure 5.8 Dislocations loops lying in $(111)_{\alpha}$, where $B = [111]_{\alpha}$ (Al-0.2Cu-1.7Mg, 17 h at 150°C).

perpendicular to the plane in which the loop resides. This is in agreement with the published literature [162,164,168,172]. Note that these loops do not contain a stacking fault, and are shown prior to the onset of precipitation. The corners of the hexagon are not sharp, and in many cases the loop appears smoothly curved.

The majority of loops that were formed first as a stacking faults parallel to $\{111\}_\alpha$ were observed to remain in the same plane following conversion of the Burgers vector, although this was not always adhered to. Loops lying in $\{111\}_\alpha$ planes with a Burgers vector of $\frac{1}{2}\langle 110 \rangle_\alpha$ are energetically metastable and they are expected [173,174] to seek reorientation to the $\{110\}_\alpha$ plane normal to their Burgers vector by a process of glide reduce the dislocation line length. *Partial reorientation* of a dislocation loop refers to a loop that resides parallel to a plane intermediate between its original $\{111\}_\alpha$ habit plane and the $\{110\}_\alpha$ plane perpendicular to its Burgers vector. Figure 5.9 schematically displays the expected loop projection from the relevant $\langle 100 \rangle_\alpha$ viewing direction for three cases – 5.9(a) the loop is parallel to $\{111\}_\alpha$, 5.9(b) the loop is parallel to $(011)_\alpha$ and 5.9(c) the loop is parallel to an intermediate plane.

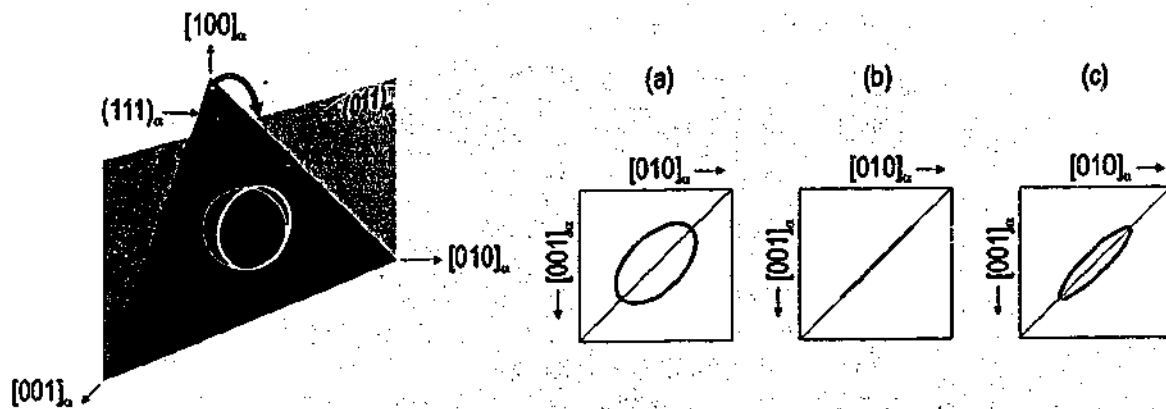


Figure 5.9 Loop projections parallel to $[100]_\alpha$ of a loop defect lying in (a) $(111)_\alpha$, (b) $(011)_\alpha$ and (c) a plane intermediate between $(111)_\alpha$ and $(011)_\alpha$.

Figure 5.10 shows such a partially reoriented dislocation loop in alloy Al-0.8Cu-1.7Mg, where subsequent precipitation upon the loop has enabled the projection (in $[100]_a // [100]_s$) of the loop to be readily determined. In this case, the precipitates are S-phase, although the nature of the precipitate is irrelevant. It is assumed here that precipitation upon a loop occurs such that the location of the precipitate provides an accurate indication of where the dislocation line originally lay. Superimposed on the image is a projection of where a perfectly circular $\{111\}_a$ dislocation loop core would lie. Based upon extensive microstructural examination, only a very small fraction of dislocation loops reside on a plane that is intermediate between $\{111\}_a$ and $\{110\}_a$.

Although the numerous $\{110\}_a$ loops in the high-Mg alloys may have originated as loops parallel to $\{111\}_a$ that subsequently undergo prismatic glide as described, this would appear unlikely. Loops in $\{110\}_a$ were observed following 60 s ageing at 150°C , in conjunction with a significant number of faulted loops that were indicative of Frank sessile loops on $\{111\}_a$. This suggests that many of the $\{111\}_a$ loops were yet to undergo a $\mathbf{b} = \frac{1}{3}\langle 111 \rangle_a \rightarrow \mathbf{b} = \frac{1}{2}\langle 110 \rangle_a$ transition after 60 s ageing. After extended (many days) ageing, the relative proportions of loops lying parallel to $\{110\}_a$ and $\{111\}_a$ remains similar to that following 60 s ageing.

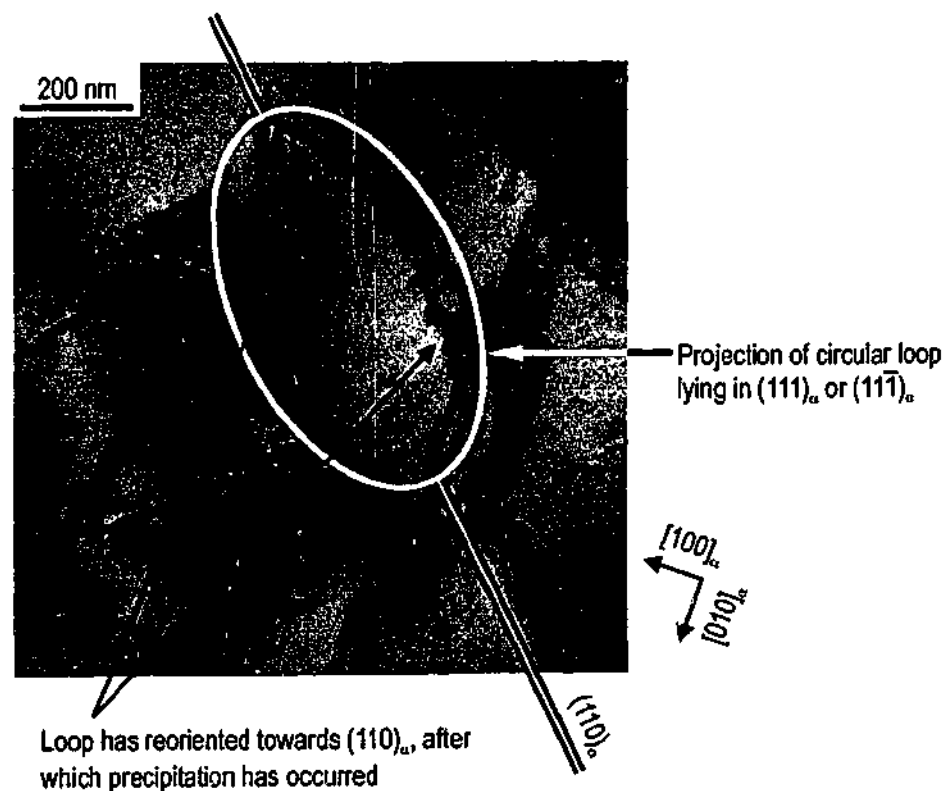


Figure 5.10 Migration of $\{111\}_a$ dislocation loop to the $\{110\}_a$ plane perpendicular to its Burgers vector (alloy Al-0.8Cu-1.7Mg, 20 d at 150°C).

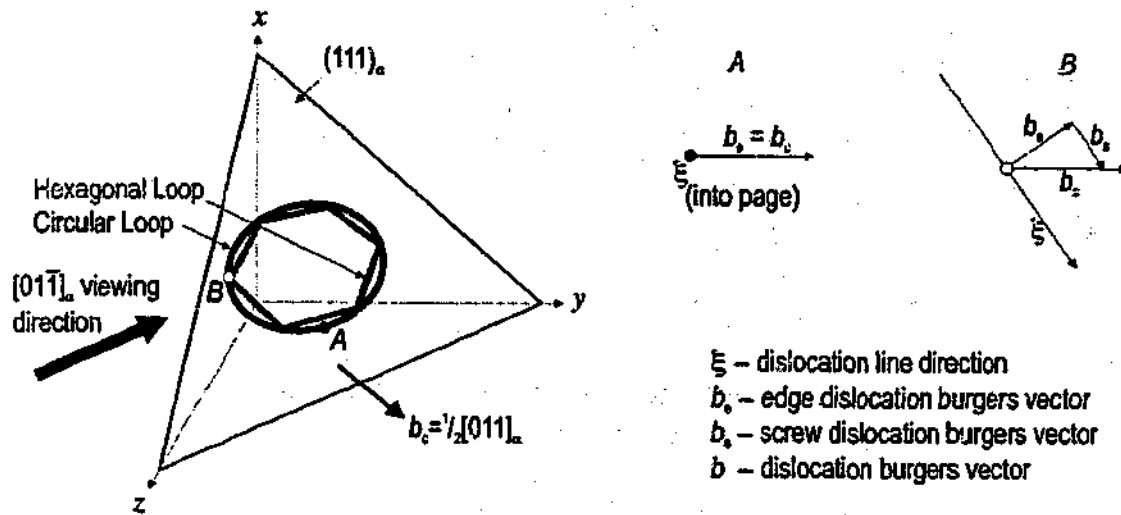


Figure 5.11 Vector diagram demonstrating the presence of edge and screw components in $\{111\}_\alpha$ dislocation loops.

A perfect dislocation loop in $\{111\}_\alpha$ is depicted in figure 5.11. Both cases of a circular and hexagonal shape are considered. At position *A* the Burgers vector is pure edge and 0.286 nm in magnitude. For a smoothly curved loop, every other position apart from *A* is characterised edge and screw component, both of which can be resolved. The screw component of the dislocation increases continuously from 0 at position *A* to 0.165 nm at position *B*, while the edge component decreases from 0.286 nm to 0.234 nm over the same dislocation segment (fig. 5.12). While the

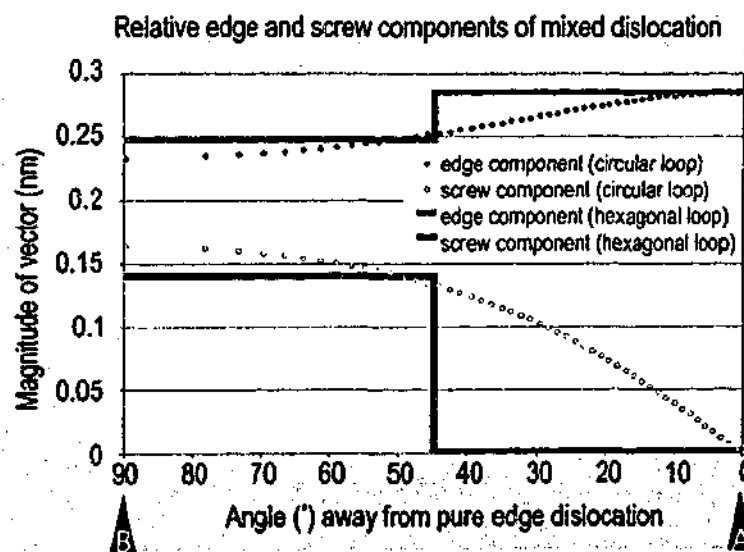


Figure 5.12 Changes in magnitude of the edge and screw components of loop Burgers vector through a quadrant of a $\{111\}_\alpha$ dislocation loop, for both the perfectly circular and the perfectly hexagonal case. The positions *A* and *B* are those defined in figure 5.11.

magnitude of the Burgers vector is invariant, this variation in the components of \mathbf{b} is repeated in the remaining quadrants of the loop according to symmetry. If the loop is hexagonal in form with linear segments parallel to $\langle 110 \rangle_\alpha$, then there are two opposing segments that are pure edge, and four which are mixed in character, with relative edge and screw components as shown in figure 5.12.

5.1.3 Summary of Loop Characteristics

A summary of the significant loop characteristics has been provided below.

Table 5.2 Characteristics of the loops found in the present work.

Loop Type	\mathbf{b}	ξ
$\{110\}_\alpha$	$\mathbf{b} = \frac{1}{2}\{110\}$ Always perpendicular to the plane of the loop. Pure edge dislocation.	Segments parallel to: $\{100\}_\alpha$ and $\{110\}_\alpha$ directions in high Cu-Mg ratio alloys; $\{112\}_\alpha$ directions in low Cu-Mg ratio alloys.
$\{111\}_\alpha$	$\mathbf{b} = \frac{1}{2}\{110\}$ Not perpendicular to the plane of the loop. Mixed (edge-screw) dislocation.	Effectively continuously circular in the habit plane (i.e. continuously changing). Some evidence of hexagonal shape with segments parallel to $\{110\}_\alpha$ directions.

5.2 Precipitation of θ' -Phase at Dislocation Loops

The presence of θ' phase was identified from SAED patterns in microstructures of Al-1.1Cu-0.2Mg and Al-1.1Cu-0.5Mg aged to maximum hardness. The precipitate forms as plates parallel to $(001)_{\alpha}$ [202], and this was confirmed in the present work. Under the applied processing conditions and in the absence of pre-ageing prior to elevated temperature ageing, the phase nucleates *exclusively* at dislocation loops in the alloy Al-1.1Cu-0.5Mg. At this low Mg content, only loops parallel to $\{110\}_{\alpha}$ form. Since loops parallel to $\{111\}_{\alpha}$ do not form in alloy compositions expected to contain the Cu-rich θ' phase at the ageing temperature of 150°C, the possibilities of θ' nucleation at $\{111\}_{\alpha}$ loops is not considered. Figure 5.13(a) displays the precipitation of second-phase material at a dislocation loop. The dislocation loop is deduced to lie in $(110)_{\alpha}$, as revealed by the collective arrangement of precipitates in this plane. Figure 5.13(b) displays the same precipitate arrangement rotated by $\sim 35^{\circ}$ from the position in figure 5.13(a) and about the axis indicated. Precipitates of the θ' phase formed at all parts of the loop, although the particles that form at the end of the loops (θ'_1 , θ'_2 and θ'_4 in fig. 5.13) are invariably the largest plates of θ' in a single colony. The increased size may be due to less competition for solute atoms at the end of the loops, rather than nearer the middle of the loop where there are several θ' plates each requiring long-range diffusion to sustain growth.

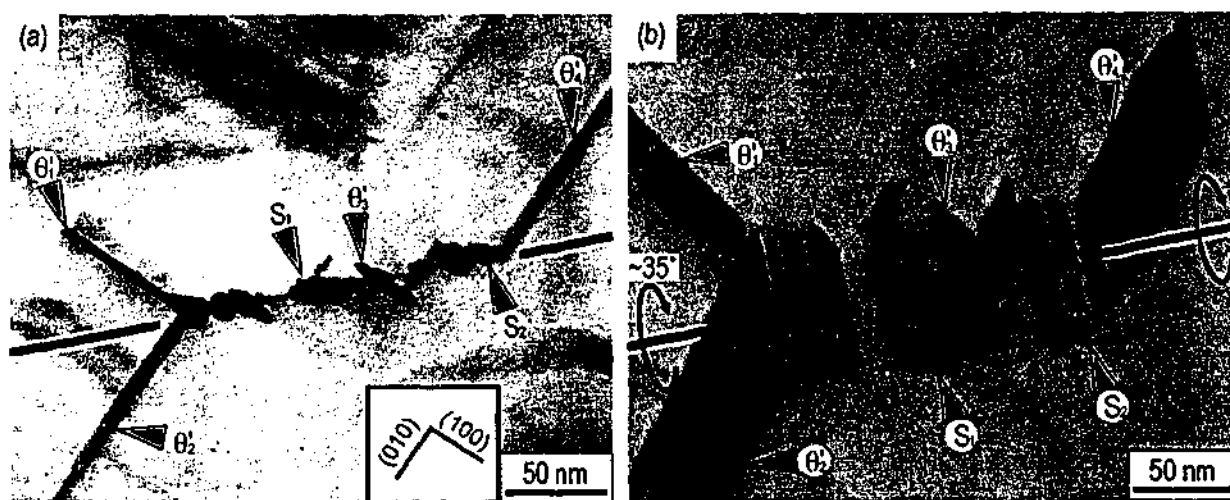


Figure 5.13 (a) θ' precipitates (and S-phase) arranged at a dislocation loop in Al-1.1Cu-0.5Mg (10 d at 150°C). (b) $\sim 35^{\circ}$ rotation about the indicated axis reveals the plate-like nature of the θ' precipitates.

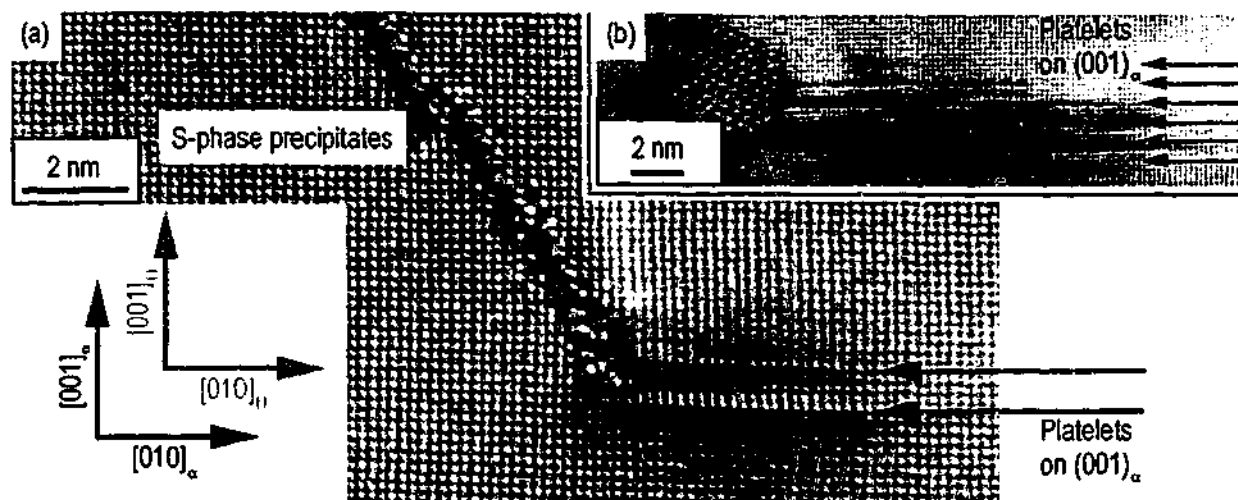


Figure 5.14 Al-1.1Cu-0.5Mg aged 3 d at 150°C, displaying (a) two and (b) six platelets of second-phase material at the end of a $\{110\}_\alpha$ dislocation loop. The θ' phase is later observed to form at these locations.

The HREM image of figure 5.14 contains evidence of platelets of second-phase material at the ends of the loops following 3 d elevated temperature ageing. The θ' phase is later observed to form at these precise locations. It is therefore assumed that the θ' phase is formed via the evolution of a precursor phase consistent in appearance with the θ'' phase (Al_3Cu) that forms as platelets of Cu on every fourth $\{002\}_\alpha$ layer [189]. The artificial ageing temperature of 150°C is therefore below the θ'' solvus for the alloy Al-1.1Cu-0.5Mg. Hence at this ageing temperature and composition, investigation of the direct nucleation of θ' at dislocations is not possible. However, since the presence of the strengthening θ' -phase is important, nucleation of the θ'' -phase is also important. Nucleation of θ'' upon a single dislocation loop lying in $\{110\}_\alpha$ results in the selection of only two of the three possible $\{002\}_\alpha$ habit planes, and this is schematically represented in figure 5.15.

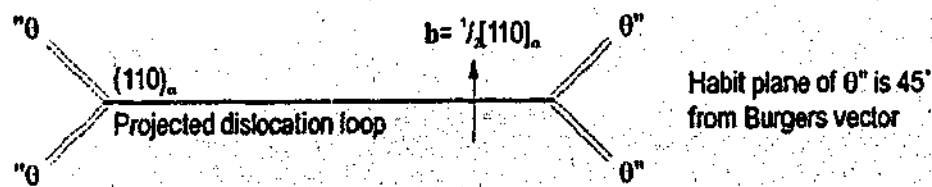


Figure 5.15 Two variants of θ'' form at the ends of projected loops lying in $\{110\}_\alpha$. The habit plane of the selected variants is always 45° from the Burgers vector of the loop.

5.3 Precipitation of Ω -phase at Dislocation Loops

Following pre-ageing of the alloys with high Cu:Mg ratio (Al-1.1Cu-0.2Mg and Al-1.1Cu-0.5Mg), the precipitate Ω -phase appears to nucleate in the vicinity of the dislocation loops. However, despite extensive efforts, the phase was never observed to form at the defect loops prior to the nucleation and significant growth of θ' and S-phase. Accordingly, the direct nucleation of the phase upon dislocations was never observed. As reference to figure 5.16 suggests, precipitate plates consistent in appearance with the Ω -phase appear in association with precipitates of the S-phase. The plates of Ω -phase may have nucleated upon S-phase, or impinged upon it as growth occurred. The complex arrangement of precipitates prevented detailed characterisation of the nucleation event, and no evidence was found for direct nucleation of the phase on either the dislocation or other precipitates.

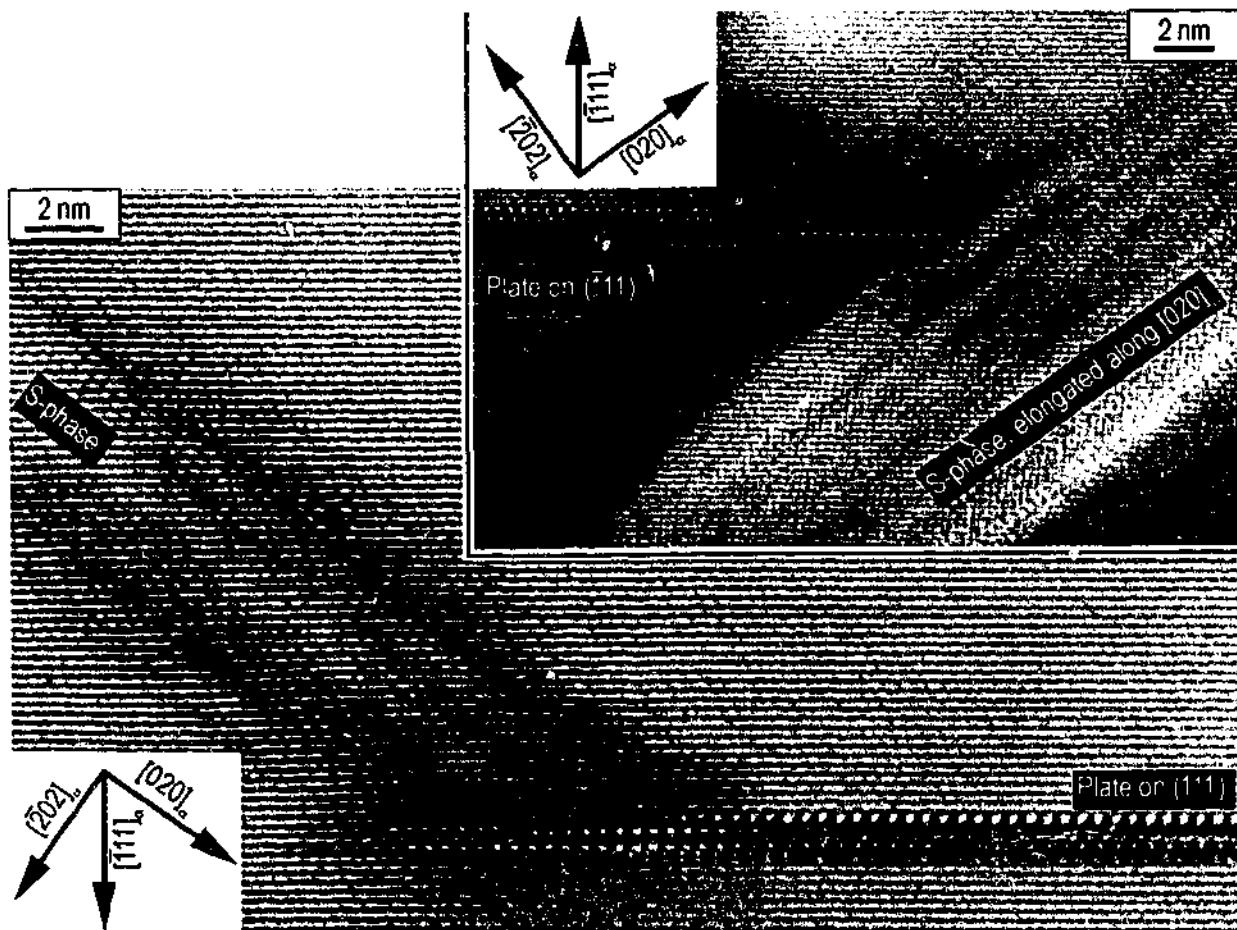


Figure 5.16 Two examples of the association of plates of the Ω -phase with precipitates of the S-phase (alloy Al-1.1Cu-0.5Mg, aged 10 d at 150°C).

5.4 Precipitation of S-phase at Dislocation Loops

In §4.2 and §4.3, electron diffraction evidence was provided for the presence of the S-phase in microstructures aged to maximum hardness in all four core-group alloys examined in the present work. Conventional TEM revealed that the precipitates occurred in localised concentrations clearly related to the position of former dislocation loops formed during early ageing, and examples of nucleation upon loops lying in both $\{110\}_\alpha$ and $\{111\}_\alpha$ matrix planes were observed. Thus, precipitation of S-phase at dislocations provides a unique opportunity to thoroughly investigate the correlation between the defect character and the precipitate crystallography in its vicinity. In the present chapter, HREM will be used to carefully examine the form of these precipitate colonies, where a colony is defined as a group of precipitates that have nucleated at a discrete dislocation loop.

The accepted axis of precipitate elongation is $[100]_s // [100]_\alpha$ [58,59,61,62,87-89,107,126-151]. Therefore, the cross-sectional area of the particle that presents orthogonal to the electron beam is minimised when examined in this orientation, and provides the most suitable description of precipitate morphology. The depiction of the lath-type precipitate 1 in figure 5.17 is thus suitably arranged for examination, while the lath-shaped precipitate 3 is not. The axis of elongation is also the accepted axis of lattice rotation [75,107,131]. If present, the lattice rotation is apparently

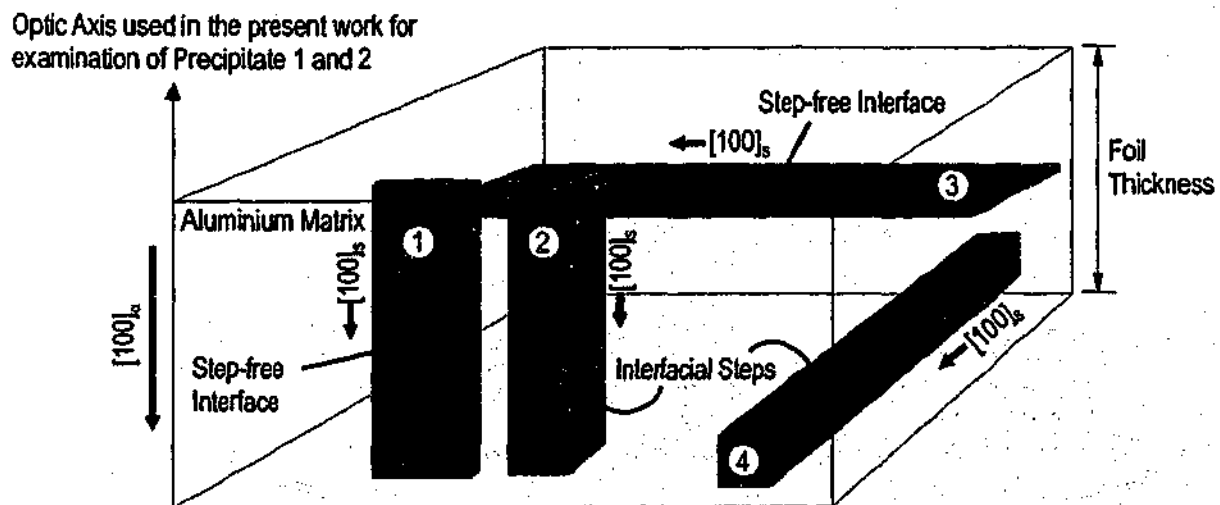


Figure 5.17 Precipitates 1 and 3 – precipitates with broad, step-free interfaces. Precipitates 2 and 4 – precipitates with steps at the interface.

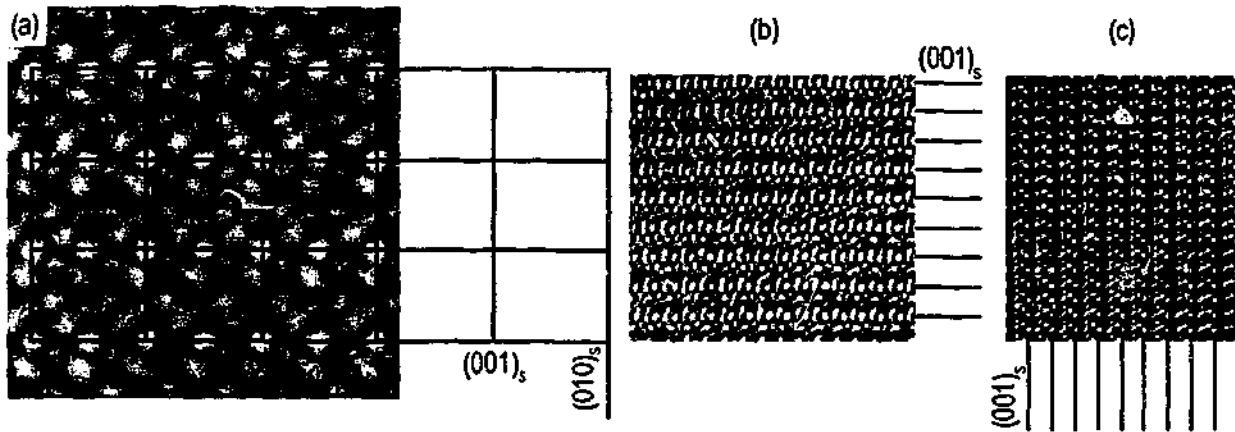


Figure 5.18 (a) Identification of the S-phase unit cell from an atomic resolution HREM image. (b) and (c) Examples of the identification of the $(001)_s$ planes from the image contrast.

accompanied by changes in the particle morphology in $(100)_s // (100)_\alpha$ [107,126], and the likely inclusion of steps and ledges at the interfaces parallel to $[100]_s // [100]_\alpha$ [107,126]. Therefore, the orientation relationship and morphological features of precipitates of the S-phase that are rotated about $[100]_s // [100]_\alpha$ are most suitably examined by orienting the embedded S-phase crystal of interest such that the electron beam is parallel to $[100]_s // [100]_\alpha$. The rotated precipitate 2 is optimally arranged for examination in figure 5.17, while precipitate 4 is not suitably arranged.

In a typical HREM image of the S-phase oriented parallel to $[100]_s$, such as that shown in figure 5.18(a), a rectangle drawn with its corners matched against periodic bright contrast of the image has an aspect ratio of approximately 1.3. This corresponds well with the aspect ratio of the S-phase unit cell in the appropriate orientation, as shown. The $(001)_s$ planes of the S-phase are readily recognisable from HREM images due to the bright spots. There is no assumption required that the contrast in the HREM images presented is a direct projection of the actual atomic positions in the volume of S-phase. Figures 5.18(b) and 5.18(c) are examples of the manner in which the $(001)_s$ planes are identified readily in the S-phase. The subsequent presentation of results relies only upon this atomic resolution in the planes of the S-phase for an appreciation of precipitate orientation and morphology. For example, a particle of standard orientation (§2.3.4) using HREM is shown in figure 5.19(a). The superimposed lattice of atoms in both the α -Al matrix and the S-phase are positioned such that they indicate the orientation and size of a unit cell in the respective phases, and clearly indicate that $(001)_s // (0\bar{2}1)_\alpha$. Figure 5.19(b) is a simulated diffraction pattern representing the predicted orientation relationship between matrix and particle in figure 5.19(a). Implicit in this simulated pattern are the accepted lattice

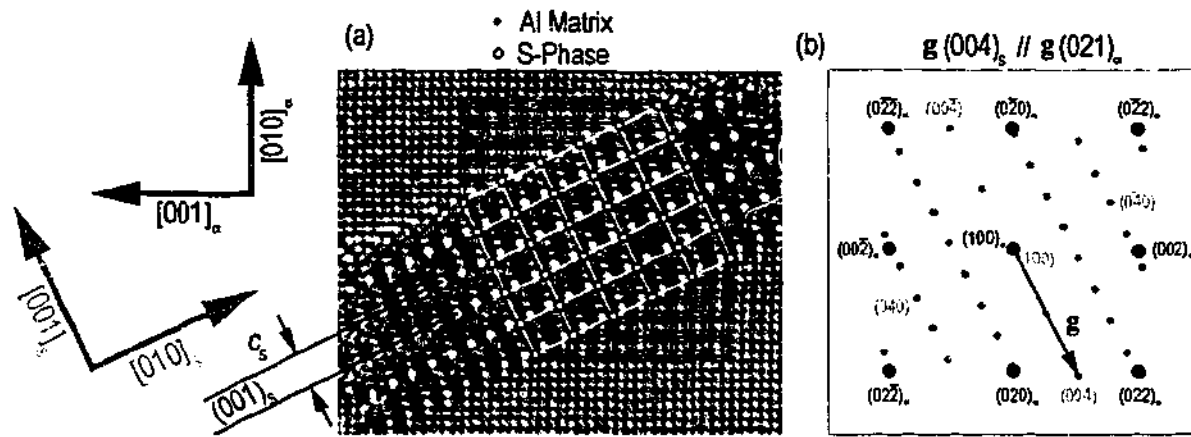


Figure 5.19 (a) Precipitate of the S-phase in standard orientation, including $(001)_s // (0\bar{2}1)_\alpha$. (b) Simulated diffraction pattern of the assumed orientation relationship (alloy Al-0.2Cu-1.7Mg, aged 80 d at 150°C).

spacings and the *three-dimensional* orientation of the orthorhombic unit cell in the fcc matrix phase. For instance, $g(004)_s // g(021)_\alpha$, indicating that the represented planes are parallel.

It will be assumed that the arrangement of precipitates at precipitate colonies, when viewed parallel to $[100]_s // [100]_\alpha$, is an approximation of the original *projected* position of the dislocation segment upon which nucleation first occurred (fig. 5.20). This is a reasonable assumption since (1) the nucleation event is assumed to take place at or near the core of the dislocation and (2) following nucleation, the volume of second-phase material is assumed to remain fixed in position. Characterisation of S-phase precipitates at $\{110\}_\alpha$ loops is examined first, followed by precipitates at $\{111\}_\alpha$ loops and on loops on planes intermediate between $\{110\}_\alpha$ and $\{111\}_\alpha$.

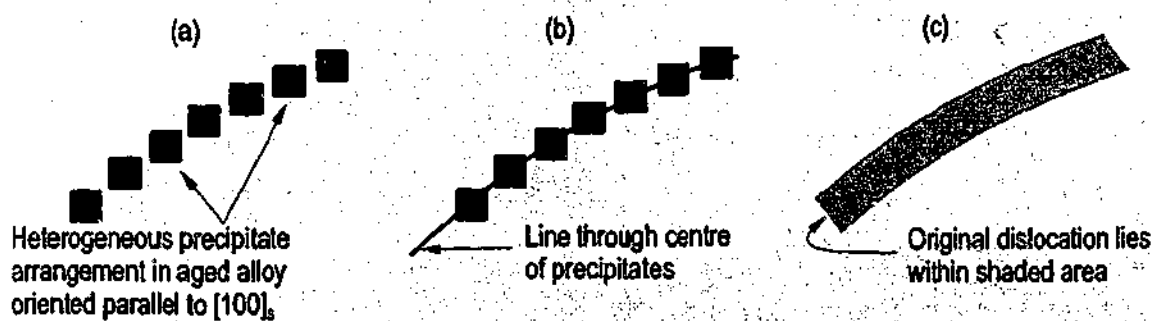


Figure 5.20 (a) Precipitates arranged in a row, suggestive of heterogeneous nucleation at a line defect (b) A line is drawn through the centre of the precipitates. (c) The original dislocation projection previously lay in the shaded region.

5.4.1 Nucleation Upon Dislocation Loops Lying in $\{110\}_\alpha$

S-phase particles in aged microstructures viewed parallel to $[100]_s // [100]_\alpha$ are observed to occur in colonies of numerous individual particles collectively parallel to $\{110\}_\alpha$ planes projected end-on, as shown in figure 5.21. Therefore, it is assumed that the original defect loop (or segment of loop) upon which nucleation and growth of precipitates has proceeded is parallel to the appropriate $\{110\}_\alpha$. Of the two varieties of defect loops found in the present work, only those lying in $\{110\}_\alpha$ planes may be observed as parallel to $\{110\}_\alpha$ in the $\langle 100 \rangle_\alpha$ projection, clear evidence that the linear arrays of precipitates have formed on defect loops lying in $\{110\}_\alpha$.

The microstructure in figure 5.21 (alloy Al-1.1Cu-0.5Mg, aged 10 d at 150°) contains not only the precipitate particles whose elongated axis ($[100]_s$) is parallel to the electron beam direction, but also precipitates of the two alternative growth directions $\pm[010]_\alpha$ and $\pm[001]_\alpha$, as indicated. The length of the S-phase particles along $[100]_s$ growth direction is in the range 100 nm - 200 nm in the alloys examined at the defined heat treatment.

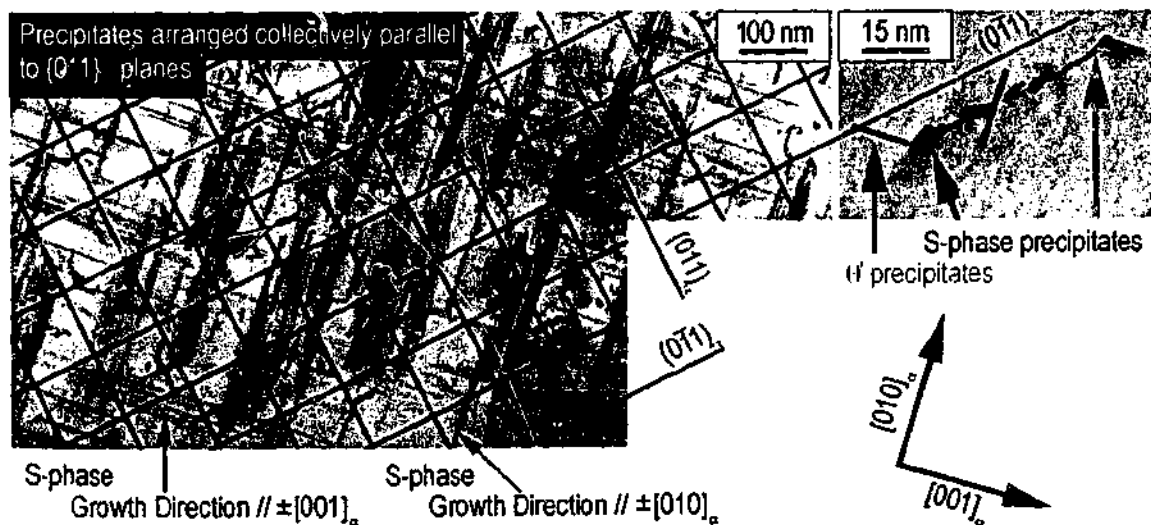


Figure 5.21 When viewed parallel to $[100]_s // [100]_\alpha$, precipitates are linearly arranged in colonies parallel to $\{110\}_\alpha$ at single dislocation loops (arrowed) in Al-1.1Cu-0.5Mg alloy aged 10 d at 150°C.

The precipitates in the HREM image of figure 5.22, found in the microstructure of Al-0.8Cu-1.7Mg aged to maximum hardness (10 d at 150°C), are arranged collectively parallel to $(011)_\alpha$, as indicated. These precipitates are notable for the presence of a planar interface parallel to $(001)_s // \{021\}_\alpha$, as shown. Corroborating evidence leads to the conclusion that the vast majority of precipitates at $\{110\}_\alpha$ loops are lath precipitates of the standard orientation relationship. A colony of S-phase precipitate particles nucleated at a *single* $\{110\}_\alpha$ dislocation loop has the following characteristics, schematically represented in figure 5.23:

- Nucleation of the precipitates occurs at all points on loop, such that individual precipitates abut one another.
- All particles have a *common* growth direction (or lath axis) adhering to $[100]_s // [100]_\alpha$.

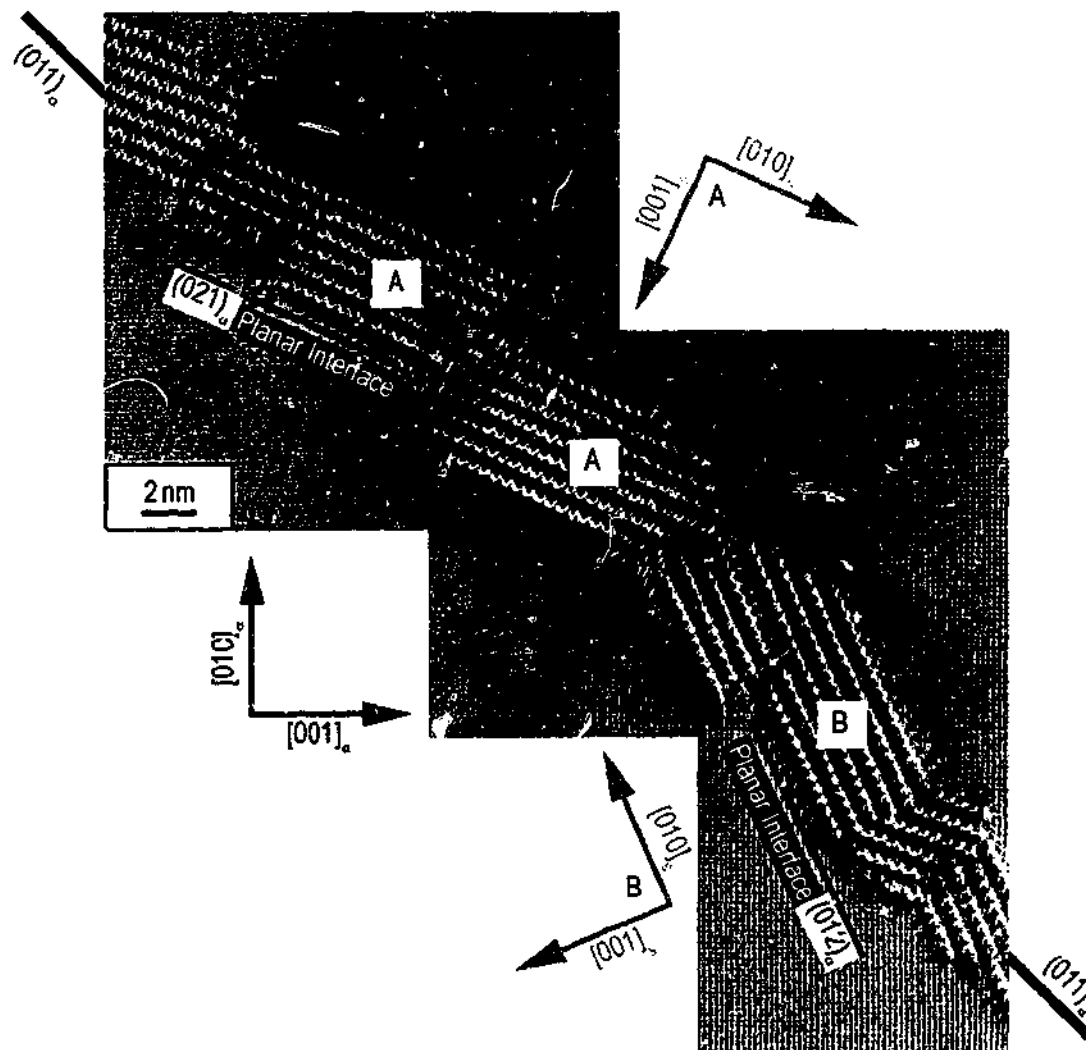


Figure 5.22 A single dislocation loop provides the environment for the nucleation and growth of only two of a possible 12 variants of the S-phase (alloy Al-0.8Cu-1.7Mg, aged 10 d at 150°C).

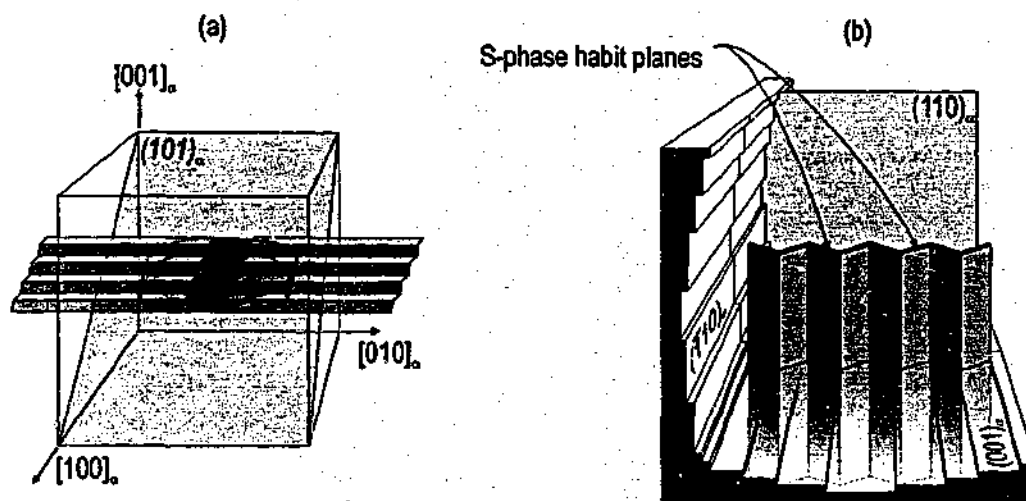


Figure 5.23 Schematic representation of S-phase precipitation on loops lying in $\{011\}_\alpha$.

- The growth direction is consistently in the plane of the loop.
- Of the four variants (for a given growth direction) of $\{210\}_\alpha$ planes that could potentially be parallel to $(001)_s$ (the habit plane of the precipitate in standard orientation), the unit cell of the S-phase is aligned such that the c -plane is parallel to two variants only.
- The two variants to form are those where the $[010]_s$ direction is parallel to the $\{210\}_\alpha$ planes that are 18.44° from the habit plane of the loop.

The extreme end portion of a colony of precipitates at a $\{110\}_\alpha$ loop in alloy Al-0.2Cu-1.7Mg (aged 80 d at 150°C) is shown in figure 5.24. Precipitates A_1 through A_3 are approximately lath-type precipitates, and the characteristic particle-matrix interfaces parallel to $(001)_s // (0\bar{1}2)_\alpha$ are indicated. Since two variants of the S-phase per single $\{110\}_\alpha$ dislocation loop may form it is expected that precipitate B is oriented such that $(001)_s // (0\bar{2}1)_\alpha$, and the superimposed $(001)_s$ and $(0\bar{2}1)_\alpha$ planes are labelled in figure 5.24. Is it clear, however, that $(001)_s$ and $(0\bar{2}1)_\alpha$ are not parallel, and precipitate B is rotated about $[100]_s // [100]_\alpha$ from the standard orientation relationship expected. This is typical of S-phase precipitates that form at the end of a colony of particles at individual $\{110\}_\alpha$ dislocation loops.

Note that the rotation of precipitate B is always a departure from one of the two standard orientation relationships described to form on a single dislocation loop. Thus, the introduction of precipitate rotation does not imply the selection of a new $\{210\}_\alpha$ plane to which the $(001)_s$

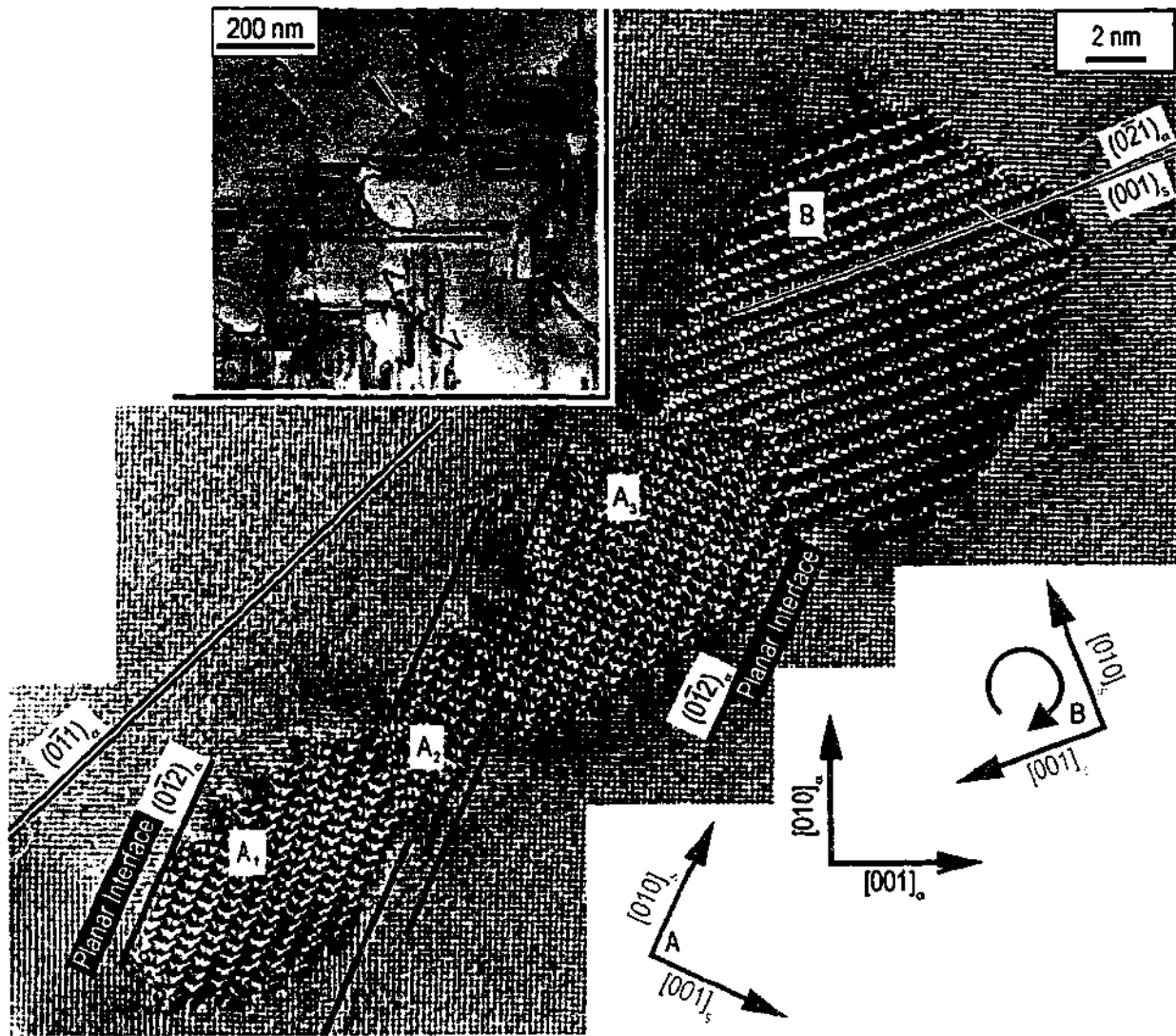


Figure 5.24 S-phase precipitation on a loop lying in $(0\bar{1}1)_\alpha$. Note the rod-like precipitate at the end of the loop (main picture), and its corresponding appearance at lower magnification (inset) (alloy Al-0.2Cu-1.7Mg, aged 80 d at 150°C).

approximates itself, but rather a slight modification of one of the expected orientations. Rotated particles at the extreme end of projected $\{110\}_\alpha$ loops were not recorded in either Al-1.1Cu-0.2Mg or Al-1.1Cu-0.5Mg alloys. This is presumably due to the thermodynamically favourable formation of θ' at these locations, as previously reported in §5.2.

Rotated particles at the end of a row of precipitates arranged at $\{110\}_\alpha$ loops in Al-0.2Cu-1.7Mg and Al-0.8Cu-1.7Mg are characterised by a particle-matrix interface that is composed exclusively of steps. Figure 5.25(a) displays the interface of precipitate B and compares it directly with the form of the interface exhibited by the Type II precipitates of Radmilovic *et al.* [107] (fig. 5.25(b)), where the c -parameter of the unit cell is indicated and the $2c_s$ step height identified by Radmilovic *et al.* [107] is clear. Figure 5.25(c) superimposes an interface profile comprising $2c_s$

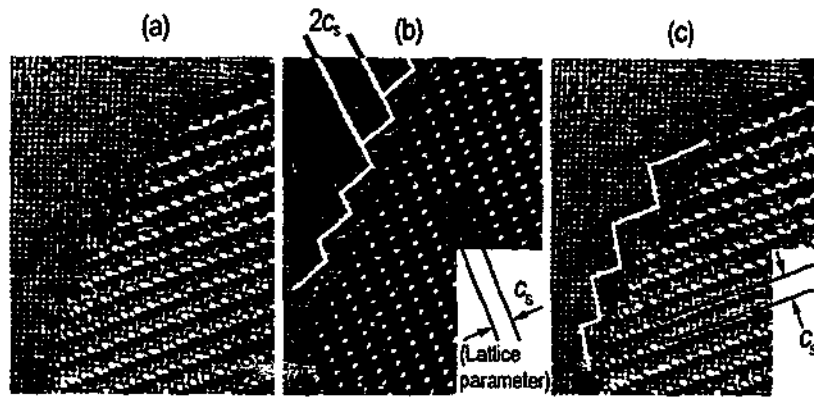


Figure 5.25 (a) The particle-matrix interface displayed by precipitate B in figure 5.27. (b) An interface described by $2c_s$ steps at the interface (after [50]). (c) An interface profile containing $2c_s$ steps at the interface, superimposed upon (a).

step height ledges upon the interface presented in figure 5.25(a). It is clear that the interfacial step height is dissimilar and the steps are smaller than $2c_s$. Particles characterised by a distinct rotation about $[100]_s // [100]_a$, yet not displaying steps $2c_s$ in height, are too complex to be characterised using the Type I/Type II nomenclature applied in the literature.

The differences in the nature of the interface will not be discussed in the present chapter. However, they will form an integral component of the differentiation in precipitate morphology as part of the following chapter. Nevertheless, the differences are briefly introduced to indicate that particles significantly rotated away from the standard orientation relationship about $[100]_s // [100]_a$ are not necessarily characterised by a broad interface composed of $2c_s$ ledges.

5.4.2 Nucleation Upon Dislocation Loops Lying in $\{111\}_a$

Using both conventional and high-resolution electron microscopy, nucleation and growth of precipitates upon dislocation loops lying in $\{111\}_a$ was not detected while a stacking fault was present in the plane of the $\{111\}_a$ loop. This may be because precipitates were not detected until at least 17 hrs ageing at 150°C , before which all stacking faults had been removed.

Observation parallel to the $(100)_a$ axis of specimens of Al-0.2Cu-1.7Mg and Al-0.8Cu-1.7Mg alloys identified precipitate colonies in the shape of an ellipse, as shown in figure 5.26 (alloy Al-0.2Cu-1.7Mg aged 120 d at 150°C). The ellipse is similar in size and aspect ratio to the inclined dislocation loops lying in $\{111\}_a$ planes discussed previously (see fig. 4.8). This observation

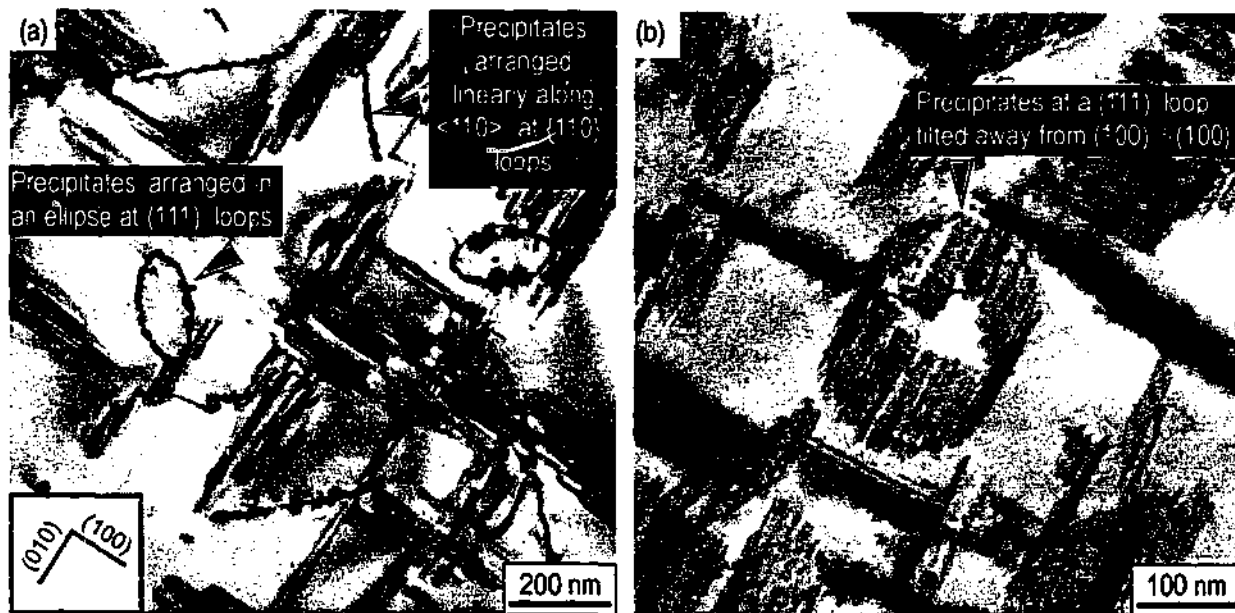


Figure 5.26 (a) S-phase at $\{111\}_\alpha$ loops, arranged as an ellipse (arrowed) when observed parallel to the growth direction. (b) A typical ellipse (arrowed) rotated by a large tilt angle away from the growth direction, showing the elongated shape of the precipitates. (Alloy Al-0.2Cu-1.7Mg aged 120 d at 150°C).

provides ready identification of nucleation upon $\{111\}_\alpha$ loops, whereas a string or straight line of precipitates collectively parallel to $\{110\}_\alpha$ is indicative of precipitation upon $\{110\}_\alpha$ loops (see §5.4.1). Nucleation of the precipitates occurs at all points on the perimeter of the ellipse, such that individual precipitates abut one another. All precipitates nucleating and growing at a single $\{111\}_\alpha$ loop have a common elongation axis ($[100]_s // [100]_\alpha$).

Figure 5.27 is a HREM image of a fraction of a colony of precipitates that have formed at a $\{111\}_\alpha$ dislocation loop, as indicated in the inset, in alloy Al-0.2Cu-1.7Mg aged 120 d at 150°C. Precipitates 1 and 9 display broad and step-free interfaces parallel to the respective $(001)_s$ precipitate plane (white lines in figure 5.27). Superimposed upon precipitates 1 and 9 are the $\{021\}_\alpha$ planes (black lines) that are closest in orientation to the respective $(001)_s$ precipitate planes. In precipitates 1 and 9, the broad and step-free interface is also parallel to $\{021\}_\alpha$. Hence, both the lattice orientation and the morphology of precipitates 1 and 9 indicate that they are precipitate laths of the standard orientation. Precipitates 2 through 8 are described by a $(001)_s$ plane orientation that is, on visual inspection of the micrographs, close but not precisely parallel to that of the $\{021\}_\alpha$ planes that define the broad interfaces of precipitates 1 and 9.

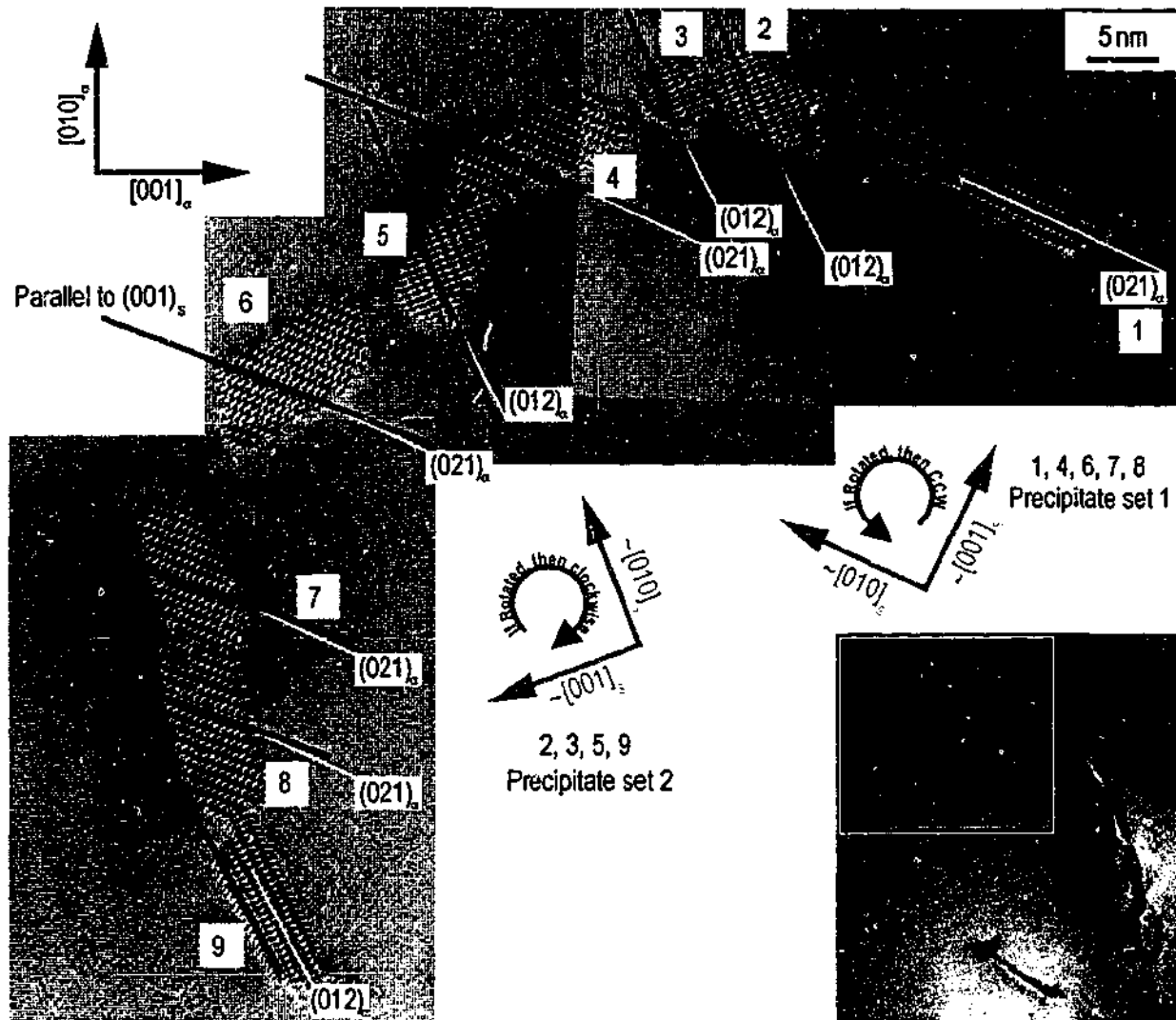


Figure 5.27 S-phase at a single $\{111\}_\alpha$ dislocation loop (inset). Precipitate morphology changes for particles located at different segments of the loop (alloy Al-0.2Cu-1.7Mg aged 120 d at 150°C).

Up to several degrees, the precise magnitude of which will not be discussed at this point, precipitates 2 through 8 are rotated slightly from a variant of the standard orientation relationship. Precipitates 1, 4, 6, 7, and 8 can be selected according to an approximately equivalent $(001)_s : \{021\}_\alpha$ orientation, and collectively the group of precipitates is termed a *set* (precipitate set 1). Similarly, precipitates 2, 3, 5, and 9 (precipitate set 2) are grouped together. Furthermore, these precipitates do not have broad interfaces parallel to their respective $(001)_s$ plane. Therefore, the lattice orientation and morphology of precipitates 2 through 8 indicate that they are *not* laths of standard orientation.

Precipitate set 1 in figure 5.27 rotate clockwise in the viewing direction selected, while precipitate set 2 rotate counter-clockwise. Therefore, the lattice rotation about $[100]_s // [100]_\alpha$ from the standard orientation relationship is *sense-consistent* for a given *set* of S-phase precipitates.

The extent to which these precipitates rotate and the changes in precipitate morphology and precipitate/matrix interface characteristics will be discussed extensively in chapter 6.

Precipitates nucleated at loops in $\{111\}_\alpha$ are arranged such that the particles characterised by a lattice rotation are adjacent to one another, suggesting that *either* particles of standard orientation *or* particles rotated from the standard orientation relationship and about the growth axis nucleate and grow at designated positions on the dislocation loop. Numerous dislocation loops lying in $\{111\}_\alpha$ have been segmented into equal 16ths and the presence or absence of a lattice rotation away from the standard orientation relationship has been recorded as a function of the segment in which the precipitate is found. Loops lying in $\{111\}_\alpha$ are inclined to an electron beam parallel to $[100]_s // [100]_\alpha$ by an angle of $\cos^{-1}(1/\sqrt{3})$. Inclination of the loops causes a distortion to the angular boundaries described, and necessitates re-calculation of the angles defining each of the four segments in each quarter of the loop. It can be shown geometrically that:

$$\alpha = \tan^{-1} \left(\tan \theta \left(\frac{1}{\sqrt{3}} \right) \right) \quad \text{where:} \quad \alpha = \text{projected angle in } \langle 001 \rangle_\alpha, \theta = \text{actual angle in } \langle 111 \rangle_\alpha.$$

The distribution of precipitate orientation (either rotated away from, or in, the standard orientation relationship) is represented in figure 5.28 as a function of position. Rotated particles form at loop segments that are opposite the minor axis of the projected ellipse (segments 1 and

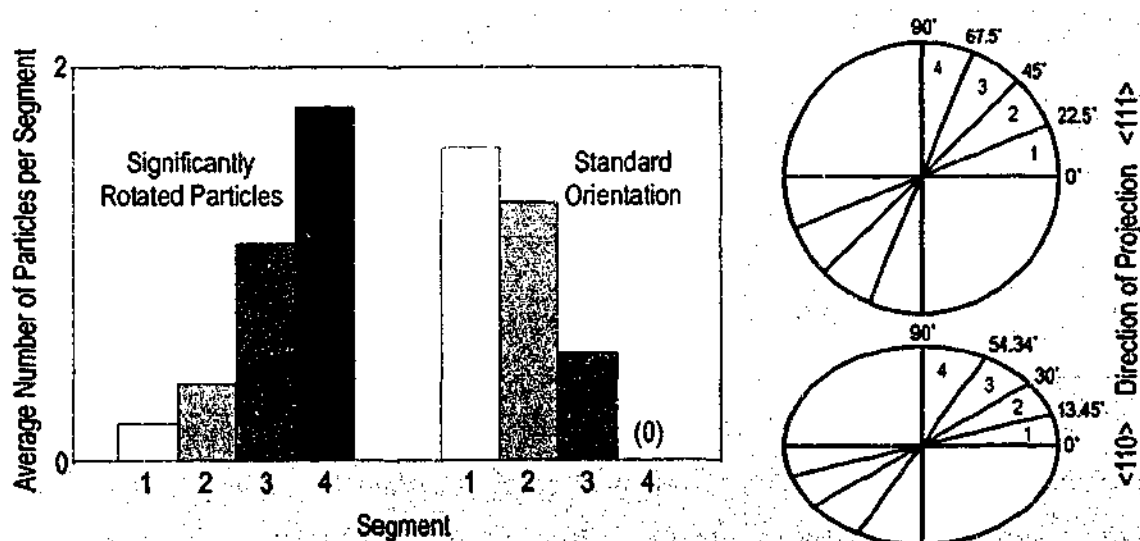


Figure 5.28 Distribution of lattice rotation at $\{111\}_\alpha$ dislocation loops. Precipitates are defined as either adhering to or rotated away from the standard orientation relationship.

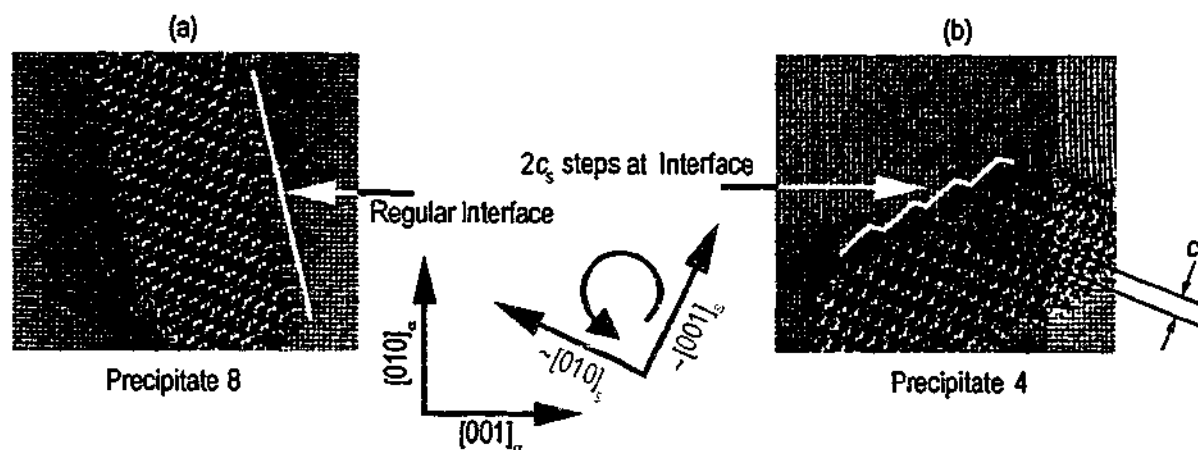


Figure 5.29 (a) The 'regular' interface of precipitate 8 and (b) $2c_s$ steps at the interface of precipitate 4.

2), while non-rotated particles form at the segments opposite the major axis (segments 3 and 4), suggesting that the differentiation in orientation relationship is strongly dependent upon precipitate location. Although all S-phase precipitates 2 through 8 exhibit a lattice rotation about $[100]_s // [100]_a$ and away from the standard orientation relationship, the nature of the particle-matrix interface is varied. For example, precipitate 4 has obvious steps at the broad particle-matrix interface while others, such as precipitate 8, do not have such obvious interfacial steps, figure 5.29. Precipitate 8 can not be classified using the Type I/Type II nomenclature. Precipitate 4 contains steps that are $2c_s$ in height and is likely to be an exponent of Type II morphology as described by Radmilovic *et al.* [107].

It is clear from numerous examples, including figure 5.27, that the growth of individual S-phase particles in the $(100)_s // (100)_a$ plane are arranged such that the broad habit plane is parallel to the projection of the dislocation line. This is observed both for particles of the standard orientation relationship and particles rotated from this condition, and is clearly demonstrated in figure 5.30, a silhouette image of figure 5.27.

The high-resolution image of figure 5.31(a) displays a ring of precipitates at a $\{111\}_a$ loop, and an assortment of precipitate morphology is represented. The colony of precipitates displayed appears discontinuous, clearly devoid of precipitates at finite loop segments as indicated. This is in contrast to the evidence presented in figure 5.26, §4.2.3 and §4.3.4, all which indicate that continuous precipitation around the perimeter of the ellipse is the general observation. If portions of the ellipse are devoid of precipitates in the examined volume, they are generally those that are approximately parallel to the major axis of the projected ellipse, and this appears regularly under

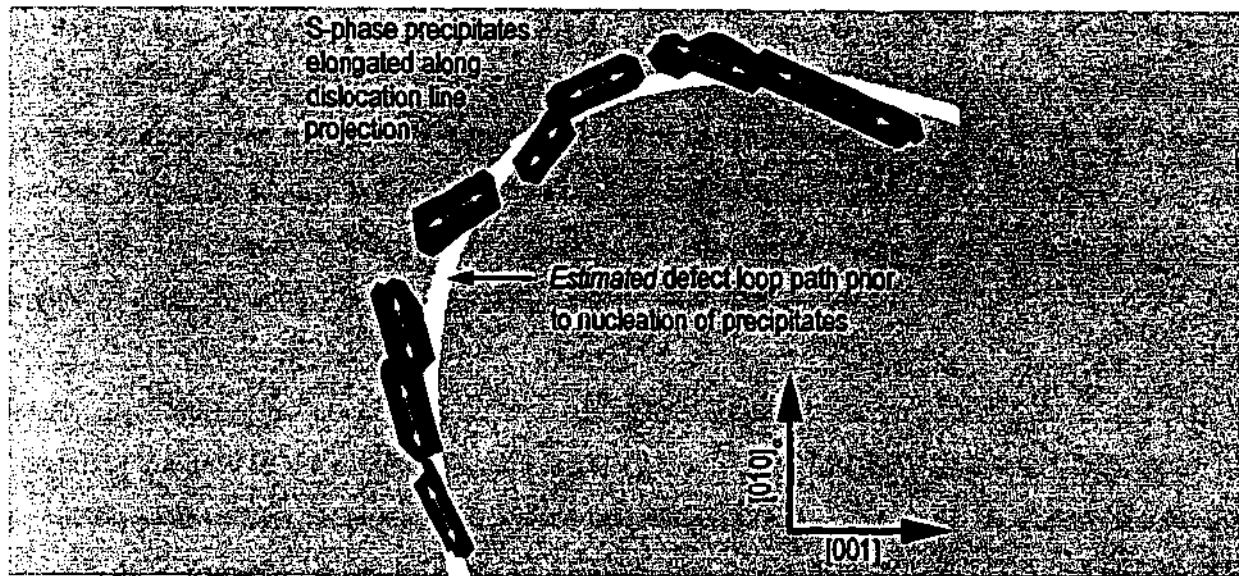


Figure 5.30 Silhouette of the precipitates at a $\{111\}_\alpha$ loop previously referred to in figure 5.27.

high-resolution conditions. Effective HREM relies upon the examination of thin volumes of material. Shorter precipitates may be truncated along the $[100]_s$ axis during specimen preparation (fig. 5.31(b)). Those precipitates truncated are clearly those in the standard orientation relationship, indicating that precipitates in this orientation are generally shorter.

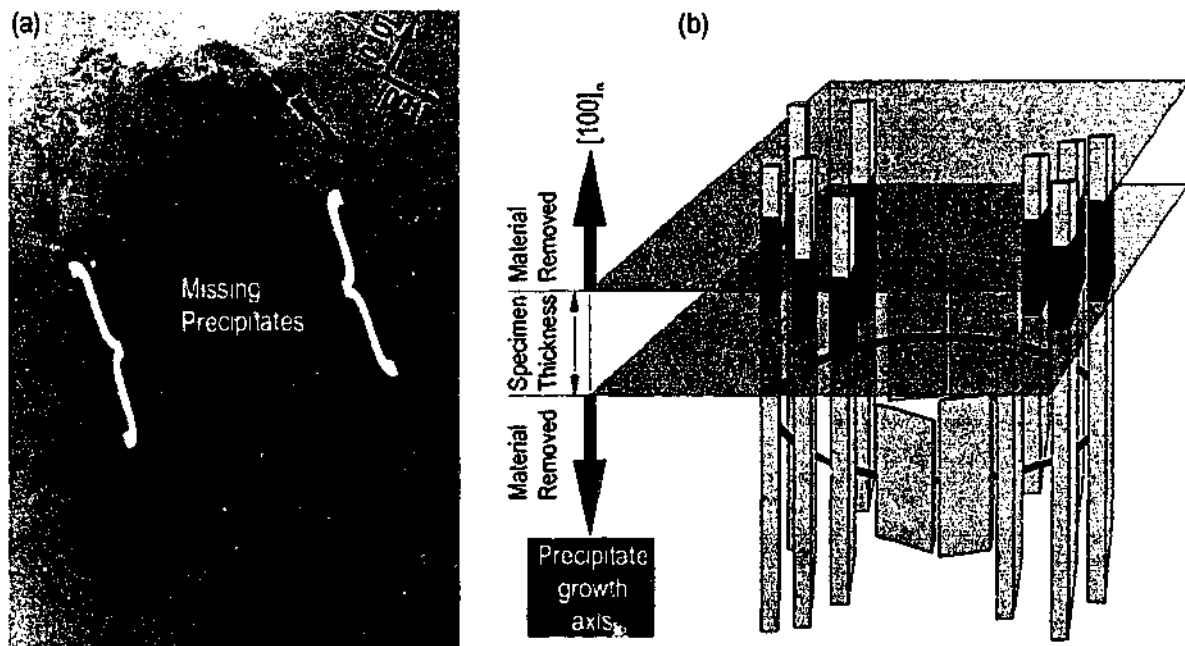


Figure 5.31 (a) A HREM image of precipitates arranged at a $\{111\}_\alpha$ dislocation loop in Al-0.2Cu-1.7Mg aged 20 d at 150°C. (b) A rationalisation of the observed microstructure.

The factors that lead to a change in the length of particles may include longer incubation times for nucleation of precipitates in the standard orientation. A delay in nucleation of the phase may mean that growth of the particle begins well after the inception of growth in the rod-shaped particles. Additive to this is the likelihood that the ambient supersaturation of alloying elements will be less for those precipitates that nucleate later, which may impede the growth of particles that are reliant upon long-range solute diffusion for continued growth.

Finally, it could be speculated that differences in the lattice parameter ratio of the S and matrix phases, particularly in the direction parallel to the growth direction, may lead to differences in the lengthening rates of the particles. If the good matching of $(100)_s$ and $(100)_\alpha$ is disturbed slightly, and the generation of lattice strain and/or misfit dislocations ensues, this may inhibit growth rates. This effect can occur in conjunction with possible differences in the incubation times, as described above.

5.4.3 Nucleation on Loops Intermediate between $\{111\}_\alpha$ and $\{011\}_\alpha$

It is relevant to recall the small percentage of $\{111\}_\alpha$ dislocation loops that significantly re-orient following removal of the stacking fault and prior to the onset of ageing, such that their habit plane lies intermediate between the original $\{111\}_\alpha$ and the $\{011\}_\alpha$ plane that is perpendicular to its Burgers vector. An example of S-phase precipitates upon such a loop in Al-0.8Cu-1.7Mg aged 10 d at 150°C is shown in figure 5.32. The predicted original projection of the dislocation loop parallel to $\{111\}_\alpha$ is shown. The precipitate arrangement suggests formation upon a dislocation loop that is partially reoriented to the $(0\bar{1}1)_\alpha$ plane in figure 5.32. The habit plane of all precipitates is parallel to $(001)_s$ and planes of the type $\{021\}_\alpha$. Hence, S-phase precipitation upon these loops is almost all purely laths in the standard orientation. There were very few particles of the S-phase that were not of the standard orientation at loops such as these.

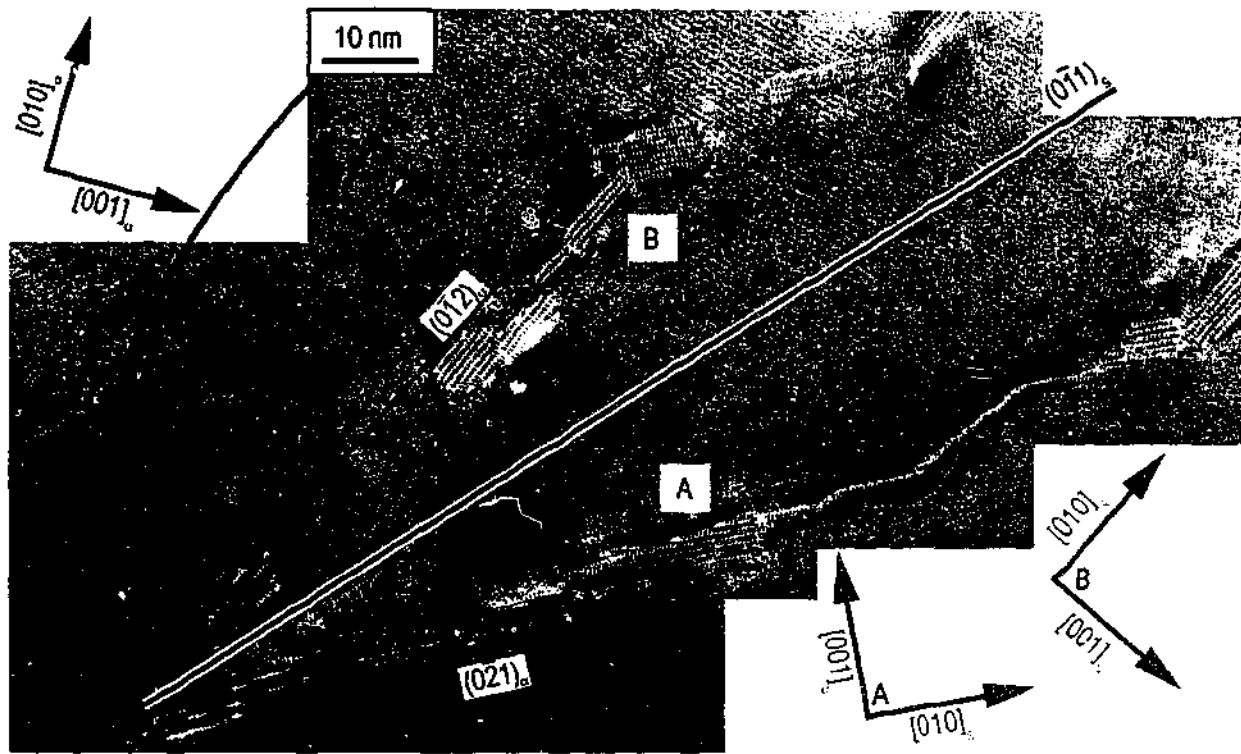


Figure 5.32 Precipitates of standard orientation on a loop intermediate between $\{111\}_{\alpha}$ and $\{110\}_{\alpha}$ (alloy Al-0.8Cu-1.7Mg aged 10 d at 150°C)..

5.5 Interpretation of Results

The dislocation loop and precipitate crystallography have been described separately thus far. It is intended here to examine the *relationship* between the crystallography of precipitates in aluminium-rich Al-Cu-Mg alloys and the characteristics of the strain field at the line defect where nucleation proceeds. The three precipitate species observed to nucleate at dislocations under the experimental conditions applied, θ' (θ''), Ω and S, will be discussed. It is of interest to examine only those cases where the involvement of the dislocation strain field is unambiguously implicated in the nucleation event.

The two experimentally derived rules for precipitate selection at dislocations (§2.2.2) are as follows: (1) The principal misfit vector of the precipitate must not be perpendicular to the edge Burgers vector of the dislocation, and (2) the habit plane of the precipitate must lie approximately parallel to the dislocation. These will be investigated for the present observations where possible.

θ' (θ'') Formation of the θ'' phase preceded that of the θ' phase in alloy Al-1.1Cu-0.5Mg, and nucleation was observed to occur adjacent to dislocations loops lying in $\{110\}_\alpha$. A significant lattice misfit vector (representing a contraction of 4.95%) parallel to $[001]_\beta // [001]_\alpha$ characterises the formation of the θ'' structure (§2.3.1), and is oriented 45° from the Burgers vector, $\mathbf{b} = \frac{1}{2}\langle 110 \rangle_\alpha$, of the dislocation. The volume of matrix material prior to transformation to θ'' is in compression outside of the loop [32], and the formation of the phase at these positions is considered rational. As depicted schematically in figure 5.33, only two of the three variants of θ'' are formed at the projected dislocation loop, since there is no long range compressive strain field for one of the variants. In all cases, the dislocation lay in the habit plane of the precipitate.

In addition to formation at the dislocation loops, the θ'' -phase can be formed at positions away from dislocations following prescribed heat treatment regimes. Figure 5.34 displays the microstructure of alloy Al-1.1Cu-0.2Mg that has been solution treated (525°C), air-cooled (20°C), and artificially aged (150°) for 17 h. In agreement with the observations of precipitation in binary Al-Cu alloys by Nicholson *et al.* [113,114] and many other workers, the θ'' -phase is generally observed to form away from dislocations.

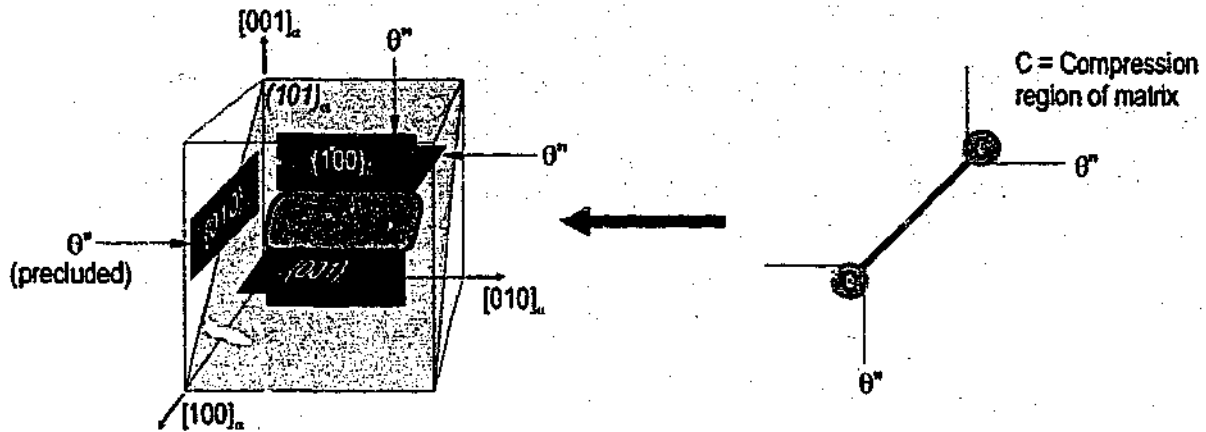


Figure 5.33 Nucleation of the θ'' -phase in the compressed volume of matrix material adjacent to the pure edge dislocation loop in $\{110\}_\alpha$.

The observation that nucleation of θ'' precipitates at loops is dominant and occurs in preference to nucleation away from the dislocations in Al-1.1Cu-0.5Mg under the applied heat treatments in this work may be a consequence of the high density of dislocation loops formed. The high concentration of line defect in these alloys may provide sufficient sites for the θ'' phase as the alloy decomposes. Alternatively, the dislocation loops may provide an environment that is comparatively rich in Cu via the migration of vacancy-solute complexes to vacancy sinks during

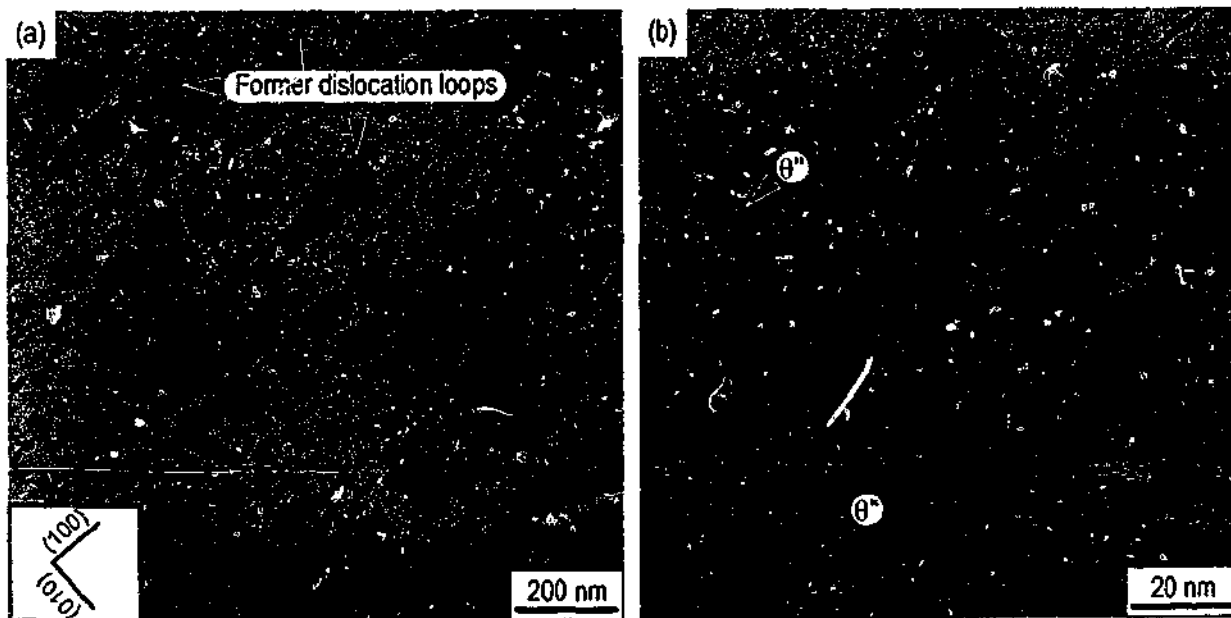


Figure 5.34 Alloy Al-1.1Cu-0.2Mg processed according to the following regime: solution treatment (525°), air cool (20°C) and artificial ageing at 150°C . (a) Low magnification, showing several dislocation loops. (b) Higher magnification.

early ageing [69]. In any case, it is clear that the θ'' -phase can form both at or away from dislocations, although the former is preferred and will be used if available. The observation that precipitates of θ'' may form in the absence of an obvious dislocation implies that the volume contraction of 4.95% is not an insurmountable barrier to nucleation in the absence of a dislocation strain field.



Despite extensive attempts, there were no examples found of a precipitate of the Ω -phase nucleating directly upon a dislocation. The precipitates may have nucleated as consequence of local chemistry at or near the dislocation loops, favouring the formation of the Cu-rich Ω -phase, although this can not be directly inferred from the present work.



Particles of the S-phase in the standard orientation relationship have been observed in the present work. In addition, a large proportion of particles of the S-phase are rotated about the elongated growth direction of $[100]_s // [100]_a$ by a few degrees from the standard orientation relationship, although the magnitude and direction of this rotation is yet to be quantified in the present work. Detection of lattice rotation in the present work has confirmed the results of others [75,107,131], and recent results in the literature suggest that rotation may be up to $\sim 6^\circ$ about $[100]_s // [100]_a$ [131]. In addition to the distinctive precipitate laths in the standard orientation relationship (with habit plane $(001)_s // (021)_a$), precipitates of the S-phase in alloys Al-0.2Cu-1.7Mg and Al-0.8Cu-1.7Mg form consistently in at least three additional morphologies in the present work. These include particles with large steps $2c_s$ in height, precipitates with smaller steps equivalent in height to $1c_s$, and a lath-type particle with a comparatively smooth habit plane that is not parallel to $(001)_s // (021)_a$. All particles described by these alternative morphologies are oriented consistent with a lattice rotation about the growth axis of $[100]_s // [100]_a$. Apart from the precipitate with steps $2c_s$ at the interface, which is apparently analogous to the Type II precipitates reported by Radmilovic *et al.* [107], the existence of these additional precipitate morphologies is not recorded in the literature.

Apart from the end of the projected loops, lath-shaped precipitates of the standard orientation relationship dominated the precipitate colonies at former loops lying in $\{110\}_a$, and this is represented schematically in figure 5.35(a). The shaded area represents those segments where the lath (with a growth direction perpendicular to $[100]_s // [100]_a$) would form. Particles in the

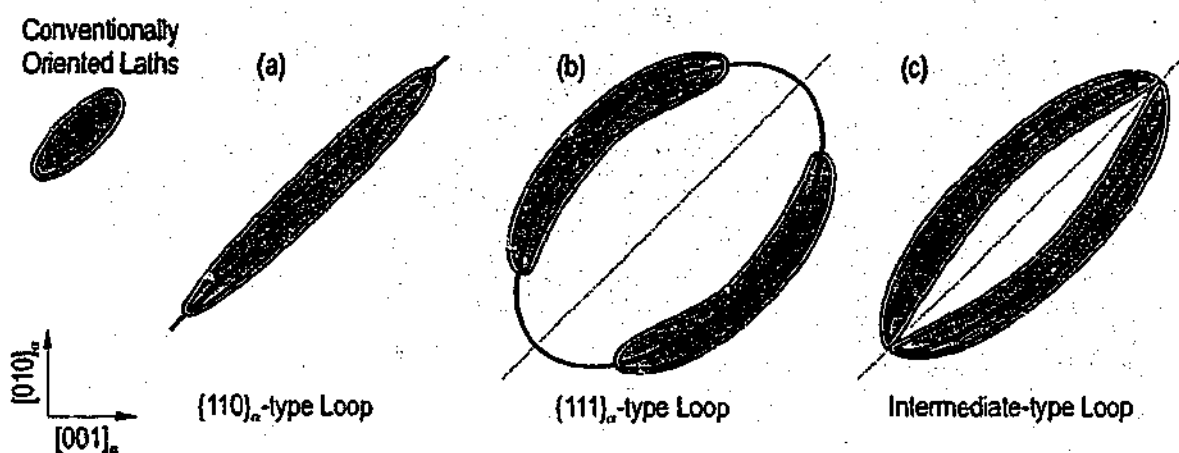


Figure 5.35 Location (shaded area) at which S-phase particles ($[100]_S // [100]_{\alpha}$) of the standard orientation are found on (a) $\{011\}_{\alpha}$, (b) $\{111\}_{\alpha}$ loops, and (c) intermediately-oriented loops.

standard orientation form at loops lying in $\{111\}_{\alpha}$ at dislocation sections that were approximately parallel to the long-axis of the projected dislocation loops. Formation of precipitates of the standard orientation relationship upon loops that are partially reoriented from $\{111\}_{\alpha}$ to $\{110\}_{\alpha}$, figure 5.35(c) confirms that laths prefer projected dislocation directions not significantly removed from $\langle 110 \rangle_{\alpha}$ directions.

The two variants that form at the defect loops are shown schematically in figures 5.36(a) and 5.36(b) for loops lying in both $\{110\}_{\alpha}$ and $\{111\}_{\alpha}$ respectively. The Burgers vector of the $\{111\}_{\alpha}$ dislocation loop in figure 5.36(b) can be determined by observing the crystallography of the precipitates, and retrospectively calculating the Burgers vector based upon the orientation relationship between S-phase particles and the Burgers vector at $\{110\}_{\alpha}$ loops (where \mathbf{b} is *always* perpendicular to the loop plane). In these cases, the two $[010]_S$ directions selected are $\sim 71.6^\circ$ from the Burgers vector. Assuming that the crystallographic relationship between Burgers vector and final precipitate crystallography is maintained for precipitation upon $\{111\}_{\alpha}$ loops (and this seems reasonable considering that we are dealing with the same characteristic Burgers vector and approximate dislocation line direction), the direction of the Burgers vector of the former loop in figure 5.36(b) is $\pm \frac{1}{2} [0\bar{1}1]_{\alpha}$. Figure 5.36(c) displays the two precipitate variants with parallel growth directions (i.e. $[100]_S // [100]_{\alpha}$) that do not form on a dislocation loop with the defined Burgers vector.

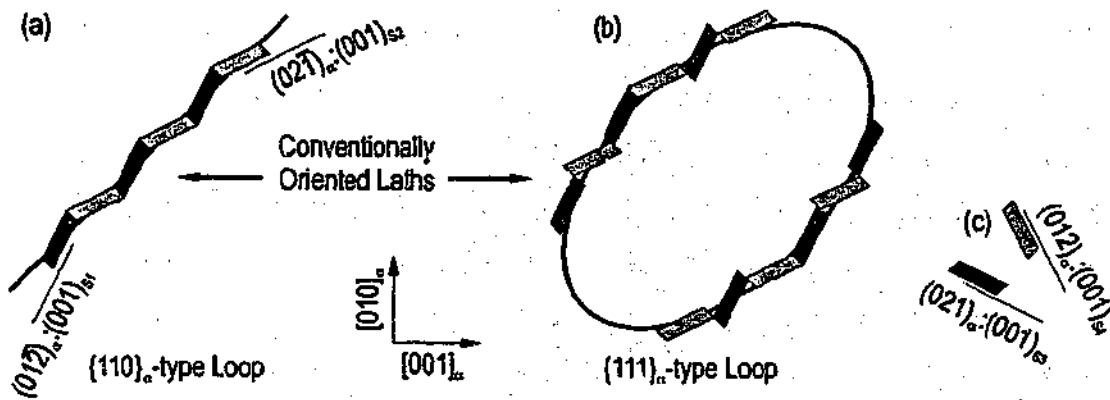


Figure 5.36 Variant selection of precipitate on a (a) $\{110\}_\alpha$ loop and (b) $\{111\}_\alpha$ loop. (c) The variants that do not form on dislocations with the specific Burgers vector described.

Figure 5.37 represents diagrammatically the unique relationship between the burgers vector and the particle of standard orientation relationship. There are a possible six Burgers vectors that describe the strain environment at dislocation loops lying parallel to $\{110\}_\alpha$. Therefore, the full 12 standard variants of S-phase may form through heterogeneous nucleation in microstructures that contain all variants of the $\{110\}_\alpha$ loop defect. Loops lying parallel to the $\{111\}_\alpha$ planes with Burgers vector $\frac{1}{3}\langle 111 \rangle_\alpha$ may give rise to three alternative $\frac{1}{2}\langle 110 \rangle_\alpha$ Burgers vectors, and analysis shows that the full variance of six $\frac{1}{2}\langle 110 \rangle_\alpha$ Burgers vectors can originate from the four $\frac{1}{3}\langle 111 \rangle_\alpha$ Burgers vector (i.e. all $\frac{1}{2}\langle 110 \rangle_\alpha$ vectors are 35.26° from a vector $\frac{1}{3}\langle 111 \rangle_\alpha$). Therefore, all 12 variants of the standard orientation relationship can potentially nucleate in volumes that contain all variants of $\{111\}_\alpha$ loops.

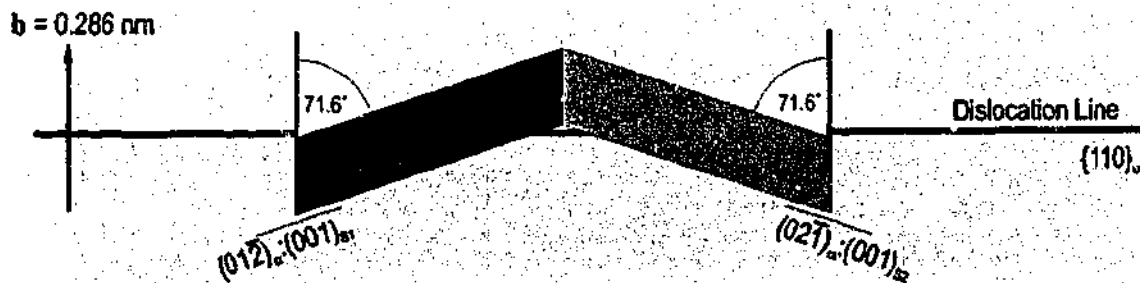


Figure 5.37 (a) Nucleation of two variants of S-phase on a discrete $(011)_\alpha$ dislocation loop.

The elongated nature of the precipitates suggests good atomic matching in this direction, with the absence of a significant misfit vector parallel to $[100]_s // [100]_a$ for the transformation. Calculation of the principal lattice misfit vector perpendicular to $[100]_s // [100]_a$ for these nucleation events is dependent only upon accurate measurement of the lattice parameters. Owing to the wide range of lattice parameters that are proposed to describe precipitates of the S-phase (§2.3.4), calculation of the volume change is subject to significant errors if incorrect data is used. In the following chapter, analysis of lattice parameters is undertaken such that a more accurate appreciation of the volume change may be gained. In general, particles in the standard orientation always lie with the broad habit plane parallel to or nearly parallel to the projection of the dislocation line.

The presence of precipitate particles that display a *lattice rotation* away from the standard orientation relationship and around the elongated $[100]_s // [100]_a$ precipitate axis has been established for particles nucleating at defect loops lying in both $\{110\}_a$ and $\{111\}_a$. In the former case, the relevant particles form at the end of a row of particles that collectively lie in the plane of the $\{110\}_a$ loop. In the latter case, particles exhibiting a lattice rotation are accounted for only at segments of the dislocation loop that are mixed in character. Figure 5.38 summarises these observations. Clearly there exists a relationship between the characteristics of the dislocation line and the morphology of the precipitates that form upon it, although an investigation can proceed only with a greater understanding of the crystallography of precipitates of the S-phase. The relevant literature contains no reference to a site-specificity of S-phase morphology for those particles characterised by a lattice rotation away from the standard orientation relationship, and bears no appreciation for the role that a changing strain field might play in morphology selection.

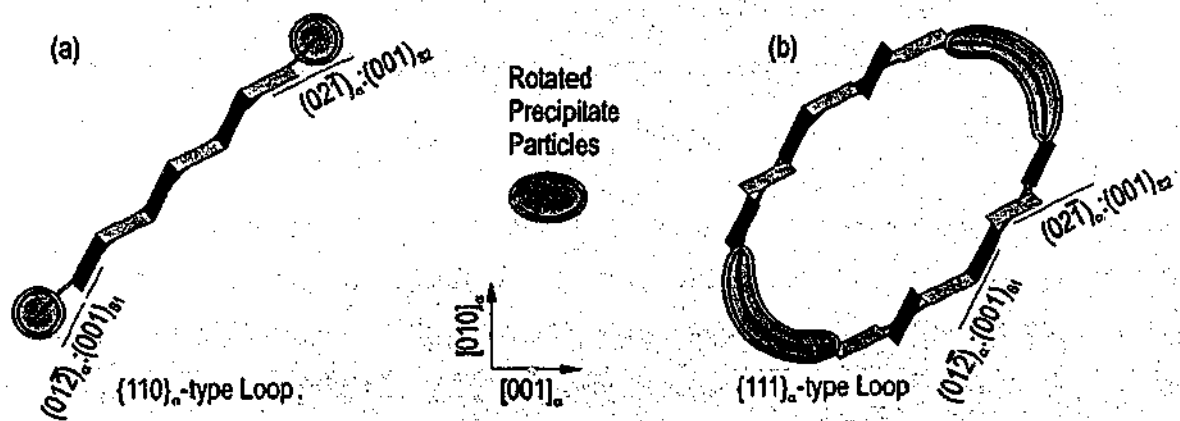


Figure 5.38 Location at which S-phase particles displaying a lattice rotation are found on (a) $\{011\}_a$ and (b) $\{111\}_a$ loops. In the case presented, the rotation of the particles is about the $[100]_s // [100]_a$ axis.

5.6 Chapter Summary and Directions for Present Research

The intention of this chapter was to assess all observations of heterogeneous nucleation at dislocations in the Al-Cu-Mg system with respect to their potential to contribute to the aims of this work. The following summary focuses upon this aspect.

θ' (θ'')

A great deal of research has been applied to the nucleation and growth of θ' owing to the technological importance of plate-shaped precipitates, and the historical significance of Al-Cu binary alloys in which these precipitates are predominant e.g. [105,135,202-206]. Both here and in the wider literature, the θ' phase (via its precursor θ'') is shown to nucleate in the vicinity of edge dislocation line segments, presumably taking advantage of the compressive strain field located there.

Apart from selection of variant, there is no apparent change in the morphology or crystallography of θ'' as a function of the type of dislocation upon which the phase nucleates, nor are there obvious differences between the nature of precipitates nucleated at or away from dislocations. Furthermore, neither the presence of θ'' nor θ' spans the compositional range of the core alloy group investigated in this work, and therefore examples are limited. Considering these points, analysis of θ' phase formation at defects in these alloys will not significantly advance the aims of this research effort, and further investigation will not be undertaken here.

Ω

There is no evidence to suggest that Ω forms directly on line defects, despite its localised presence. Further discussion of its nucleation with respect to the present discussion is irrelevant.

S

Owing to its presence at maximum alloy hardness in all four alloy compositions selected (regardless of the thermal regime applied), the S-phase precipitate is of obvious technological significance. The large variation in S-phase precipitate morphology is neither well characterised nor well understood [107,126,131,132], particularly considering the results of the present chapter, which suggest that there is a greater range of morphology than currently appreciated. The S-phase forms at line defects in these alloys, confirming previous work [88,207,208], and

therefore it is surprising that there has not been a systematic evaluation of the influence of the characteristics of the strain field on local precipitate crystallography. In this chapter, the crystallography and morphology of the precipitate particles is consistently shown to rely upon the characteristics of the line defect upon which the precipitate nucleates. This influence extends from a selection of precipitate growth direction through to the orientation and morphology of the particle. The wide variety of complex crystallography of the S-phase may be regarded as a bonus to an investigation of the relationship between the dislocation and the precipitate, since systematic changes in precipitate crystallography may be correlated with systematic changes in the line defect. If the physical processes leading to the nucleation and growth of either plate-shaped or rod-shaped particles could be understood, the nanostructural design of alloys may be assisted. Therefore, from both a theoretical and technological perspective, further study of S-phase characteristics and stability is considered worthwhile.

However, accurate correlation of these systematic changes relies upon a sound knowledge of the full range of possible S-phase crystallography. The present chapter has demonstrated that the S-phase displays a wider variety of crystallography than is currently appreciated in the literature. To ameliorate this shortcoming, the following chapter (chapter 6) will examine the crystallography of the S-phase precipitate in great detail, particularly with regard to the lattice orientation, the nature of the interface of individual precipitates, and the lattice parameters. With this knowledge, differentiation in precipitate morphology as a function of the line defect upon which nucleation takes place will be revisited in chapter 7.

6.0 Crystallography and Morphology of S-Phase

The presence, at or near crystal defects, of various forms of second-phase precipitate in a range of Al-Cu-Mg alloys under various thermal treatments has been demonstrated in chapters 4 and 5. Prominent among these observations was that of the nucleation and growth of multiple orientations of the orthorhombic S-phase, and a *prima facie* case was made for a *strategic relationship* between the crystallography of the precipitate and the strain environment in which it nucleated. It was concluded that an improved understanding of the varied crystallography of embedded particles of the S-phase was necessary for further understanding of this strategic relationship.

The present chapter will include an analysis of the variation in orientation and the associated variation in morphology of individual particles of S-phase, with particular reference to the nature of the particle/matrix interface. The focus will be on the crystallography of the S-phase and not the specific contribution of the line defect upon which the individual precipitates grow. It is anticipated that an improved knowledge of S-phase crystallography will provide a platform for revealing the relationship between S-phase crystallography and the strain environment in which it nucleates, and this relationship will be revisited in chapter 7. Following a justification of the alloy chemistry and heat treatment selection in the present work, this chapter will begin with some experimental observations defining the extent to which the S-phase lattice can rotate with respect to the parent aluminium matrix. Following this, both the orientation of the macroscopic interface plane between particle and matrix phases, and the aspect ratio of the particles will be analysed as a function of lattice rotation. The lattice spacing (where possible) and the planar coherency of the various observed forms of the interface will then be characterised prior to a discussion of the assembled results.

6.1 Alloy Selection and Heat Treatment

An important component of the current research was the strategic selection for study of four alloys. To achieve the objectives of the present chapter, two of these four alloys, Al-0.2Cu-1.7Mg and Al-0.8Cu-1.7Mg, were chosen for examination. Since the experimental approach of this chapter is based upon HREM characterisation of individual precipitates of the S-phase, the rationale determining alloy selection was as follows:

- *The selected alloys contained fewer dislocation loops (and therefore fewer precipitate colonies) per unit volume, resulting in less impingement between colonies.*
- *The loops were typically larger in the chosen alloys. Particularly in the case of the $\{111\}_\alpha$ loops, this implied a decreased rate of change per unit length of dislocation line of both the line direction and the Burgers vector. If changes in the dislocation line imply changes in the morphology of the precipitates that nucleate upon it, then a slow rate of change per unit length of dislocation is preferred, so that morphological differences in sequential precipitates may be detected in the precipitates that nucleate there.*
- *Two forms of loops were present in the selected alloys. Given previous observations that different precipitate morphologies appeared to form at the different loop types, it was essential to target those alloy compositions that provided the full range of loop types.*
- *Results of the analysis are expected to be of direct relevance to technologically important alloys. The alloy Al-0.8Cu-1.7Mg is close in composition to both the industrial alloy 2618, and the well-studied alloy Al-1.1Cu-1.7Mg [61,75]. The alloy Al-0.2Cu-1.7Mg has a similar Cu:Mg ratio to those in sheet alloys typically used in car-body applications [204,209,210].*

Pre-ageing for periods up to 24 h at room temperature did not significantly improve the hardening response during subsequent artificial ageing in the selected alloys, and pre-ageing was therefore not considered to be of potential technological interest. Furthermore, pre-ageing was observed to induce a complicated arrangement of line defects in the Al-0.2Cu-1.7Mg alloy, and an apparently unchanged microstructure in the Al-0.8Cu-1.7Mg alloy. Neither of these outcomes presented a compelling case for the incorporation of pre-ageing, and all alloys were immediately aged following quenching. So that precipitate particles were of an appreciable size during examination, microstructures were generally observed in the over-aged condition (120 days at 150°C) unless stated otherwise.

6.2 Orientation of S-Phase

The orientation relationship between embedded precipitates of S-phase and aluminium matrix is commonly described as rational and of the form [88,107,126,131,132,152]:

$$(100)_S // (100)_\alpha, [001]_S // [021]_\alpha \text{ and } [010]_S // [01\bar{2}]_\alpha.$$

The precipitates are typically described [88,107] as laths elongated parallel to the $[100]_S // [100]_\alpha$ axis, and it is recognised [75,107,131] that the S-phase lattice may be rotated by 4.8° about this axis. A particle of the S-phase adhering to the standard rational orientation relationship has, until this point in the thesis, been identified in HREM images by its lath-like form and distinctive planar interface which lies parallel to a plane of the type $\{021\}_\alpha$ and $(001)_S$. However, for those particles not displaying the well-known lath morphology typical of particles of standard orientation, the precise orientation of the S-phase lattice is not easily measured. Hence, an accurate and universal test of orientation has been implemented here to treat both those particles that are of the standard orientation and those that are rotated about $[100]_S // [100]_\alpha$.

6.2.1 Magnitude of Rotation

Orientation data for specific examples of the precipitate are available via *in-situ* electron diffraction in the electron microscope, and the technique of SAED was introduced in §2.4.2. Each diffracted beam in the SAED pattern defines a projection of the reciprocal lattice vector g representing a set of lattice planes, and the angle between pairs of planes in precipitate and matrix phases may be measured directly as the angle between the relevant vectors g .

So that the collected diffraction data may be readily traced back to a specific crystal of the S-phase, the selected specimen area should ideally contain only one precipitate crystal and the matrix phase. However, in the present work, precipitates of the S-phase nucleated at dislocations rarely occurred in isolation. Each dislocation loop could be regarded as providing a site for nucleation of a colony of particles of the S-phase representing multiple orientations and two variants of a given orientation (§5.4). Depending upon scale, a given loop contained anywhere between five and 20 individual precipitate particles. The selection of an area to contain only those particles that formed at a single dislocation loop required typically a *virtual aperture* 300 –

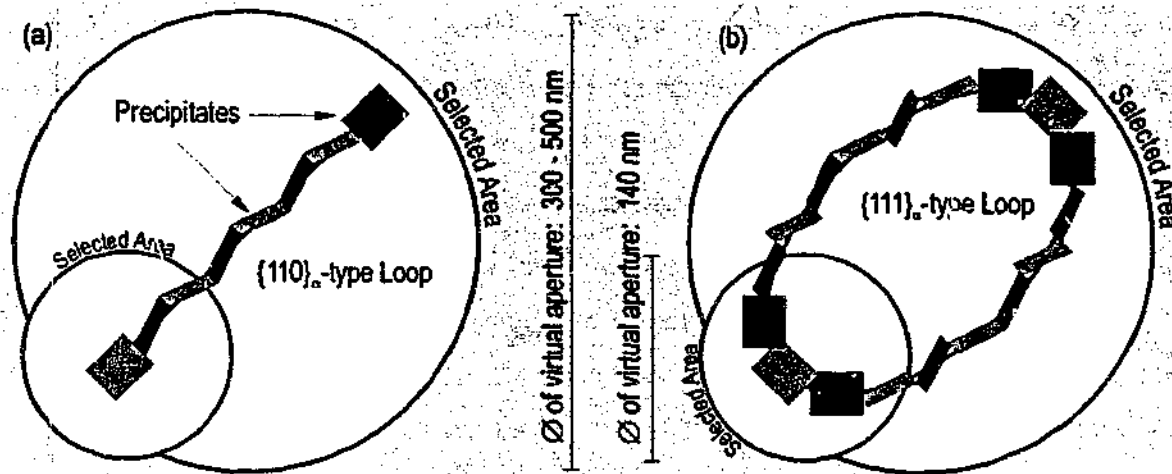


Figure 6.1 Selected areas from which to collect scattered electrons during SAED of precipitates heterogeneously nucleated at (a) $\{110\}_\alpha$ and (b) $\{111\}_\alpha$ dislocation loops.

500 nm in diameter, as shown schematically in figure 6.1. Precipitate nucleation and growth at both $\{110\}_\alpha$ and $\{111\}_\alpha$ loops (figs. 6.1(a) and 6.1(b) respectively) is represented, and the axis of rotation ($[100]_s$) is invariably parallel to the direct electron beam. Selection of a virtual aperture of the minimum diameter available (140 nm) on the microscope (JEOL 2011) limited the number of precipitates in the selected area, as shown in figures 6.1(a) and 6.1(b), but rarely was it possible to isolate an individual precipitate nucleated heterogeneously at a dislocation loop.

Owing to the imperfection of the lens system, beams diffracted further from the optic axis by the specimen are always bent more strongly as they pass through the objective lens. For rays that enter the objective lens at an angle α to the optic axis, the image formed is translated by a distance, $r_M = MC_s\alpha^3$ nm in a direction parallel to the projection of the relevant vector g (where M is the magnification and C_s is the spherical aberration) [199]. Therefore, the specimen area selected in the first image plane (using the SAED aperture) corresponds to the volume from which the electron diffraction pattern is formed only for the direct beam. Since the error is proportional to the angle α , the higher order diffracted beams originate from volumes that are translated further from the area viewed through the aperture in the first image plane [184]. In a microscope of the type used in the present work, $C_s = \sim 1.1$ mm. Consider the $(002)_\alpha$ reflection in a $B[100]_\alpha$ diffraction pattern of aluminium ($a_0 = 0.4048$ nm):

$$2d \sin\theta = n\lambda, \text{ where } d = 0.2024 \text{ nm}, \lambda = 0.00273 \text{ nm at } 200 \text{ keV and } n = 1$$

$$\therefore \theta = 0.006744 \text{ rad and } \alpha = 2\theta = 0.0135 \text{ rad, and since } \frac{r_M}{M} = C_s\alpha^3, \therefore \frac{r_M}{M} = 2.7 \text{ nm.}$$

Therefore, the beams diffracted from $\{002\}_\alpha$ planes have originated from an area translated 2.7 nm from the selected area observed in the field-limiting aperture. Figure 6.2 contains the relative translation of the specimen areas from which progressively higher order $(0b0)_\alpha$ spots originate. The translation of the specimen area for the beams forming the $\{042\}_\alpha$ focal points, ~ 30 nm (also shown in fig. 6.2), is considered the limit of reasonable error ($\sim 20\%$ translation), and these diffracted beams define the largest projection of vectors \mathbf{g} considered in the present work. The larger d -spacing of the planes in the S-phase leads to a smaller error than that generated for the planes in the matrix. For instance, the $(040)_s$ and $(004)_s$ spots in the SAED patterns originate from areas translated by 1.78 nm and 4.04 nm respectively, which is small compared to the size of the aperture, and can be used with confidence. The size of the field-limiting aperture does not impact upon the *position* of the intensity maxima in the SAED pattern since the aperture is placed below the back focal plane of the objective lens, and any deviation from that expected from the true crystallography of the specimen is a product of lens imperfection (C_s). As will be demonstrated, however, the position of the intensity maxima can be checked against that which is expected for the undistorted cubic matrix phase, and good agreement is reached.

Three examples are now presented that demonstrate the determination of lattice orientation by SAED. The first concentrates on particles of approximately standard orientation, while the second example is that of a rotated particle. Here, several alternative methods of measuring the lattice rotation are also presented. The third example is that of a selected area containing several particles of differing lattice rotation.

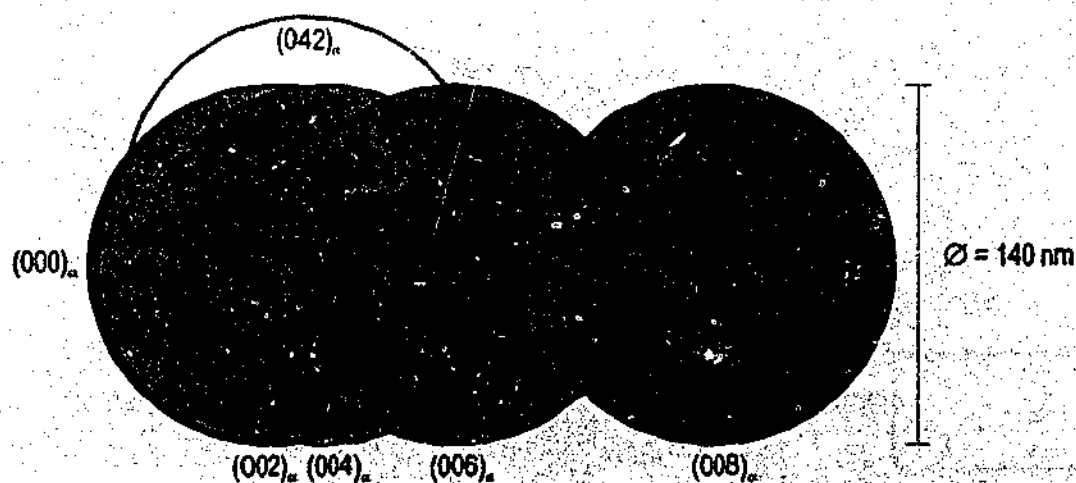


Figure 6.2 Translation of the area from which the diffracted beams in the SAED pattern originate. The direct beams, $(000)_\alpha$, is the only beam to originate from precisely the area selected in the virtual aperture.

Particles of the Standard Orientation

Figure 6.3(a) is a HREM image of a selected area of matrix material with embedded particles of the S-phase observed parallel to $[001]_s // [001]_a$. The selected area ($\varnothing \sim 140$ nm) contains several precipitates, of which two, labelled precipitates 1 and 2, are significantly larger than the remainder. The aspect ratio of particles 1 and 2, and the orientation of the broad interfaces parallel to $(001)_s$ (see enlargement), suggests that the particles are in the standard orientation. Figure 6.3(b) is a simulated diffraction pattern based upon the standard orientation relationship assumed from the images, comparing well with the experimental SAED pattern in figure 6.3(c).

On closer inspection, the intensities of individual diffraction maxima in the experimental SAED pattern (fig. 6.3(c)) originating from the S-phase are elongated parallel to $g(021)_a$. This observation is consistent with the well-known shape factor effect [184], where thin crystals evoke a streaking in the diffraction pattern parallel to the direction in which the crystal dimension is reduced. This is confirmed in the present case, where elongation in the intensity maxima is orthogonal to the elongation of the particle. In the example provided, there are two closely-

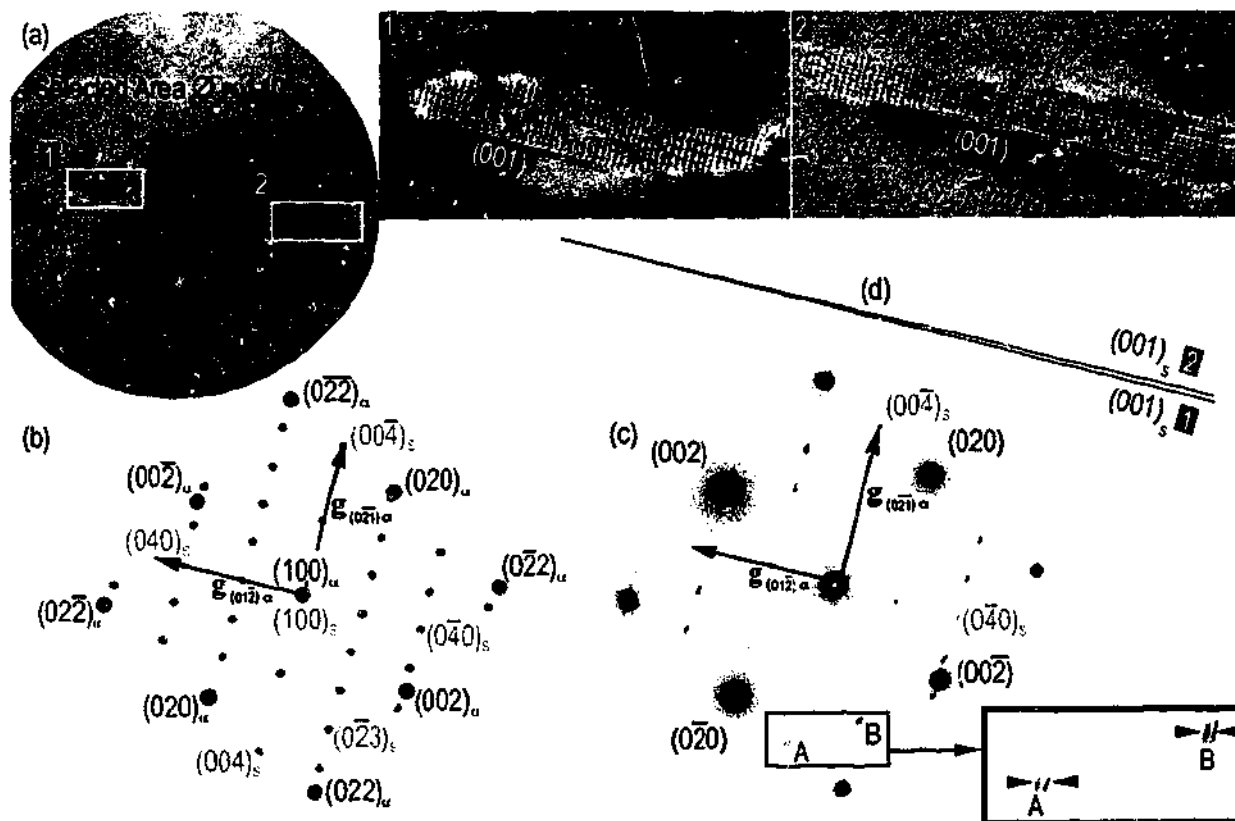


Figure 6.3 (a) Selected area of approximately 140 nm diameter. (b) Simulated diffraction pattern where precipitates 1 and 2 are assumed to be particles of the standard orientation relationship. (c) Experimental SAED pattern of the selected area. (d) Relative orientation of $(001)_s$ in precipitates 1 and 2.

spaced, but resolved, diffraction streaks at most of the S-phase positions, and those at position A (defining $g(004)_s$) and B (defining $g(0\bar{2}3)_s$) in figure 6.3(c) are indicated. This suggests that two individual, slightly misoriented, precipitates have contributed to the diffraction pattern. It is to be expected that this misorientation would be distinguishable in the atomic resolution image, and the misorientation of the respective $(001)_s$ planes in figure 6.3(d) confirms this. Since precipitate 1 is rotated slightly CW from precipitate 2 in the HREM image, vectors g defined by diffracted beams from precipitate 1 are rotated slightly CW about the direct beam from the corresponding vectors g of precipitate 2. Accordingly, the $(004)_s$ diffraction maxima have been labelled individually for precipitates 1 and 2 in figure 6.4, an enlargement of the $(0\bar{2}2)_\alpha$ quadrant.

Firstly, the position of the matrix-diffracted beams with respect to the direct beam was verified. In all cases, the angle between nominally orthogonal vectors $g\{002\}_\alpha$ was within $90^\circ \pm 0.5^\circ$ ($\pm 0.6\%$ error). The source of this error was assumed to be a combination of *systematic observer error*, the microscope lens error and the potential distortion of the photographic film during processing and developing, and is assumed to act homogeneously across the surface of the film.

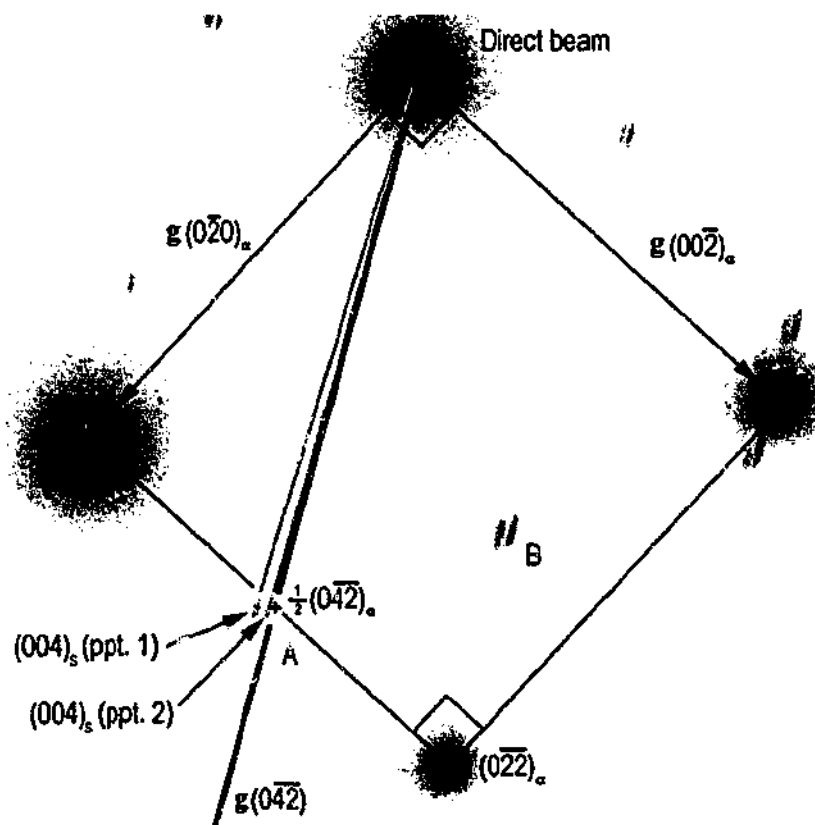


Figure 6.4 Enlargement of the $(0\bar{2}2)_\alpha$ quadrant of the experimental SAED pattern in figure 6.3(c).

With the aid of 10X magnification eye-piece, the cross-hair of a rotating protractor was placed parallel to the vector $g(0\bar{4}2)_\alpha$ (see fig. 6.4). The line also passes through the forbidden $g\frac{1}{2}(0\bar{4}2)_\alpha$ spot, and the arbitrary orientation of the line was recorded to an accuracy of 5' (0.083°). The orientation of $g(004)_s$ (ppt. 1) was recorded by the same procedure while the negative was maintained in position, and the angle between $g(0\bar{4}2)_\alpha$ and $g(004)_s$ (ppt. 1) was calculated. Note that in particles adhering to the standard orientation relationship, these vectors are parallel. The intensity maxima formed by diffracted beams from the precipitate were of a dimension approximately equal to that of the width of the cross-hair in this orientation, enabling reproducible measurement, and eleven measurements were taken. Ideally, the relative orientation of $(040)_s$ would also be measured, but the angle between $g(040)_s$ and $g(0\bar{4}2)_\alpha$ was not easily determined from intensity maxima that were streaked perpendicular to $g(040)_s$ such that attempts to find the centre of the spot introduced large errors of measurement. Accordingly, in all cases of thin precipitates of standard orientation, only the relative orientation of $g(004)_s$ was recorded. The process was repeated for the angle between $g(0\bar{4}2)_\alpha$ and $g(004)_s$ (ppt. 2), and the misorientation data is recorded in table 6.1.

Statistical analysis of the data for precipitate 1 suggests 95% confidence that the misorientation between $(001)_s$ and $(0\bar{2}1)_\alpha$ is between 1.0° and 1.26°, while the misorientation of precipitate 2 is between 0° and 0.18°. The error of ~0.6% in the film is additive to the total error, but because the measured angles are so small, the 95% confidence limit is not significantly affected. The larger size and diffuse nature of the matrix spots in the SAED patterns means that the centre may be difficult to locate, and the small random error of measurement may merely reflect the ability to reproduce consistently the angle between two vectors g . As such, the error margin was approximately doubled in the present work to $\pm 0.25^\circ$ for angular measurements taken directly from the negative film.

Table 6.1 Lattice misorientation between S and α planes of precipitates 1 and 2 in figure 6.4, including an analysis of the errors of measurement (SD – standard deviation, CL – confidence limit).

Misorientation between $g(004)_s$ and $g(0\bar{4}2)_\alpha$					Avge.	SD	95%CL	
Ppt 1	1°10' 50'	1°15' 1°5'	1°20' 1°	1°20' 1°10' 40'	1°20' 1°10'	1.13	0.215	0.127
Ppt 2	5' 15' 10' 25' 0' -5' 5' -5' 0' 10' 0'				0.09	0.151	0.09	

Rotated particles

In addition to such precipitates of approximately standard orientation, numerous particles in the present work were observed to be rotated about $[100]_s // [100]_a$, and in previous work [107,131] this rotation has been estimated to be 4.8° [107]. Figure 6.5(a) shows a selected area of matrix material that contains an embedded particle oriented such that $[100]_s // [100]_a$ is parallel to the electron beam. In this case, the particle of the S-phase was not obviously nucleated at a dislocation, but serves as an example of the applicability of small aperture SAED to determination of the lattice rotation. Figure 6.5(b) is the corresponding SAED pattern. The shape factor of small embedded particles that are equiaxed in the plane perpendicular to the beam implies that any distortion of the diffracted spots should be equiaxed, and the intensity distribution of spots diffracted from the S-phase confirms this.

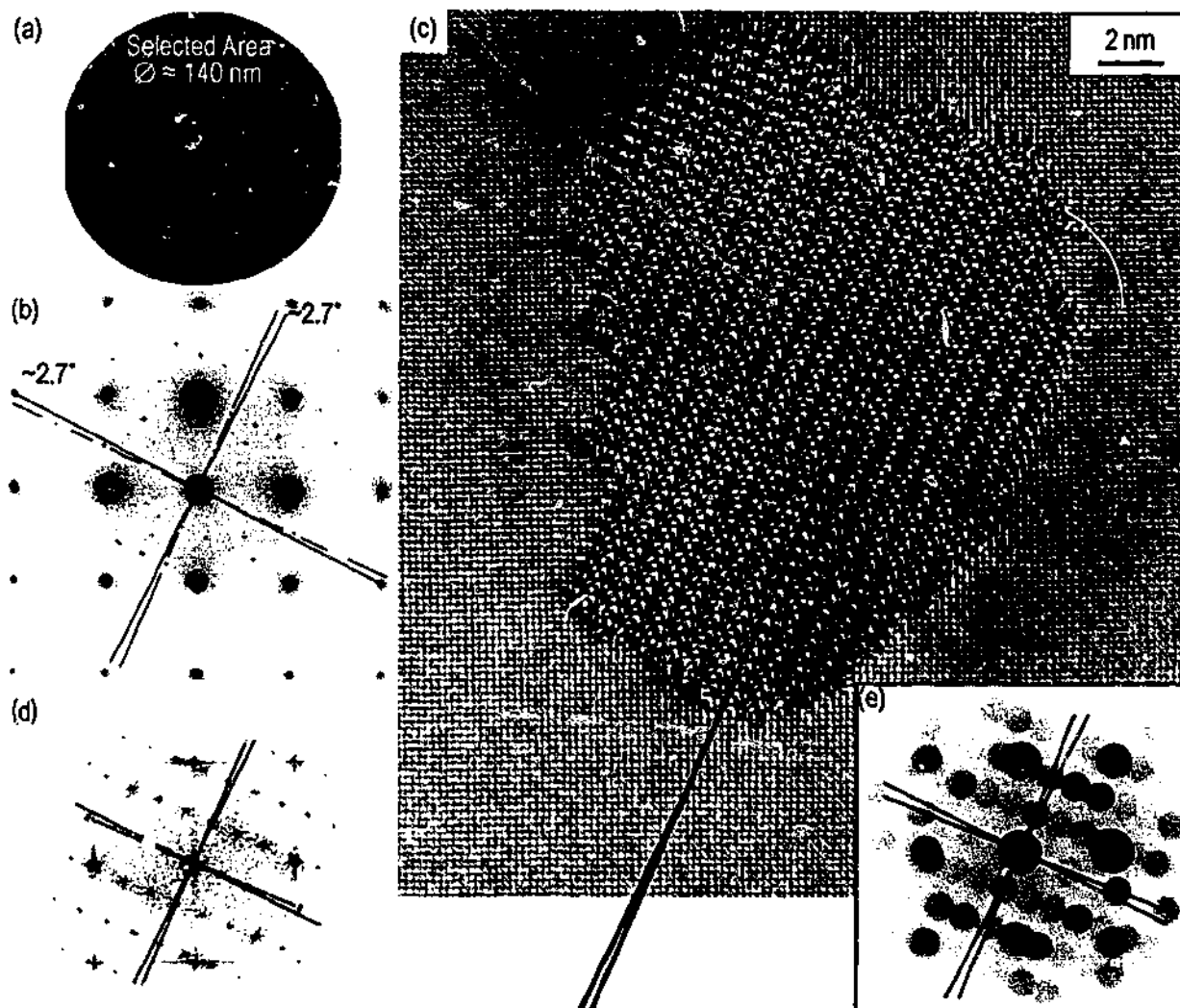


Figure 6.5(a) Selected area of ~ 140 nm diameter. (b) SAED pattern from the selected area. (c) HREM image of the embedded particle. (d) Fast-Fourier transform of the image intensity in figure 5.4(c). (e) NBED pattern of the precipitate and matrix immediately surrounding the precipitate.

The uniform shape of the intensity maxima meant that, in contrast to the elongated lath-type precipitates, the magnitude of lattice rotation could be measured as the *average* misorientation of both $g(004)_s$ and $g(040)_s$ vectors from the nearest set of orthogonal vectors $g\{042\}_\alpha$. Table 6.2 contains 11 measurements of the misorientation between $g(040)_s$ and $g\{042\}_\alpha$ using a rotating protractor, and the statistics suggest, with a confidence level of 95%, that the orientation of the precipitate is in the range of 2.58° and 2.86° away from the standard orientation. As previously, the error margin of $\pm 0.25^\circ$ is suggested.

Relative orientation of the vectors g in the experimental SAED pattern is not the only way to measure lattice orientation. Figure 6.5(d) is a calculated diffractogram, the squared modulus of the Fourier Transform of the atomic resolution image presented in figure 6.5(c) and additional matrix phase surrounding the precipitate. The Fourier transform processes the periodic intensity of an atomic resolution image and returns a spot pattern representing reciprocal space [188]. There are some inherent dangers in the interpretation [188]; for instance, the diffracted-beam intensities are incorrect. Nevertheless, they may be used satisfactorily to determine the misorientation of two lattices, and in the present case, can be used to determine the lattice rotation of the precipitate in the matrix (table 6.2). Finally, a nano-beam electron diffraction (NBED) pattern is provided in figure 6.5(e), from which the misorientation of the lattices can also be determined (table 6.2).

Particle orientation determinations using both FFT and NBED patterns have comparatively large error limits. Poor resolution of the calculated diffractogram leads to poor data. In the NBED pattern, large discs caused difficulties in identification of the centre of diffracted maxima, and it proved more accurate to measure the orientation of a series of small spots in the SAED pattern.

Table 6.2 Lattice misorientation between S and α planes, including an analysis of the errors of measurement (1: SAED, 2: FFT diffractogram, 3: NBED).

	Misorientation between $g(040)_s$ and $g\{042\}_\alpha$	Avge.	SD	95%CL
1	$2^\circ 35' \ 2^\circ 40' \ 2^\circ 15' \ 3^\circ 0' \ 3^\circ 5' \ 2^\circ 45' \ 2^\circ 40' \ 2^\circ 30' \ 2^\circ 55' \ 2^\circ 50' \ 2^\circ 45'$	2.72°	0.235°	0.139°
2	$2^\circ 50' \ 2^\circ 30' \ 2^\circ 10' \ 2^\circ 45' \ 2^\circ 5' \ 2^\circ 45' \ 2^\circ 30' \ 2^\circ 55' \ 2^\circ 50' \ 2^\circ 5' \ 2^\circ 20'$	2.70°	0.414°	0.244°
3	$3^\circ 10' \ 2^\circ 50' \ 2^\circ 5' \ 2^\circ 35' \ 2^\circ 50' \ 2^\circ 40' \ 2^\circ 35' \ 2^\circ 35' \ 2^\circ 40' \ 2^\circ 15' \ 2^\circ 50'$	2.64°	0.294°	0.174°

General example of several precipitates in a colony

Precipitate colonies often contain both laths of the standard orientation *and* related particles of the S-phase. For wide applicability, orientation determination using SAED must be capable of distinguishing between variously oriented precipitates in a single selected area. Such a case is presented in figure 6.6(a), which is a selected area that contains three large precipitates. Figure 6.6(b) is a magnified image of the three precipitates, and precipitates 1 and 2 have broad interphase boundaries of $(001)_S // (021)_\alpha$, implying that these particles are near to the standard orientation. Precipitate 3 shares a broad interphase boundary with the matrix that is not parallel to $(001)_S$. Furthermore, the $(001)_S$ plane is misoriented from $(012)_\alpha$ and, therefore, precipitate 3 is rotated about $[100]_S // [100]_\alpha$ and away from the standard orientation relationship. The precipitate arrangement is typical of that found at dislocation loops lying parallel to $\{011\}_\alpha$, where the precipitate at the end of a row of precipitates is not of the standard orientation relationship (§5.4.1). Figure 6.6(c) is the corresponding experimental SAED pattern of the

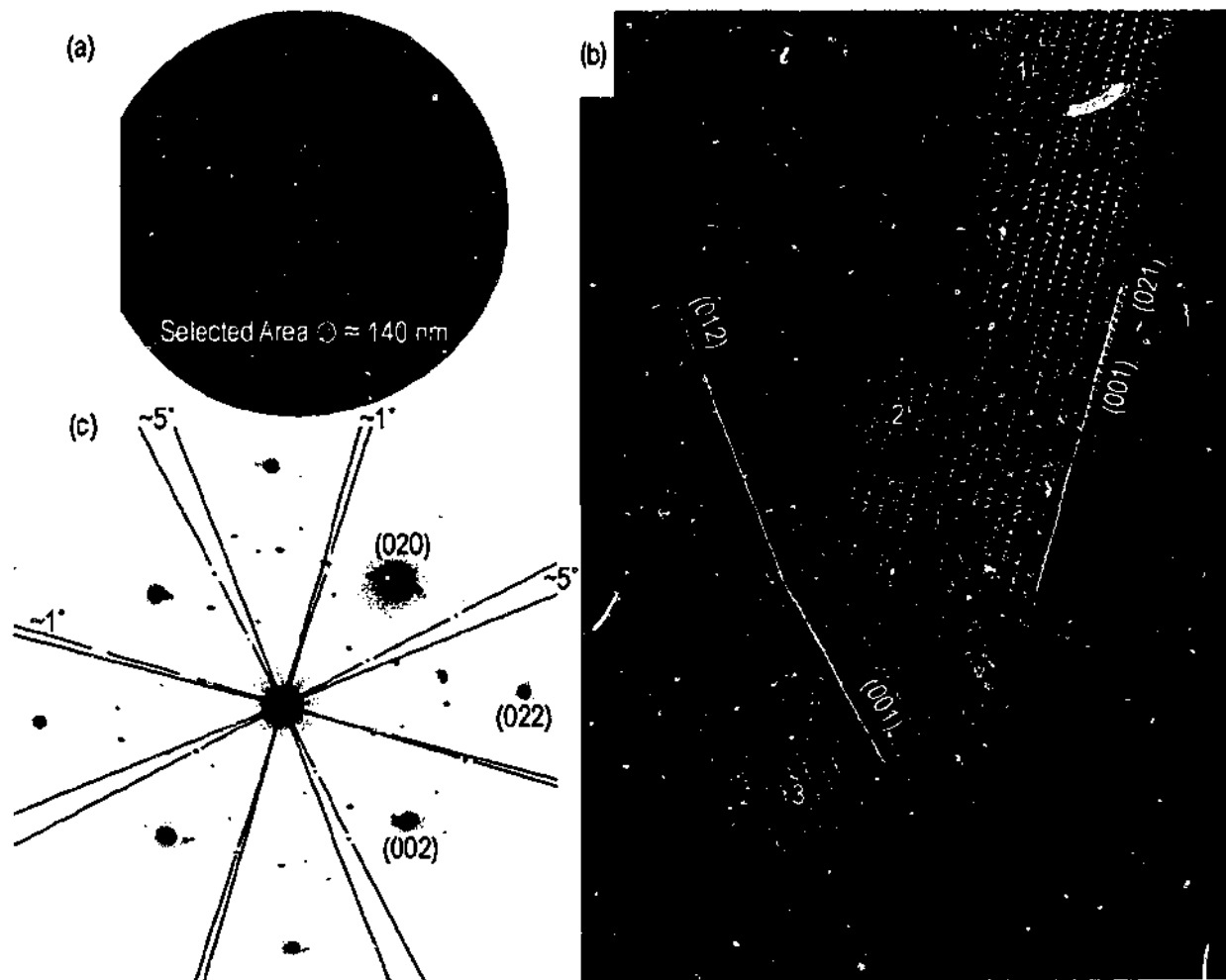


Figure 6.6 Selected area of approximately 140 nm diameter. (b) HREM image of the three embedded particles. (c) SAED pattern from the selected area.

selected area shown in figure 6.6(a). It is presumed that the SAED pattern of precipitates 1 and 2 are superimposed and it is observed that they are slightly rotated away from the standard orientation ($1^\circ \pm 0.25^\circ$) while precipitate 1 is rotated by $5^\circ \pm 0.25^\circ$. The data clearly discriminates between the particles of differing rotation about the $[100]_s // [100]_a$ growth axis and verifies the ability of small aperture SAED to differentiate between particles of different orientation relationship. Hence, the magnitude of lattice rotation was deduced from experimental SAED patterns, and data was verified from high-resolution images (if available) via direct measurements of the orientation of the planes in the image and FFT analysis if necessary.

Arranged in increasing order, figure 6.7 displays the measured magnitude (not crystallographic sense or direction) of lattice rotation of precipitates of the S-phase away from the standard orientation relationship for a large number of precipitates analysed in the present work using SAED. Data is sourced from individual S-phase precipitate particles in both Al-0.2Cu-1.7Mg and Al-0.8Cu-1.7Mg (overaged) that have nucleated exclusively at dislocations, and the 'rotation' describes that average angle through which the mutually perpendicular $(010)_s$ and

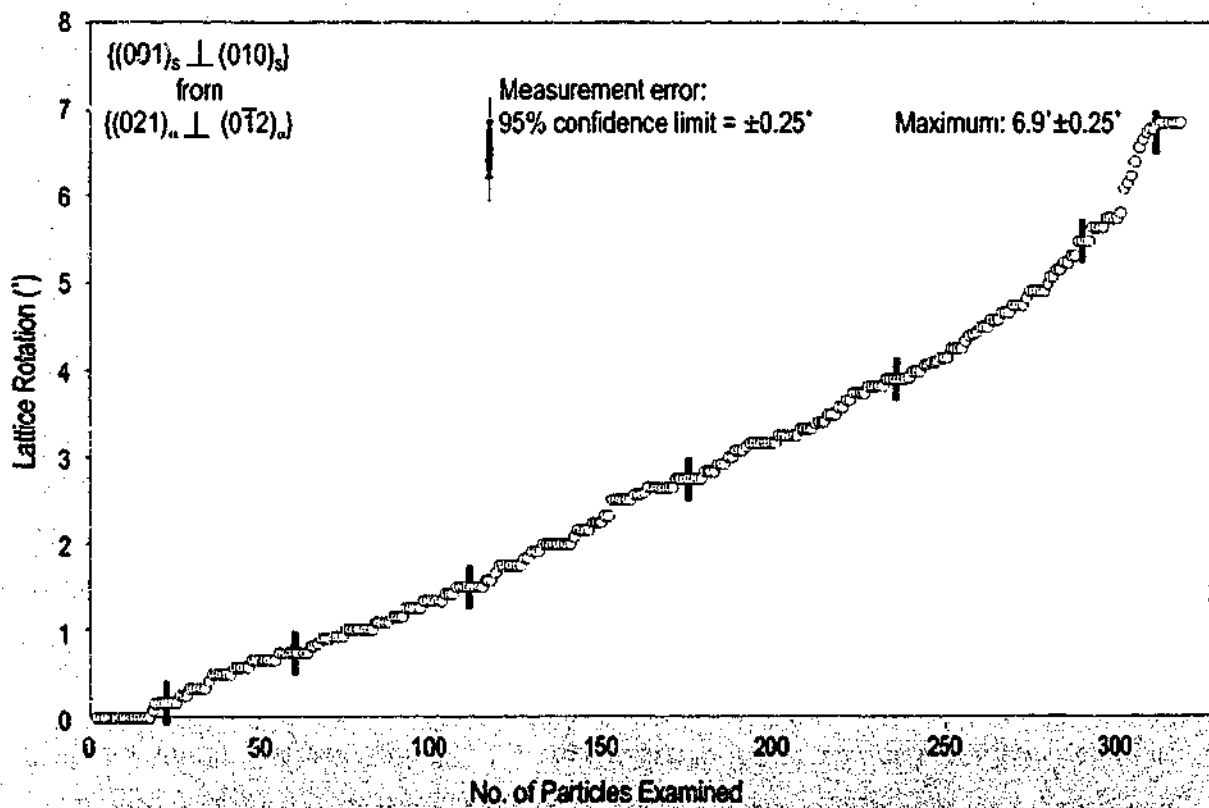


Figure 6.7 The magnitude of lattice rotation of precipitates as the angle between $(001)_s \perp (010)_s$ and $(021)_s \perp (012)_s$. In the standard orientation relationship, the misorientation is zero.

$(001)_s$ planes rotate from the respective $\{021\}_a$ planes with which they are parallel in the standard orientation. From figure 6.7, there is an apparently continuous range of rotation up to a maximum of $6.9^\circ \pm 0.25^\circ$ displayed by the precipitate population within the limits of confidence defined.

Summary

In the present work, the magnitude of the rotation of precipitates of the S-phase in the aluminium matrix has been performed routinely using SAED. Using a virtual aperture of 140 nm, the orientation of individual particles of the S-phase has been determined against a matrix volume that is approximately 700 $\{002\}_a$ matrix planes wide at its widest point. The technique has been useful to determine the effective continuity of the lattice rotations between the maxima observed. In addition to the diffraction data, HREM images can also provide a great deal of information regarding relative orientations of precipitate and matrix planes. The inspection of HREM images to determine the misorientation of precipitates from the standard orientation relationship relies on high-quality images so that the lattice planes are clearly distinguishable. Furthermore, it relies on optimum microscope conditions such that the positions of the intensity accurately reflect the position of the planes. Notwithstanding these issues, the advantage of using HREM images to determine the lattice rotation is that accurate *local* information can be gained in a way that may be missed by the SAED technique owing to the *averaging* of the orientation of sets of planes. Local information may include distorted matrix planes in the vicinity of the interface, oriented such that they are not reflective of the orientation of the planes at positions further from the precipitate. Using suitable HREM images, rotations of up to 8° away from the standard orientation have been observed.

Considering these observations, the magnitude of rotation of precipitates of the S-phase in the present work will be measured by the SAED technique. This is representative of the microstructure such that each individual precipitate is referenced against a fixed matrix lattice, rather than the local strain environments in the vicinity of individual particles. Regardless of this, however, the measured rotation of the precipitate may be slightly different to that observed using HREM images when the local distortion is taken into account.

Considered alone, the magnitude of lattice rotation provides only limited detail of the crystallography of the deviation from the standard orientation relationship, and the sense of the rotation should also be considered. This topic will now be introduced.

implying that $(0\bar{2}1)_s$ and $(014)_\alpha$ are approximately parallel within the experimental error limits. The angle between these two planes is 7.31° in the standard orientation relationship according to the latest structural model and lattice parameters of S-phase [107] (and ranges up to 8.6° using the lattice parameters of others [112,130,152]) and the lattice rotation has *reduced* the angle between these two planes. Analysis of SAED patterns of numerous particles of the S-phase displaying rotations of between 0 and $6.9^\circ \pm 0.25^\circ$ reveals that the lattice rotation always occurs in a sense that *reduces* the angle between $(0\bar{2}1)_s$ (or $(021)_s$) and the plane of the type $\{014\}_\alpha$ that is $7.31^\circ - 8.6^\circ$ away from $(0\bar{2}1)_s$ (or $(021)_s$) in the standard orientation relationship. This can be represented in the four stereographic projections of figure 6.9, which represent the four standard variants of S-phase such that $(100)_s // (100)_\alpha$:

Variant 1	$[001]_s // [021]_\alpha, [010]_s // [01\bar{2}]_\alpha$
Variant 2	$[001]_s // [0\bar{1}2]_\alpha, [010]_s // [021]_\alpha$
Variant 3	$[001]_s // [012]_\alpha, [010]_s // [02\bar{1}]_\alpha$
Variant 4	$[001]_s // [02\bar{1}]_\alpha, [010]_s // [0\bar{1}2]_\alpha$

In figure 6.9(a), CW rotation of the precipitate lattice in the matrix phase increases the angle between the plane pair $(0\bar{2}1)_s : (014)_\alpha$. However, a CCW lattice rotation of the precipitate lattice reduces the angle between the planes, and rotated particles of the S-phase always rotate CCW for the defined orientation relationship. Figure 6.10(b) is a stereographic projection of an orientation relationship that is equivalent to that presented in figure 6.10(a), but is rotated by 90° around the $[100]_\alpha$ axis. In this case, lattice rotation of the particle proceeds in a sense that allows the orientation of $(021)_s$ (i.e. not the $(0\bar{2}1)_s$ plane) to approach the orientation of a plane of the type $\{014\}_\alpha$. However, the sense of the rotation is still CCW. Figures 6.10(c) and 6.10(d) reveal that, of the four variants that have a common growth direction, two variants rotate CCW while two variants rotate CW.

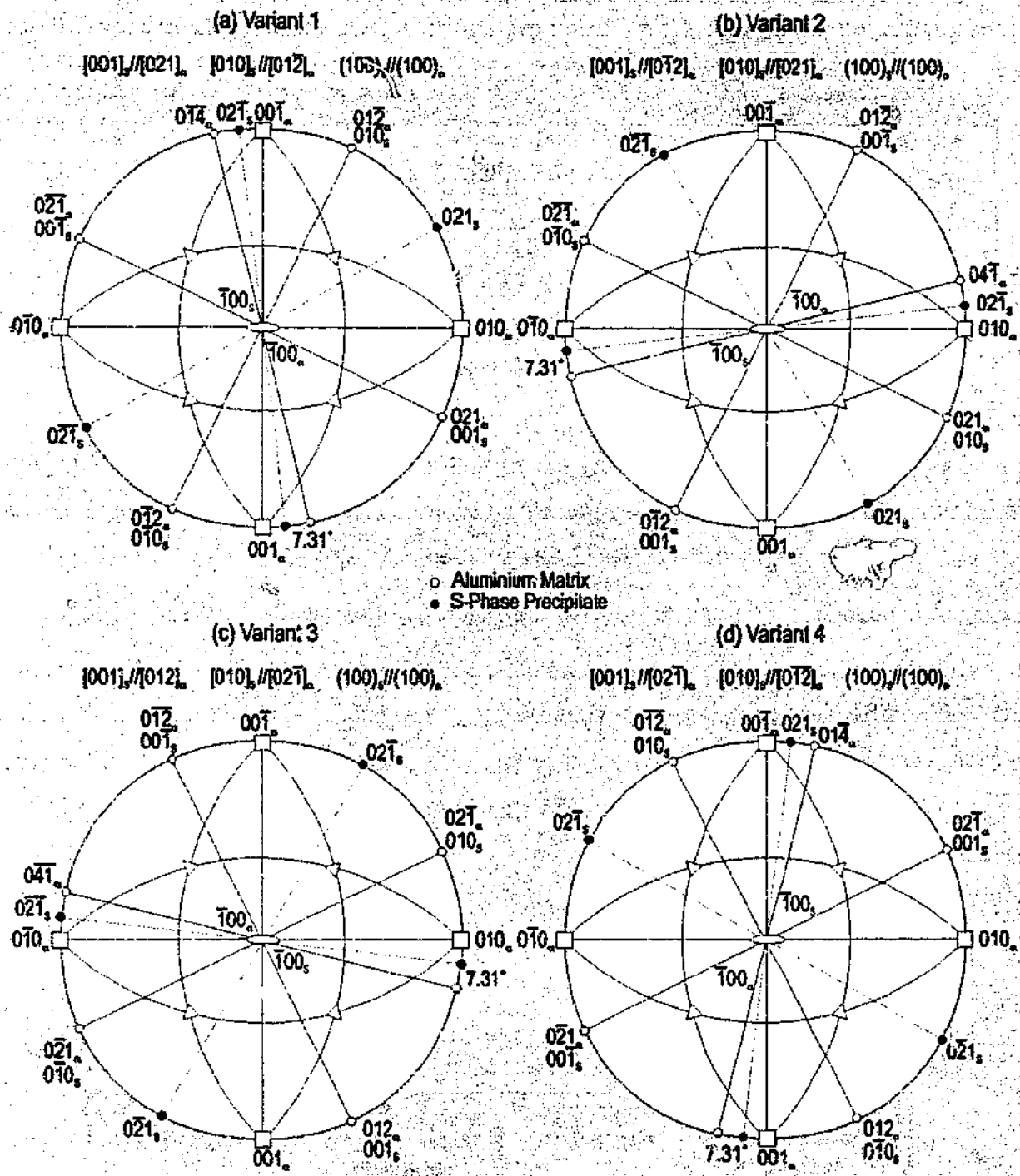


Figure 6.9 Stereographic projection of the four variants of the standard orientation relationship of S-phase such that $[100]_s // [100]_a$, observed parallel to $[100]_a$ (using the lattice parameters of Radmilovic [107]).

Table 6.3 contains the pairs of planes relevant to determination of the sense of rotation for the four variants shown in figure 6.9. The closure of the angle between the relevant planes during lattice rotation is obviously not restricted to the $(\bar{0}21)_s$ or $(021)_s$ planes and the corresponding plane of the type $\{041\}_a$. Table 6.4 contains the relatively low-index plane pairs (up to a Millers

Table 6.3 Four equivalent orientation relationships incorporating $(100)_S // (100)_\alpha$, giving the critical planes in both the S and matrix phases following a rotation of the maximum observed in the present work.

Orientation Relationship	S-Phase Plane of Interest	Matrix Plane of Interest	Sense of Rotation
1 $[001]_S // [021]_\alpha, [010]_S // [01\bar{2}]_\alpha$	$(0\bar{2}1)_S$	$(014)_\alpha$	CCW
2 $[001]_S // [0\bar{1}2]_\alpha, [010]_S // [021]_\alpha$	$(02\bar{1})_S$	$(04\bar{1})_\alpha$	CCW
3 $[001]_S // [012]_\alpha, [010]_S // [02\bar{1}]_\alpha$	$(021)_S$	$(041)_\alpha$	CW
4 $[001]_S // [02\bar{1}]_\alpha, [010]_S // [0\bar{1}2]_\alpha$	$(021)_S$	$(0\bar{1}4)_\alpha$	CW

index of 4) between the S-phase (according to the latest lattice parameters [107]) and the aluminium matrix (in the orientation described by Variant 1 in figure 6.9) that are separated by an angle of up to 7.31° . However, isolation of the plane pair of $(0\bar{2}1)_S$ or $(021)_S$ and the corresponding $\{041\}_\alpha$ is useful because the angle between them in the standard orientation relationship (7.31°) is larger, but close, to the maximum observed rotation of the S-phase lattice ($6.9^\circ \pm 0.25^\circ$). The planes are, therefore (1) approximately parallel in particles exhibiting maximum rotation, and (2) the rotation of the lattice is not likely to go further than the point at which these planes are parallel when the error limits of the orientation data are considered.

Table 6.4 Angle between low-index α -Al and S-phase planes in the standard orientation relationship (Variant 1 in figure 6.9) (up to 7.31°) - (using the lattice parameters of Radmilovic *et al.* [107]).

Plane Pair	Angle between planes in Standard OR ($^\circ$)	Plane Pair (cont...)	Angle between planes in Standard OR ($^\circ$)
$(01\bar{1})_S : (0\bar{1}2)_\alpha$	0.41	$(03\bar{2})_S : (0\bar{1}3)_\alpha$	3.79
$(0\bar{1}4)_S : (04\bar{1})_\alpha$	1.75	$(01\bar{3})_S : (04\bar{3})_\alpha$	3.93
$(01\bar{2})_S : (0\bar{1}1)_\alpha$	2.4	$(03\bar{2})_S : (02\bar{1})_\alpha$	4.34
$(0\bar{3}1)_S : (001)_\alpha$	2.92	$(0\bar{3}1)_S : (0\bar{1}1)_\alpha$	5.21
$(03\bar{4})_S : (0\bar{3}4)_\alpha$	3.18	$(0\bar{1}2)_S : (0\bar{1}0)_\alpha$	5.73
$(0\bar{1}1)_S : (04\bar{1})_\alpha$	3.32	$(02\bar{1})_S : (04\bar{3})_\alpha$	6.73
$(02\bar{1})_S : (03\bar{2})_\alpha$	3.55	$(01\bar{3})_S : (03\bar{2})_\alpha$	7.11
$(01\bar{4})_S : (03\bar{2})_\alpha$	3.65	$(02\bar{1})_S : (0\bar{1}4)_\alpha$	7.31

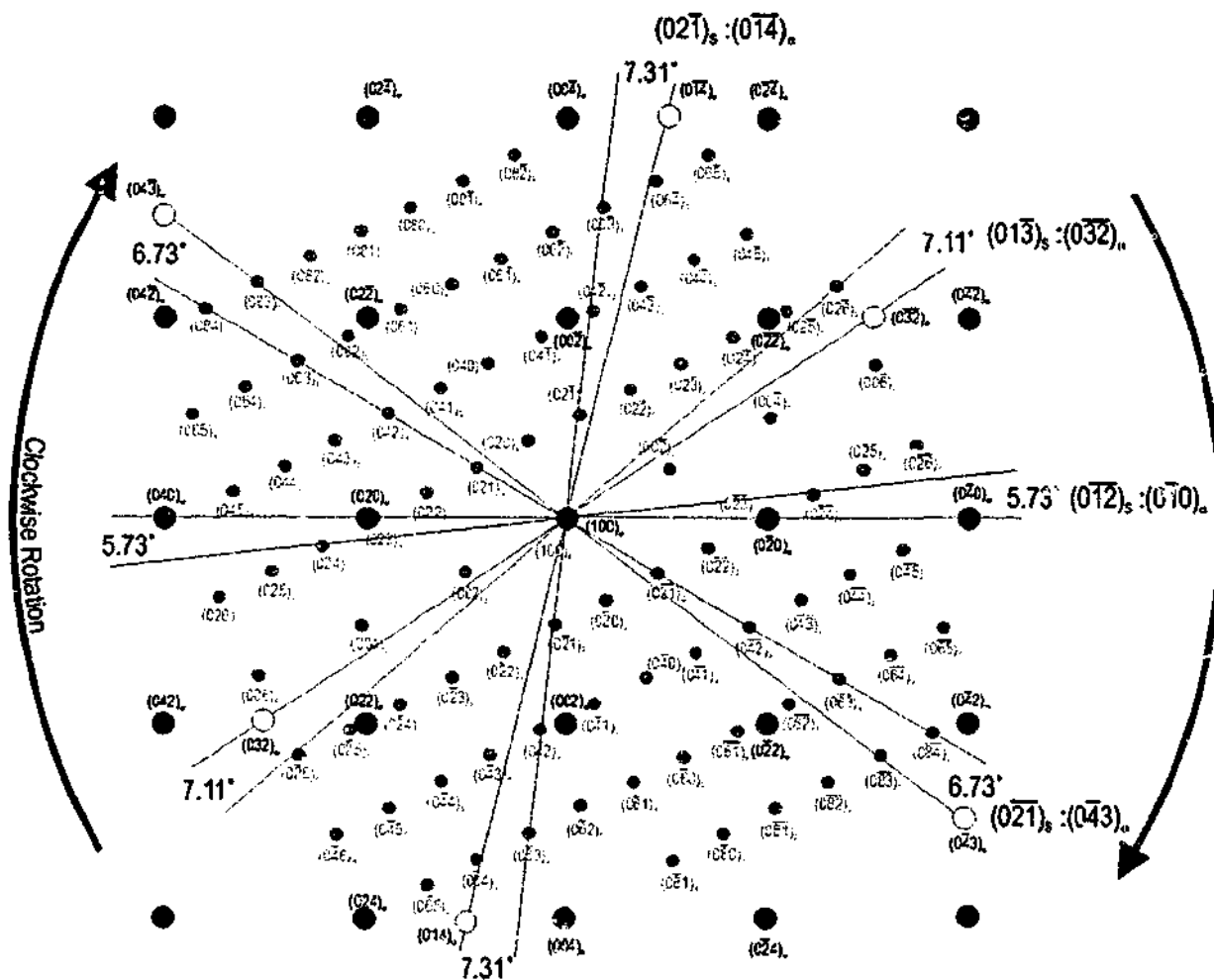


Figure 6.10 Simulated diffraction pattern of the standard orientation relationship described in the stereographic representation of figure 6.9(a), using the lattice parameters of Radmilovic *et al.* [107].

Figure 6.10 is a simulated diffraction pattern of the standard orientation relationship described in the stereographic representation of figure 6.9(a). The direction of precipitate lattice rotation is indicated, and several of the plane pairs identified in table 6.3 are isolated.

6.3 The Macroscopic Habit Plane of the S-Phase

While the characteristic planar interface parallel to $\{021\}_\alpha$ (and $(001)_s$) for laths in standard orientation has been confirmed in the present work, evidence presented in the previous chapter suggests that many embedded particles of the S-phase are characterised by a series of steps at the particle-matrix interface. The presence of steps forces a redefinition of the interface (habit) plane of the particle, and this section attempts to identify a systematic change in interface orientation as a function of the lattice orientation of the embedded particles.

6.3.1 The Habit Plane of Interfaces with Ledges

Steps on the interface are described by a riser height and a terrace width, as depicted in figure 6.11. The macroscopic interface plane is defined as the plane that passes through the risers or terraces at a prescribed position consistent for all risers or terraces (i.e. the top of the riser in fig. 6.11). This is a relatively uncomplicated exercise for interfaces consisting of regularly spaced ledges, and the orientation of typical examples in the present work were reproducibly measured within $\pm 2^\circ$. In cases where the ledges are irregularly and/or widely spaced, the macroscopic interface plane can not be concluded with an equivalent certainty.

An example of a macroscopic interface plane defined by widely and regularly-spaced interfacial ledges is shown in figure 6.13 for a particle of the S-phase embedded in an aluminium matrix. The orientation of the interface is approximately parallel for the two broad particle-matrix interfaces, and based upon measurements taken from the HREM image of figure 6.13(a), the



Figure 6.11 Definition of the macroscopic interface plane of a stepped interface.

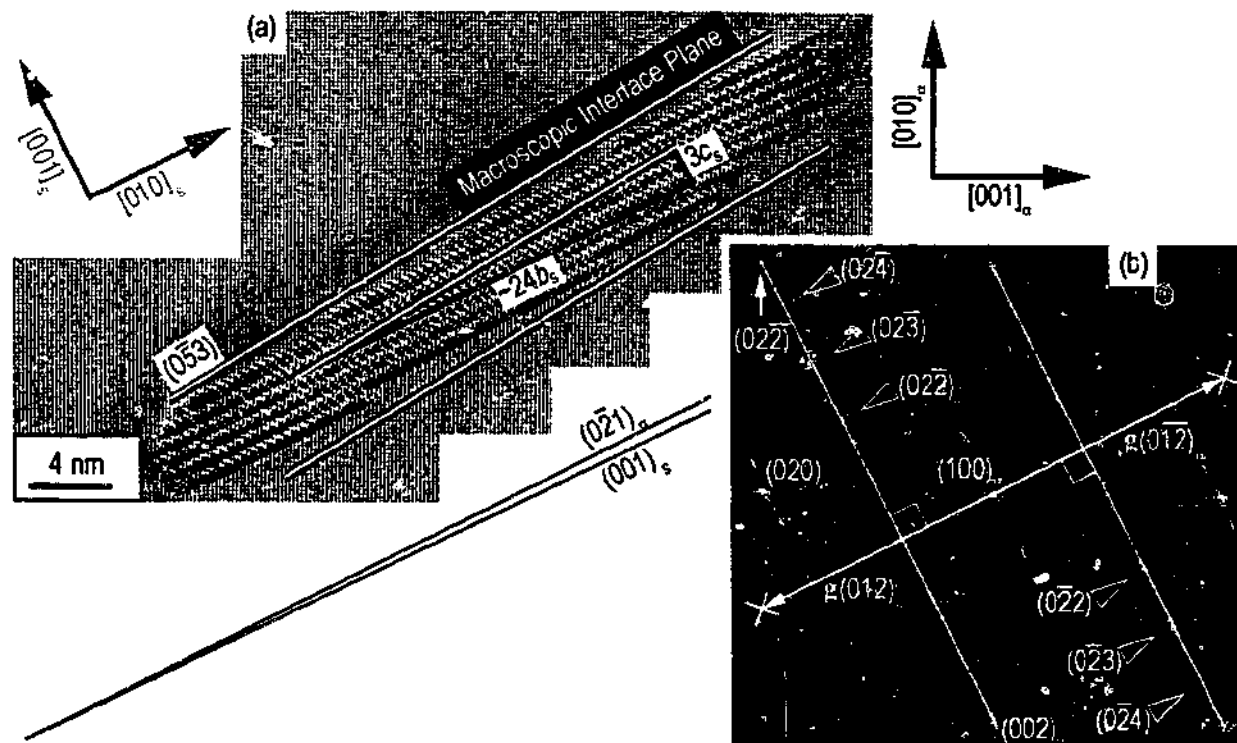


Figure 6.12 Definition of the macroscopic interface plane proceeds as described above.

macroscopic interface is *approximately* parallel to $(0\bar{5}3)_a$. The interface plane is also approximately parallel to $(0\bar{1}8)_s$, as indicated in the image. The lattice orientation relationship between the precipitate particle and the matrix in figure 6.13(a) has been estimated by two techniques. Firstly, the diffractogram in figure 6.13(b) indicates that the S-phase lattice is rotated CW by a small angle from the appropriate variant of the standard orientation relationship, as indicated by the arrowed intensity maxima that deviate from straight lines perpendicular to $g(012)_a$ and $g(0\bar{1}2)_a$. Secondly, comparison of the orientation of the planes $(001)_s$ and $(0\bar{2}1)_a$ in the HREM image implies a small CW rotation of the precipitate away from a variant of the standard orientation relationship. Although small, the CW rotation is distinguishable and measurable using both techniques, and is $1^\circ \pm 0.5^\circ$, reflecting the larger error of FFT diffractograms. A particle exhibiting the variant of the standard orientation relationship from which the precipitate in figure 6.13 is slightly rotated would be expected to maintain a step-free interface parallel to $(0\bar{2}1)_a$, and the macroscopic interface of the particle, approximately parallel to $(0\bar{5}3)_a$, is $4.4^\circ \pm 2^\circ$ CCW from this orientation. In all cases, it was observed that a CW lattice rotation of the precipitate phase from the standard orientation relationship resulted in a CCW rotation of the macroscopic (stepped) particle-matrix interface, and vice versa.

The maximum lattice rotation away from the standard orientation of S-phase observed in the present work was $6.9^\circ \pm 0.25^\circ$ and an example of such a precipitate is provided in figure 6.13. The orientation of the macroscopic interface plane is parallel to $(0\bar{2}1)_s // (0\bar{4}1)_\alpha$. Numerous observations confirm that particles rotated by $6.9^\circ \pm 0.25^\circ$ from a variant of the standard orientation relationship invariably display a broad interface parallel to $(0\bar{2}1)_s$ (or $(021)_s$) and $\{041\}_\alpha$. A particle characterised by the variant of the standard orientation relationship from which the precipitate in figure 6.14 is rotated by $6.9^\circ \pm 0.25^\circ$ would be expected to maintain a step-free interface plane parallel to $(001)_s // (0\bar{1}2)_\alpha$. In order to illustrate directly the change in interface orientation commensurate with a lattice rotation of this magnitude, a particle in standard orientation and a particle rotated through $6.9^\circ \pm 0.25^\circ$ from this variant are compared (fig. 6.14).

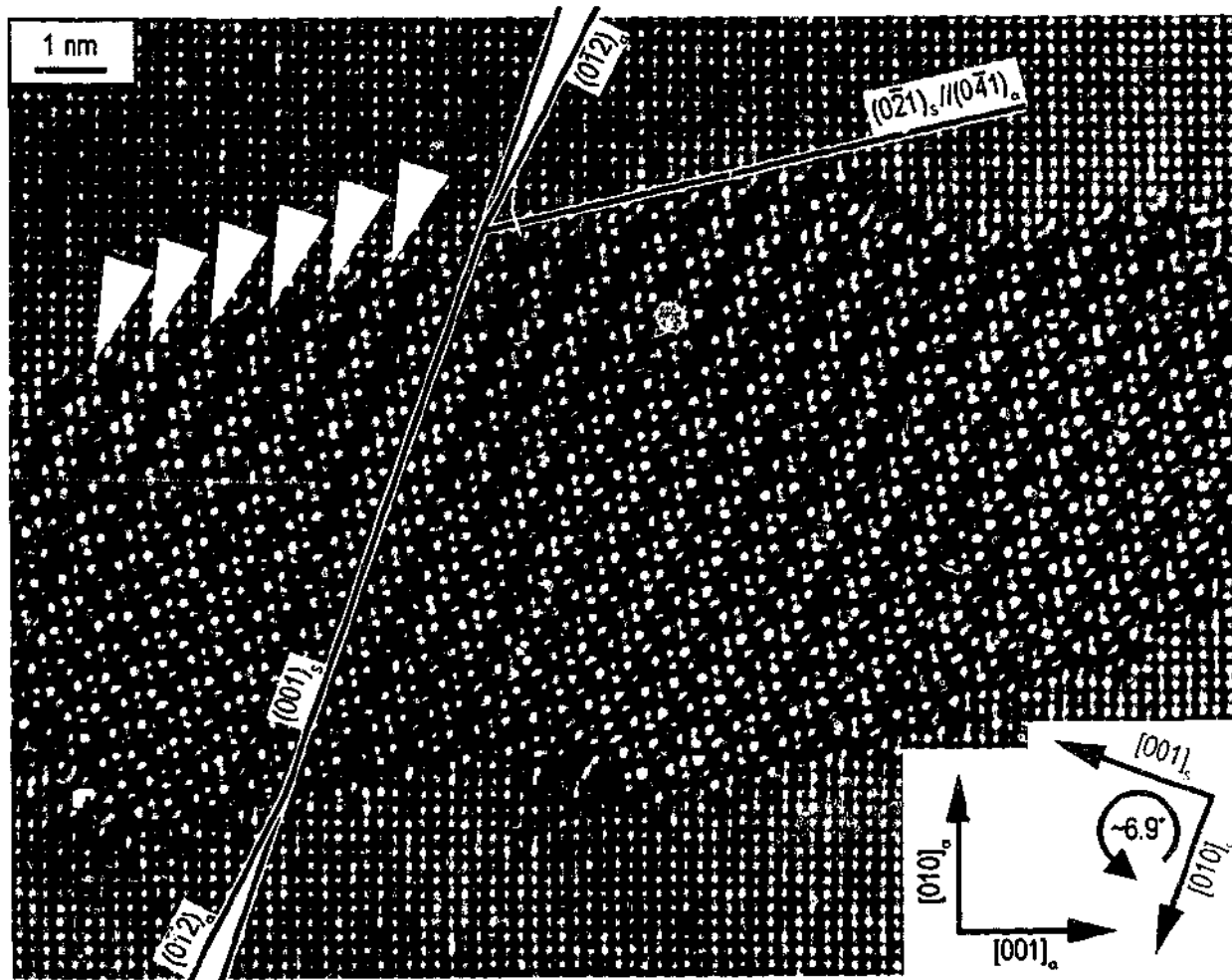


Figure 6.13 A precipitate rotated CCW by $6.9^\circ \pm 0.25^\circ$ from a variant of the standard orientation relationship, displaying the characteristic particle matrix interface of $(0\bar{2}1)_s // (0\bar{4}1)_\alpha$. The steps are indicated by the arrows at the interface.

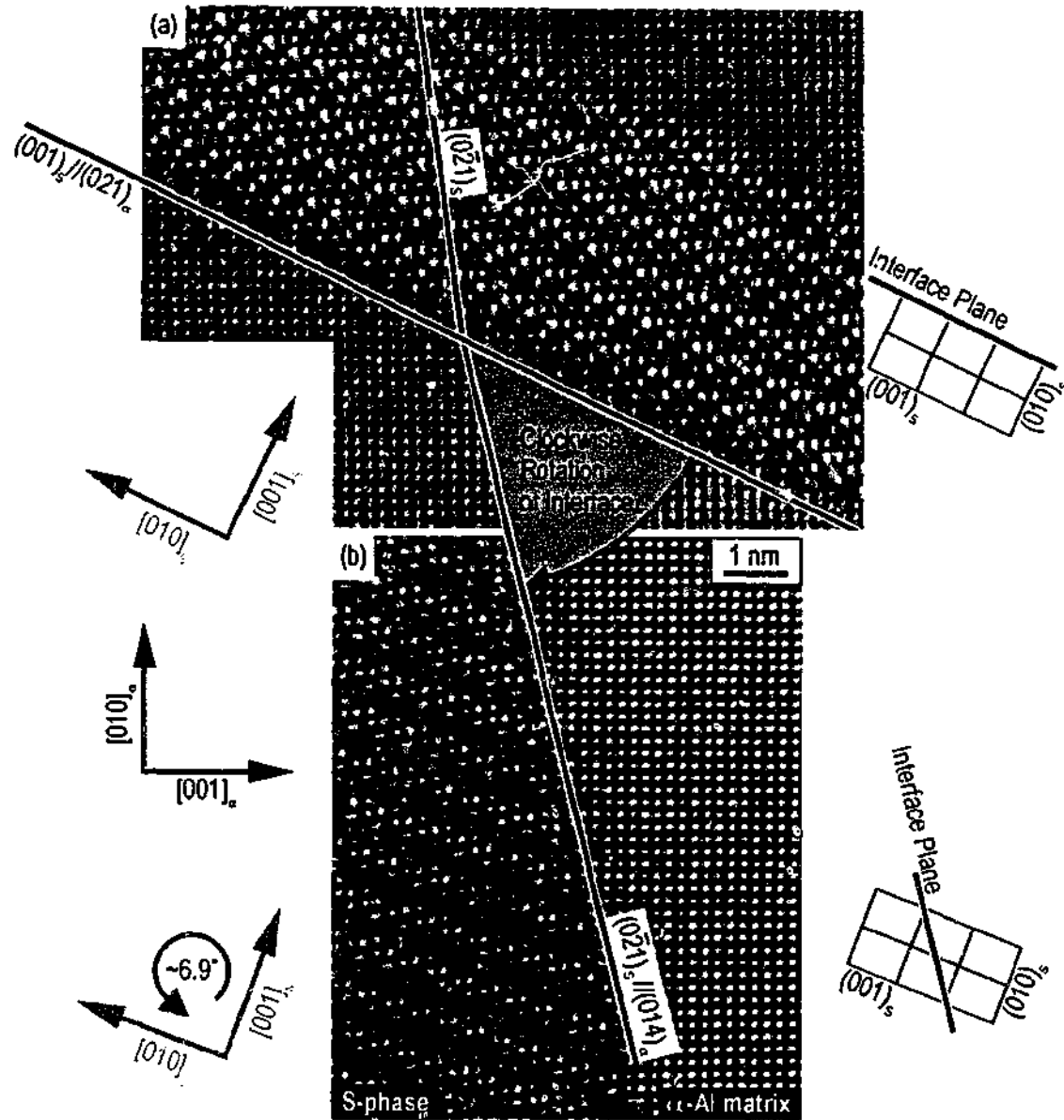


Figure 6.14 (a) Precipitates of standard orientation with macroscopic interface plane parallel to $(001)_S // (021)_\alpha$. (b) Precipitate rotated by $6.9^\circ \pm 0.25^\circ$ CCW about $[100]_S // [100]_\alpha$ from the variant of the standard orientation displayed by the precipitate in (a).

The particle-matrix interface parallel to $(001)_S // (021)_\alpha$ of a lath-type precipitate of the standard orientation relationship is shown in figure 6.14(a). Figure 6.14(b) displays the orientation of the particle-matrix interface of a particle of the S-phase for which there is a $6.9^\circ \pm 0.25^\circ$ lattice rotation from the equivalent variant of the standard orientation in figure 6.14(a). The orientation of the particle-matrix interface is reconfigured from $(021)_\alpha$ to $(014)_\alpha$ for the lattice rotation described, constituting a change in orientation of 49.4° . The macroscopic interface of the precipitate is rotated CW for a lattice rotation that is CCW, and this relative sense of the rotations was invariably observed, as it was in the case of those particles that had undergone only a slight rotation about $[100]_S // [100]_\alpha$.

In summary, it was observed that minor ($1^\circ \pm 0.25^\circ$) lattice rotations of particles of the S-phase resulted in minor ($4.4^\circ \pm 2^\circ$) rotations of the macroscopic interface away from that expected for the standard orientation relationship, while more substantial lattice rotations ($6.9^\circ \pm 0.25^\circ$) resulted in significant ($49^\circ \pm 2^\circ$) rotations of the interface. In all cases, the interface rotation was in a sense opposite to that of the lattice rotation. It could be suggested, therefore, that an intermediate rotation of the unit cell of greater than 0 but less than $6.9^\circ \pm 0.25^\circ$ might result in a rotation of the interface by an angle somewhere between 0 and 49.4° . This proposal is represented schematically in figure 6.15, where the angle ϕ is the magnitude of the rotation from the standard orientation relationship, and the angle θ is the rotation of the macroscopic particle-matrix interface away from that expected from a particle of standard orientation.

Although a rare observation in the present work, the precipitate particle shown in figure 6.16 is characterised by two distinct portions, distinguishable by a difference in lattice rotation of the S-phase and in the orientation of the interface that separates each portion from the matrix. It is potentially instructive in the present context of assessing the relationship between the lattice rotation of the S-phase and the macroscopic interface orientation. The precipitate at A in figure 6.17 is of the standard orientation relationship, while the precipitate at B is rotated CW by $4.2^\circ \pm 0.25^\circ$. The transition from 0 to -4.2° rotation is accomplished within a narrow band of material such that the precipitate can be treated as having two discrete orientations, as opposed to a continuous change in orientation.

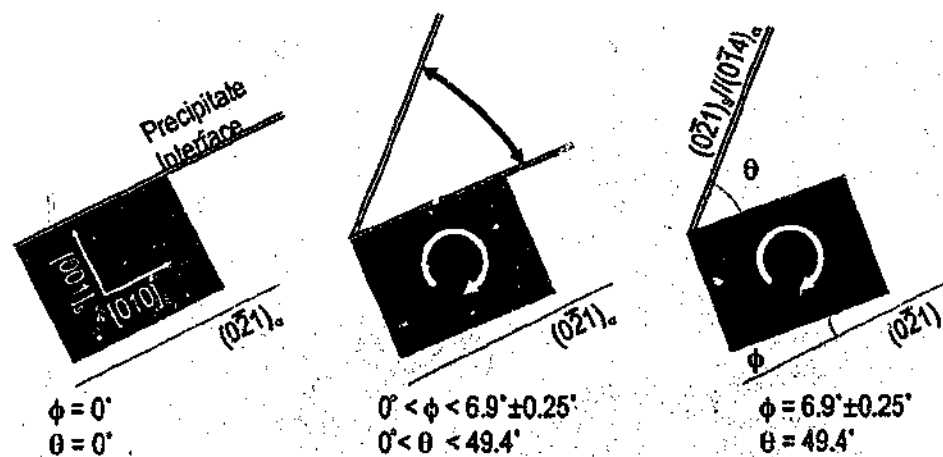


Figure 6.15 An intermediate unit cell rotation may translate into an intermediate interface rotation.

The interface orientation at A is parallel to $(001)_s // (0\bar{2}1)_\alpha$, as indicated in figure 6.16. A CW lattice rotation of $6.9^\circ \pm 0.25^\circ$ from the variant of the standard orientation relationship at A should, based on the evidence of figure 6.14, result in an interface orientation that is parallel to $(0\bar{1}4)_\alpha$, as indicated. In this case, the intermediate CW lattice rotation of $4.2^\circ \pm 0.25^\circ$ at B is associated with a particle-matrix interface that is approximately parallel to $(0\bar{3}4)_\alpha$, or $27^\circ \pm 2^\circ$ CCW from the interface of the precipitate of standard orientation at A. Extensive observation has confirmed that numerous particles characterised by lattice rotations of between 0 and $6.9^\circ \pm 0.25^\circ$ about $[100]_s // [100]_\alpha$ from the standard orientation maintain a stepped macroscopic habit plane rotated by between 0 and 49.4° from the standard lath-type interface of $\{021\}_\alpha$. Larger lattice rotations correspond to larger interface rotations. The relationship observed experimentally is depicted in figure 6.17, where it is shown that there is an approximately linear relationship between the angle of rotation of the interface and the angle of the lattice rotation of the S-phase, when both are measured systematically with respect to the standard orientation of the S-phase.

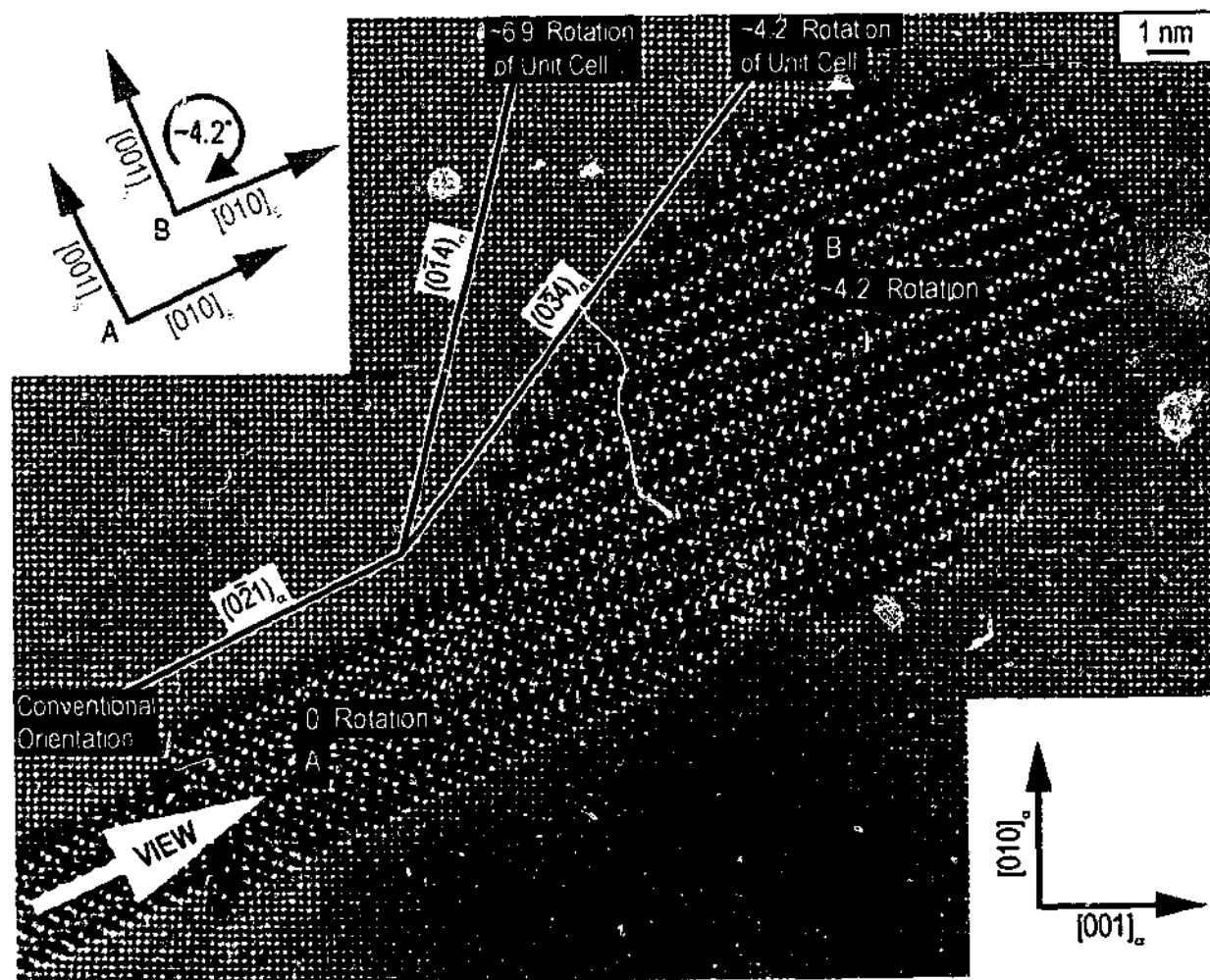


Figure 6.16 Single precipitate particle characterised by a change in unit cell rotation.

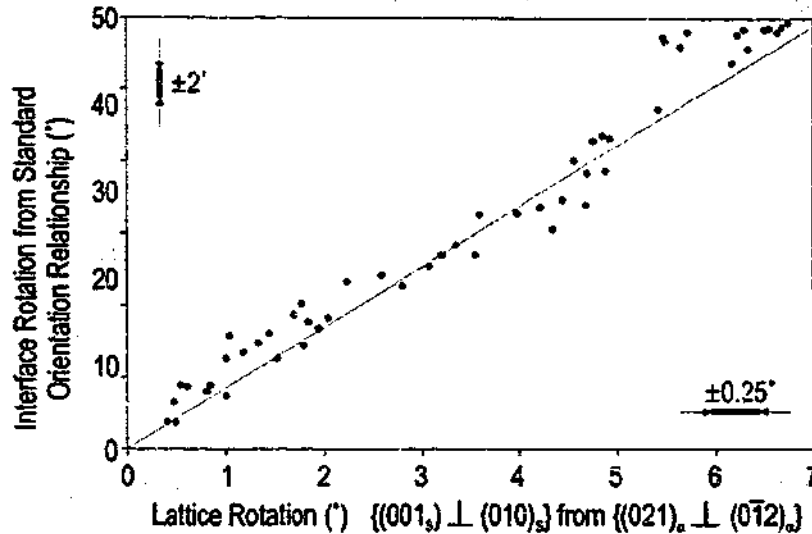


Figure 6.17 Interface rotation vs. unit cell rotation for precipitates of the S-phase in the present work.

Based upon the previous observation of a near-continuous variation in unit cell rotation from 0 to $6.9^\circ \pm 0.25^\circ$, it might be suggested that there is an equally near-continuous variation in the orientation of the macroscopic interface plane in a representative population of the S-phase.

6.3.2 Characteristics of Interfacial Steps

Achievement of spatial resolution equivalent to or less than the interatomic spacing of the constituent crystal planes in both the matrix and particle phases using phase-contrast HREM allows detailed knowledge of the interfacial steps to be gained, including the riser height and the terrace width. Figure 6.19 is a HREM image of a particle of the S-phase in which there is a CCW lattice rotation of $1.8^\circ \pm 0.25^\circ$ about $[100]_s // [100]_a$ from the appropriate variant of the standard orientation relationship. As expected, the macroscopic interface plane is rotated CW, and in this case the macroscopic interface is reconfigured by a rotation of $12^\circ \pm 2^\circ$ from that expected if there were no lattice rotation present. The terrace plane, i.e. the plane of the particle-matrix interface *between* the steps, is parallel to $(001)_s$, and this facilitates ready identification of the height of the steps, which are measured perpendicular to $(001)_s$. The steps at the interface are clearly indicated in figure 6.18, and are equivalent in height to the spacing of $(001)_s$, deduced in the manner described in §5.4. Therefore, the riser height of the interfacial steps was $1c_s$.

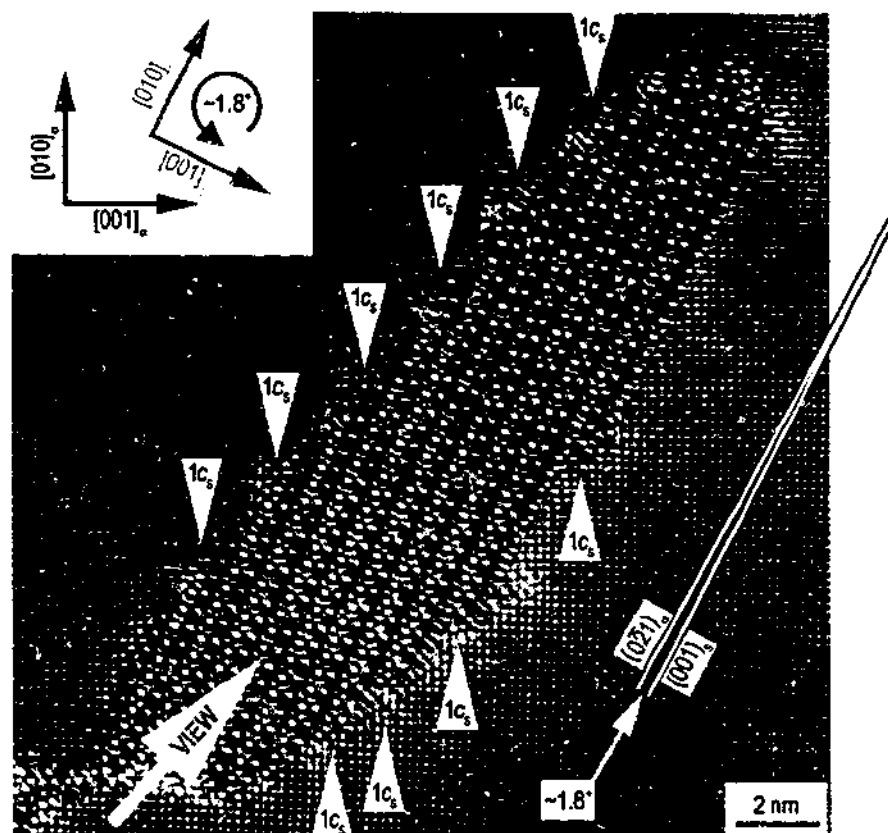


Figure 6.18 A series of interfacial steps $1c_s$ in height at the macroscopic habit plane of a particle of the S-phase exhibiting a lattice rotation of $1.8 \pm 0.25^\circ$ about $[100]_s // [100]_a$ from a variant of the standard orientation relationship.

Since both the precipitate terrace plane and the step height do not vary, the terrace width must change as the lattice rotation of the S-phase changes so that the observations of the macroscopic habit plane may be satisfied. Figure 6.19 contains three examples of precipitates of the S-phase rotated CW from the appropriate variant of the standard orientation relationship by $1^\circ \pm 0.25^\circ$, $4.2^\circ \pm 0.25^\circ$ and $6.9^\circ \pm 0.25^\circ$, and the corresponding width of the terrace plane (spacing of the steps) is indicated. The terrace plane width decreases progressively as the lattice rotation about $[100]_s // [100]_a$ increases from $\sim 1^\circ$ to $\sim 6.9^\circ$.

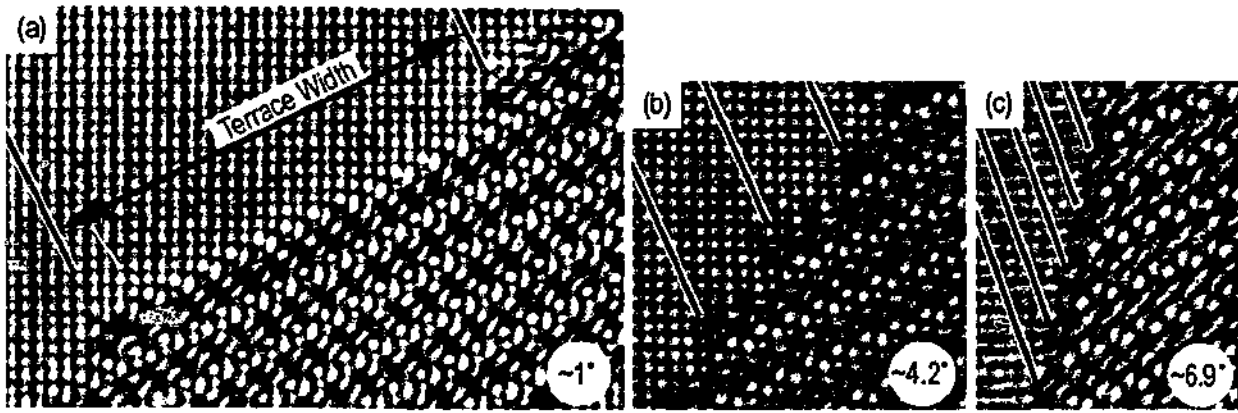


Figure 6.20 Progressive reduction in the terrace width from (a) to (c) as the rotation about increases about $[100]_S // [100]_a$ from $\sim 1^\circ$ to $\sim 6.9^\circ$ from the appropriate variant of the standard orientation relationship.

Assuming that the relationship between the lattice rotation and the macroscopic interface rotation is linear, as suggested by figure 6.17, the width of the terrace plane can be calculated as a function of the magnitude of the lattice rotation, as shown in figure 6.20. In figure 6.20(a), the interface orientation of \overline{OB} is a function of the lattice rotation ϕ . The slope of \overline{OB} , notated as $\overline{bb'}$ in figure 6.20, is equal to y/x , the magnitude of which can be readily determined using simple Cartesian geometry in terms of the step height, $1c_s$, and the terrace width.

$$\text{Terrace Width} = \frac{1c_s (1/\cos(\tan^{-1}(0.5) - \phi) + (y/x)\cos(\tan^{-1}(0.5) - \phi)\sin(\tan^{-1}(0.5) - \phi) - \sin^2(\tan^{-1}(0.5) - \phi))}{(y/x)\cos(\tan^{-1}(0.5) - \phi) - \sin(\tan^{-1}(0.5) - \phi)}$$

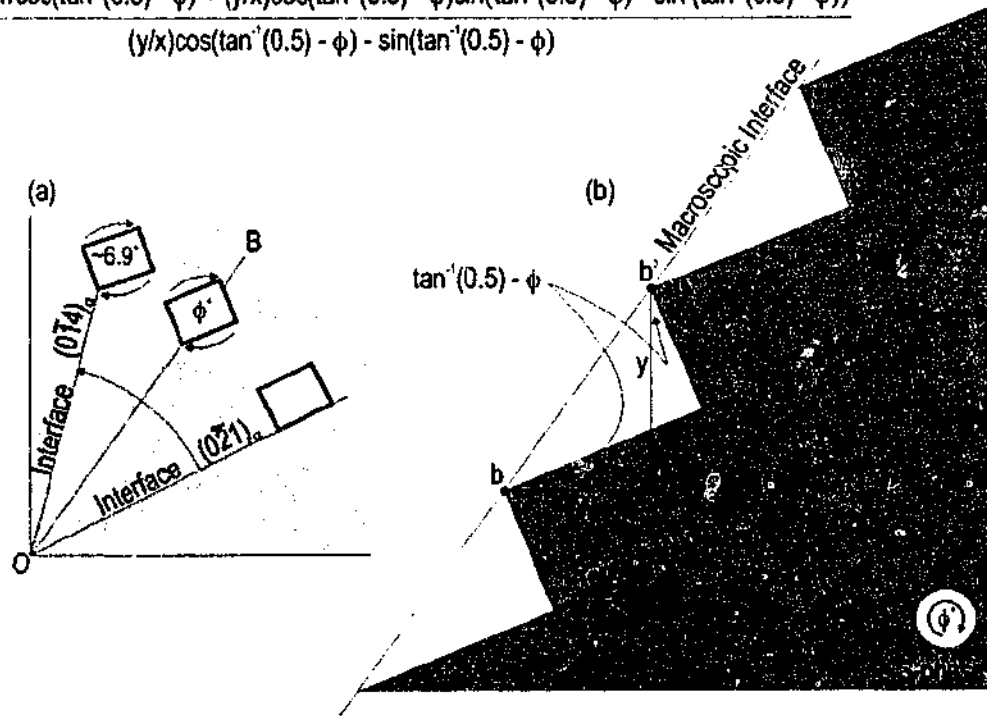


Figure 6.19 (a) Interface rotation is a function of lattice rotation. (b) The terrace width can be calculated as a function of the arbitrary lattice rotation.

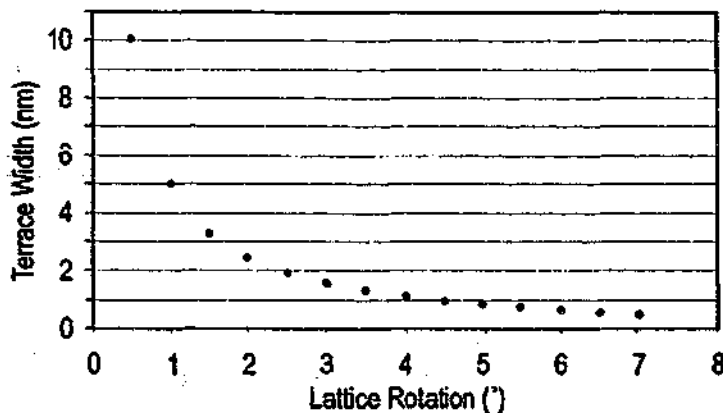


Figure 6.21 Terrace width plotted as a function of the lattice rotation, assuming that the relationship between the lattice rotation and the rotation of the macroscopic interface plane orientation is linear.

The expected width of the terrace plane (spacing between steps on the interface) is plotted as a function of the lattice rotation in figure 6.21, and the data are consistent with the requirement that the terrace width is infinite for particles in standard orientation. The terrace width of steps at particles rotated by $6.9^\circ \pm 0.25^\circ$ is close to 0.463 nm (equivalent to $0.5b_s$), and this expected since the interface plane of these particles is parallel to $(021)_s$ or $(0\bar{2}1)_s$, implying that a vector parallel to the interface and in the plane $(100)_s$ defines a transition of $0.5b_s$ for every $1c_s$.

6.3.3 Exceptions to the Model of Macroscopic Interface Orientation

The previous section presented evidence for steps at the interface that describe the macroscopic interface plane in particles that are rotated about $[100]_s // [100]_a$, and a plot of the orientation of the macroscopic interface plane as a function of lattice rotation suggests that they are linked. However, a significant (18%) proportion of the population of S-phase particles in the current alloys have a stepped macroscopic habit plane that *does not* behave in the manner described by figure 6.17. Figure 6.22(a) provides an example of a precipitate in standard orientation, with a step-free interface parallel to $(001)_s // (0\bar{1}2)_a$. In figure 6.22(b), the lattice orientation of the S-phase is $5.6^\circ \pm 0.25^\circ$ CCW from this standard orientation. Since the unit cell rotation is CCW from the nearest standard orientation relationship for the precipitate in figure 6.23(b), a CW rotation of the broad interface is to be expected, as discussed in the previous section. Instead, the broad interface is observed to rotate CCW (by $\sim 55^\circ$) with respect to the original broad interface (or 125° CW).

Closer analysis reveals that the nature of the broad particle-matrix interface at the precipitate in figure 6.22(b) is composed of steps that are larger than those observed previously in this chapter. These steps can be rationalised as $2c_s$ in height, as indicated in figure 6.23(b), and are immediately recognisable as those described by Radmilovic *et al.* [107] at the interface of the so-called Type II particles [107].

Nevertheless, the precipitate in figure 6.23(b) does have an interface that adheres to the behaviour described by figure 6.18, as indicated in figure 6.23(b). However, it is not the *broad* $2c_s$ interface, but rather the *minor* interfaces (fig. 6.23(b)), where the interface is noted to rotate by 49.4° . In this case, the shorter interface is characterised as lying approximately parallel to $(0\bar{2}1)_s // (0\bar{4}1)_a$, which is an interface orientation analogous to the broad interface previously identified for interfaces in particles rotated by $6.9^\circ \pm 0.25^\circ$.

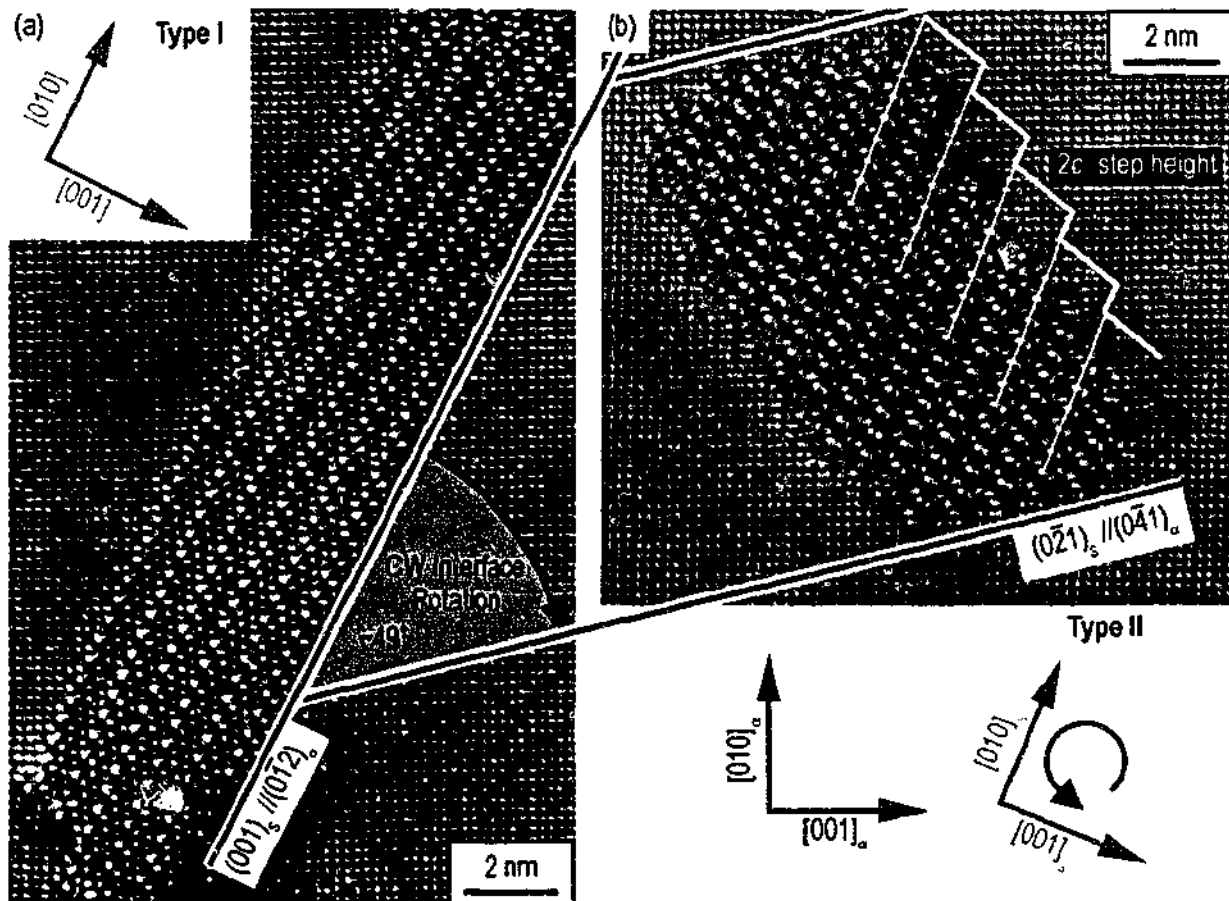


Figure 6.22 Type I and Type II precipitates, where it is demonstrated that the shorter interface is actually an interface comprising $1c_s$ steps and rotated from the interface of the standard orientation relationship from which it is rotated by a CW rotation of $\sim 49^\circ$.

6.4 Lattice Parameter of S-phase Unit Cell

Lattice parameters of the S-phase were examined by determining the length of appropriate vectors g (inversely proportional to d -spacing) in SAED patterns of volumes containing both matrix and precipitate phases. Figure 6.23 is a typical example used in the measurement of the magnitude of $g(010)_s$. The magnitude of vector $g(010)_s$ was always normalised as a fraction of the reciprocal lattice vector $g\{042\}_\alpha$ with which it was most closely aligned, and in the example provided, the normalising vector is $g(\overline{042})_\alpha$. Therefore, the first step in examining the SAED pattern of figure 6.23 was a measurement of the *magnitude* of both $g(\overline{042})_\alpha$ and $g(042)_\alpha$. Translation of the sliding cross-hair between intensity maxima defining $g(\overline{042})_\alpha$ and $g(042)_\alpha$ was performed while the cross hair was held consistently parallel to vector $g(02\bar{4})_\alpha$ (shaded line in fig. 6.23). The sum of the magnitudes of $g(\overline{042})_\alpha$ and $g(042)_\alpha$ was measured using a vernier scale with an accuracy of 0.0005 mm, and then divided by a factor of 2 to obtain the average magnitude. The magnitude of $g(010)_s$ was measured as the distance between the precipitate

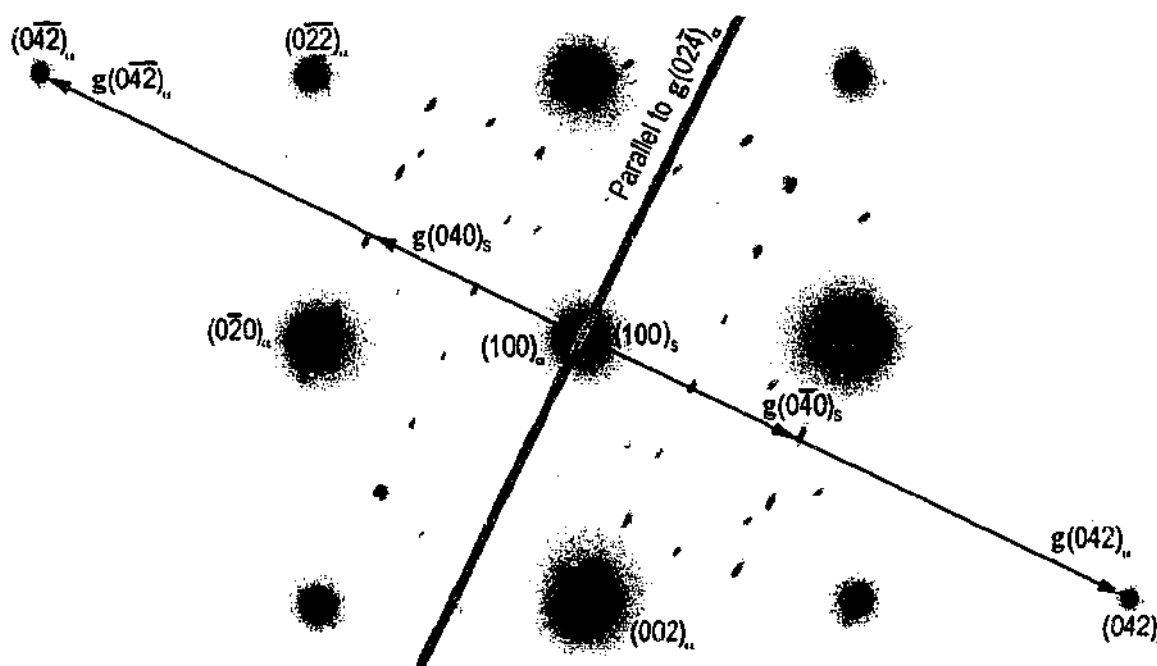


Figure 6.23 Typical SAED pattern of a volume containing both matrix and S-phase. Measurement of the magnitude of vectors $g(010)_s$ and $g(\overline{042})_\alpha$ proceeded by the placement of the cross-hair parallel to $g(02\bar{4})_\alpha$ and $g(001)_s$ respectively.

spots representing $(040)_s$ and $(\bar{0}\bar{4}0)_s$ while the cross-hair was held parallel to $g(001)_s$, and the subsequent division of this length by a factor of 8. The ratio of the magnitudes of $g(010)_s$ and $g(\bar{0}\bar{4}2)_a$ was then calculated directly.

Measurement of the magnitude of vectors g from SAED patterns was subject to the same error constraints encountered during inspection of the lattice orientation (§6.2). Errors were minimised during measurement of the magnitude of *precipitate* vectors g since the width of the cross-hair was near to the width of the intensity maxima. Potential problems were associated with placing a cross-hair on a *matrix* spot that is itself wider than the cross-hair. By using the diffracted intensity maxima defining $g\{042\}_a$ vectors, which were smaller than spots defining shorter matrix vectors g , the best possible accuracy was attained. Measurement of the ratio of the respective magnitudes of the vectors were measured reproducibly to within $\pm 0.5\%$, and at least three measurements were taken of each vector. A typical set of data is included in table 6.5. In the present case, the ratio of lattice spacing is recorded rather than an absolute value, obviously avoiding the involvement of microscope-specific parameters. Gupta *et al.* [130] suggested that the accuracy of measured lengths of vectors g in their electron diffraction patterns was 0.5%, while Hirsch *et al.* [211] suggests that the determination of lattice *parameters* from thin-film electron-diffraction techniques can not be performed with greater than 0.1% accuracy.

Figure 6.24 contains a plot of the magnitude of the ratio of $g(010)_a$ and $g\{042\}_a$ in overaged Al-0.2Cu-1.7Mg as a function of the lattice rotation for particles nucleated both at and removed from dislocations, as indicated, in overaged alloy Al-0.2Cu-1.7Mg. The ratio of the vectors decreases as the rotation increases, and can be approximated at 0.09925 for particles of the standard orientation relationship, and 0.09775 for particles rotated from the standard orientation by the maximum observed in the present work.

Table 6.5 Typical set of data collected for the calculation of $g(010)_s / g\{042\}_a$.

Rotation	$g(010)_s$ (mm)	$g\{042\}_a$ (mm)	$g(010)_s / g\{042\}_a$
$2.5^\circ \pm 0.25^\circ$	21.9600	2.1250	0.097241
	21.8875	2.13125	
	21.9000	2.13125	

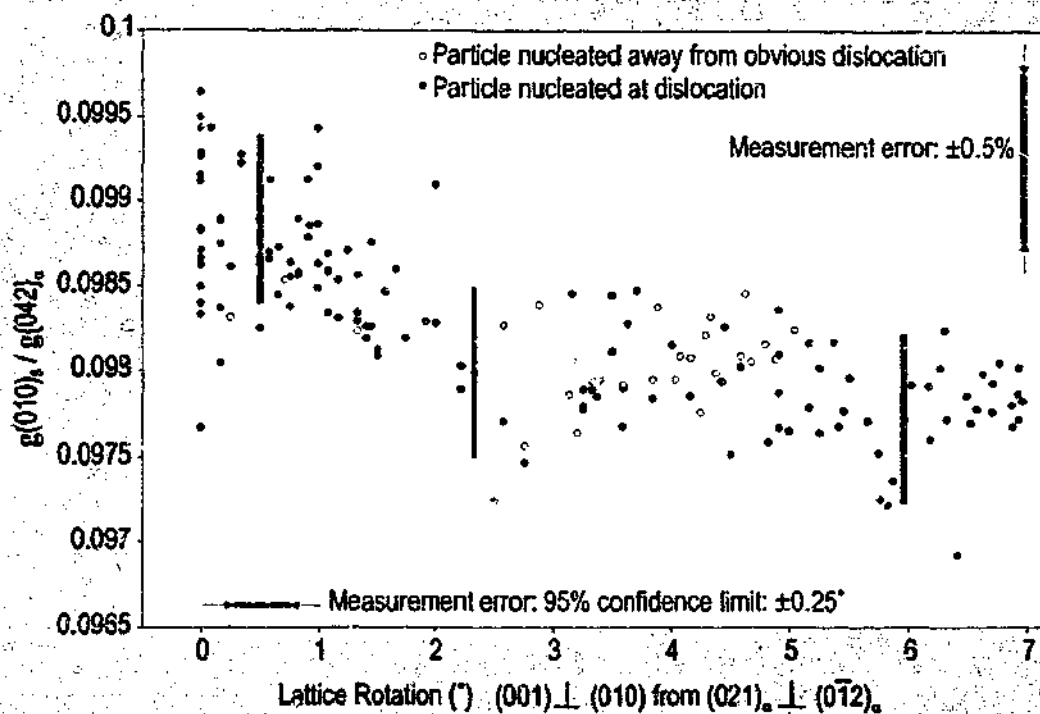


Figure 6.24 The ratio of the lengths of $g(010)_s$ and $g\{042\}_s$ from SAED patterns for particles of the S-phase nucleated both at and removed from dislocations, as indicated.

If it is assumed that the lattice parameter of the matrix phase is 0.40496 nm, then:

(i) Standard Orientation Relationship:

$$g(010)_s / g\{042\}_a = 0.09925$$

$$\therefore d\{042\}_a / d(010)_s = 0.09925$$

$$d(010)_s = d\{042\}_a / 0.09925 = 0.911 \text{ nm (within error range 0.907 nm - 0.916 nm).}$$

(ii) Orientation Rotated from the Standard by $6.9^\circ \pm 0.25^\circ$:

$$g(010)_s / g\{042\}_a = 0.09775$$

$$\therefore d\{042\}_a / d(010)_s = 0.09775$$

$$d(010)_s = d\{042\}_a / 0.09775 = 0.925 \text{ nm (within error range 0.921 nm - 0.931 nm).}$$

Owing to elongation of the diffraction maxima parallel to $g(001)_s$ for those particles of the S-phase elongated perpendicular to this vector (i.e. precipitate laths of the standard orientation, see §6.2.1), it was difficult to accurately and reliably measure the magnitude of $g(001)_s$. Therefore,

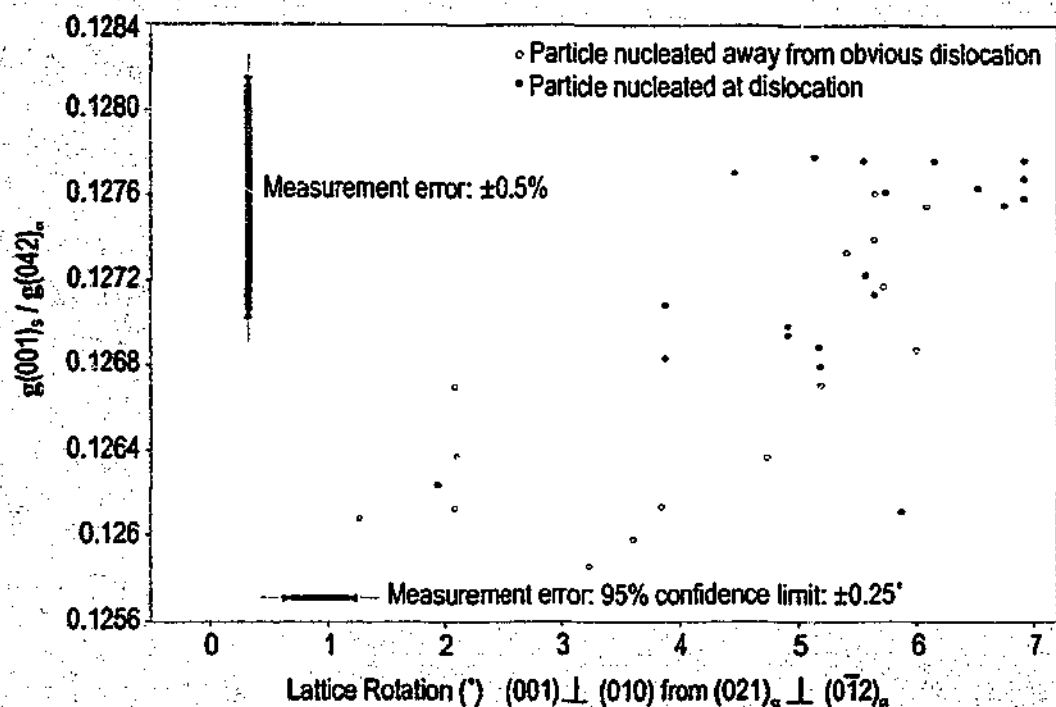


Figure 6.25 The ratio of the lengths of $g(010)_s$ and $g\{042\}_s$ from SAED patterns for particles of the S-phase nucleated both at and removed from dislocations.

only the magnitude of vectors $g(010)_s$ was recorded for laths in the standard orientation. However, the relative length of vector $g(001)_s$ was measurable for particles of a lesser aspect ratio, and the data was collected in a similar manner to that for $g(010)_s$. The normalised data is shown in figure 6.25 for particles nucleated both at and away from dislocation loops. Once again, a trend is observed, where an increasing rotation away from a variant of the standard orientation relationship results in systematic changes in the lattice spacing. However, in contrast to the case of $(010)_s$, where an increase in the lattice spacing ratio is noted as the misorientation increases, it is clear from the data in figure 6.25 that the ratio of lattice spacing $(001)_s / \{042\}_s$ decreases. This is intuitively consistent and leads to a unit cell volume that potentially remains constant. The lattice spacing of $(001)_s$ can be calculated if it is assumed that the lattice parameter of the matrix phase is 0.40496 nm, as follows.

(i) Standard Orientation Relationship:

$$g(001)_s / g\{042\}_s = 0.1256$$

$$\therefore d\{042\}_s / d(001)_s = 0.1256$$

$$d(001)_s = d\{042\}_s / 0.1256 = 0.721 \text{ nm (within error range } 0.717 \text{ nm} - 0.725 \text{ nm).}$$

(ii) Rotated from the Standard Orientation Relationship by $6.9^\circ \pm 0.25^\circ$:

$$g(001)_s / g\{042\}_\alpha = 0.1278$$

$$\therefore d\{042\}_\alpha / d(001)_s = 0.1278$$

$$d(001)_s = d\{042\}_\alpha / 0.1278 = 0.709 \text{ nm (within error range } 0.705 \text{ nm} - 0.713 \text{ nm)}.$$

Therefore, the lattice parameters of the S-phase, expressed as a ratio of the spacing in the matrix, increase parallel to $[010]_s$ and decrease parallel to $[001]_s$ when comparing particles in the standard orientation relationship to those that are rotated $6.9^\circ \pm 0.25^\circ$ from the standard orientation. This represents an anisotropic shape change of the unit cell.

6.5 Aspect Ratio of S-phase Precipitates

The aspect ratio of particles of the S-phase in projection parallel to $[100]_s // [100]_a$ was calculated by taking the quotient of the largest precipitate dimension and the width 90° to this dimension. Two representative examples (schematic) are provided in figure 6.26(a). Figure 6.26(b) presents the aspect ratio data collected according to the manner described. Precipitates in the standard orientation display a large aspect ratio of up to 7:1. Precipitates characterised by a high rotation ($6.9^\circ \pm 0.25^\circ$) and an interface parallel to $(0\bar{2}1)_s // (01\bar{4})_a$ have an aspect ratio that approaches that of the lath precipitate of standard orientation relationship. Particles intermediately oriented between these extremes always have a smaller aspect ratio, reaching unity at a misorientation of between $\sim 2^\circ$ and $\sim 4^\circ$.

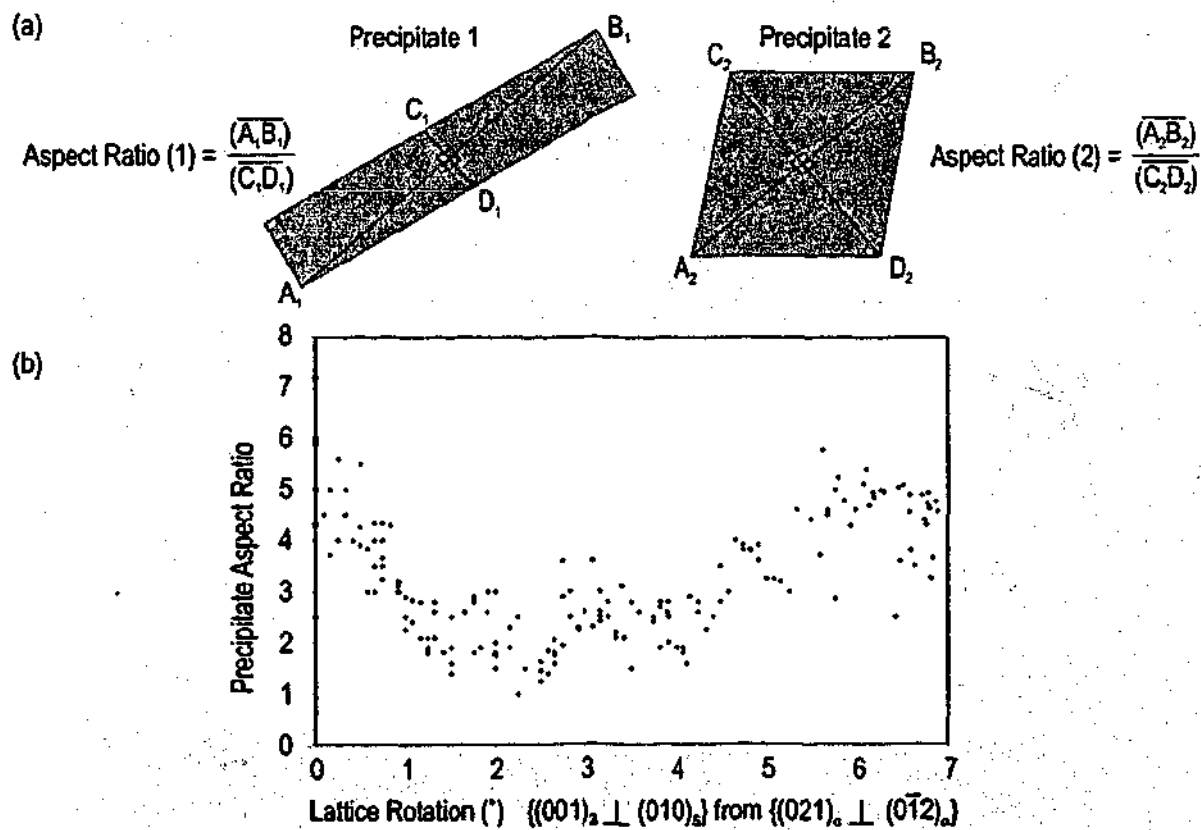


Figure 6.26 Calculation of aspect ratio, based only upon precipitate dimensions and regardless of S phase crystallography.

6.6 Interfacial Coherency

The planar coherence of the interface between S-phase particles and the matrix has been examined by phase contrast HREM and theoretical plane matching using a Moiré intersection approach. Firstly, the coherent interfaces of the *laths in the standard orientation relationship* have been examined. Secondly, interfaces comprising ledges $1c_s$ in height have been examined with reference to their departure from the planar coherency displayed by the lath precipitate of standard orientation relationship. Finally, the subset of particles with broad interfaces that are significantly more irregular and contain steps $2c_s$ in height will be addressed.

Consider two sets of planes $(h_1k_1l_1)$ and $(h_2k_2l_2)$ with prescribed interplanar spacing and misorientation, such as those described in figure 6.27. Both sets of planes, and therefore the plane of intersection, are parallel to the viewing direction. The orientation of the interface is then a function of the relative interplanar spacing of the plane sets and the angle between them, and in figure 6.24 the orientation of the intersection, β , is calculated with respect to the orientation of $(h_1k_1l_1)$. In the event that the planes $(h_1k_1l_1)$ and $(h_2k_2l_2)$ belong to different crystal structures, the plane of intersection defines the orientation of the heterophase interface between the two materials. Effective continuity of planes across the interface is described as *coherent* for any pairs of planes that match one-for-one across the interface. The ratio of interplanar spacing for

$$\beta = \sin^{-1} \left(\frac{d_2 \sin \theta}{d_2^2 + d_1^2 - 2d_1 d_2 \cos \theta} \right) \quad \text{and} \quad \beta = \sin^{-1} \left(\frac{\sin \theta}{(1 + R^2 - 2R \cos \theta)^{0.5}} \right)$$

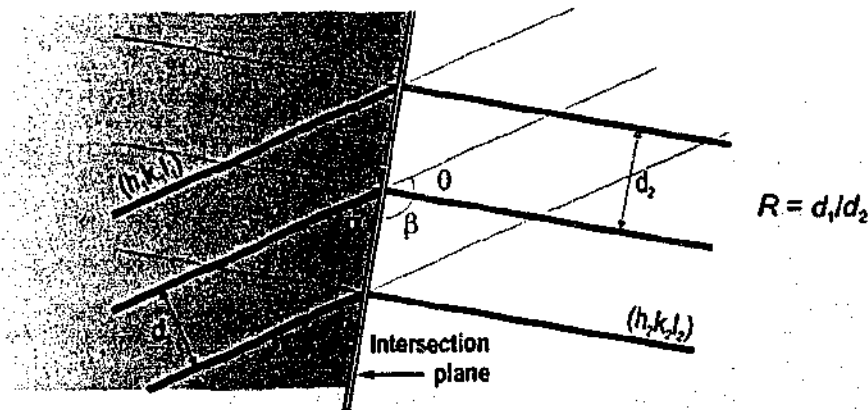


Figure 6.27 Geometrical representation of the orientation of the interface plane between a coherent pair of planes.

the two phases, $R = d_1/d_2$, may be used, together with the angle between the planes, to calculate the orientation of the interface, as described in figure 6.26. If the two sets of planes $(h_1k_1l_1)$ and $(h_2k_2l_2)$ do not meet coherently at the interface, the interface orientation *can not* be determined. In this case, the interface is termed either *partially coherent* or *incoherent*, where the former describes an interface with areas of coherent interface separated by the cores of *anticoherency dislocations*. In the latter case, the interface is characterised by the complete destruction of coherency such that the density of anticoherency dislocations within the interface is so great that their cores are indistinguishable [212].

According to Sutton and Balluffi [212], over the past 30 years there has been a proliferation in the types of interfacial dislocations that have been identified, and the application of different names for the same interfacial defect. Terms such as intrinsic, extrinsic, anticoherency, twinning, transformation, primary or crystal lattice interfacial dislocations, secondary, tertiary, virtual, surface, misfit, perfect, partial, Somigliana, Volterra and DSC dislocations have appeared in the literature [212]. It is not the purpose of the present investigation to treat exhaustively the structure of the heterophase interfaces with respect to the dislocation sub-structure. However, for selected cases, incoherency across the interfaces will be identified.

6.6.1 Coherent Interfaces of Laths of Standard Orientation

The lath precipitate of S-phase in figure 6.28 is described by a variant of the standard orientation relationship such that $(100)_S // (100)_\alpha$, $[001]_S // [0\bar{1}2]_\alpha$ and $[010]_S // [021]_\alpha$. Observation of the lattice fringes in the image are directly interpretable as lattice planes lying parallel to $[100]_S // [100]_\alpha$ (the elongation axis), at least with respect to the interplanar spacing (§3.4.3.2). Beginning with the $\{002\}_\alpha$ planes in the aluminium matrix, attempts are made to determine the planes in the S-phase that match the aluminium planes one-for-one at the interface, as indicated. This is also performed for the $\{022\}_\alpha$ planes. The coherency of the plane pairs is appreciated best by viewing the image near the plane of the page and parallel to the projections of the planes under investigation.

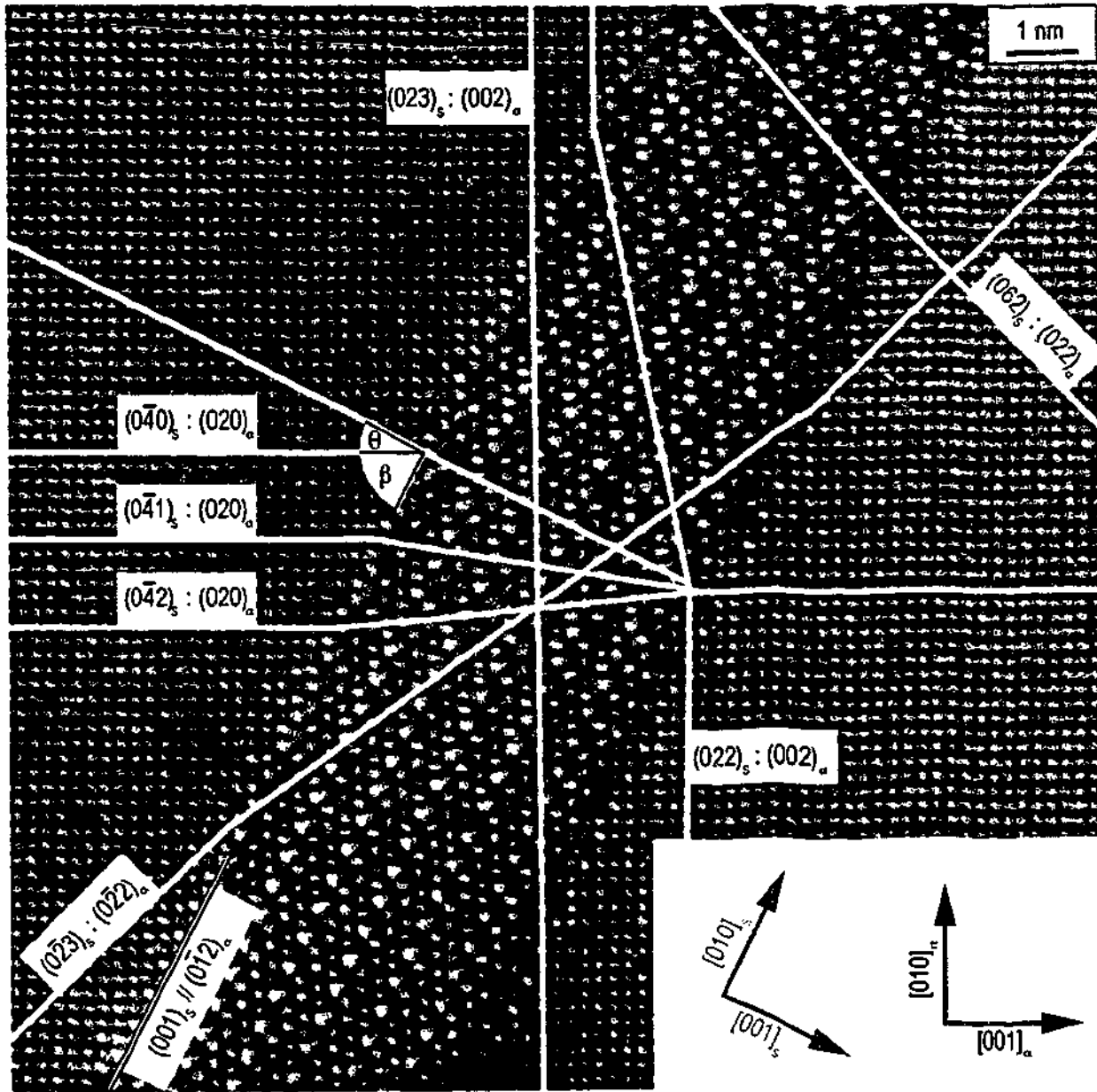


Figure 6.28 HREM image of lath precipitate of standard orientation, indicating the cases of low-index 1:1 plane matching across the atomically flat interface.

The *observed* angle θ_0 between the coherent planes identified is presented in table 6.6, together with the observed angle β_0 between the interface plane and the matrix plane. The ratio of lattice plane spacing for the precipitate and matrix planes implicated in the coherent pairs has been calculated according to the geometry of figure 6.26 and is purely based upon the observations of θ_0 and β_0 in figure 6.28 and may other examples similar to it. Note that the list of plane pairs identified is not exhaustive, but provides several obvious cases of coherency between low-index planes across the interface.

Table 6.6 Analysis of precipitates of standard orientation : θ_0 = observed angle between planes, β_0 = observed interface orientation, $R = d_S/d_\alpha$ is the ratio of lattice spacing for the planes implicated.

$(h_1k_1l_1) : (h_2k_2l_2)$	θ_0	β_0	$R = d_S/d_\alpha$
$(0\bar{4}1)_S : (020)_\alpha$	$9 \pm 0.25^\circ$	$63.5 \pm 2^\circ$	1.066
$(023)_S : (002)_\alpha$	$1.0 \pm 0.25^\circ$	$26 \pm 2^\circ$	1.036
$(062)_S : (022)_\alpha$	$3.5 \pm 0.25^\circ$	$108 \pm 2^\circ$	0.978
$(0\bar{2}3)_S : (0\bar{2}2)_\alpha$	$9.5 \pm 0.25^\circ$	$18.5 \pm 2^\circ$	1.480
$(0\bar{4}2)_S : (020)_\alpha$	$6.5 \pm 0.25^\circ$	$116 \pm 2^\circ$	1.049
$(0\bar{4}0)_S : (020)_\alpha$	$26.5 \pm 0.25^\circ$	$63.5 \pm 2^\circ$	1.117
$(022)_S : (002)_\alpha$	$12.2 \pm 0.25^\circ$	$26 \pm 2^\circ$	1.411

6.6.2 Interfaces with Ledges

6.6.2.1 *Ledges of l_S Riser Height*

All particles rotated from the standard orientation about $[100]_S // [100]_\alpha$ contains steps l_S in height. It is useful to examine first the particles that are rotated by the maximum observed in the present work. The precipitate shown in figure 6.29 is a precipitate of the S-phase that is rotated by $6.9^\circ \pm 0.25^\circ$ about $[100]_S // [100]_\alpha$ from a variant of the standard orientation relationship, exhibiting a broad particle-matrix interface that is parallel to $(0\bar{2}1)_S // (041)_\alpha$. The seven identified pairs of planes that are coherent across the interface of the laths of standard orientation are investigated for coherency across the $(0\bar{2}1)_S // (041)_\alpha$ interface. Solid lines in figure 6.26 indicate plane pair coherency while broken lines indicate discontinuity.

Upon inspection, three plane pairs are coherent across the interface of the original seven coherent plane pairs at laths of standard orientation: $(0\bar{4}1)_S : (020)_\alpha$, $(023)_S : (002)_\alpha$ and $(062)_S : (022)_\alpha$. The remaining four of the seven pairs of planes identified are no longer coherent across the interface.

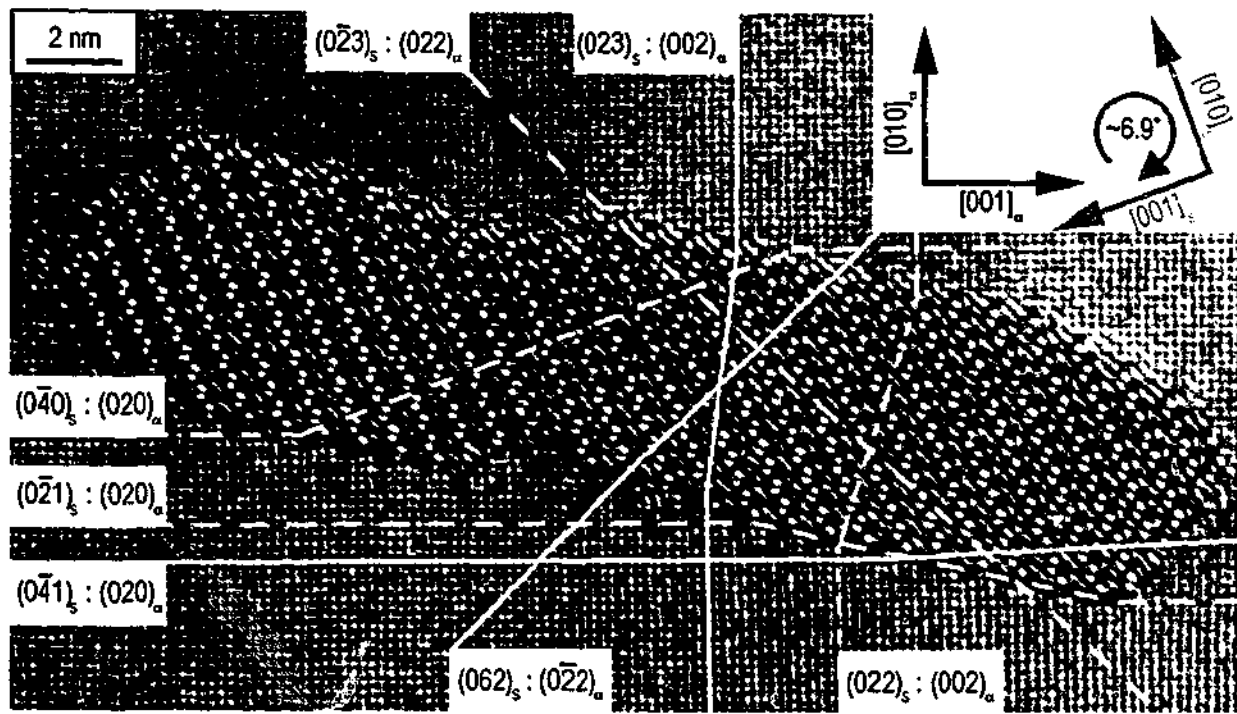


Figure 6.29 HREM image of a particle of the S-phase that is rotated $6.9^\circ \pm 0.25^\circ$ from a variant of the standard orientation relationship, indicating the cases of low-index 1:1 plane matching across the atomically flat interface. Dotted lines represent plane pairs that were matched 1:1 in the laths of standard orientation, but not in these highly rotated particles.

The observed values of θ_0 and β_0 are provided in table 6.5 for those cases where the planes are coherent, together with the calculated $R = d_S/d_\alpha$ for the observations. For those cases where coherency was not maintained, calculation of the plane spacing ratio was not possible.

Table 6.7 Analysis of precipitates of the S-phase rotated $6.9^\circ \pm 0.25^\circ$ from a variants of the standard orientation relationship: θ_0 = observed angle between planes, β_0 = observed interface orientation, $R = d_S/d_\alpha$ is the ratio of lattice spacing for the planes implicated..

$(h_1 k_1 l_1) : (h_2 k_2 l_2)$	θ_0	β_0	$R = d_S/d_\alpha$
$(0\bar{4}1)_S : (020)_\alpha$	$\sim 1.1^\circ$	$\sim 14^\circ$	1.077
$(023)_S : (002)_\alpha$	$\sim 7.5^\circ$	$\sim 76^\circ$	1.024
$(062)_S : (0\bar{2}2)_\alpha$	$\sim 1.25^\circ$	$\sim 122^\circ$	0.986
$(0\bar{2}3)_S : (022)_\alpha$		Incoherent	
$(0\bar{4}2)_S : (020)_\alpha$		Incoherent	
$(0\bar{4}0)_S : (020)_\alpha$		Incoherent	
$(022)_S : (002)_\alpha$		Incoherent	

The precipitate of the S-phase in the HREM image of figure 6.30 is rotated CW by $4.2^\circ \pm 0.25^\circ$ from a variant of the standard orientation relationship. The planar coherency between $(0\bar{4}1)_S$ and $(020)_\alpha$ is indicated by a continuous line across the interface. Similarly, the 1:1 coherency of $(023)_S$ and $(002)_\alpha$, and $(062)_S$ and $(0\bar{2}2)_\alpha$ are indicated. Coherent plane matching between $(0\bar{2}3)_S$ and $(022)_\alpha$ is absent. Similarly, the $(0\bar{4}0)_S : (020)_\alpha$, $(022)_S : (002)_\alpha$ and $(0\bar{4}2)_S : (020)_\alpha$ plane pairs do not display coherency across the interface. This resembles the observations of particles rotated by $6.9^\circ \pm 0.25^\circ$ about $[100]_S : [100]_\alpha$, and suggests that all particles rotated from the standard orientation maintain perfect planar coherency in these three planes pairs only.

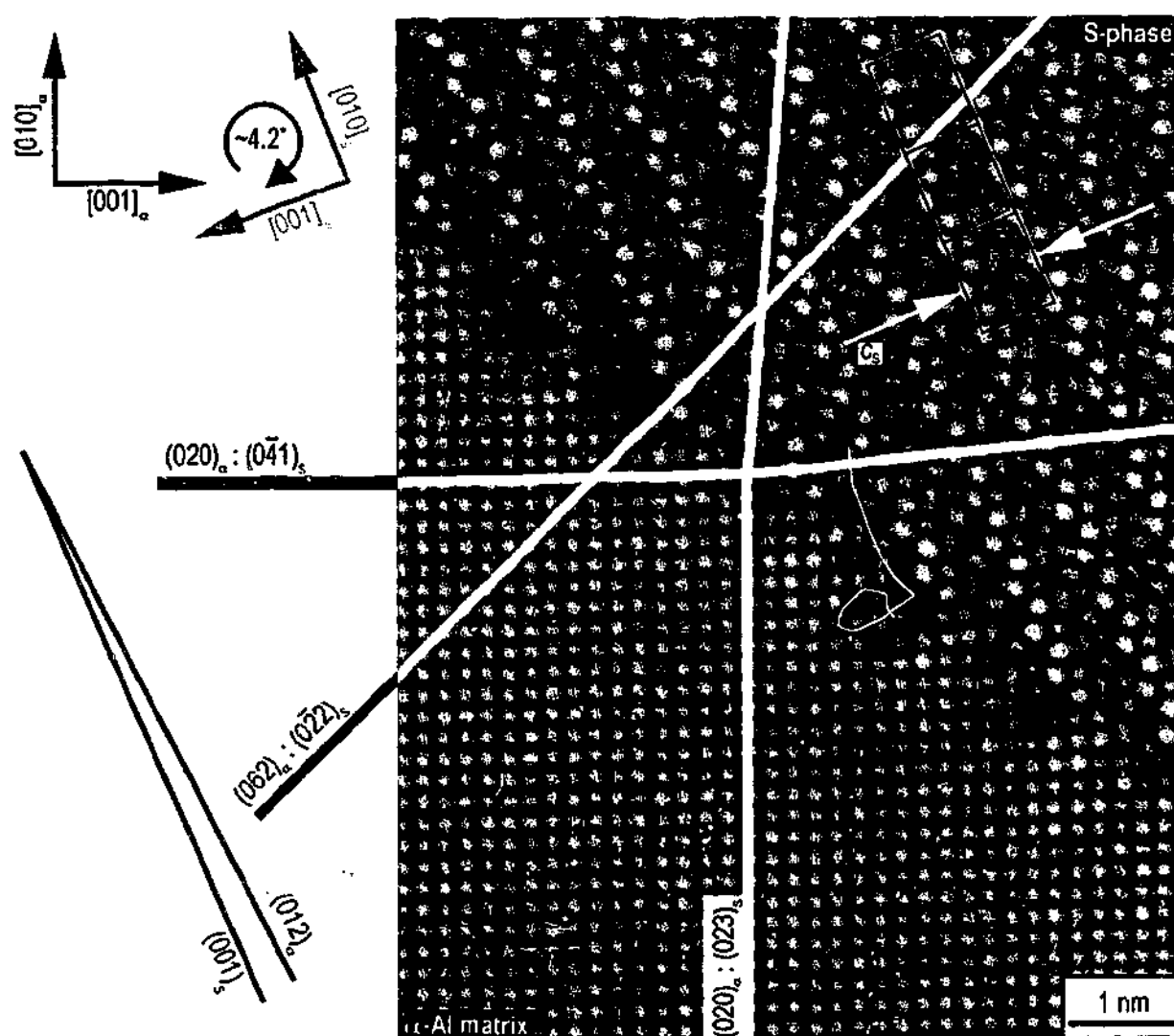


Figure 6.30 S-phase precipitate rotated from the standard orientation relationship by $4.2^\circ \pm 0.25^\circ$. The interface is composed of steps $1c_s$ in height.

6.6.2.2

Ledges of $2c_S$ Step Height

Figure 6.31 is a HREM image of the interface structure of an interphase boundary between matrix and precipitate, characterised by ledges of $2c_S$ step height. The riser plane of the S-phase is apparently parallel or near to parallel to $(011)_\alpha$, while the terrace plane of $(001)_S$ is parallel to the $(0\bar{1}2)_\alpha$ matrix plane. The latter arrangement is similar to the habit plane of the S-phase laths as previously recorded, where good atomic matching is observed. Note the analogy between this arrangement of step separated by good atomic matching and the situation described previously for the ledges of $1c_S$ step height.

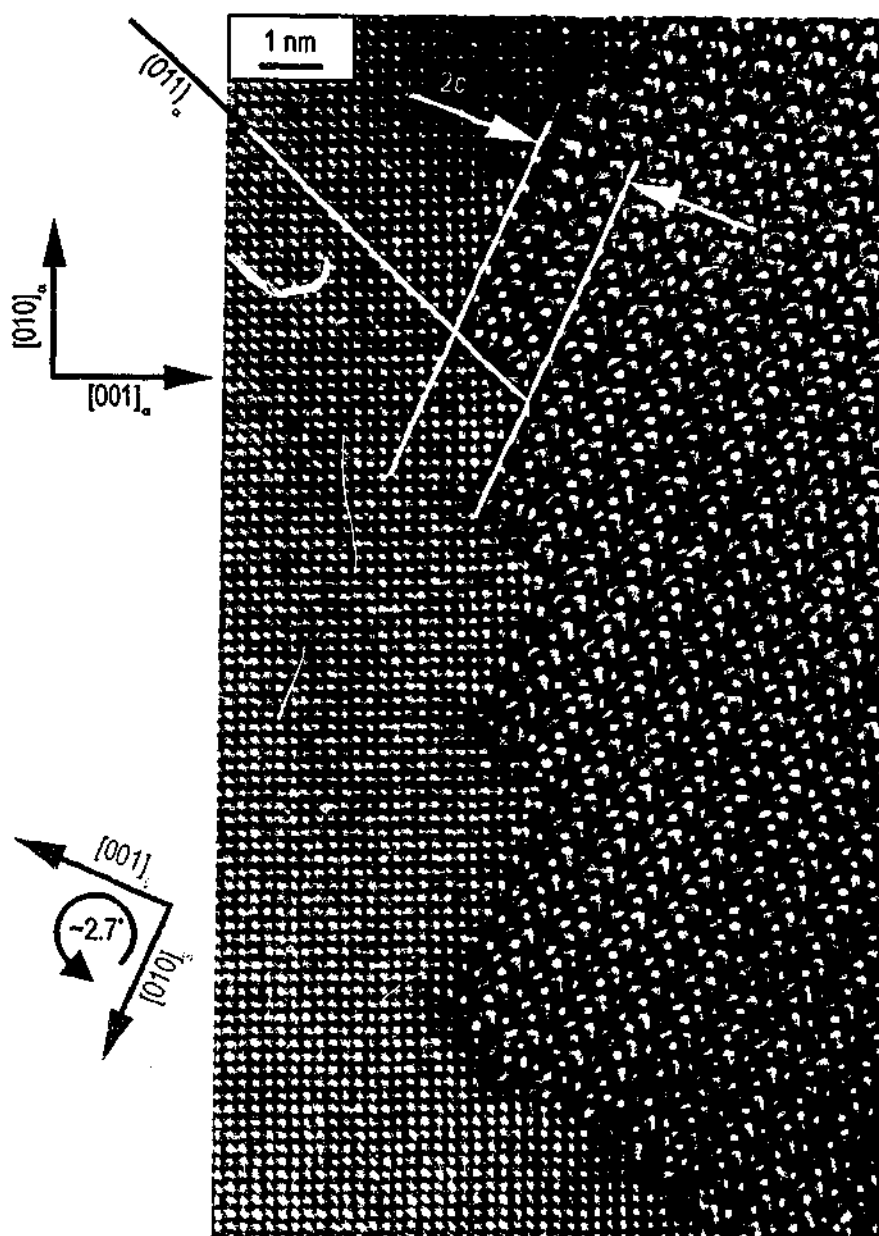


Figure 6.31 Matrix-S-phase interface structure characterised by ledges of $2c_S$ step height.

Table 6.8 Analysis of interfaces with steps $2c_s$ in height. The interfaces have been examined for planar coherency of the three plane pairs identified to consistently maintain coherency across all $1c_s$ interfaces.

$(h_1 k_1 l_1) : (h_2 k_2 l_2)$	Comments
$(0\bar{4}1)_s : (020)_a$	Coherent between steps but a $(020)_a$ plane terminates at every $2c_s$ step
$(023)_s : (002)_a$	Coherent between steps but a $(002)_a$ plane terminates at every $2c_s$ step
$(062)_s : (022)_a$	Coherent

Coherency across the interface containing steps $2c_s$ in height has been investigated for the three coherent plane pairs previously identified. In both cases implicating $\{002\}_a$ planes, an antioherency dislocation in the matrix (i.e. a terminating $\{002\}_a$ plane) occurs at every step, between which the matching is perfect (table 6.8). This terminating fringe of matrix material could be observed at the $2c_s$ ledges at the interface of real particles using HREM, as shown in figure 6.32 for the case of the plane pair of $(0\bar{4}1)_s : (020)_a$. Similarly, although it is not shown, an extra half-plane can be observed 90° from $(020)_a$, i.e., $(002)_a$, where the matching plane in the S-phase is $(023)_s$. The ledges that contain the dislocations are closely spaced (often only less than 1 nm) such that detection by conventional diffraction contrast is difficult.

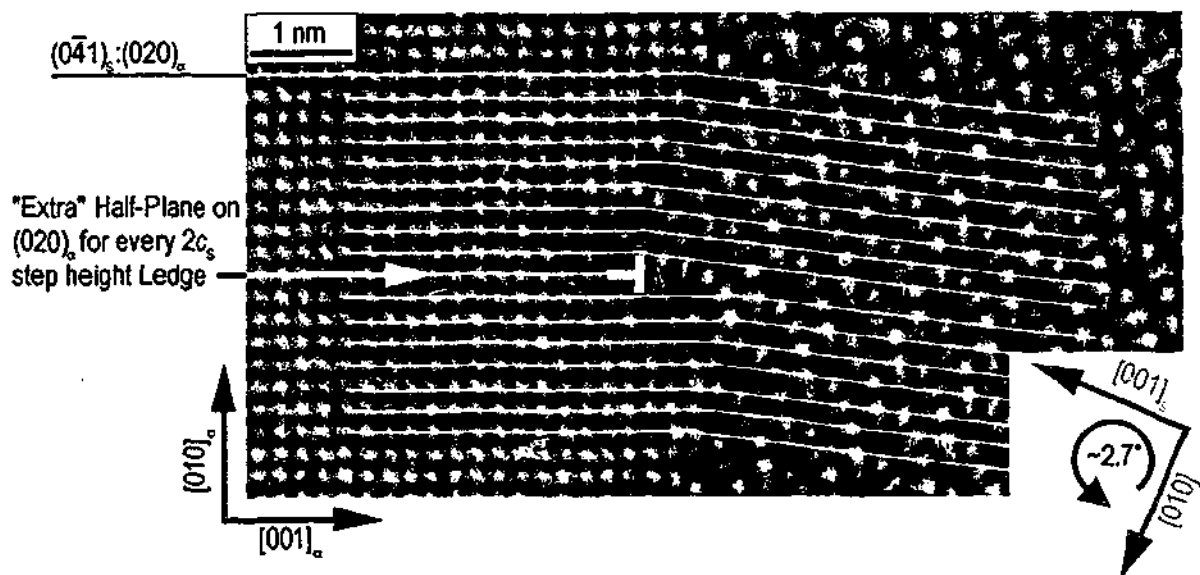


Figure 6.32 Plane matching of $(0\bar{4}1)_s$ and $(020)_a$, revealing extra matrix plane at every $2c_s$ step.

6.7 Interpretation of Results

In this chapter, the following key results have been recorded:

- The range of orientations that precipitates of S-phase may exhibit corresponds to an apparently continuous rotation of up to $6.9^\circ \pm 0.25^\circ$ of the mutually orthogonal $(010)_S$ and $(001)_S$ planes away from the standard orientation about the long axis ($[100]_S // [100]_a$). The lattice rotation always leads to a reduction in the angle between $(0\bar{2}1)_S$ (σ_1 $(021)_S$) and $\{041\}_a$. The angle between these planes is calculated between 7.31° [107] and 8.6° [130] in the standard orientation relationship.

- The orientation of the particle-matrix interface containing steps $1c_S$ in height varies systematically with the apparently continuous lattice rotation about $[100]_S // [100]_a$. The interface is parallel to $\{021\}_a$ at particles in the standard orientation relationship, and 49.4° away and parallel to $\{014\}_a$ at particles in lattice orientation rotated $6.9^\circ \pm 0.25^\circ$ from the standard orientation. The rotation of the interface occurs in a sense opposite to the lattice rotation.

- The aspect ratio of the precipitates in the plane normal to the long axis of the precipitate is a function of the lattice rotation, and particles in standard orientation and those that are rotated by $6.9^\circ \pm 0.25^\circ$ about $[100]_S // [100]_a$ from the standard orientation have the highest aspect ratio.

- Interfaces are composed of ledges either $1c_S$ or $2c_S$ in height, each representing contrasting departures from the planar, coherent interface of laths of standard orientation.

- The ratio of the lattice parameter b_S to the matrix lattice spacing appears to increase by $\sim 1.5\%$ between the standard orientation and those particles rotated by $6.9^\circ \pm 0.25^\circ$ about $[100]_S // [100]_a$, while the c_S lattice parameter ratio appears to decrease by a similar amount.

- Moiré intersection plane analysis suggests that the ratio $R = d_S/d_a$ is different for laths in the standard orientation and those in an orientation rotated $6.9^\circ \pm 0.25^\circ$ from the standard orientation about $[100]_S // [100]_a$ by approximately 1%.

An interpretation of the results follows, leading to a significantly expanded description and understanding of the crystallography of embedded particles of the S-phase.

6.7.1 Redefinition of the Orientation of S-phase Precipitates

The results of the current chapter (§6.2.2) reveal that the rotation about $[100]_S // [100]_a$ is unidirectional and may be up to $6.9^\circ \pm 0.25^\circ$, resulting in a reduction in the angle between vectors g representing $(\bar{0}21)_S$ and $(014)_a$ in composite SAED patterns (§6.2.2). The HREM images of particles rotated by the extent described are always characterised by a particle-matrix interface that is parallel to $(014)_a$ and $(\bar{0}21)_S$. Hence, the rotation not only reduces the angle between these planes, but obviously makes them parallel. The angle between these two planes in the standard orientation relationship depends upon the lattice parameters used, and is approximately 8° (§6.2.2). The manner in which a rotation of only $6.9^\circ \pm 0.25^\circ$ leads to the closure of an angle of this magnitude will be discussed in the following section. Figure 6.33 displays a particle in standard orientation, where the characteristic broad interface parallel to $(001)_S // (021)_a$ is indicated. The orientations of both $(021)_S$ and $(\bar{0}21)_S$ are included, as are the orientations of the four possible variants of $\{041\}_a$ parallel to $[100]_S // [100]_a$. It is clear that an angle of $\sim 8^\circ$ exists only between the pair of planes $(\bar{0}21)_S$ and $(014)_a$, and therefore these planes are parallel following the observed maximum rotation. If these planes are parallel, then they must also be parallel to the interface of a particle that is rotated by $6.9^\circ \pm 0.25^\circ$ from the standard orientation described.

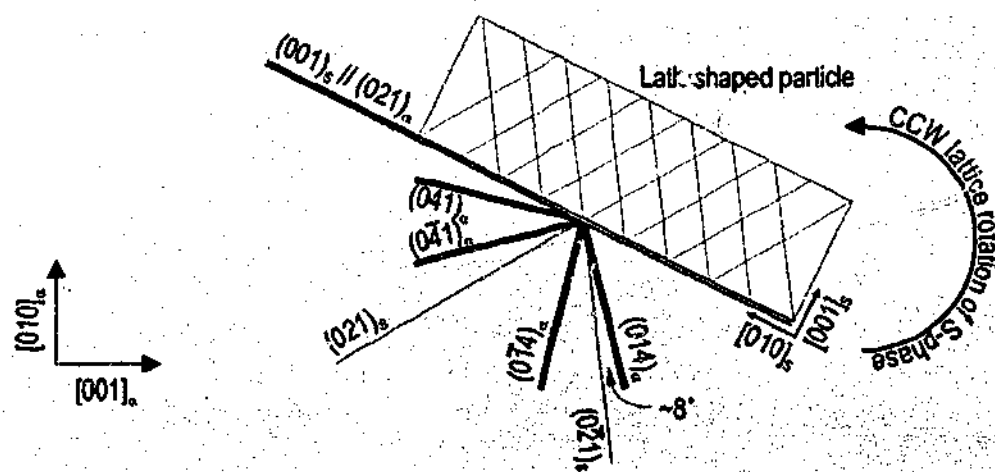


Figure 6.33 Orientation of $(021)_S$ and $(\bar{0}21)_S$, and the four $\{041\}_a$ planes parallel to $[100]_S // [100]_a$. The critical pair of planes that are parallel to the particle-matrix interface are separated by an angle of $\sim 8^\circ$.

Figure 6.34 displays the four variants of the S-phase parallel to $[100]_s // [100]_a$ and the broad interfaces parallel to $(001)_s // \{021\}_a$ are labelled in all cases. The precipitate in figure 6.34(a) is an example of Variant 1 of the standard orientation relationship, where the variant nomenclature (i.e. Variant 1, Variant 2 etc.) is consistent with that used in the stereographic projections of figure 6.9. In figure 6.34, rotated particles belonging to the set of precipitates defined by Variant 1 and Variant 2 must rotate CCW, while rotated particles belonging to the set of precipitates defined by Variant 3 and Variant 4 must rotate CW, in agreement with the lattice rotation indicated in figure 6.9. As an example of the symmetry of the S-phase, a rotational operation of

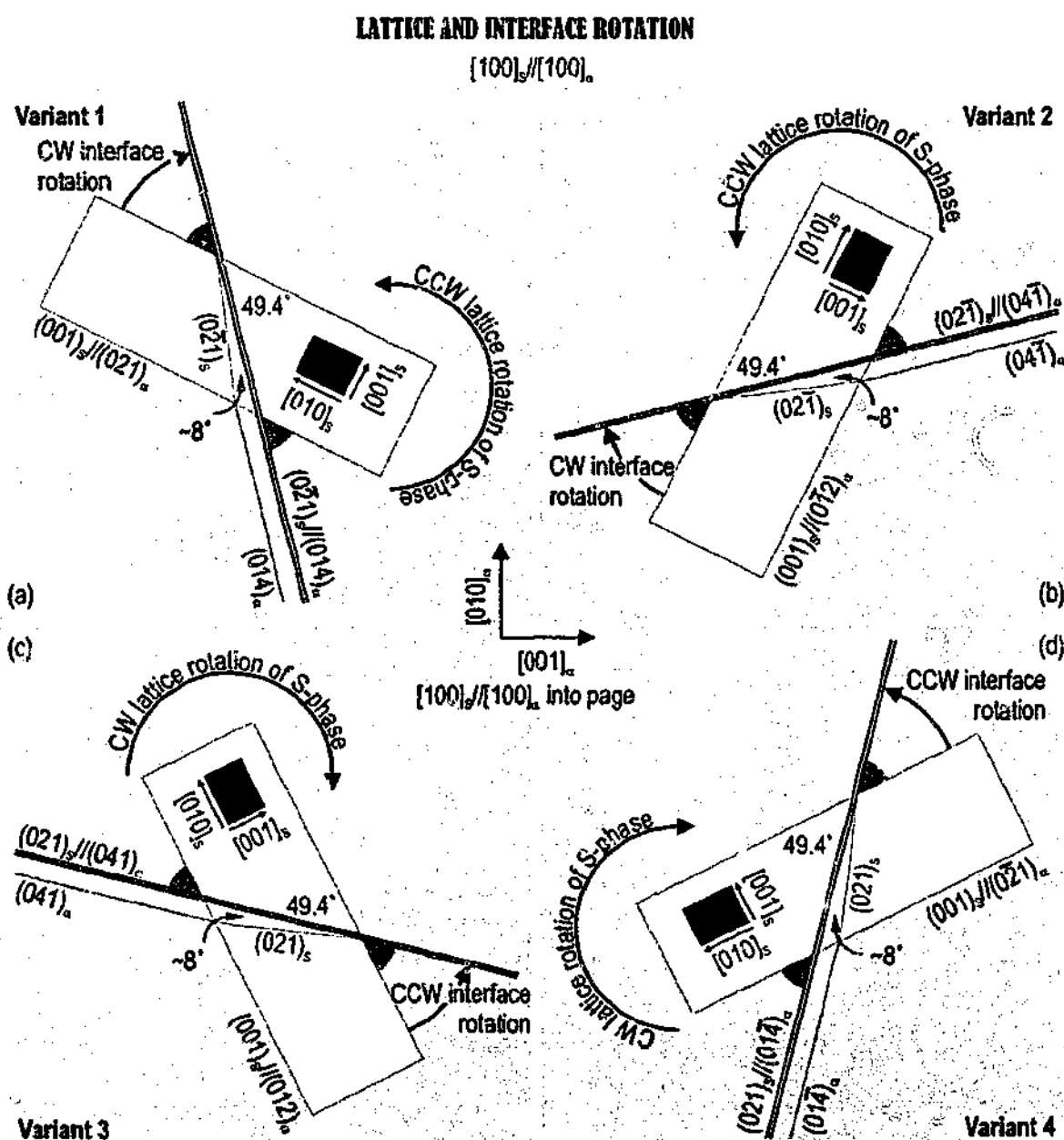


Figure 6.34 The four variants of the standard orientation of precipitates of the S-phase in an aluminium matrix. The nomenclature (Variant 1, Variant 2 etc.) is consistent with that used in figure 6.9.

180° about $[010]_\alpha$ of Variant 1 reveals an orientation analogous to that of Variant 4. In all particles rotated by the maximum observed in the present work, $6.9^\circ \pm 0.25^\circ$, the interface is rotated 49.4° away from the original lath interface, and as described in the experimental results of this chapter (§6.3.1), a rotation of the broad particle-matrix interface occurs in a sense opposite to that of the lattice rotation.

The morphology and orientation relationship of particles rotated by $6.9^\circ \pm 0.25^\circ$ from the standard orientation relationships are such that it is useful to label it as a separate orientation relationship rather than a rotation away from a defined orientation relationship. The standard orientation relationship $[125]$ will now be referred to as Rational Orientation Relationship 1 (ROR1), and the particles rotated by $6.9^\circ \pm 0.25^\circ$ about $[100]_s // [100]_\alpha$ from ROR1 as Rational Orientation Relationship 2 (ROR2). These are formally defined as:

$$(100)_s // (100)_\alpha, [001]_s // [021]_\alpha \text{ and } [010]_s // [01\bar{2}]_\alpha \quad (\text{ROR1})$$

$$(100)_s // (100)_\alpha, [0\bar{2}1]_s // [014]_\alpha \quad (\text{ROR2})$$

Therefore, in representative microstructures of appropriately aged Al-Cu-Mg alloys, there will be 12 variants of ROR1 and 12 variants of ROR2.

6.7.2 The Strained Lattice of the S-phase in ROR1 and ROR2

Several observations, either directly or indirectly, suggest that the unit cell dimensions of S-phase may vary with orientation. These observations include:

- Direct measurement of the ratio of lattice parameters of pairs of precipitate/matrix planes using SAED. The measurements were not absolute, but they detected a clear trend.
- A lattice rotation of $6.9^\circ \pm 0.25^\circ$ of the precipitate in the fixed lattice from ROR1 to ROR2 results in $(0\bar{2}1)_S$ oriented parallel to $(014)_\alpha$. However, the angle between these planes is 8.32° in ROR1.
- To maintain coherency across the broad interfaces of precipitates in both ROR1 and ROR2, it can be shown that the unit cell size can not be constant (if the lattice is unchanged) within the range of lattice parameters observed here or in the literature.
- The predictions of $R = d_S/d_\alpha$ for the three specific and coherent sets of planes across all interfaces of arbitrary orientation is different for particles in ROR1 and ROR2.

The following discussion focuses upon cross-correlating and verifying these independent issues that indicate a change in lattice parameter ratio. Because of the obvious elongation axis parallel to $[100]_S // [100]_\alpha$, the lattice spacing of the planes $(100)_S // (100)_\alpha$ was not considered. Instead, interest was concentrated upon planes in the precipitate phase that were parallel to $[100]_S // [100]_\alpha$, since these are the planes that define the morphology of particles in $(100)_S$. Finally, reference has been made to data in the literature and to the historical debate over the range of lattice parameters observed in precipitates of the S-phase.

The lattice parameters of the S-phase determined by the ratio of reciprocal lattice vectors g in SAED patterns measured here are consistent with an anisotropic change in the shape of the unit cell in $(100)_S$, where:

$$\begin{array}{llll}
 b_S = 0.911 \pm 0.005 \text{ nm} & c_S = 0.721 \pm 0.004 \text{ nm} & \{\text{area in } (100)_S = 0.6568 \text{ nm}^2\} & \text{ROR1} \\
 b_S = 0.925 \pm 0.005 \text{ nm} & c_S = 0.709 \pm 0.004 \text{ nm} & \{\text{area in } (100)_S = 0.6558 \text{ nm}^2\} & \text{ROR2}
 \end{array}$$

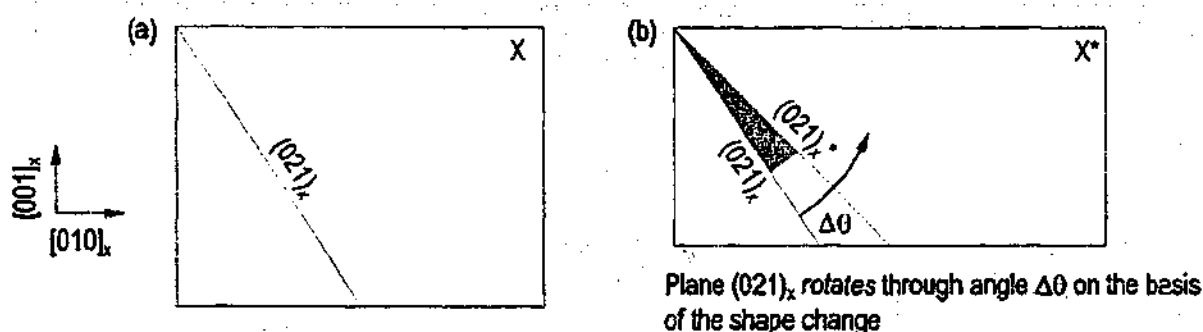


Figure 6.35 (a) Generic unit cell of X. The orientation of $(021)_X$ is shown. (b) Unit cell of X^* , a strained version of the unit cell of X, elongated parallel $[010]_X$ and contracted parallel to $[001]_X$. The lattice strain effects a CCW rotation of $(021)_X$.

The difference in orientation between a variant of ROR1 and the nearest variant of ROR2 is a $6.9^\circ \pm 0.25^\circ$ lattice rotation about $[100]_S // [100]_a$ according to the SAED data, and is assessed as the misorientation of the mutually perpendicular $(010)_S$ and $(001)_S$ planes from the respective $\{021\}_a$ planes with which they are parallel in the standard orientation. Particles in ROR2 are defined by a pair of parallel planes, $(0\bar{2}1)_S // (014)_a$, that are misoriented by 8.32° in ROR1, which is significantly greater than $6.9^\circ \pm 0.25^\circ$. Local lattice distortions at the interface may allow such a rotation to be observed, and rotations of up to $\sim 8^\circ$ from ROR1 and about $[100]_S // [100]_a$ have been detected in the local vicinity at the particle-matrix interface in HREM images of particles in ROR2. However, in the general case, the local rotation from ROR1 was equivalent to that measured by SAED, and its greatest deviance was only marginally ($\sim 0.5^\circ$) different to the SAED data. If two candidate planes are parallel following a lattice rotation, and the misorientation between these planes prior to rotation is greater than the magnitude of the actual rotation, an anisotropic shape change of the unit cell is required. The shape change of the unit cell causes a *virtual rotation* in the precipitate plane prior to the lattice rotation, and this has been illustrated for the general case in figure 6.35, resulting in a CCW virtual rotation of $(021)_X$ through an angle $\Delta\theta$. Upon subsequent lattice rotation, $\Delta\theta$ is either additive or subtractive for CCW and CW lattice rotations respectively. Therefore, in the present case, a change in unit cell aspect ratio is expected between particles in ROR1 and ROR2.

The invocation of an anisotropic change in the unit cell can also be shown by the observations of planar coherency across the broad interfaces. Figure 6.36(a) superimposes a unit cell of the S-phase upon the matrix lattice consistent with ROR1, and coherency implies that $b_{S(ROR1)} = \sqrt{5}a_a$. The length of c_S , which ranges in size from $0.761b_S [107]$ to $0.8b_S [130]$ as a scaled product of b_S ,

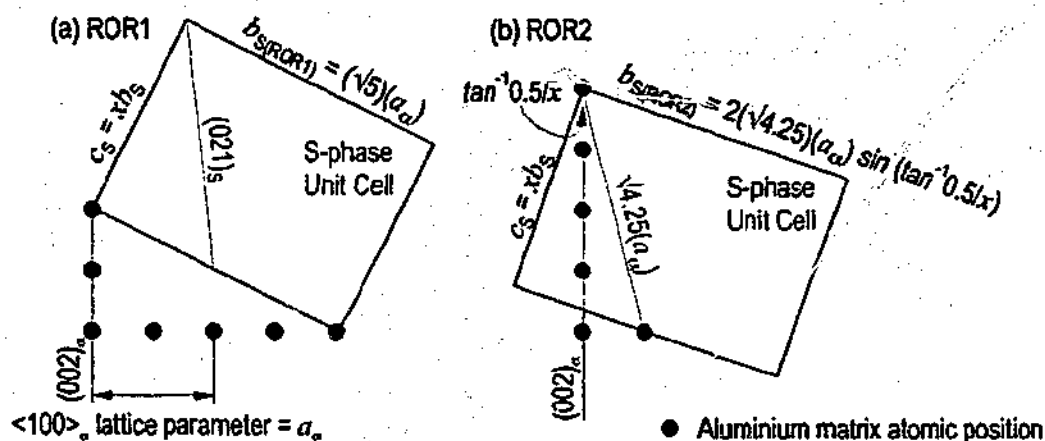


Figure 6.36 The coherent habit planes of precipitates of the S-phase parallel to (a) $\{021\}_\alpha$ and $(001)_s$ (ROR1) and (b) $\{014\}_\alpha$ and $(021)_s$ (ROR2).

is unimportant with respect to coherency at the interface since the lattice vector lies perpendicular to the particle habit plane. Figure 6.36(b) superimposes a unit cell of the S-phase upon the matrix in a manner consistent with ROR2. In this case, c_s is important, since it is a component of all vectors parallel to the broad particle-matrix interface $(021)_s$, and its arbitrary length with respect to the length of b_s is defined as xb_s where x is a scalar multiple. The length of b_s in ROR2 can be calculated as a function of x and the length of matrix vector $\frac{1}{2}\langle 014 \rangle_\alpha = \sqrt{4.25}(a_\alpha)$, as shown. If the length of $b_{s(ROR2)} = b_{s(ROR1)} = \sqrt{5}a_\alpha$ (i.e. an unchanged unit cell size) then $x = 0.775$ and $c_s = 0.701$ nm (assuming $a_\alpha = 0.40496$ nm). Therefore, coherency can be maintained across the broad interfaces of particles in both ROR1 and ROR2 if $b_s = 0.905$ nm and $c_s = 0.701$ nm. However, coherence is established only by a lattice rotation of the S-phase equal to 7.75° , calculated as follows:

$$\begin{aligned} & \text{Angle between } (021)_s \text{ and } (002)_\alpha: \\ \text{ROR1: } & \tan^{-1}\left(\frac{0.905/2}{0.701}\right) - 26.56^\circ = 6.28^\circ \\ \text{ROR2: } & \tan^{-1}(0.25) = 14.03^\circ \end{aligned}$$

$$\therefore \text{Misorientation in } (021)_s \text{ between ROR1 and ROR2} = 7.75^\circ$$

A lattice rotation of 7.75° can not be reconciled with the experimental data. Furthermore, there is no justification in the literature [107,112,130,148,152] for a c_s lattice parameter as small as 0.701 nm. Hence, an anisotropic shape change of the unit cell of the S-phase must again be invoked.

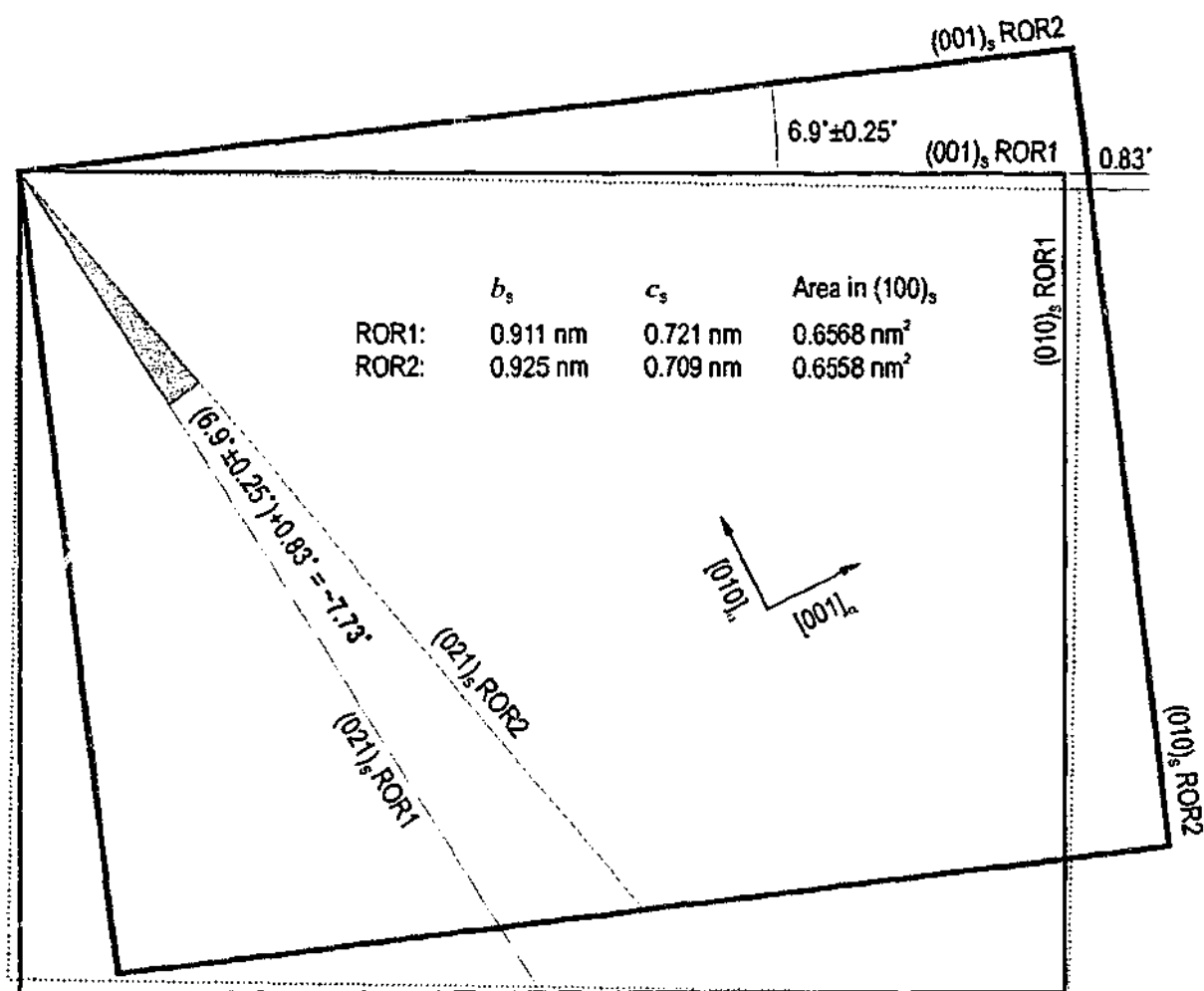


Figure 6.37 A rotation of the unit cell of the S-phase in ROR1 (black outline) by the observed maximum in the present work, $6.9^\circ \pm 0.25^\circ$ results in

The unit cell labelled ROR1 in figure 6.37 is described by the appropriate lattice parameters found in this work for particles in this orientation. The unit cell labelled ROR2 is found rotated CCW by $6.9^\circ \pm 0.25^\circ$ from the nominally orthogonal bounding planes of the unit cell in ROR1, and has a unique set of lattice parameters. The dotted unit cell outline has the altered lattice parameters of precipitates in ROR2, but is oriented such that $(021)_s$ is parallel to $(021)_{S(ROR1)}$. This is accomplished by a CW rotation of 0.83° . Therefore, the *measured* misorientation of $(021)_s$ between ROR1 and ROR2 is $6.9^\circ \pm 0.25^\circ + 0.83^\circ = \sim 7.73^\circ$ with respect to a reference plane outside of the unit cell. The misorientation thus approaches the actual angle between $(\bar{0}21)_s$ and $(014)_s$ in ROR1, 8.3° . The angle through which the precipitate must rotate is reduced since a proportion of the apparent rotation is achieved by a change in the aspect ratio of the unit cell.

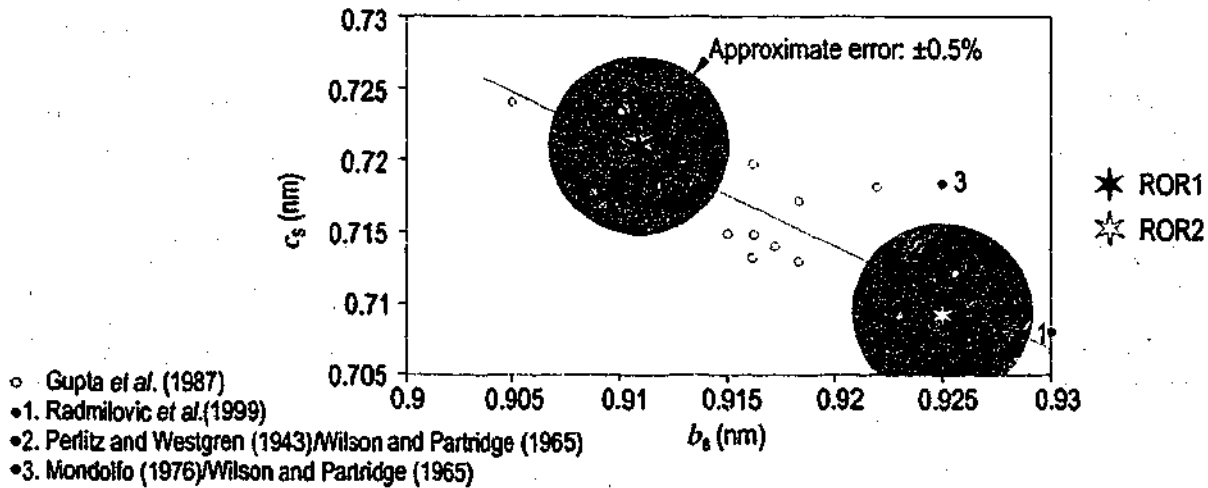


Figure 6.38 Plot of $1c_s$ against $1b_s$ for lattice parameters of the S-phase from several sources in the literature [Gupta, 1987 #409; Mondolfo, 1976 #388; Perlitz, 1943 #245; Radmilovic, 1999 #226; Wilson, 1965 #117].

The lattice parameters determined for ROR1 and ROR2 are included in a plot of c_s versus b_s using several suggestions of the lattice parameter of the S-phase in the literature [88,107,112,130,152] in figure 6.37, inclusive of the errors describing the reproducibility of the data. As b_s increases, c_s decreases, and the parameters determined for ROR1 and ROR2 fit well with a line of best fit through the data.

Using the newly confirmed unit cell parameters, d -spacing ratios between precipitate and matrix planes can be calculated and compared to the discrepancies in the calculation of $R = d_s/d_a$ that were identified using the Moiré intersection analysis (§6.6) as in independent verification. Firstly, $R = d_s/d_a$ values first calculated in §6.6 as a function of the interface orientation and the angle between the planes is compared in table 6.9 for three cases of coherent planes across the broad interface ($1c_s$) of all arbitrarily oriented particles. Using as an example the pair of planes $(\bar{041})_s : (020)_a$, $R(\text{ROR1}) = 1.066$, while $R(\text{ROR2}) = 1.077$, representing a -1.03% change in the ratio. Using the lattice parameters found in this work that describe the unit cell of the S-phase in two dimensions, $R = d_s/d_a$ is calculated for the unit cell in both orientations. The difference in R for particles in ROR1 and ROR2 is calculated and also shown in table 6.9. There is good agreement between the two columns representing the changes in R between ROR1 and ROR2, and this is confirmation that the unit cell in ROR1 and ROR2 are strained versions of the other.

The ratio $R = d_s/d_a$ for the plane pairs $(\bar{041})_s : (020)_a$ and $(023)_s : (002)_a$ are predicted to be marginally larger for a given orientation (i.e. ROR1, ROR2) if calculated directly from the unit

Table 6.9 Comparison of $R = d_S / d_\alpha$ from Moiré plane analysis and calculated values using lattice parameters

Plane Pair	$R = d_S / d_\alpha$ (from Moiré plane analysis)			$R = d_S / d_\alpha$ (calculated from confirmed size of unit cell)		
	ROR1	ROR2	% Δ	ROR1	ROR2	% Δ
$(0\bar{4}1)_S : (020)_\alpha$	1.066	1.077	+1.03%	1.07256	1.08579	+1.2%
$(023)_S : (002)_\alpha$	1.036	1.024	-1.15%	1.04979	1.03936	-1%
$(062)_S : (022)_\alpha$	0.978	0.986	+0.8%	0.97733	0.98744	+1%

cell size determined from SAED when compared to the ratio calculated from the Moiré plane analysis (table 6.9). The unit cell size of the matrix used in this latter calculation was assumed to be 0.40496 nm. Aluminium has a coefficient of linear expansion at 20°C of $25 \times 10^{-6} (\text{C}^\circ)^{-1}$ [180]. At the ageing temperature of 150°C, linear expansion in the lattice spacings may be approximately 0.3% greater than the spacing at room temperature. This leads to a corresponding decrease in $R = d_S/d_\alpha$ and may explain a proportion of the discrepancy.

It is interesting to compare the differences in lattice parameter of the S-phase observed in precipitates of alternative orientation relationships in the present work with the differences in the character of S and S', the basis of which is a lattice strain. Gupta *et al.* [130] noted changes in the lattice parameters as ageing time increases, and justified them to be a result of the breaking of coherency between the S'-phase and the matrix from an initially fully-coherent interface, and the transformation of coherent laths to incoherent or semicoherent rods as ageing time increases. Gupta *et al.* [130] collected the electron diffraction data by placing a selected area aperture (size not specified) over an area containing numerous precipitates in 12 variants. Hence, the data is an average of the precipitate population at a specific point in the ageing treatment, and is insensitive to differences in lattice parameters between two individual particles at a given time. In the present work, the co-existence of precipitates with a variation in lattice parameter was detected, and correlated to orientation. It was not possible to confirm the work of these authors [130] that the lattice parameter of the S-phase changes as ageing time continues, since data was not recorded at different ageing times.

The work presented here does not support the notion that heterogeneously-nucleated coherent laths in ROR1 transform to particles in ROR2, but rather, these precipitates obey a *nucleation site specificity*. Therefore, they are precluded from acting as precursors to the other.

Up to date, there has been no research reported in the literature detecting a change in lattice parameter with changes in orientation (i.e. lattice rotation). The present work has, for the first time, provided an *independent* calculation of the volume change in the S-phase unit cell. This has been achieved by observing and defining an alternative habit plane for the S-phase in an orientation labelled ROR2, and then normalising the S-phase lattice constants against the (assumed) fixed matrix positions.

6.7.3 Thickness of Particles in ROR1

Prior to the more complex case of particle thickness in S-phase precipitates in ROR2, the thickness of particles in ROR1 is addressed. The thickness perpendicular to the defined habit plane of $(001)_s // (021)_a$ of well-developed particles in ROR1 is always an integral multiple of unit cells (fig. 6.39). This implies that all particles of the S-phase are xc_s thick where x is an integer,

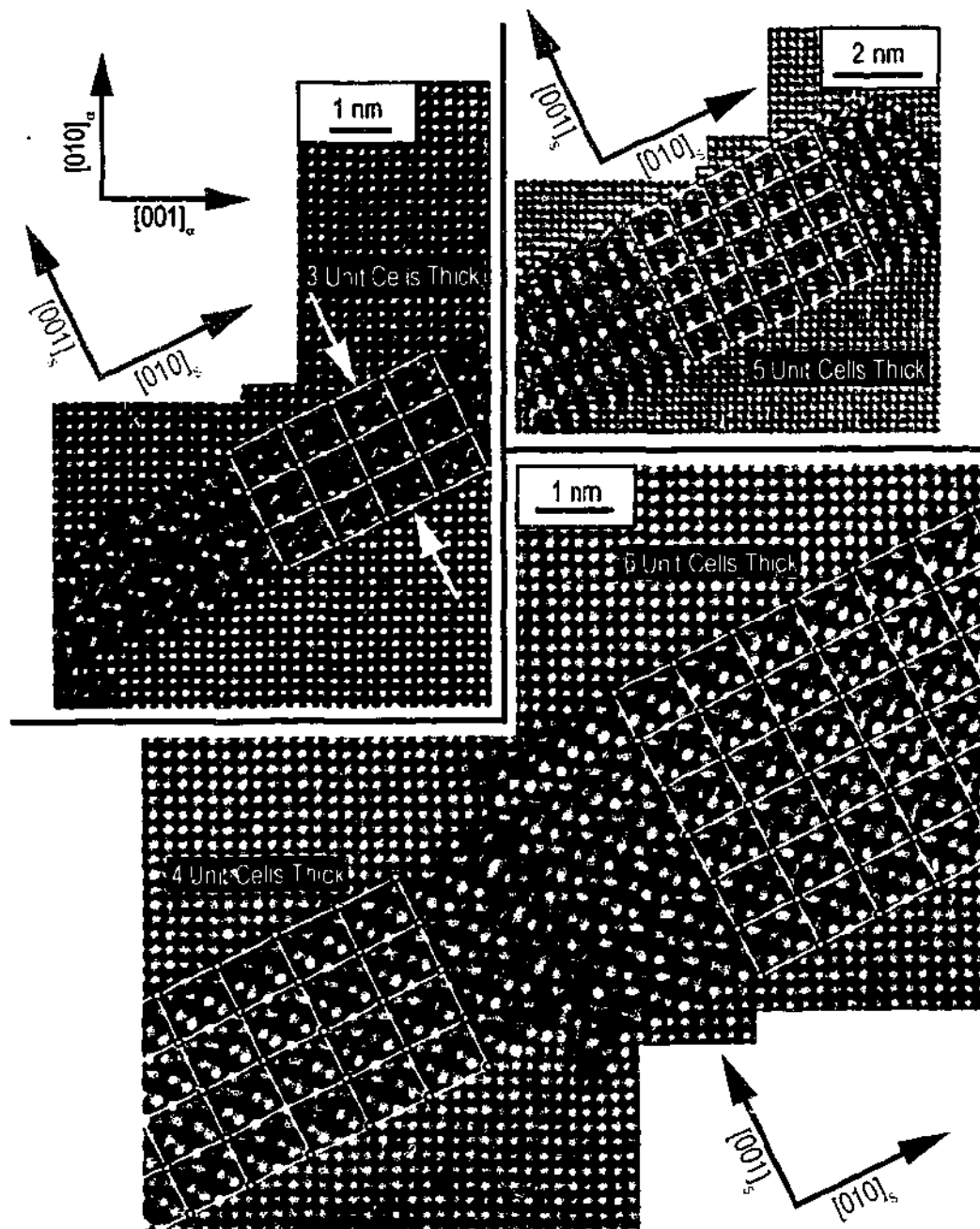


Figure 6.39 Four examples of well-developed particles of the S-phase in ROR1; thickness = xc_s .

and c_s is the lattice parameter of the precipitate phase parallel to $(001)_s$. However, this was not the case for precipitates that first nucleated at dislocations in the present work, where particles less than a unit cell in thickness were observed. However, detailed work was not performed on particles at such early growth stages.

6.7.4 Moiré Intersections and Precipitate Thickness in ROR2

The S-phase in the form of precipitates in ROR2 have not previously been described, and further discussion of the characteristics of these precipitates is included here.

The precipitate in figure 6.40 has two minor interfaces parallel to $(0\bar{2}1)_s // (0\bar{4}1)_\alpha$, implying that the particle lies in ROR2. The broad interfaces contain ledges $2c_s$ in height. These steps are clearly coincident with terminating planes of both $(002)_\alpha$ and $(020)_\alpha$ in the 1:1 plane matching of the plane pairs $(023)_s // (002)_\alpha$ and $(0\bar{4}1)_s // (020)_\alpha$ (§6.6.2.2). Figure 6.40 shows that there is a 5-plane discrepancy between the number of $(002)_\alpha$ planes across the broad interface when compared to the corresponding number of $(023)_s$ planes, which translates to 5 ledges with height $2c_s$, as indicated. A similar result would be achieved for the $(0\bar{4}1)_s : (020)_\alpha$ pair.

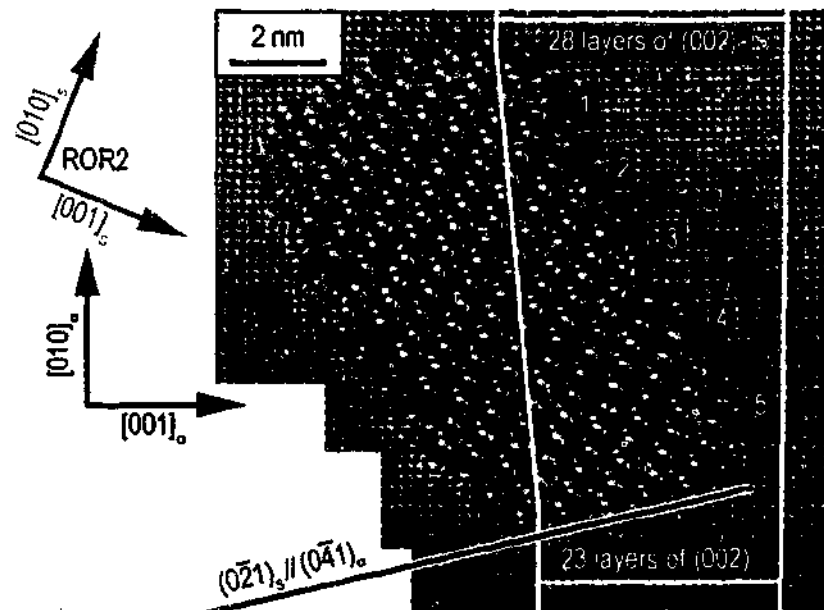


Figure 6.40 A precipitate in ROR2, where a 5-plane surplus in the number of $(002)_\alpha$ planes when matched with $(023)_s$ across the interface containing steps $2c_s$ in height corresponds to 5 $2c_s$ ledges.

In the same manner described in figure 6.40, the identification of terminating matrix planes might lead to a conclusion of the presence of steps $2c_s$ in height in those cases where the $2c_s$ steps are not obvious. Such a case might arise when the particle has a broad and coherent interface parallel to $(0\bar{2}1)_S // (014)_\alpha$ in particles with high aspect ratios. A small particle in ROR2 is presented in figure 6.41. The planar coherency between the two plane pairs $(0\bar{4}1)_S : (020)_\alpha$ and $(023)_S : (002)_\alpha$ is used to construct an enclosure around the minor interface of the particle. Outside of the enclosure, two extra planes each of $(002)_\alpha$ and $(020)_\alpha$ are required in the matrix phase at the minor interface. This can be conceived as being equivalent to the presence of two $2c_s$ ledges in the S-phase at the minor interface. It should be noted that adjacent precipitates abut, significantly obscuring the atomic arrangement existing between the minor interface and the matrix. Nevertheless, the large number of candidate particles examined in the present work lends confidence to the conclusion that all particles of the S-phase in ROR2 have *both* $1c_s$ -type (parallel to $(0\bar{2}1)_S // (014)_\alpha$) and $2c_s$ -type interfaces, although it is clear that one of these interface types is dominant in well-developed particles.

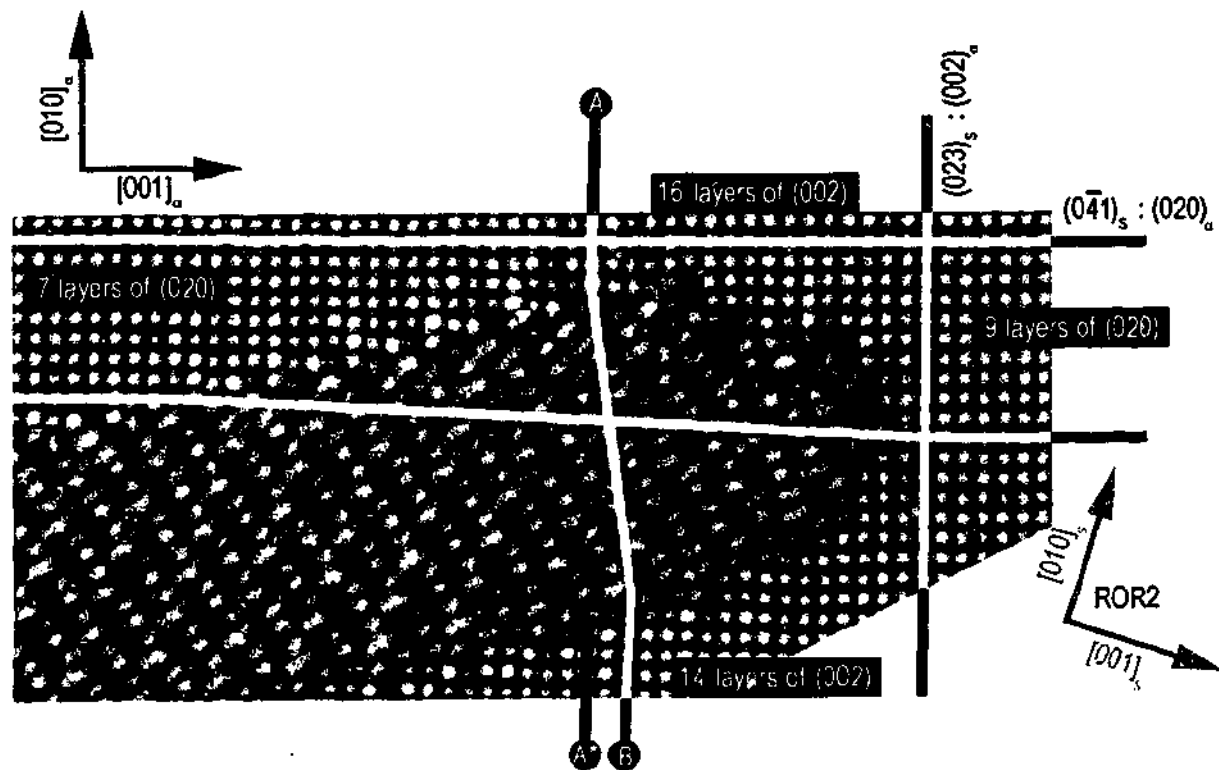


Figure 6.41 Small particle of the S-phase in ROR2. Two planes each of $(002)_\alpha$ and $(020)_\alpha$ terminate at the minor interface, and can be conceptualised as representing 2 steps $2c_s$ in height.

Point A and B in figure 6.41 are connected by a pair of planes that are coherent. Considering that there are two terminating planes of the matrix phase at the minor interface, then the plane at A* can be considered as the continuation of the original plane at A. Therefore, the thickness of the particle is twice the spacing of the Moiré intersection planes of the planes $(002)_\alpha$ and $(023)_s$. The Moiré intersection thickness is illustrated schematically in figure 6.42 for the relevant parameters for the plane pair $(023)_s : (002)_\alpha$ in ROR2 ($\theta_0 = 7.5^\circ$ and $R = 1.024$), the thickness of the spacing is 1.57 nm. The thickness of the particle perpendicular to the habit plane in figure 6.41 is ~3.1 nm, deriving its thickness from two Moiré intersections.

Virtually all precipitates in ROR2 are of a thickness that is an integral multiple of the spacing of the Moiré intersection planes. Figure 6.43 is a HREM image of a well-developed particle in ROR2. This thickness of the particle perpendicular to the habit plane is observed to be 4 Moiré intersections spacings thick for the given conditions. The particle in figure 6.43 is expected to contain 4 ledges $2c_s$ in height at the minor interface.

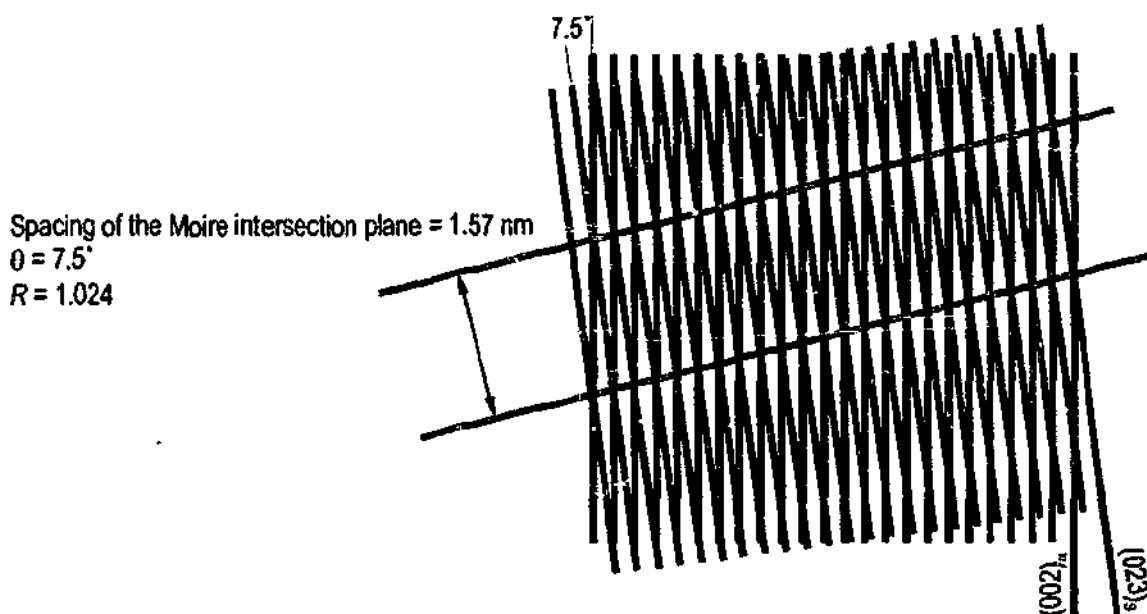


Figure 6.42 Spacing of the Moiré intersection planes for the plane pair $(023)_s : (002)_\alpha$ in ROR2.

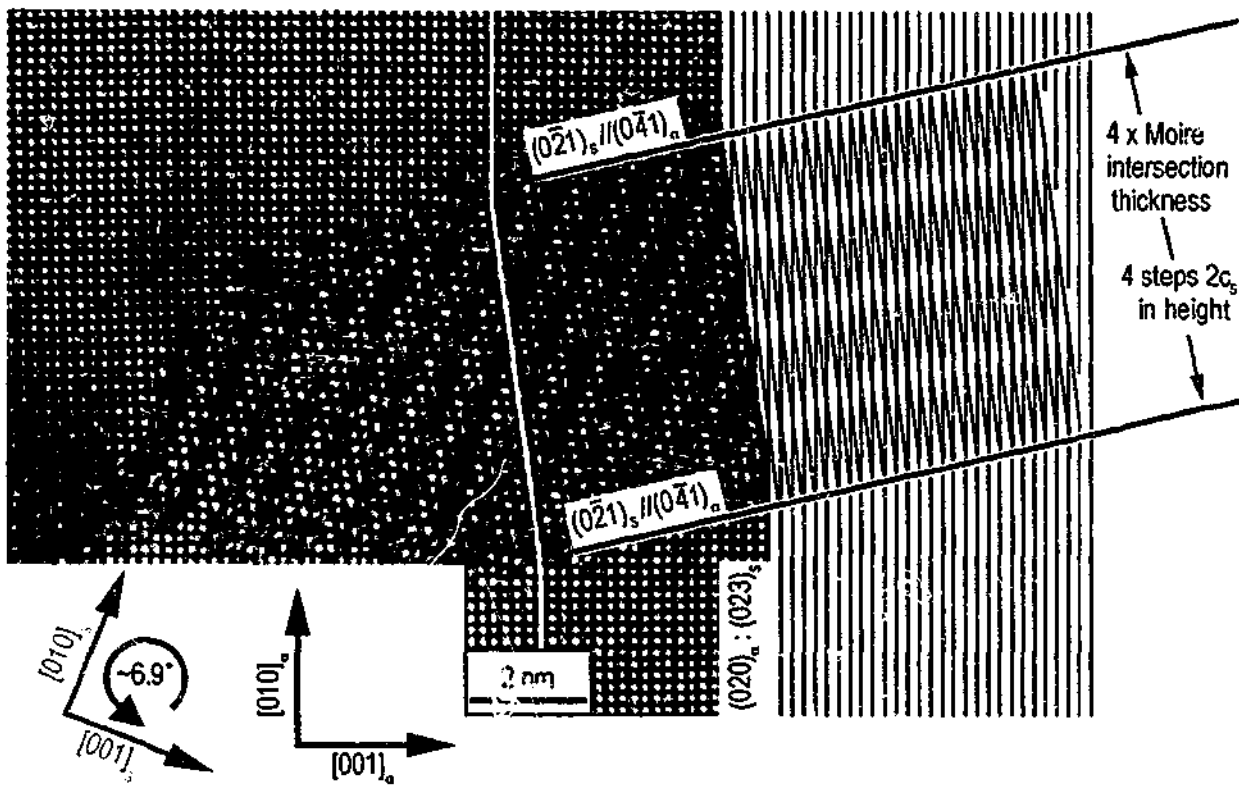


Figure 6.43 Precipitate of the S-phase in ROR2, exactly 4 times the thickness of the Moiré intersection thickness. This is associated with the expected presence of 4 steps $2c_s$ in height at the minor interfaces.

6.8 Chapter Summary

The current chapter has described the crystallography and morphology of particles of the S-phase more fully than previously in the literature. Importantly, a new orientation of the phase has been defined (ROR2), in addition to the well-known and accepted orientation (ROR1):

$$(100)_S // (100)_\alpha, [001]_S // [021]_\alpha \text{ and } [010]_S // [01\bar{2}]_\alpha \quad (\text{ROR1})$$

$$(100)_S // (100)_\alpha, [0\bar{2}1]_S // [014]_\alpha \quad (\text{ROR2})$$

Intermediate between these two orientations, which are separated by a lattice rotation of the bounding planes of the unit cell of $6.9^\circ \pm 0.25^\circ$ about $[100]_S // [100]_\alpha$, a near-continuous set of orientations is observed.

Coherent habit planes for particles in both ROR1 and ROR2 have been defined, and only three sets of planes are consistently coherent across the interfaces:

$$(0\bar{4}1)_S : (020)_\alpha, (023)_S : (002)_\alpha \text{ and } (062)_S : (022)_\alpha.$$

Satisfaction of the above observations requires that the lattice parameters of the S-phase vary for particles in ROR1 and ROR2, and this has been verified by electron diffraction.

Particles in ROR1 are a multiple of unit cells thick in a direction perpendicular to the coherent habit plane. The width of particles in ROR2 perpendicular to the coherent habit plane is always a multiple of the separation of the Moiré intersection formed by the planes $(023)_S$ and $(002)_\alpha$. Steps $2c_S$ in height are rationalised as a feature of $n/1$ particles in ROR2.

The above observations offer a new understanding of the complex precipitate particles of the S-phase. The following chapter revisits the strain environment in which individual precipitates nucleate and grow, benefiting greatly from the observations recorded here.

7.0

Nucleation and Growth of the S-Phase Revisited

In chapters 4 and 5, the presence of three species of precipitate was identified to occur locally at the site of former dislocation loops: θ' (θ''), Ω and S. The heterogeneous nucleation θ'' precipitates at dislocations was rationalised as an accommodation of the 4.95% contraction parallel to $[001]_0$, within the pre-existing strain field of the defect. The Ω phase in pre-aged, Cu-rich alloys could not be unequivocally associated with the dislocation during nucleation, and may have formed in the vicinity of the loop due to the local chemistry to be found there. Alternatively, it may have formed through an interaction with the other precipitate phases in the precipitate network. Finally, the S-phase was observed to form directly upon dislocation loops in all alloys under all thermal regimes applied. In chapter 5, it was suggested that precipitates of the standard orientation and those rotated from the standard orientation were nucleated only at specific sites on the lattice defects such that a strategic relationship existed between the precipitate and dislocation crystallography. However, further progress in understanding was not possible for two reasons: (1) it was attempted in chapter 5 to maintain a balance in reporting of the different precipitate species at defects, and (2) it was concluded that the current state of the literature inadequately described the complexity of the crystallography of S-phase.

In chapter 6, a significant contribution has been made to the knowledge of S-phase crystallography by defining a second rational orientation relationship (ROR2) in addition to the well-known orientation relationship, labelled ROR1 here. Differences in the lattice parameters of particles in these two orientations were recorded. It is the purpose of the current chapter to extend the results and discussion of Chapter 5 (insofar as they relate to the S-phase), incorporating the knowledge gained and reported in Chapter 6.

7.1 Location of Precipitates in ROR1 and ROR2 at Dislocation Loops

The rational lattice orientation relationships for S-phase formed at dislocations loops are as follows:

$$(100)_S // (100)_\alpha, [001]_S // [021]_\alpha \text{ and } [010]_S // [01\bar{2}]_\alpha \quad (\text{ROR1})$$

$$(100)_S // (100)_\alpha, [0\bar{2}1]_S // [014]_\alpha \quad (\text{ROR2})$$

The two orientation relationships are related by a rotation of $(010)_S \perp (001)_S$ (the bounding planes of the unit cell of the S-phase parallel to $[100]_S$) of $6.9^\circ \pm 0.25^\circ$ about $[100]_S // [100]_\alpha$. The lattice parameters are measurably different for particles in these orientations:

$$b_S = 0.911 \pm 0.005 \text{ nm} \quad c_S = 0.721 \pm 0.004 \text{ nm} \quad (\text{ROR1})$$

$$b_S = 0.925 \pm 0.005 \text{ nm} \quad c_S = 0.709 \pm 0.004 \text{ nm} \quad (\text{ROR2})$$

Nucleation of the S-phase proceeded both at loops lying parallel to $\{110\}_\alpha$ and $\{111\}_\alpha$. Precipitates in ROR1 were commonly observed at pure edge dislocation loops parallel to $\{110\}_\alpha$. In addition, precipitates oriented intermediate between the two defined orientations (up to $\sim 5^\circ$ rotation from ROR1 about $[100]_S // [100]_\alpha$) were formed at the extreme end of a row of precipitates forming at a dislocation line segment. Precipitates in ROR2 did not form at these loops

Precipitates in both ROR1 and ROR2 formed at dislocation loops lying in $\{111\}_\alpha$. Defined segments of these loops have a Burgers vector with a significant screw component (§5.1.2), in addition to sections of pure edge, and the character of the dislocation systematically changes with position. Particles in ROR1 were observed to be associated with segments of pure edge or significantly edge character, while precipitates in ROR2 were observed to form at segments with a larger screw component. The presence of precipitates in ROR1 at positions of pure edge on $\{111\}_\alpha$ loops (§5.5) is analogous to the formation of precipitates in ROR1 at loops lying parallel to $\{110\}_\alpha$. Therefore the principles discussed for the formation precipitates at $\{111\}_\alpha$ will provide an adequately broad study of variance and orientation of precipitates of the S-phase.

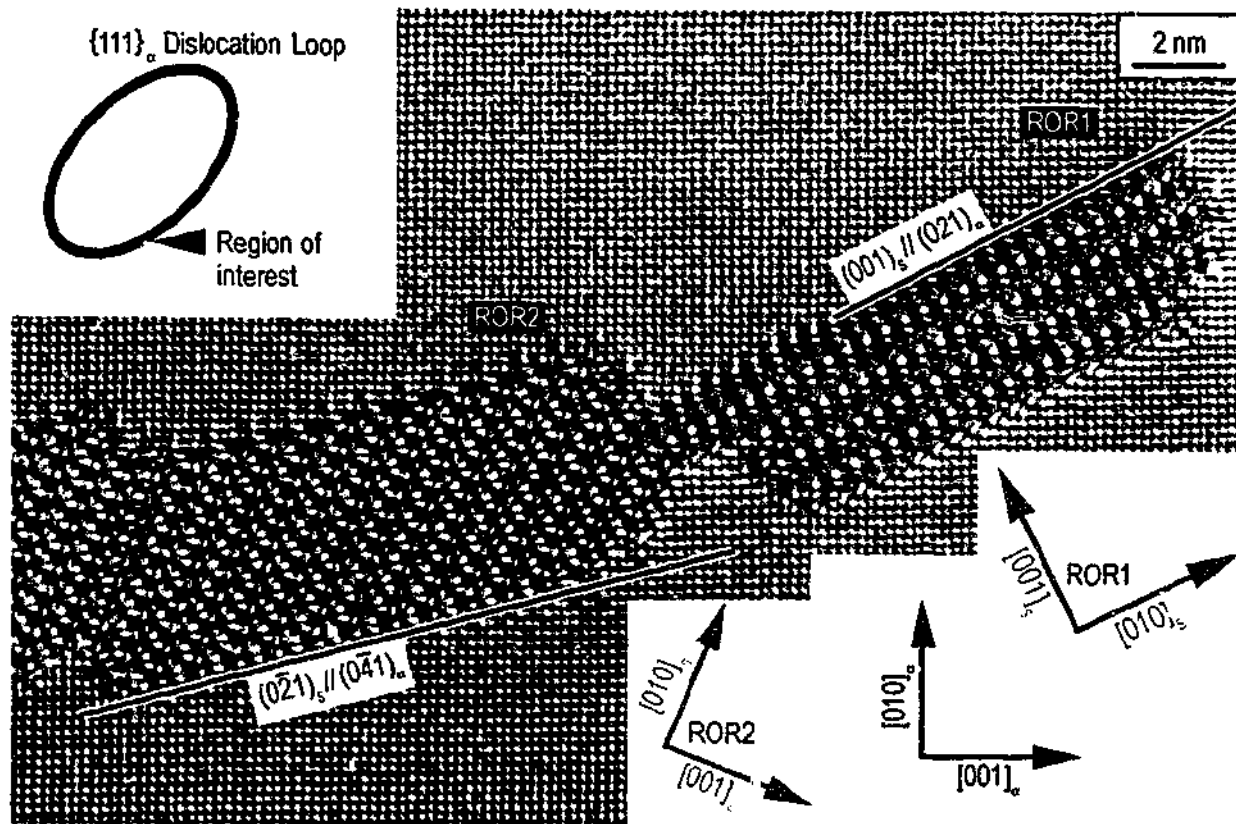


Figure 7.1 Precipitates of the S-phase in ROR1 and ROR2 at a single $\{111\}_\alpha$ dislocation loop.

Only two of the 12 ROR1 variants form upon a single dislocation. In the same manner, two of the 12 variants of the newly defined orientation relationship, ROR2, form at a single $\{111\}_\alpha$ dislocation loop. Figure 7.1 is a HREM image of two precipitates of the S-phase in the aluminium matrix, each representing one of the two rational orientation relationships.

7.2 Selection of Precipitate Crystallography

In chapter 5, the selection of precipitate morphology of the S-phase was investigated with respect to the two experimentally-derived selection criteria for nucleation at dislocations [36,94,95,100-102,109-111]. Firstly, it was attempted to calculate the principal misfit vector of the transformation. However, owing to the historical conjecture over the lattice parameters of the S-phase, it was not possible to calculate the lattice misfit vector for the transformation from matrix to precipitate. Secondly, it was observed that precipitates of the S-phase in ROR1 were oriented such that their habit plane was nearly parallel to the projection of the dislocation line upon which it nucleated. Inspection of figure 7.1 suggests that particles in ROR2 are also arranged such that their coherent plane is approximately parallel to the dislocation line direction at the point at which the precipitate nucleates and grows. The results of chapter 6 have led to a formal understanding of the absolute lattice parameters of precipitates in ROR1 and ROR2 (within reasonable error limits), and calculations of the lattice misfit may now be made with greater confidence. From this point, the analysis will proceed under the framework of the equation for the changes in free energy for nucleation at dislocations, which was referred to in §2.2.2. The energy balance is presented again here:

$$\Delta F = -\Delta F_v + \Delta F_s + \Delta F_e + \Delta F_d + \Delta F_i \quad \text{Equation 7.1}$$

where ΔF_v = difference in free energy between parent and product

ΔF_s = the interfacial free energy

ΔF_e = the elastic strain energy in the matrix and nucleus

ΔF_d = the difference in line energy of the dislocation and that part remaining in the nucleus volume

ΔF_i = the interaction of the stress fields of the dislocation and nucleus.

ΔF_d and ΔF_i are specific to the dislocation upon which the precipitation takes place, and must be negative and large enough to overcome ΔF_s and ΔF_e . The role of the dislocation is to reduce the ΔF_s and ΔF_e contributions to the total energy change by reducing the interfacial free energy and the total strain energy respectively of the new embryo.

Interfacial Energy ΔF_i

It is reported in the literature that dislocations are not very effective for reducing the interfacial energy contribution in equation 7.1 [189]. Hence, the planar, coherent (and therefore relatively low energy) interfaces of the type exhibited by precipitates in ROR1 and ROR2 are expected. Furthermore, the elongated nature of these precipitates implies that only a very small fraction of the precipitate is in "contact" with the dislocation. The relief afforded by the dislocation with respect to the surface energy can not act for the entire precipitate since the precipitate is not confined to a cylinder immediately surrounding the dislocation core. Therefore, the increment in interfacial energy derived from the creation of new particle-matrix interface is not thought to be a major influence upon precipitate selection.

Elastic Strain Energy ΔF_e

The dislocation can reduce ΔF_e and therefore assist nucleation in two ways, if it is assumed that the misfit between the embryo and the matrix has both a dilatational and shear component. Consider the case of particles in ROR1 initially. Calculation of the dilatational misfit between precipitate and matrix from a plane-matching criterion has been performed by various researchers [88,107], and the direction perpendicular to the habit plane of the precipitate is always incorporated into the calculations. The plane spacing perpendicular to $[100]_s/[100]_a$ was not measured, and hence the strains parallel to this direction are not considered in this context. Nevertheless, it is suggested that the greatest influence upon the morphology of laths perpendicular to the elongated growth direction are the planes that lie parallel to the growth direction (i.e. $(0kl)_s$). Table 7.1 displays the dilatational strains parallel to the principal axes of the S-phase, $[010]_s$ and $[001]_a$, (-0.48% and +0.61% respectively). These strains are less than those observed by Radmilovic *et al.* [107] (-2.28% and +2.69% respectively). Using the lattice parameters observed by Gupta *et al.* [130] for those particles nucleated early in the heat-treatment, $b_s = 0.905$ nm and $c_s = 0.724$ nm, the strains are -0.07% and 0.06% parallel to $[001]_s$ and $[010]_s$ respectively.

Table 7.1 Lattice misfit calculations in ROR1

Corresponding Planes	Al d -spacing (nm)	S-phase d -spacing (nm)	Strain (%)
ROR1 $(001)_s$	$4(01\bar{2})_a = 0.7245$ nm	0.721 nm	-0.48%
ROR1 $(010)_s$	$5(021)_a = 0.9055$ nm	0.911 nm	+0.61%

Table 7.2 Lattice misfit calculations in ROR1

Corresponding Planes	Al d -spacing (nm)	S-phase d -spacing (nm)	Strain (%)
ROR2 (021) _s	4(014) _a = 0.3929 nm	0.3874 nm	-1.4%

As for precipitates in ROR1, the lattice parameters of precipitates in ROR2 can be used to calculate the principal strains for this orientation. However, the orientation relationship only describes a single set of parallel planes apart from those defining the long axis of the precipitates. The volume change perpendicular to the habit plane is calculated in table 7.2, and a contraction of only 1.4% contraction is required.

The minimal volume changes can be compared to the 4.95% contraction that is required to form the θ'' phase, whose presence away from dislocations under certain conditions was discussed in §5.5. Lath-type precipitates in ROR1 or ROR2 were not observed to form away from dislocation loops in alloys Al-0.2Cu-1.7Mg and Al-0.8Cu-1.7Mg under any circumstances. Given the minimal volumetric change for the matrix-to-precipitate transformation in both ROR1 and ROR2, it appears that there may another form of accommodation provided by the dislocation that has not been accounted for up until this point.

In the absence of an obvious dilatational volume change during the transformation, the strong preference for heterogeneous nucleation of the S-phase at dislocations may perhaps be explained by the accommodation of a shear strain energy during transformation. The shear strain energy component of the elastic strain energy was referred to in §2.2.2. There is some conjecture surrounding the implication of shear in the transformation of particles in systems that have traditionally been regarded as giving rise to diffusion-controlled transformations. However, several authors have discussed the potential for a shear strain energy in the formation of precipitate plates in substitutional alloys where a compositional change occurs between the parent and product phases [103,104]. Others have directly demonstrated the importance of a shear strain in the formation of second-phase precipitates in aluminium alloys including θ' in Al-Cu alloys [105], Q-phase in Al-Mg-Si-Cu alloy [106], S-phase in Al-Cu-Mg alloys [107], and T1 phase in Al-Li-Cu [108]. Radmilovic *et al.* [107] discussed the possibility of a shear component in the formation of Type II precipitates, but the associated particle rotation applied can not be justified in the present work. Furthermore, these authors observed a small shear displacement of

the matrix planes at nucleation of particles in the standard orientation relationship, but could not take the analysis any further [107,132].

The transformation strain can be determined only if the lattice correspondence is mathematically defined. When parent and product phases in a solid state phase transformation are coherent, then it is generally possible to define a lattice correspondence between them, and to describe the structural change by a homogeneous lattice strain, S_T [104]. For certain transformations, this strain is an invariant plane strain (IPS), and the invariant plane defines a planar coherent interface. Typically, identification (by inspection) of the correct lattice correspondence is based on that relationship which involves the smallest atomic displacements [213], and the choice of the operating lattice correspondence is based on the assumption that it delivers a transformation strain involving the minimum principal strains. When the parent and product phases have a simple crystal structure, e.g. fcc and bcc respectively in the case of an austenite to ferrite transformation in steels, the lattice correspondence can usually be defined intuitively from simple inspection of the crystal structures of the parent and product, and the observed orientation relationship between them. However, in the present example of aluminium matrix transforming to the complex orthorhombic unit cell of the S-phase containing 16 atoms, identification of the lattice correspondence is not straightforward. Furthermore, the models of S-phase are under review [154], and some conjecture continues regarding the true structure of the phase, including the atomic positions.

The issue is further complicated by the variation in orientation of the S-phase as described fully for the first time in this work. Traditionally, in cases in which there is a unique orientation relationship between parent and product lattices, it is standard practice to adopt a unique correspondence. The presence of two rational orientation relationships and the observation of a near continuous range of orientations of the product structure between these two limits, for individual particles of the S-phase, suggests the possibility that there may be more than a single lattice correspondence operating. However, the prospect that a single lattice correspondence operates for two orientations is very interesting in its own right. There are currently no rules for selecting the lattice correspondence(s) in these cases, and the situation is further complicated by the fact that significant changes in the lattice parameters of the phase has been identified as a function of orientation.

In the absence of a clear lattice correspondence in the present transformation, there are several analytical methods that may be applied. One of these is based on the O-lattice or coincident site lattice (CSL) of Bollman [214]. This method requires the identification of one or more sets of vectors Δg in the diffraction pattern that lie normal to the habit plane of the particle. The vector Δg is defined as a difference vector between two vectors g_1 and g_2 representing sets of planes in the two phases bounding the interface (the habit plane). Therefore, the vectors g_1 and g_2 are said to be correlated if they are related by the transformation strain linking the two lattices [106]. In the case that they are correlated, Δg is perpendicular to the habit plane. A simulated SAED pattern of a particle of the S-phase in ROR1 is provided in figure 7.2(a), using the lattice parameters determined from the experimental results of chapter 6. An example is provided of the vector calculation of Δg , using $g_1 = g(02\bar{2})_s$ and $g_2 = g(0\bar{2}2)_a$. Clearly, Δg is perpendicular to the superimposed orientation of the habit plane, which lies parallel to $(001)_s // (021)_a$. There are numerous alternative pairs of plane where the resultant vector Δg is perpendicular to the interface for particles in ROR1, and selection of the correct pair is formidable.

Figure 7.2(b) is a simulated SAED pattern of a particle in ROR2, the orientation of which is 6.9° CW from the position of ROR1 in figure 7.2(a). The unique lattice parameters for the S-phase in ROR2 have been used in the construction of the pattern, and the habit plane of $(001)_s // (014)_a$ is indicated.

If it were assumed that particles in both ROR1 and ROR2 formed with the same lattice correspondence, then it might be expected that a unique vector Δg is perpendicular to the precipitate interface in both orientations. Figure 7.2(b) indicates those plane pairs that maintain a vector Δg perpendicular to the broad and coherent interfaces of particles in both ROR1 and ROR2. It appears that the three pairs of planes that are coherent across the broad interface of particles of *all arbitrary orientations*, $(0\bar{4}1)_s : (020)_a$, $(023)_s : (002)_a$ and $(062)_s : (022)_a$, (§6.6), including those particles in ROR1 and ROR2, are also implicated in the transformation strain of particles in both ROR1 and ROR2.

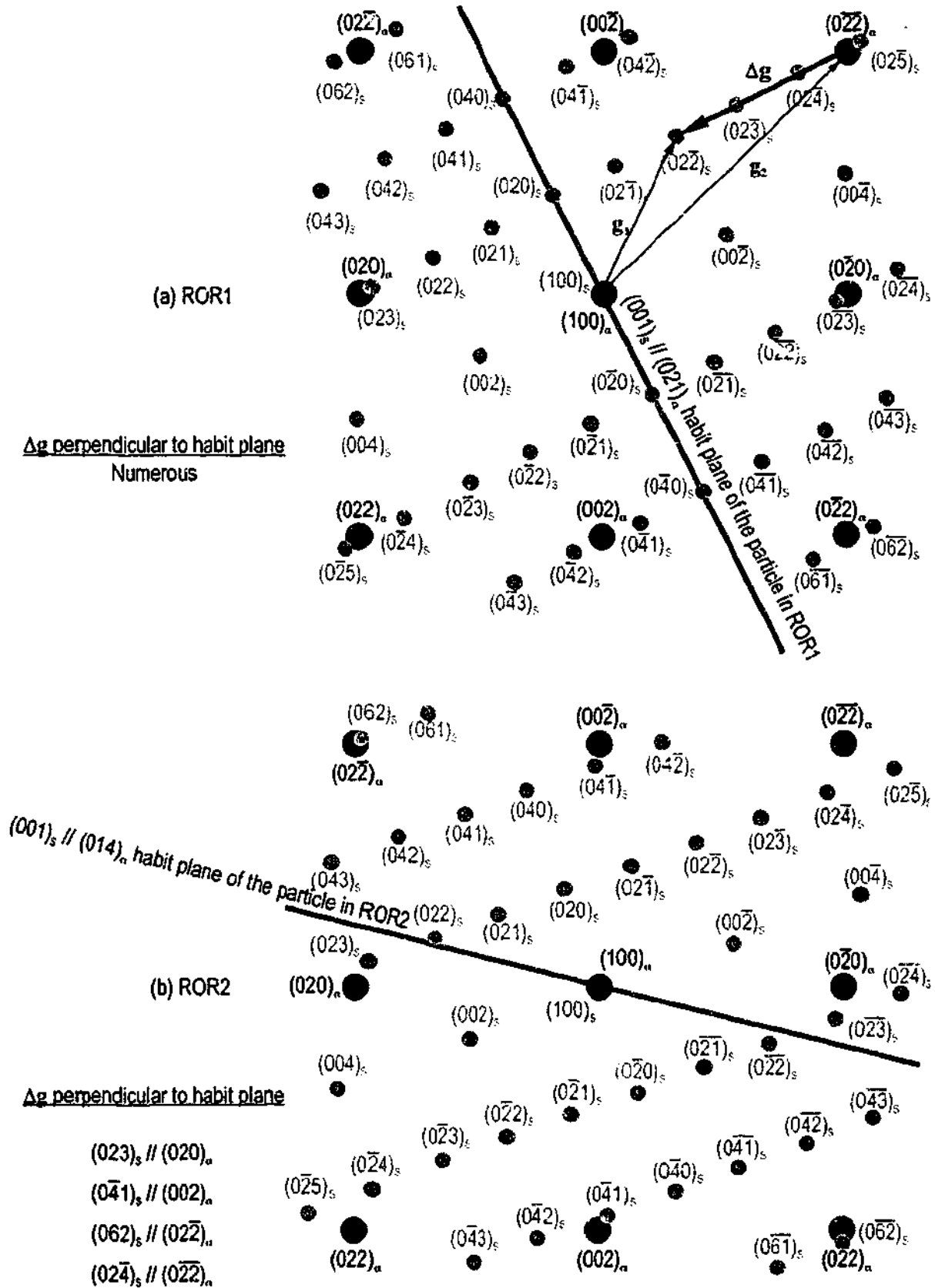


Figure 7.2 (a) Simulated SAED pattern of embedded particle of the S-phase in ROR1. (b) S-phase particles in ROR2, indicating the common pairs of planes that give rise to Δg perpendicular to the broad and coherent interfaces for both orientations.

The structure factor of planes of the S-phase have been calculated according to the latest structural model provided by Radmilovic *et al.* [107] and are shown in table 7.3. The three plane pairs that are observed in 1:1 correspondence for *all arbitrary orientations*, $(0\bar{4}1)_S : (020)_\alpha$, $(023)_S : (002)_\alpha$ and $(062)_S : (0\bar{2}2)_\alpha$, are all described by structure factors that rank in the top four for planes of the S-phase.

The orientation of two of these coherent plane pairs, $(0\bar{4}1)_S : (020)_\alpha$ and $(023)_S : (002)_\alpha$, are indicated both in ROR1 (Variant 3 in figs. 6.9 and 6.34) and ROR2 in figure 7.3. In particles in ROR1, $(041)_S$ is misoriented by $9^\circ \pm 0.25^\circ$ from $\{002\}_\alpha$, but in particles of ROR2 the misorientation is reduced to near zero. In contrast, $(0\bar{2}3)_S$ is approximately parallel to $\{002\}_\alpha$ of particles in ROR1, while in ROR2 the misorientation is increased to $7.5^\circ \pm 0.25^\circ$. The lattice rotation of the S-phase in aluminium matrix thus appears to operate within the bounds of the two planes of *highest* structure factor, such that the orientation does not rotate past the point at which they are parallel with the $\{002\}_\alpha$ matrix plane with which they are associated.

Finally, the thickness of particles in ROR2 is always observed to be a multiple of the spacing of the Moiré intersections planes formed by the matching plane pair $(023)_S : (002)_\alpha$ (§6.7.4).

Although not conclusive, it would appear that the transformation of matrix to S-phase is intimately reliant upon one or more of the plane pairs $(0\bar{4}1)_S : (020)_\alpha$, $(023)_S : (002)_\alpha$ and $(062)_S : (0\bar{2}2)_\alpha$ to describe the lattice correspondence.

Table 7.3 Structure factor of planes of the S-phase (using the structure of Radmilovic *et al.* [107]).

Plane	Struct. Factor	d-spacing	Plane (cont...)	Struct. Factor	d-spacing
(023)	27.4	2.1044	(042)	15.3	1.9433
(041)	26.0	2.2089	(020)	13.7	4.65
(004)	24.3	1.77	(043)	11.4	1.6563
(062)	19.6	1.4199	(082)	11.3	1.1045
(006)	19.3	2.0499	(064)	10.0	1.1661
(040)	17.5	2.325	(002)	9.8	6.54
(045)	17.3	1.2094	(063)	7.1	1.2955

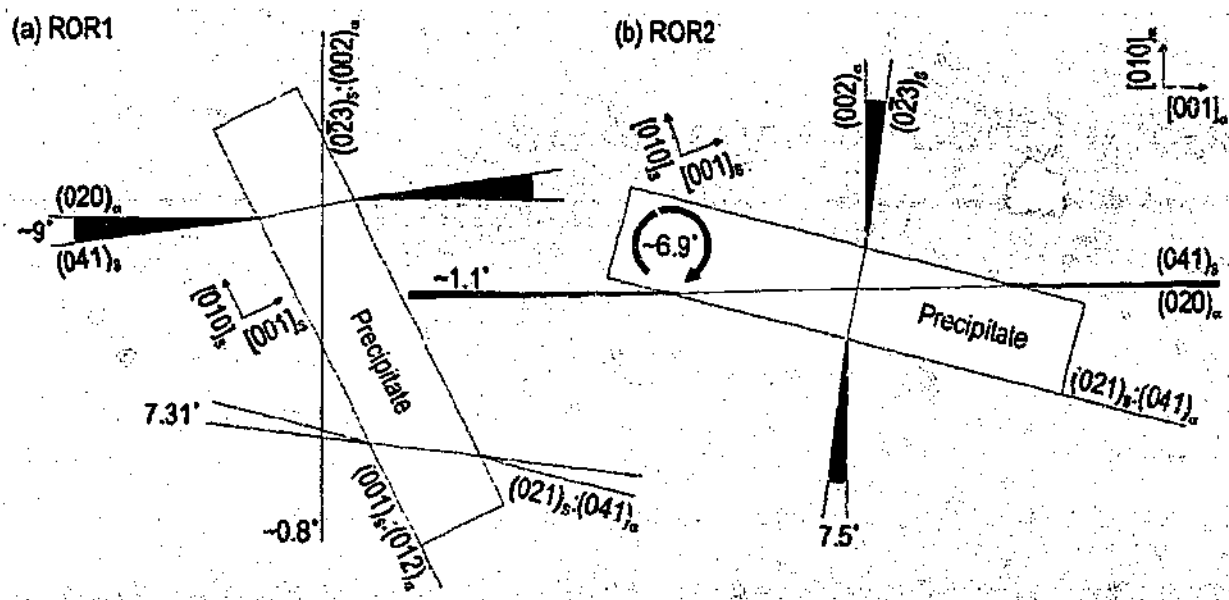


Figure 7.3 Schematic representations of particles in (a) ROR1, and (b) ROR2.

The traditional appreciation of the elongated morphology of particles of the S-phase as being due to good atomic matching in this direction may be challenged. Since the volume change is minimal in all three principal directions for the particle in ROR1, it might be reasonable to expect not to observe a dominant growth direction. The observation that particles of the S-phase are invariably elongated parallel to $[100]_s // [100]_a$ suggests that this growth direction is not subject to the same potential shear strains as the transformation that takes place in $(100)_s$.

8.0

Summary and Conclusions

The results have clearly shown the close relationship between the morphology of S-phase and the location at which it nucleates upon dislocations loops. Based upon this analysis, an additional orientation relationship of the S-phase has been established, in addition to the well-known orientation relationship. A small but detectable difference in the lattice strain of the precipitates for the two orientations extends further the understanding of S-phase stability. Finally, the volume change during transformation of matrix to S-phase is not considered to be a dilatational change. The details are explained as follows:

From an initial matrix of 10 Al-rich Al-Cu-Mg alloys, detailed analysis of the processes and characteristics of heterogeneous precipitation at dislocations in four selected alloys has been undertaken in the work presented here. With careful control of specimen dimension and thermal processing conditions, alloy specimens have been solution treated, quenched and aged in a manner leading to the formation of a high and uniform density of dislocation loops.

- The dislocation loops form through the coalescence of vacancies into discs which subsequently collapse to form areas bound by a line defect.
- The dislocation loops are not observed to change in size following the first 60 s of ageing at 150°C.
- A single form of loop was formed in alloys with a Cu:Mg ratio greater than 0.65, and were parallel to $\{110\}_\alpha$ with a Burgers vector $\mathbf{b} = \frac{1}{2}\langle 110 \rangle_\alpha$.
- Loops lying parallel to $\{110\}_\alpha$ and $\{111\}_\alpha$ matrix planes were formed in alloys with a Cu:Mg ratio less than 0.65. The former loops had similar characteristics to those found in the high-Cu alloys. The latter were characterised as Frank sessile loops ($\mathbf{b} = \frac{1}{3}\langle 111 \rangle_\alpha$)

that subsequently decomposed to loops of perfect dislocation character ($\mathbf{b} = \frac{1}{2}\langle 110 \rangle_{\alpha}$) while, in the general case, remaining parallel to the plane in which they formed.

The early stages of precipitation at 150°C in these alloys have been observed, together with the distribution of precipitates throughout the matrix at the point of maximum hardness and in an overaged condition. The strengthening precipitates θ'' (precursor to θ' at 150°C), Ω (with pre-ageing) and S-phase were observed to nucleate heterogeneously at or near dislocations loops. However, nucleation of Ω could not unequivocally be linked to the dislocation, and probably formed in the local area around the loops because of the favourable chemistry to be found there.

Nucleation of θ'' occurred exclusively at dislocation loops lying in $\{110\}_{\alpha}$ matrix planes under the applied thermal regime.

- Two variants of θ'' formed at a given loop, the habit planes of which were 45° from the plane of the loop.
- The contraction of 4.95% parallel to $[001]_{\beta}$ during formation of the tetragonal unit cell is apparently accommodated in the region of compression associated with loops lying parallel to $\{110\}_{\alpha}$.
- The maximum misfit vector (parallel to $[001]_{\beta}$) is 45° from the direction of the edge Burgers vector.
- Observations that precipitates of θ'' form at positions well removed from dislocations under modified thermal treatments both here and in the work of others [113,114] suggests that while the accommodation afforded by the dislocation strain field is utilised when available, it is not necessary for nucleation to proceed.
- The volume change expressed as a component of the elastic strain energy term ΔF_e in the equation of free energy (equation 8.1) does not act as a prohibitive barrier to nucleation in the absence of a dislocation.

$$\Delta F = -\Delta F_v + \Delta F_s + \Delta F_e + \Delta F_d + \Delta F_i \quad \text{Equation 8.1}$$

The localised presence of precipitates of the S-phase at dislocation loops lying in both $\{110\}_\alpha$ and $\{111\}_\alpha$ was observed. Comparatively little is known of the crystallography and morphology of these common but complex precipitates. Therefore, precipitates of the S-phase were first characterised with respect to the crystallographic and morphological range exhibited.

- Precipitates of the S-phase were observed in a rational orientation relationship (ROR1) with the matrix such that:

$$(100)_S // (100)_\alpha, [001]_S // [021]_\alpha \text{ and } [010]_S // [01\bar{2}]_\alpha \quad (\text{ROR1})$$

- Precipitates in ROR1 were predominantly elongated parallel to $[100]_S // [100]_\alpha$ and were characterised by a broad and coherent habit plane parallel to $(001)_S // \{021\}_\alpha$.
- The aspect ratio of the precipitates projected perpendicular to $(100)_S$ was up to $\sim 7:1$, leading to description as laths.
- These observations are consistent with those precipitates commonly reported in the literature [84,85,125] of which there are 12 equivalent variants.

A second rational orientation relationship (ROR2) has been defined for the first time in the present work.

- Precipitates of the S-phase in ROR2 are oriented such that:

$$(100)_S // (100)_\alpha, [0\bar{2}1]_S // [014]_\alpha \quad (\text{ROR2})$$

- Precipitates of the S-phase in ROR2 are characterised by a coherent habit plane parallel to $\{014\}_\alpha // (021)_S$ and an elongated axis parallel to $[100]_S // [100]_\alpha$.
- The coherent habit plane can be understood as a series of steps $1c_S$ in height with a terrace plane $0.5b_S$ in width.
- The aspect ratio of these precipitates is up to ~ 5 , and there are 12 equivalent variants.
- While coherent and parallel to $[0\bar{2}1]_S // [014]_\alpha$ on two of its four sides, precipitates in ROR2 form with steps $2c_S$ in height at the remaining two interfaces.

- The thickness of particles between the two coherent interface planes of $\{014\}_\alpha // (021)_s$ is always a multiple of the Moiré intersection spacing of $\{002\}_\alpha$ and $(023)_s$.
- The so-called Type II precipitates observed in the literature [107] are a special case of particles in ROR2 where the coherent interface plane of the particle is comparatively minor and the major interface is partially coherent and stepped.

The existence of two rational orientation relationships extends significantly upon current descriptions of precipitates of the S-phase. With respect to the relationship between the two orientations:

- A precipitate in ROR1 is separated from the nearest variant of ROR2 by an average lattice rotation of the bounding planes of the unit cell $\{(010)_s : (001)_s\}$ of $6.9^\circ \pm 0.25^\circ$ about the common axis of $[100]_s // [100]_\alpha$.
- Although a lattice rotation about $[100]_s // [100]_\alpha$ and away from the well-characterised orientation relationship (ROR1) has been detected [75,107,131], a consistent assessment has not been made of the extent to which the particles can rotate. Knowledge of the extent to which the particles can rotate is necessary for an orientation relationship to be defined.
- The definition of an alternative and coherent habit plane for "rotated" particles has not been achieved prior to the reported results in this work.

In addition to the two rational orientation relationships ROR1 and ROR2, there is an apparently near-continuous range of orientations distinguished by the angle of rotation about $[100]_s // [100]_\alpha$ within the angular arc of $6.9^\circ \pm 0.25^\circ$ between the two orientations. This is a rare observation in microstructures. The coherent interface is parallel to $\{021\}_\alpha$ at particles in ROR1, and 49.4° away and parallel to $\{014\}_\alpha$ for particles in ROR2. For particles oriented at rotations intermediate between the two rational orientations:

- The orientation of the particle-matrix interface containing steps $1c_s$ in height systematically varied with the apparently continuous lattice rotation about $[100]_s // [100]_\alpha$.
- The rotation of the partially coherent interface containing steps $1c_s$ in height occurs in a sense opposite to that of the lattice rotation.
- The terrace width between steps $1c_s$ in height reduce from an infinite width (ROR1) to $0.5b_s$ (ROR2) on particles intermediately oriented.

It has been shown that particles in ROR1 and ROR2 have different lattice parameters in the common plane of $(100)_s // (100)_a$ perpendicular to the elongated axis of the particles.

- Using SAED, the lattice parameters have been defined as:

$$b_s = 0.911 \pm 0.005 \text{ nm} \quad c_s = 0.721 \pm 0.004 \text{ nm} \quad (\text{ROR1})$$

$$b_s = 0.925 \pm 0.005 \text{ nm} \quad c_s = 0.709 \pm 0.004 \text{ nm} \quad (\text{ROR2})$$

- A change in the ratio of atomic plane spacing in the precipitate-matrix phase is consistent with the requirement that coherency is maintained for several sets of planes across the partially coherent interface.
- The effective change in the aspect ratio of the unit cell of precipitates in ROR1 and ROR2 has been correlated to the historical differences that have led to separate designations of S' and S phases.
- For the first time, changes in the particle-matrix orientation relationship are implicated in a potential definition of S' and S for those particles nucleated at a dislocation. Current understanding assumes that any change in lattice parameter originates during transitions from intermediate to equilibrium phases.

A strategic relationship between precipitate and dislocation crystallography has been reported here. Rationalisation of S-phase crystallography at dislocation loops is significantly assisted by the new knowledge gained of the variation in crystallography and morphology of precipitates in a typical microstructure. Regarding those precipitates that form at loops lying parallel to $\{110\}_a$:

- Precipitates formed only in ROR1, or in orientations described by a lattice rotation about $[100]_s // [100]_a$ of up to $5^\circ \pm 0.25^\circ$ from ROR1.
- Only two crystallographic variants of the precipitates in ROR1 formed at a single loop.
- In all cases, the variants to form were those for which (1) the elongated growth direction ($[100]_s // [100]_a$) was in the plane of the loop and (2) $[010]_s$ was 18.44° from the loop plane.
- Particles in ROR1 were oriented such that the precipitate habit planes were approximately parallel to the projected direction of the dislocation line, confirming this selection rule for precipitation at dislocations.

At loops lying parallel to $\{111\}_\alpha$ matrix planes:

- Precipitates in ROR1 formed exclusively on dislocation segments that were pure or near pure edge in character.
- Precipitates in ROR2 formed exclusively on dislocation segments of mixed character, containing an appreciable screw component.
- As for precipitates in ROR1, precipitates in ROR2 are oriented such that the dislocation line projection lies in the coherent habit plane of the precipitate, again confirming this selection rule for precipitation at dislocations.

The volume change during nucleation of particles in ROR1 and ROR2 was found to be virtually zero, particularly for particles in ROR1.

- Therefore, the volumetric component of the elastic strain energy is apparently not a significant factor leading to exclusive precipitation of these orientations at dislocations.
- There is another form of accommodation that is offered by the dislocation to the transforming matrix, leading to the clear preference for heterogeneous nucleation displayed by these precipitates.
- It has been proposed that this accommodation is in the form of a shear strain component.

The operative lattice correspondence, if it exists, connecting vectors and planes in the matrix phase to those in the product S-phase, is essential to further understanding of this system. The lattice correspondence is likely to rely upon one or more of the plane pairs $(0\bar{4}1)_S : (020)_\alpha$, $(023)_S : (002)_\alpha$ and $(062)_S : (0\bar{2}2)_\alpha$.

9.0 References

1. Wilm, A. (1911) Metallurgie. Zeitschrift für die gesamte Hüttekunde 8 (reprinted in *Precipitation Hardening* by Martin, J.W. (Butterworth-Heinemann, 2nd Edition, 1998))
2. Martin, J.W. (1968). **Precipitation Hardening**. Oxford, Pergamon Press.
3. Jeffries, Z. and Archer, R.S. (1921) Chemical and Metallurgical Engineering 44 p. 1057.
4. Merica, P.D., Waltenburg, R.G., and Scott, H. (1919) Bull. A.I.M.E. 21 p. 913.
5. Teed, P.L. (1937). **Duralumin and its Heat-Treatment**. London, Charles Griffin and Company, Limited.
6. Murakami, Y. (1995) in *Mater. Sci. Tech.*, 8. K.H. Matucha. VCH: Weinheim, p. 213.
7. Polmear, I.J. (1995). **Light Alloys: Metallurgy of the Light Metals**. 3rd Edition. London, Edward Arnold.
8. Shih, H.-C., Ho, N.-J., and Huang, J.C. (1996) Metall. Mater. Trans. A 27 (9) p. 2479.
9. Nabarro, F.R.N. (1947) Proc. Phys. Soc. 59 p. 256.
10. Peierls, R.E. (1940) Proc. Phys. Soc. 52 p. 23.
11. Orowan, E. (1934) Zeitschrift für Phys. 89 p. 605.
12. Orowan, E. (1934) Zeitschrift für Phys. 89 p. 634.
13. Polanyi, M. (1934) Zeitschrift für Phys. 89 p. 660.
14. Taylor, G.I. (1934) Proc. Roy. Soc. A 145 p. 362.

15. Foreman, A.J.E. and Makin, M.J. (1966) Philos. Mag. 14 p. 911.
16. Haasen, P. (1996) in *Physical Metallurgy*, Vol. 3. Elsevier Science: Amsterdam, p. 2009.
17. Hanson, K. and Norris, J.W.J. (1975) J. Appl. Phys. 46 (6) p. 2378.
18. Cottrell, A.H. (1953) 44 (355) p. 829.
19. Cottrell, A.H. and Jawson, M.A. (1949) Proc. Roy. Soc. A 199 p. 104.
20. Fleischer, R.L. (1961) Acta metall. 9 p. 996.
21. Fleischer, R.L. (1963) Acta metall. 11 p. 203.
22. Fleischer, R.L. (1966) Acta metall. 14 p. 1867.
23. Kocks, U.F. (1965) p. 541.
24. Kocks, U.F., Labusch, R., and Schwarz, R.B., *Proceed. 4th Internat. Conf. on Strength of Metals and Alloys*, Nancy, France (1976) p. 275.
25. Labusch, R. (1970) Phys. Stat. Sol. 41 p. 659.
26. Labusch, R. (1972) Acta metall. 20 p. 917.
27. Labusch, R. (1977) J. Appl. Phys. 48 (11) p. 4550.
28. Lukac, P. and Trojanova, Z., *Proceed. 5th Internat. Conf. on Strength of Metals and Alloys*, Aachen, West Germany (1979) p. 1061.
29. Schwarz, R.B. and Labusch, R. (1978) J. Appl. Phys. 49 (10) p. 5174.
30. Wynliffe, P., Kocks, U.F., and Embury, J.D. (1980) Scripta metall. 14 p. 1349.
31. Hirsch, P.B. and Kelly, A. (1965) Philos. Mag. 12 p. 881.
32. Hirth, J.P. and Lothe, J. (1982). *Theory of Dislocations*. 2nd Edition. Malabar, Florida, Krieger Publishing Company.
33. Fisher, J.C. (1954) Acta metall. 2 p. 9.
34. Brown, L.M. and Ham, R.K. (1971) in *Strengthening methods in crystals*, A. Kelly and R.B. Nicholson. Elsevier Publishing Company Limited: Essex, p. 9.
35. Ardell, A.J. (1985) Metall. Mater. Trans. A 16 p. 2131.

36. Kelly, A. and Nicholson, R.B. (1963) Progress in Materials Science 10 p. 149.
37. Martin, J.W. (1983). **Worked Examples in the Strength of Metals and Alloys**. London, The Institution of Metallurgists.
38. Martin, J.W. (1998). **Precipitation Hardening**. 2nd Edition. Oxford, Butterworth-Heinemann.
39. Blankenship, C.P.J., Hornbogen, E., and Starke, E.A.J. (1993) Mater. Sci. Eng. A 169 p. 33.
40. Brown, L.M., *Proceed. 5th Internat. Conf. on Strength of Metals and Alloys*, Aachen, West Germany (1979) 3 p. 1551.
41. Lee, B.C. and Park, J.K. (1997) Philos. Mag. Letters 76 (6) p. 385.
42. Lee, J.K. (1998) Metall. Mater. Trans. A 29 p. 2039.
43. Zhu, A.W. and Starke, E.A.J. (1999) Acta mater. 47 (11) p. 3263.
44. Zhu, A.W., Csontos, A., and Starke, E.A.J. (1999) Acta mater. 47 (6) p. 1713.
45. Zhu, A.W., Chen, J., and Starke, E.A.J. (2000) Acta mater. 48 (9) p. 2239.
46. Nembach, E. (1997). **Particle Strengthening of Metals and Alloys**. New York, John Wiley and Sons, Inc.
47. Nie, J.F., Muddle, B.C., and Polmear, I.J. (1996) Mater. Sci. For. 217-222 p. 1257.
48. Orowan, E., *Symposium on Internal Stresses in Metals and Alloys*, London (1948) Institute of Metals p. 451.
49. Nie, J.F. and Muddle, B.C. (1998) J. Phase Equil. 19 (6) p. 543.
50. Brook, G.B. (1965). **Fulmer Research Inst., Special Report. No. 3**.
51. Silcock, J.M. and Parsons, B.A. (1958). **Fulmer Research Inst. Rep. (R. 10/67)**.
52. Garg, A., Chang, Y.C., and Howe, J.M. (1990) Scripta metall. mater. 24 p. 677.
53. Hardy, H.K. (1951-1952) J. Inst. Metals 80 p. 483.
54. Polmear, I.J. and Sargant, K.R. (1963) Nature 200 (4907) p. 669.
55. Hardy, H.K. (1954-55) J. Inst. Metals 83 p. 17.
56. Sofyan, B.T. (2003). PhD, Monash University, Melbourne.

-
57. Sofyan, B.T., Kaviprasad, K., and Ringer, S.P. (2000) Mater. Sci. For. 331-337 p. 977.
 58. Ratchev, P., Verlinden, B., De Smet, P., and Van Houtte, P. (1998) Acta mater. 46 (10) p. 3523.
 59. Ringer, S.P., Sakurai, T., and Polmear, I.J. (1997) Acta mater. 45 (9) p. 3731.
 60. Ringer, S.P., Hono, K., Sakurai, T., and Polmear, I.J. (1997) Scripta mater. 36 (5) p. 517.
 61. Vietz, J.T. and Polmear, I.J. (1966) J. Inst. Metals 94 p. 410.
 62. Ratchev, P., Verlinden, B., and Zahra, A.-M. (2000) Mater. Sci. For. 331-337 p. 1095.
 63. Chester, R.J. (1983). PhD Thesis, Monash University, Melbourne, Australia.
 64. Reich, L., Ringer, S.P., and Hono, K. (1999) Philos. Mag. Letters 79 (9) p. 639.
 65. Yamamoto, R., Takai, O., and Doyama, M. (1974) Crystal Lattice p. 45.
 66. Takai, O., Yamamoto, R., Doyama, M., and Hisamatsu, Y. (1975) Phys. Stat. Sol. 69 p. K5-K8.
 67. Somoza, A., Dupasquier, A., Polmear, I.J., Folegati, P., and Ferragut, R. (2000) Physical Review B 61 (21) p. 14454.
 68. Somoza, A., Dupasquier, A., Polmear, I.J., Folegati, P., and Ferragut, R. (2000) Physical Review B 61 (12) p. 14464.
 69. Nagai, Y., Murayama, M., Tang, Z., Nonaka, T., Hono, K., and Hasegawa, M. (2001) Acta mater. 49 (5) p. 913.
 70. Hono, K. (1999) Acta mater. 47 (11) p. 3127.
 71. Hono, K., Murayama, M., and Reich, L., *International Conference on Solid-Solid Phase Transformations*, Kyoto (1999) p. 97.
 72. Hono, K., Sakurai, T., and Polmear, I.J. (1994) Scripta metall. mater. 30 (6) p. 695.
 73. Ringer, S.P., Caraher, S.K., and Polmear, I.J. (1998) Scripta mater. 39 (11) p. 1559.
 74. Ringer, S.P. and Hono, K. (2000) Materials Characterisation 44 p. 101.
 75. Ringer, S.P., Hono, K., Polmear, I.J., and Sakurai, T. (1996) Applied Surface Science 94/95 p. 253.
 76. Ringer, S.P., Hono, K., Polmear, I.J., and Sakurai, T. (1996) Acta mater. 44 (5) p. 1883.
 77. Ringer, S.P., Hono, K., and Sakurai, T. (1995) Metall. Mater. Trans. A 26 p. 2207.
-

-
78. Garg, A. and Howe, J.M. (1991) Acta metall. mater. 39 (8) p. 1925.
 79. Knowles, K.M. and Stobbs, W.M. (1988) Acta Crystallog. B44 p. 207.
 80. Muddle, B.C. and Polmear, I.J. (1989) Acta metall. 37 (3) p. 777.
 81. Schueller, R.D., Sachdev, A.K., and Wawner, F.E. (1992) Scripta metall. mater. 27 p. 617.
 82. Schueller, R.D., Wawner, F.E., and Sachdev, A.K. (1994) J. Mater. Sci. 29 (1) p. 239.
 83. Schueller, R.D., Wawner, F.E., and Sachdev, A.K. (1994) J. Mater. Sci. 29 (2) p. 424.
 84. Bagaryatsky, Y.A. (1952) Doklady Acad. Nauk. SSSR 87 p. 559.
 85. Silcock, J.M. (1960-1961) J. Inst. Metals 89 p. 203.
 86. Wilson, R.N. and Forsyth, P.J.E. (1966) J. Inst. Metals 94 p. 8.
 87. Wilson, R.N. (1969) J. Inst. Metals 97 p. 80.
 88. Wilson, R.N. and Partridge, P.G. (1965) Acta metall. 13 p. 1321.
 89. Sen, N. and West, D.R.F. (1969) J. Inst. Metals 97 p. 87.
 90. Kovarik, L., Gouma, P.I., Kisielowski, C., Court, S.A., and Mills, M.J. (2002) Mater. Sci. For. 396-402 p. 1043.
 91. Larche, F.C. (1979) in Dislocations in Solids, 4. F.R.N. Nabarro. North-Holland Publishing Company: Amsterdam, p. 135.
 92. Cahn, J.W. (1957) Acta metall. 5 p. 169.
 93. Katgerman, L. and Vsan Liere, J. (1978) Acta metall. 26 p. 361.
 94. Beaven, P.A. and Butler, E.P. (1980) Acta metall. 28 p. 1349.
 95. Gomez-Ramirez, R. and Pound, G.M. (1973) Metall. Trans. 4 (6) p. 1563.
 96. Dollins, C.C. (1970) Acta metall. 18 p. 1209.
 97. Barnett, D.M. (1971) Scripta metall. 5 (4) p. 261.
 98. Eshelby, J.D. (1957) Proc. Roy. Soc. A 241 p. 376.
 99. Eshelby, J.D. (1959) Proc. Roy. Soc. A 252 p. 561.
-

-
100. Thomas, G. and Nutting, J. (1956). **Phase Transformations in Metals**. London, Institute of Metals.
 101. Sandaram, R. and Laird, C. (1976) Acta metall. 24 p. 517.
 102. Aaronson, H.I., Aaron, H.B., and Kinsman, K.R. (1971) Metallography 4 p. 1.
 103. Christian, J.W. (1997) Progress in Materials Science 42 p. 101.
 104. Muddle, B.C. and Nie, J.F., *International Conference on Solid-Solid Phase Transformations '99 (JIMIC-3)*, Kyoto, Japan (1999) the Japan Institute of Metals. p. 1128.
 105. Dahmen, U. and Westmacott, K.H. (1983) Scripta mater. 17 p. 1241.
 106. Weatherly, G.C., Perovic, A., Mukhopadhyay, N.K., Lloyd, D.J., and Perovic, D.D. (2001) Metall. Mater. Trans. A 32 (2) p. 213.
 107. Radmilovic, V., Kilaas, R., Dahmen, U., and Shiflet, G.J. (1999) Acta mater. 47 (15) p. 3987.
 108. Cassada, W.A., Shiflet, G.J., and Starke, E.A.J. (1991) Metall. Trans. A 22 (2) p. 287.
 109. Allen, R.M. and Vander Sande, J.B. (1980) Acta metall. 28 p. 1197.
 110. Allen, R.M. and Vander Sande, J.B. (1980) Acta metall. 28 p. 1185.
 111. Keh, A.S. and Wriedt, H.A. (1962) Trans. AIME 224 p. 561.
 112. Mondolfo, L.F. (1976). **Aluminium Alloys: Structure and Properties**. Boston, Butterworths.
 113. Nicholson, R.B., Thomas, G., and Nutting, J. (1958-1959) J. Inst. Metals 87 p. 429.
 114. Nicholson, R.B. and Nutting, J. (1958) Philos. Mag. 8 (3) p. 531.
 115. Thomas, G. and Nutting, J. (1959) Acta metall. 7 p. 515.
 116. Silcock, J.M. (1960) Acta metall. 8 p. 589.
 117. Polmear, I.J. (1987) Mater. Sci. For. 13-14 p. 195.
 118. Reich, L., Murayama, M., and Hono, K. (1998) Acta mater. 46 (17) p. 6053.
 119. Hutchinson, C.R., Fan, X., Pennycook, S.J., and Shiflet, G.J. (2000) Mater. Sci. For. 331-337 p. 965.
 120. Hutchinson, C.R., Fan, X., Pennycook, S.J., and Shiflet, G.J. (2001) Acta mater. 49 (14) p. 2827.
-

121. Garg, A. and Howe, J.M. (1991) Acta metall. mater. 39 (8) p. 1939.
122. Suh, I.S. and Park, J.K. (1995) Scripta metall. mater. 33 (2) p. 205.
123. Murayama, M. and Tono, K. (1998) Scripta mater. 38 (8) p. 1315.
124. Ringer, S.P., Muddle, B.C., and Polmear, I.J. (1995) Metall. Mater. Trans. A 26 (7) p. 1659.
125. Bagaryatsky, Y.A. (1952) Doklady Acad. Nauk. SSSR 87 p. 397.
126. Radmilovic, V., Thomas, G., Shiflet, G.J., and Starke, E.A.J. (1989) Scripta metall. 23 (7) p. 1141.
127. Charai, A., Walther, T., Alfonso, C., Zahra, A.-M., and Zahra, C.Y. (2000) Acta mater. 48 (10) p. 2751.
128. Gregson, P.J., Flower, H.M., Tite, C.N., and Mukhopadhyay, A.K. (1986) Mater. Sci. Tech. 2 (4) p. 349.
129. Flower, H.M. and Gregson, P.J. (1987) Mater. Sci. Tech. 3 p. 81.
130. Gupta, A.K., Gaunt, P., and Chaturvedi, M.C. (1987) Philos. Mag. A 55 (3) p. 375.
131. Majimel, J., Molenat, G., Danoix, F., Blavette, D., Lapasset, G., and Casanove, M.J. (2002) Mater. Sci. For. 396 p. 1025-1030.
132. Radmilovic, V., Ratkovic, S., and Dahmen, U. (1997) Microscopy and Microanalysis 3 (1) p. 665.
133. Ye, H.Q. (1990) Colloque De Physique 51 p. C1-373.
134. Zhang, C.B., Sun, W., and Ye, H.Q. (1989) Philos. Mag. Letters 59 (6) p. 265.
135. Weatherly, G.C. and Nicholson, R.B. (1968) Philos. Mag. 17 p. 801.
136. Starink, M.J. and Gregson, P.J. (1995) Scripta metall. mater. 33 (6) p. 893.
137. Ratchev, P., Verlinden, B., and Van Houtte, P. (1994) Scripta metall. mater. 30 p. 599.
138. Ahmad, M. and Ericsson, T. (1985) Scripta metall. 19 p. 457.
139. Khireddine, D., Rahouadj, R., and Clavel, M. (1988) Scripta metall. 22 p. 167.
140. Wyss, R.K. and Sanders, R.E.J. (1988) Metall. Trans. A 29 (10) p. 2523.
141. Mukhopadhyay, A.K. and Rama Rao, V.V. (1999) Mater. Sci. Eng. A 268 (1-2) p. 8.

142. Mukhopadhyay, A.K., Singh, V., Prasad, K.S., and Chakravorty, C.R. (1996) Acta mater. 44 (8) p. 3115.
143. Hutchinson, C.R. and Ringer, S.P. (2000) Metall. Mater. Trans. A 31 (11) p. 2721.
144. Hutchinson, C.R., Raviprasad, K., and Ringer, S.P., *International Conference on Solid-Solid Phase Transformations (JIMIC-3)* (1999) p. 169.
145. Gao, N. (2002) Mater. Sci. For. 396-402 p. 923.
146. Raviprasad, K., Hutchinson, C.R., Sakurai, T., and Ringer, S.P. (2003) Acta mater. 51 (17) p. 5037.
147. Rainforth, W.M. and Jones, H. (1997) J. Mater. Sci. Letters 16 (6) p. 420.
148. Yan, J., Chunzhi, L., and Minggao, Y. (1990) J. Mater. Sci. Letters 9 p. 421.
149. Cuisat, F., Duval, P., and Graf, R. (1984) Scripta metal. 18 p. 1051.
150. Weatherley, G.C. (1966). PhD Thesis, University of Cambridge, Cambridge.
151. Jin, Y., Li, C.Z., and Yan, M.G. (1990) J. Mater. Sci. 26 p. 241.
152. Perlitz, H. and Westgren, A. (1943) Arkiv for kemi, mineralogi och geologi 16B p. 1.
153. Kilaas, R. (2001) Ultramicroscopy 88 p. 63.
154. Wolverton, C. (2001) Acta mater. 49 (16) p. 3129.
155. Dahmen, U. (1994) Metall. Mater. Trans. A 25 (9) p. 1857.
156. Bergman, G., Waugh, J.L.T., and Pauling, L. (1952) Nature 169 p. 1057.
157. Bergman, G., Waugh, J.L.T., and Pauling, L. (1957) Acta Crystallog. 10 p. 254.
158. I.aves, F., Lohberg, K., and Witte, H. (1935) Metallwirtschaft 14 p. 793.
159. Reich, L., Suvegh, K., Lendvai, J., and Vertes, A. (2001) Philos. Mag. Letters 81 (3) p. 145.
160. Boyd, J.D. and Edington, J.W. (1971) Philos. Mag. 23 (183) p. 633.
161. Carpenter, G.J.C. (1976) Phys. Stat. Sol. 37 (1) p. K61.
162. Condat, M. and Fayard, M. (1977) Phys. Stat. Sol. 41 (1) p. K5.
163. DiMelfi, R.J. and Siegel, R.W. (1971) Philos. Mag. 24 (188) p. 279.

-
164. Edington, J.W. and Smallman, R.E. (1965) Philos. Mag. **11** p. 1109.
 165. Foreman, A.J.E. (1969) Philos. Mag. **19** (161) p. 931.
 166. Horiuchi, S. (1970) Philos. Mag. **21** (171) p. 623.
 167. Jackson, K.A. (1962) Philos. Mag. **7** p. 1117.
 168. Loretto, M.H., Clareborough, L.M., and Humble, P. (1966) Philos. Mag. **13** (125) p. 953.
 169. Osetsky, Y.N. and Bacon, D.J. (1999) Philos. Mag. Letters **79** (5) p. 273.
 170. Siebert, P., Werner, M., and Loffler, H. (1984) Phys. Stat. Sol. **86** (2) p. 543.
 171. Tunstall, W.J. (1969) Philos. Mag. **20** (166) p. 701.
 172. Yoshida, S., Kiritani, M., and Shimomura, Y. (1963) Journal of the Physical Society of Japan **18** (2) p. 175.
 173. Kuhlmann-Wilsdorf, D. and Wilsdorf, H.G.F. (1960) J. Appl. Phys. **31** (3) p. 516.
 174. Kuhlmann-Wilsdorf, D. (1965) in **Lattice Defects in Quenched Metals**, R.M.J. Cotterill, M. Doyama, J.J. Jackson, and M. Meshii. Academic Press: New York and London, p. 269.
 175. Schoeck, G. and Tiller, W.A. (1959) Philos. Mag. p. 43.
 176. Siegel, R.W. (1978) J. Nuc. Mater. **69 & 70** p. 117.
 177. Amelinckx, S. (1964). **The Direct Observation of Dislocations**. Solid State Physics - Advances in Research and Applications. New York and London, Academic Press.
 178. Friedel, J. (1964). **Dislocations**.
 179. Smallman, R.E. and Eikum, A. (1964) in **Lattice Defects in Quenched Metals**, R.M.J. Cotterill, M. Doyama, J.J. Jackson, and M. Meshii. Academic Press: New York and London, p. 591-637.
 180. Giancoli, D.C. (1988). **Physics for Scientists and Engineers**. 2nd Edition., Prentice-Hall International, Inc.
 181. Holman, J.P. (1992). **Heat Transfer**. 7th Edition. London, McGraw-Hill.
 182. Thomas, G. (1962). **Transmission Electron Microscopy of Metals**. London, Wiley.
 183. Commonwealth Scientific and Industrial Research Organisation (CSIRO) Division of Applied Physics (1979-1996)
-

184. Williams, D.B. and Carter, C.B. (1996). **Transmission Electron Microscopy**. New York, Plenum Press.
185. Kubota, M. (2001). PhD, Monash University, Melbourne.
186. Hillert, M. (1994) Metall. Mater. Trans. A 25 (9) p. 1957.
187. Smith, D.J. and Barry, J.C. (1988) in **High-Resolution Transmission Electron Microscopy**, P.R. Buseck, J.M. Cowley, and L. Eyring. Oxford University Press: New York.
188. Spence, J.C.H. (2003). **High Resolution Electron Microscopy**. Monographs on the Physics and Chemistry of Materials. 3rd Edition. Oxford, Oxford University Press.
189. Porter, D.A. and Easterling, K.E. (1992). **Phase Transformations in Metals and Alloys**. 2nd Edition. London, Chapman and Hall.
190. Hull, D. and Bacon, D.J. (1984). **Introduction to Dislocations**. 3rd Edition. Oxford, Pergamon Press.
191. Schulthess, T.C., Turchi, P.E.A., Gonis, A., and Nieh, T.-G. (1998) Acta mater. 46 (6) p. 2215.
192. Abis, S., Massazza, M., Mengucci, P., and Riontino, G. (2001) Scripta mater. 45 (6) p. 685.
193. Furuhashi, T. and Maki, T. (2001) Mater. Sci. Eng. A 312 (1-2) p. 145.
194. Luo, C.P. and Weatherley, G.C. (1989) Acta metall. 37 (3) p. 791.
195. Kovacs, I. and Zsoldos, L. (1973). **Dislocations and Plastic Deformation**. International Series of Monographs in Natural Philosophy. Oxford, Pergamon Press.
196. Weertman, J. and Weertman, J.R. (1964). **Elementary Dislocation Theory**. Macmillan Series in Materials Science. New York, Macmillan.
197. Smallman, R.E. and Westmacott, K.H. (1972) Mater. Sci. Eng. 9 p. 249.
198. Westmacott, K.H., Barnes, R.S., Hull, D., and Smallman, R.E. (1961) Philos. Mag. 6 p. 929.
199. Edington, J.W. (1976). **Practical Electron Microscopy in Materials Science**. New York, Van Nostrand Reinhold Company.
200. Kelly, A. and Groves, G.W. (1970). **Crystallography and Crystal Defects**. London, Longman.
201. Hirsch, P.B., Silcox, J., Smallman, R.E., and Westmacott, K.H. (1958) Philos. Mag. 3 p. 897.

-
202. Laird, C. and Aaronson, H.I. (1966) Acta metall. **14** (2) p. 171.
 203. Dahmen, U. and Westmacott, K.H. (1983) Phys. Stat. Sol. **80** p. 249.
 204. Fujita, H. and Lu, C. (1992) Materials Transactions, JIM **33** (10) p. 892.
 205. Stobbs, W.M. and Purdy, G.R. (1978) Acta metall. **26** (7) p. 1069.
 206. Philips, V.A. (1975) Acta metall. **23** (6) p. 751.
 207. Ozbilen, S. (1996) Turkish Journal of Engineering and Environmental Sciences **20** (2) p. 103.
 208. Ozbilen, S. and Flower, H.M. (1989) Acta metall. **37** p. 2993.
 209. Kamatsubara, T. and Matsuo, M. (1989). SAE paper no. 890712. Society of Automotive Engineers, Warrendale, PA.
 210. Kamatsubara, T., Muramatsu, T., and Matsuo, M. (1990) European Patent no. 0259700 B1.
 211. Hirsch, P.B., Howie, A., Nicholson, R.B., Pashley, D.W., and Whelan, M.J. (1965). Electron Microscopy of Thin Crystals. Sevenoaks, Butterworth.
 212. Sutton, A.P. and Balluffi, R.W. (1995). Interfaces in Crystalline Materials. Monographs on the Physics and Chemistry of Materials. Oxford, Oxford University Press.
 213. Wayman, C.M. (1964). Introduction to the Crystallography of Martensitic Transformations. New York, Macmillan.
 214. Bollman, W.A. (1970). Crystal Defects and Crystalline Interfaces. Berlin, Springer.